



TECHNISCHE
UNIVERSITÄT
DARMSTADT

The In-Medium No-Core Shell Model as Comprehensive Ab-Initio Tool

VOM FACHBEREICH PHYSIK
DER TECHNISCHEN UNIVERSITÄT DARMSTADT

ZUR ERLANGUNG DES GRADES
DOCTOR RERUM NATURALIUM
(DR. RER. NAT.)

GENEHMIGTE DISSERTATION
VON TOBIAS MONGELLI, M.SC.
GEBOREN IN FRANKFURT AM MAIN

REFERENT: PROF. DR. ROBERT ROTH
KORREFERENT: PRIV.-DOZ. DR. KAI HEBELER

DARMSTADT 2022
D17

The In-Medium No-Core Shell Model as Comprehensive Ab-Initio Tool
Das In-Medium No-Core Shell Model als umfassendes Ab-Initio Tool

Referent: Prof. Dr. Robert Roth

Korreferent: Priv.-Doz. Dr. Kai Hebeler

Tag der Einreichung: 07.06.2022

Tag der mündlichen Prüfung: 18.07.2022

Mongelli, Tobias: The In-Medium No-Core Shell Model as Comprehensive Ab-Initio Tool

Darmstadt, Technische Universität Darmstadt

Jahr der Veröffentlichung auf TUPrints: 2022

URN: urn:nbn:de:tuda-tuprints-216719

URL: <https://tuprints.ulb.tu-darmstadt.de/id/eprint/21671>



Veröffentlicht unter CC BY-NC-ND 4.0 International

<https://creativecommons.org/licenses/by-nc-nd/4.0/>

Abstract

In this work we apply and extend the in-medium no-core shell model (IM-NCSM), which is a combination of the multi-reference in-medium similarity renormalization group (IM-SRG) and the no-core shell model (NCSM). The IM-NCSM contains the best features of both methods, i.e., the exact diagonalization of the NCSM giving direct access to ground-state and excited-state properties and the multi-reference state decoupling of the IM-SRG accelerating the convergence of the NCSM diagonalization. Therefore, the IM-NCSM is a very powerful method to investigate properties of open-shell medium-mass nuclei in the sd -shell and beyond.

We have used the IM-NCSM to compute scalar and non-scalar observables for a large range of even and odd isotopes in the oxygen, carbon and neon isotopic chains with a new family of chiral interactions consisting of nucleon-nucleon (NN) interactions by Entem, Machleidt and Nosyk and three-nucleon (3N) interactions by H  ther et al. This includes a full estimation of many-body and interaction uncertainties. The latter are estimated using a model based on Bayesian statistics. With these interactions we obtain converged results for ground-state energies, spectra, charge radii, and electromagnetic observables for even and odd isotopes of the aforementioned isotopic chains. In comparison with experimental results the new family of interactions gives good results for all scalar observables, even for the fully open-shell neon isotopes.

Since we systematically underestimate electric quadrupole transition strengths of oxygen and neon isotopes we extended the IM-NCSM by a leading-order three-body correction (LOTC) for the inclusion of induced three-body terms. This correction alone does not solve the underlying problem of underestimated transition strengths, but it can be used as a tool to obtain an error estimate when neglecting induced three-body contributions. With the LOTC a corner stone for future research in the IM-NCSM is set.

Zusammenfassung

In dieser Arbeit haben wir das In-Medium No-Core Shell Model (IM-NCSM) als Kombination aus der Multi-Reference In-Medium Similarity Renormalization Group (IM-SRG) und dem No-Core Shell Model (NCSM) angewendet und erweitert. Das IM-NCSM enthält die besten Aspekte beider Modelle, das heißt die exakte Diagonalisierung des NCSM, welche einen direkten Zugang zu Eigenschaften von Grundzuständen und angeregten Zuständen ermöglicht, und die Multi-Referenz Entkopplung der IM-SRG, die das Konvergenzverhalten der NCSM Diagonalisierung beschleunigt. Daher ist das IM-NCSM eine sehr mächtige Methode, um Eigenschaften von mittelschweren Kernen mit offenen Schalen bis in die *sd*-Schale und darüber hinaus zu untersuchen.

Wir haben das IM-NCSM mit einer neuen Familie chiraler Wechselwirkungen, die aus Nukleon-Nukleon (NN) Wechselwirkungen von Entem, Machleidt und Nosyk und Drei-Nukleon (3N) Wechselwirkungen von Hüther et al. besteht, verwendet, um skalare und nicht-skalare Observablen für eine Reihe von geraden und ungeraden Isotopen in der Sauerstoff-, Kohlenstoff- und Neon-Isotopenkette zu berechnen. Die Rechnungen enthalten eine vollständige Bestimmung von Vielteilchen- und Wechselwirkungsunsicherheiten. Letztere werden mit einem auf Bayes'scher Statistik beruhenden Modell abgeschätzt. Mit diesen Wechselwirkungen erhalten wir konvergierte Ergebnisse für Grundzustandsenergien, Spektren, Ladungsradien sowie elektromagnetische Observablen für gerade und ungerade Isotopen der vorgenannten Isotopenketten. Im Vergleich mit experimentellen Ergebnissen liefert die neue Wechselwirkungsfamilie unter Verwendung des IM-NCSM gute Ergebnisse für alle skalaren Observablen, auch für Neon-Isotope mit vollständig offenen Schalen.

Da wir systematisch elektrische Quadrupol-Übergangsstärken in Sauerstoff- und Neon-Isotopen unterschätzen, haben wir das IM-NCSM um eine Dreiteilchen-Korrektur in führender Ordnung (LOTC) erweitert. Diese Korrektur alleine löst nicht das zugrundeliegende Problem unterschätzter Übergangsstärken, kann jedoch als Werkzeug eingesetzt werden, um eine Fehlerabschätzung für die Vernachlässigung induzierter Dreiteilchenbeiträge zu erhalten. Mit dem LOTC wurde ein Grundstein für weitere Forschungen im IM-NCSM gelegt.

List of Abbreviations

3N	three-nucleon
BCH	Baker-Campbell-Hausdorff
χ -EFT	chiral effective field theory
EFT	effective field theory
EMN	Entem, Machleidt, and Nosyk
HF	Hartree-Fock
HO	harmonic oscillator
IM-NCSM	in-medium no-core shell model
IM-SRG	in-medium similarity renormalization group
IT-NCSM	importance-truncated no-core shell model
LEC	low-energy constant
LENPIC	low energy nuclear physics international collaboration
LO	leading order
LOTC	leading-order three-body correction
MCPT	multi-configurational many-body perturbation theory
MR-NO	multi-reference normal order
NAT	natural orbital
NCSM	no-core shell model
NLO	next-to-leading order
N ² LO	next-to-next-to-leading order
N ³ LO	next-to-next-to-next-to-leading order
NN	nucleon-nucleon
NO2B	normal-ordered two-body
ODE	ordinary differential equation
PGCM	projected generator coordinate method
PGCM-PT	projected generator coordinate method perturbation theory
SCS	semi-local coordinate space
SMS	semi-local momentum space
SR-NO	single-reference normal order
SRG	similarity renormalization group
QCD	quantum chromodynamics

VSSM valence-space shell model

Contents

1	Introduction	1
2	The No-Core Shell Model	5
2.1	Basic Concepts and Symmetries	5
2.2	Importance Truncation	9
2.3	The NCSM in Different Single-Particle Bases	10
3	Normal Ordering and the Wick Theorem	13
3.1	Normal Ordering With Respect to the Vacuum	13
3.2	Normal Ordering With Respect to a Single-Reference State	15
3.3	Normal Ordering With Respect to a Multi-Reference State	18
4	The Similarity Renormalization Group	23
5	The In-Medium SRG	27
5.1	Motivation and Concept	27
5.2	Normal-Ordered Hamiltonian	29
5.2.1	Vacuum- and Reference-State Normal Ordering	29
5.2.2	Normal-Ordered Two-Body Approximation	31
5.3	The IM-SRG(2)	32
5.4	The IM-SRG With the Magnus Expansion	33
5.5	Magnus(2)	34
5.6	Multi-Reference IM-SRG Commutator Equations	36
5.6.1	Spherical Natural Orbitals and m -Scheme Equations	36
5.7	Angular Momentum Theory	41
5.7.1	Angular Momentum Coupling	41
5.7.2	The Wigner-Eckart Theorem	45
5.7.3	Vacuum- and Reference-State Normal Ordering for Spherical Equations	46
5.8	J -Coupled Scalar Commutator Equations in Natural Orbitals	47
5.9	J -Coupled Non-Scalar Commutator Equations in Natural Orbitals	48
5.10	Generators of the IM-SRG	50

5.10.1	The Wegner Generator	50
5.10.2	The White- and Imaginary-Time Generators	51
5.10.3	Decoupling Patterns	53
6	Derivation of a Leading-Order Three-Body Correction	55
6.1	Strategy for the LOTC	55
6.2	Three-Body Commutators and the LOTC	56
6.2.1	Derivation of the Three-Body Commutators	56
6.2.2	LOTC Approximation	64
6.3	Implementation of the Two-Body Equations	66
6.4	Programmatical Derivation of Commutators for the IM-SRG Framework	71
7	The In-Medium No-Core Shell Model	75
7.1	The IM-NCSM Scheme	75
7.2	Particle Attachment and Removal	76
7.3	Observables in the IM-NCSM	77
7.3.1	Radius Operator	77
7.3.2	Electromagnetic Observables	79
7.4	Hamiltonians and Uncertainty Estimation	81
7.4.1	Hamiltonians and Truncations	81
7.4.2	Uncertainty Estimation	82
8	Results	85
8.1	Analysis of ^{12}C	86
8.2	Ground-State Energies and Charge Radii	95
8.2.1	Ground-State Energies	95
8.2.2	Charge Radii	100
8.3	Excitation Spectra	105
8.4	Electromagnetic Observables	112
8.4.1	Electric Quadrupole Observables	112
8.4.2	Magnetic Dipole Observables	123
8.5	Isotopic Chains	127
8.6	Leading-Order Three-Body Correction	131
9	Conclusion and Outlook	135
A	Working Equations of the LOTC	139
	Bibliography	151

1. Introduction

The main focus of theoretical nuclear structure physics is to explore the properties of nuclei in the low-energy regime across the nuclear chart. The nucleus consists of protons and neutrons, which can be described by the theory of the strong interaction, quantum chromodynamics (QCD) [PS95]. Since quarks and gluons are the underlying degrees of freedom of protons and neutrons, the interaction between nucleons is not fundamental. The key problems in the description of a nucleus are the derivation of a Hamiltonian and the solution of the many-body Schrödinger equation, which are both not trivial. The description of a nuclear Hamiltonian from QCD directly is possible using lattice QCD approaches [Bea+06; IAH07; Ino+10] but not practicable due to the non-perturbative nature in the low-energy regime as consequence of the so-called confinement. After attempts to adapt QCD inspired quark models [Pan87; Har81a; Har81b; EFV00], which are not fundamental, a breakthrough was reached by the introduction of a chiral effective field theory (χ -EFT) built on low-energy QCD, which is formulated in a perturbative approach. Following the idea of Weinberg [Wei79], the most general Lagrangian in accordance with symmetries of QCD, especially the broken chiral symmetry, is written down. In the low-energy regime pions as Goldstone bosons and nucleons are the relevant degrees of freedom instead of quarks and gluons. The existence of these Goldstone bosons indicates that the chiral symmetry is broken spontaneously. Furthermore, this symmetry is also broken explicitly due to non-vanishing quark masses [ME11].

In chiral perturbation theory the effective Lagrangian is formulated including the dynamics between pions, interactions between pions and nucleons and interactions among nucleons. Since the number of terms in the effective Lagrangian is infinite, a power counting scheme is applied by analyzing the contributions in terms of powers of small external momenta over the large scale $(Q/\Lambda_\chi)^\nu$, where Q is a generic momentum, Λ_χ is the so-called symmetry breaking scale, and ν is the chiral order. With this scheme, the number of diagrams for every chiral order is finite [Wei90; ME11]. The first order in this power counting scheme at $\nu = 0$ is the leading order (LO), followed by the next-to-leading order (NLO, $\nu = 2$) and next-to-next-to-leading order (N²LO, $\nu = 3$) and so on. The order $\nu = 1$ vanishes due to parity and time-reversal invariance [ME11]. Additionally, in the power counting scheme from N²LO on, three-nucleon (3N) forces occur [Kol94; Epe+02]. These appear only in higher orders and are therefore suppressed com-

pared to NN forces, but it has been shown that 3N interactions are necessary to close the discrepancy to experimental results [KE07]. An advantage of chiral perturbation theory is that with each order new terms enter the theory making it systematically improvable. The contributions of these interactions include low-energy constants (LECs), which can be determined by fits to experimental data [Hüt+20].

For a long time chiral NN interactions at N³LO by Entem and Machleidt [EM02] supplemented with local 3N interactions [Nav07] at N²LO have been used, which systematically underestimate nuclear charge radii [Som+14; Bin+14; CBN15; Lap+16]. With this behavior in mind, new interactions like the NNLO_{sat} interactions [Eks+15] have been developed, which corrects radii. Other available NN forces are semi-local coordinate space (SCS) and momentum space (SMS) interactions [EKM15a; EKM15b] and non-local interactions by Entem, Machleidt and Nosyk (EMN) [EMN17]. The advantage of these interactions compared to the NNLO_{sat}, for example, is the availability of several orders, which opens the possibility to quantify interaction uncertainties. One approach to estimate chiral interaction uncertainties by Epelbaum, Krebs and Meißner [EKM15a] has been used successfully [EKM15b; Bin+16; Bin+18]. Another scheme based on Bayesian statistics was developed by the BUQEYE collaboration [Fur+15; MWF17; Mel+19]. In this work, the interactions of Entem, Machleidt and Nosyk are used together with non-local 3N interactions at N²LO and N³LO [Epe+02; Heb+15] by Epelbaum and Hebeler. These interactions were recently optimized in our group to describe nuclear observables, especially in the medium-mass regime more accurately [Hüt+20]. Ongoing research on new families of interactions is performed within the low energy nuclear physics international collaboration (LENPIC) in order to construct consistent NN and 3N interactions and exchange currents for the semi-local SMS and SCS interactions [Epe+19; Mar+21]. After the Hamiltonian is constructed we have to solve the many-body Schrödinger equation, which is not possible without approximations. Over the past decade different many-body methods have been developed. First of all, we mention the free-space similarity renormalization group (SRG) [BFP07; BFS10; RNF10; Rot+14], which pre-diagonalizes the Hamiltonian by a decoupling of low and high momenta in order to improve the convergence behavior in *ab initio* calculations.

Regarding the solution of the nuclear Schrödinger equation, several methods have been developed over the past years. Two prominent representatives of shell-model approaches are the no-core shell model (NCSM) [Nav+07; Nav+09; BNV13] and the valence-space shell model (VSSM) [Kuo66; Cau+05; Cor+14]. Both methods solve an eigenvalue problem using a model space, which is constructed by a basis and the truncation of the many-body Hilbert space. The advantage is that the eigenvalues of the Hamiltonian can be computed directly making it possible to obtain ground- and excited-state observables. The difference between the NCSM and VSSM is that all nucleons in the NCSM are

considered as active degrees of freedom, while in the VSSM a subset of the nucleons are placed on fixed single-particle states, which is described as frozen core. The NCSM is very successful and widely used in *ab initio* structure physics, but the basis dimension and computing effort grow tremendously with the particle number of the considered nucleus. This restriction was relaxed up to nuclei in the p - and lower sd -shell with the introduction of an importance-truncated version of the NCSM, also called IT-NCSM [RN07; Rot09].

Other theory approaches are the self-consistent Green's functions method [DB04; CBN13], the coupled-cluster approach [Hag+07; Hag+08; Hag+14; Bin+14; Sig+15; Hag+16] and the in-medium similarity renormalization group (IM-SRG) [TBS11; TBS12; Her+16; Her16]. These methods are better suited for the description of medium-mass nuclei, since their truncation patterns are conceptionally different, i.e., the scaling with respect to the particle number is not as strong compared to the shell-model approaches. The disadvantage is that these methods in their basic formulation are restricted to ground-state observables and closed-shell nuclei.

The IM-SRG was introduced by Tsukiyama et al. [TBS11] and uses the SRG approach for a unitary transformation of the Hamiltonian in such a way that a reference state, like a single Slater determinant, is decoupled from all particle-hole excitations. If the reference state is a single Slater determinant we talk about the single-reference IM-SRG, which is restricted to ground-state observables and the description of closed-shell nuclei only is possible [TBS11]. For the description of open-shell nuclei the multi-reference IM-SRG was proposed by Hergert et al. [Her+13a; Her+14] and used together with Hartree-Fock-Bogoliubov reference states for the description of even oxygen, calcium and nickel isotopes. In order to compute excited state observables using the IM-SRG, three different approaches are possible. One is the equation-of-motion approach of the IM-SRG [PMB17], the second is the valence-space IM-SRG [Str+16; Miy+20] and the third is the combination of the multi-reference IM-SRG with the NCSM giving the so-called IM-NCSM, which has been proposed in [Geb+17]. The IM-NCSM can be described as a hybrid method, which overcomes the shortcomings of both methods. In the IM-NCSM a correlated multi-determinantal reference state is computed and used for a transformation of the Hamiltonian. The consequence is that in a post-NCSM diagonalization the convergence accelerated. This framework has been successfully applied [Geb+17; Geb17; Vob20; Hüt+20; DA1+20; Fro+22a]. The IM-NCSM has also been extended with the so-called Magnus formulation [Mag54] making it possible to transform electromagnetic operators. Furthermore, the calculation of nuclei with odd mass numbers is possible [Vob20]. Another extension affecting the IM-NCSM is the availability of different single-particle bases like the Hartree-Fock or natural orbital basis [Tic+19; Hop+21]. Especially the latter significantly accelerates the convergence of the IM-NCSM.

In this work we employ the IM-NCSM framework using a new family of chiral interactions [Hüt+20] for the exploration of properties of open- and closed-shell medium-mass nuclei. For the first time we compute scalar and non-scalar observables in the IM-NCSM framework with fully quantified many-body and interaction uncertainties. Furthermore, we present an approach for the inclusion of induced three-body interactions in the IM-NCSM.

The organization of this thesis is the following: In chapter 2 we explain the concepts of the NCSM including the importance truncation and different single-particle bases. Afterwards, we discuss the theory of normal-ordering and its importance for the IM-SRG framework in chapter 3. Chapter 4 is about the theoretical foundations of the free-space SRG. In chapter 5 we deal with the basics of the IM-SRG framework including the Magnus formulation of the flow-equations. Furthermore, we show the equations used for the solution of the IM-SRG in the so-called m -scheme, followed by the theory of angular momentum coupling. After this we discuss the j -coupled equations of the IM-SRG for scalar and non-scalar observables. We finish the chapter with a description of the generators used in the IM-SRG framework. In chapter 6 we discuss the derivation of a novel approximation for the inclusion of induced three-body contributions into the IM-SRG framework. Chapter 7 shows the basics of the IM-NCSM including an approach to access odd nuclei and the construction of the radius operator and electromagnetic multipole operators. We finish this chapter with a description of the Hamiltonians we use for the IM-NCSM calculations followed by a discussion of the uncertainty estimation. In chapter 8 we present our results from IM-NCSM calculations of open- and closed-shell nuclei in the oxygen, carbon, and neon isotopic chain. After this we show and discuss the results obtained by the three-body correction for the IM-NCSM followed by a short conclusion and outlook, which is presented in chapter 9.

2. The No-Core Shell Model

In this chapter we introduce the no-core shell model (NCSM) as an *ab initio* many-body method. After the discussion of its basic ingredients and the use of symmetries, we address the importance truncated NCSM as an extension of the standard NCSM. Finally, different bases for the NCSM are introduced and compared to each other.

2.1. Basic Concepts and Symmetries

The *ab initio* NCSM is a universal method to solve the nuclear many-body problem for light nuclei using realistical two- and two- plus three-body potentials [Nav+09; BNV13]. Formally, in a basic assumption, a system of A point-like non-relativistic interacting nucleons is considered. These nucleons are considered active meaning that no inert core exists compared to standard shell-model calculations. The NCSM is used to solve the stationary Schrödinger equation

$$\hat{H} |\psi_n\rangle = E_n |\psi_n\rangle, \quad (2.1)$$

where \hat{H} is the Hamiltonian with the eigenvalue E_n and the eigenstate $|\psi_n\rangle$. In this work, we use a Hamiltonian, which consists of an intrinsic kinetic energy \hat{T}_{int} , a nucleon-nucleon (NN) interaction V_{NN} and a three-nucleon (3N) interaction V_{3N}

$$\hat{H} = \hat{T}_{\text{int}} + \hat{V}^{[2]} + \hat{V}^{[3]} = \frac{1}{A} \sum_{i < j} \frac{(\hat{\mathbf{p}}_i - \hat{\mathbf{p}}_j)^2}{2m} + \sum_{i < j} V_{\text{NN},ij} + \sum_{i < j < k} V_{\text{3N},ijk}, \quad (2.2)$$

where $\hat{\mathbf{p}}_i$ is the single-particle momentum, A is the number of nucleons and m is the nucleon mass.

The eigenstates are expanded in an orthonormal basis of A -body states $|\phi_i\rangle$,

$$|\psi_n\rangle = \sum_i c_i^{(n)} |\phi_i\rangle, \quad (2.3)$$

where $c_i^{(n)}$ denotes the expansion coefficient. The Schrödinger equation can then be rewritten as a matrix eigenvalue problem, which is solved numerically

$$\sum_i \langle \phi_j | \hat{H} | \phi_i \rangle c_i^{(n)} = E_n c_j^{(n)}. \quad (2.4)$$

The basis states $|\phi_i\rangle$ are antisymmetrized A -body product states known as Slater determinants

$$|\phi_i\rangle = |p_1 p_2 \dots p_A\rangle = \sqrt{A!} \hat{\mathcal{A}} \left(\prod_{i=1}^A |p_i\rangle \right), \quad (2.5)$$

where $\hat{\mathcal{A}}$ is the antisymmetrizer and $|p_i\rangle$ are single-particle states. These Slater determinants form a basis \mathcal{B}_A of the antisymmetric A -body Hilbert space. Each single-particle state can be written as

$$|p\rangle = |n(ls)jm_jtm_t\rangle, \quad (2.6)$$

where n is the radial quantum number, l denotes the orbital angular momentum, s is the spin, j is the total ls -coupled angular momentum, m_j refers to the projection of j , t is the isospin and m_t its projection. For sake of simplicity, we omit the spin s and isospin t quantum numbers, which are both $\frac{1}{2}$ for nucleons. Since we are not able to handle an infinite A -body model space, truncations for the many-body space are introduced, e.g. with respect to the principal quantum number $e = 2n + l$, where the harmonic oscillator single-particle energy is given by $\epsilon = (e + \frac{3}{2}) \hbar\Omega$.

In the NCSM, the model space is truncated by an upper limit on the excitation energy of each many-body basis state, $N_{\max} \hbar\Omega$. For the explanation of this truncation scheme we define the energy of a Slater determinant $e(|\phi_i\rangle)$ as the sum of all single-particle energies. Further, we define the basis determinant $|\phi_0\rangle$ as the configuration with the lowest principal quantum number $e(|\phi_0\rangle)$. If we now define the number of excitation quanta as $N = \frac{E^*}{\hbar\Omega}$, where $E^* = e(|\phi_i\rangle) - e(|\phi_0\rangle)$ is the unperturbed excitation energy of a Slater determinant $|\phi_i\rangle$, the N_{\max} truncated model space can be written as

$$\mathcal{M}^{N_{\max}} = \text{span} \left(\{ |\phi_i^N\rangle : N(e(|\phi_i\rangle)) \leq N_{\max} \} \right). \quad (2.7)$$

The N_{\max} truncation scheme of the NCSM is illustrated in Fig. 2.1 with ^{12}C as example.

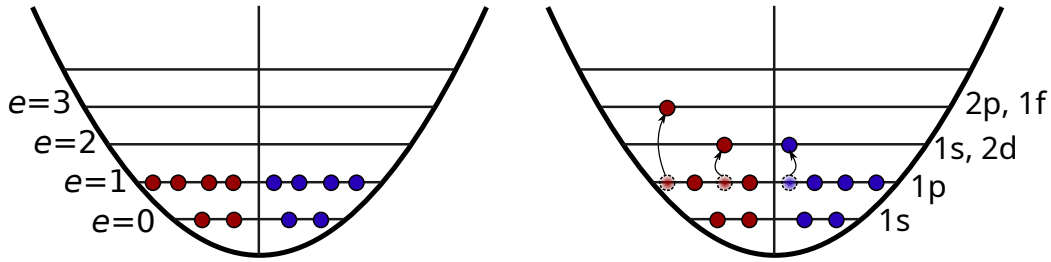


Fig. 2.1.: Schematical illustration of the truncation scheme in the NCSM that is used for an N_{\max} -truncated model space. On the left side, the configuration of ^{12}C is shown, where the $1s$ and $1p$ shell are filled up by 6 protons and 6 neutrons. On the right side, an example for a Slater determinant with $N=4$ harmonic oscillator excitation quanta is shown belonging to a model-space with $N_{\max} \geq 4$.

The model-space dimension can be further reduced by taking symmetries of the Hamiltonian like rotational invariance and parity conservation into account. The consequence of the rotational invariance is that the eigenstates of the Hamiltonian are degenerate with respect to the projection quantum number M_J , which is additive and given by

$$M_J = \sum_{i=1}^A m_{j_i}. \quad (2.8)$$

We can restrict the model space to a specific value of M_J , where the smallest allowed value is $M_J = 0$ for even and $M_J = \frac{1}{2}$ for odd particle numbers. Furthermore, the parity conservation leads to another reduction of the model-space size since we restrict it to positive or negative parity basis states only. The parity Π of a Slater determinant can be written as

$$\Pi = \prod_{i=1}^A (-1)^{l_i}. \quad (2.9)$$

Using this parity we usually restrict the model space to basis states of natural parity, which is predicted for the ground state by the naive shell model. Since eigenstates with even and odd number of excitation quanta contain opposite parities the truncation parameter N_{\max} has to be increased in steps of two.

Another symmetry of the Hamiltonian is translational invariance, which can be used for the harmonic oscillator (HO) basis in the NCSM. This basis gives the possibility to separate intrinsic and center-of-mass degrees of freedom. We are able to factorize the eigenstates into an intrinsic part $|\psi_{\text{int}}\rangle$ and a center-of-mass part $|\psi_{\text{cm}}\rangle$

$$|\psi\rangle = |\psi_{\text{int}}\rangle \otimes |\psi_{\text{cm}}\rangle. \quad (2.10)$$

From the translational invariance of the Hamiltonian it follows that the intrinsic properties of the system are not affected by the center-of-mass part of the Hamiltonian. This allows to subdivide the Hamiltonian into an intrinsic \hat{H}_{int} and a center-of-mass part \hat{H}_{cm} [Nav+09]. The center-of-mass Hamiltonian is given by

$$\hat{H}_{\text{cm}} = \frac{\hat{\mathbf{P}}^2}{2mA} + \frac{mA\Omega}{2}\hat{\mathbf{R}}^2 - \frac{3}{2}\hbar\Omega, \quad (2.11)$$

where m is the nucleon mass and $\hat{\mathbf{R}}$ and $\hat{\mathbf{P}}$ are the center-of-mass coordinate and momentum.

The energy spectrum contains center-of-mass excitations. To cancel these out, we follow the method of [RGP09]. The total Hamiltonian can be written as

$$\hat{H} = \hat{H}_{\text{int}} + \lambda\hat{H}_{\text{cm}}, \quad (2.12)$$

where λ is a positive constant controlling the strength of the center-of-mass part. This is necessary to shift eigenstates with an excited center-of-mass part to higher energies to remove these contributions from the lower-energy part of the spectrum.

In practical NCSM calculations we are interested in the computation of different observables like ground-state and excited-state energies. These are computed as function of N_{max} , where we aim for convergence. With increasing values of N_{max} , the model-space size also increases factorial depending on the particle number A and the number of excitation quanta N_{max} . Since we are only interested in the lowest-lying eigenstates, we are using a Lanczos-type algorithm [Lan50] for the diagonalization reducing the computational effort and making calculations for large model spaces up to 10^9 possible [MVS09]. But since these large model-space sizes are reached even for light nuclei, the NCSM is limited to nuclei with mass numbers $A \leq 16$ [Bin+18].

Due to the direct access to the eigenstates of the total Hamiltonian we are able to compute ground-state energies and low-lying excited energies. Furthermore, the NCSM can access other observables like charge radii and electromagnetic transition strengths and moments.

2.2. Importance Truncation

The importance-truncated NCSM (IT-NCSM) [Rot09] is a possibility to overcome the model-space limitations of the NCSM. It introduces an importance measure for a selection of the physically most important basis states for a description of specific eigenstates according to the properties of the Hamiltonian. Only these basis states are selected to construct a new model-space with a much lower dimension. Therefore, we can use the IT-NCSM to obtain results with a larger N_{\max} value and also to access heavier nuclei. The importance-truncation is constructed by using the multi-configurational many-body perturbation theory (MCPT) [RSS03; Sur+04]. The starting point is the full NCSM model space \mathcal{M} , which is spanned by a basis set $\{|\phi_\nu\rangle\}$. We need to construct a reference model space \mathcal{M}_{ref} with $|\psi_{\text{ref}}\rangle$ as a zeroth-order approximation for the eigenstate of interest. MCPT is then used to compute leading-order corrections to the reference state $|\psi_{\text{ref}}\rangle$, where we need to split the full Hamiltonian \hat{H} into an unperturbed part \hat{H}_0 and a perturbed part \hat{W} . With the reference state $|\psi_{\text{ref}}\rangle$ as starting point, the unperturbed Hamiltonian can be written as

$$\hat{H}_0 = \epsilon_{\text{ref}} |\psi_{\text{ref}}\rangle \langle \psi_{\text{ref}}| + \sum_{\nu \notin \mathcal{M}_{\text{ref}}} \epsilon_\nu |\phi_\nu\rangle \langle \phi_\nu|, \quad (2.13)$$

where $\epsilon_{\text{ref}} = \langle \psi_{\text{ref}} | \hat{H} | \psi_{\text{ref}} \rangle$ is the expectation value of the full Hamiltonian and ϵ_ν are the unperturbed energies coming from the Møller-Plesset formulation of MCPT with $\epsilon_\nu = \epsilon_{\text{ref}} + \Delta \epsilon_\nu$. The perturbation \hat{W} is defined as $\hat{W} = \hat{H} - \hat{H}_0$ and the zeroth-order contribution to the perturbation series is the reference state itself. The perturbation comes into the first-order correction, which can be written as

$$|\psi^{(1)}\rangle = - \sum_{\nu \notin \mathcal{M}_{\text{ref}}} \frac{\langle \phi_\nu | \hat{W} | \psi_{\text{ref}} \rangle}{\epsilon_\nu - \epsilon_{\text{ref}}} |\phi_\nu\rangle = - \sum_{\nu \notin \mathcal{M}_{\text{ref}}} \frac{\langle \phi_\nu | \hat{H} | \psi_{\text{ref}} \rangle}{\epsilon_\nu - \epsilon_{\text{ref}}} |\phi_\nu\rangle, \quad (2.14)$$

where $\kappa_\nu = -\frac{\langle \phi_\nu | \hat{H} | \psi_{\text{ref}} \rangle}{\epsilon_\nu - \epsilon_{\text{ref}}}$ is the so-called importance measure. Only basis states with an importance measure $|\kappa_\nu| > \kappa_{\min}$ are included in the importance-truncated model space. Since we are interested in a N_{\max} sequence to show the convergence behavior of the model-space size we combine the sequential increase of N_{\max} with the importance truncation. Let us start with a full NCSM calculation in a $N_{\max} = 2$ model-space. From this eigenstate we can construct the importance-truncated $N_{\max} = 4$ space and solve the NCSM again to obtain a new reference state. This can be used to obtain the importance-truncated $N_{\max} = 6$ reference space and so on. From a computational point of view the

most challenging part of the IT-NCSM is the construction of the importance-truncated model-space. The diagonalization on the other hand is much cheaper compared to the full NCSM calculation due to the fact that the importance-truncated space is much smaller. In this work we use an importance measure κ_{\min} , which is of the order 10^{-4} . For taking the effect of κ_{\min} into account we compute a sequence of increasing κ_{\min} values. Afterwards, to obtain the full NCSM result we perform an *a posteriori* extrapolation to the limit of $\kappa_{\min} \rightarrow 0$ for each value of N_{\max} with an uncertainty estimation for the desired observables. The extrapolation is performed by using a polynomial fit for a sequence of observables for different values of κ_{\min} .

2.3. The NCSM in Different Single-Particle Bases

As we have seen, the original formulation of the NCSM uses the harmonic oscillator single-particle basis. A disadvantage of the harmonic oscillator basis is the asymptotic behavior of the harmonic oscillator wavefunctions, which can result in a slow N_{\max} convergence. Furthermore, the observables depend on the oscillator frequency $\hbar\Omega$. For obtaining converged results, a computationally demanding frequency analysis has to be performed for each nucleus of interest. To avoid this procedure, two alternative single-particle bases will be presented in this section. These are the Hartree-Fock basis and the natural orbital basis, where especially the latter one accelerates the convergence of the (IT)-NCSM [Tic+19].

The Hartree-Fock Basis. In nuclear structure physics and quantum chemistry, the Hartree-Fock approximation is a standard tool and therefore we will not cover it by extend here but details of the Hartree-Fock method and its construction can be found in [RS80; Suh07].

The Hartree-Fock approximation is a variational calculation for the ground state of a nucleus. We use one single Slater determinant $|\phi\rangle$, where the single-particle states are the variational degrees of freedom. The starting point is the mean-field approximation, i.e., each nucleon is moving in an external field created by the other $A - 1$ nucleons. Using this approximation, the energy of $|\phi\rangle$ is minimized by solving non-linear Hartree-Fock equations iteratively until self-consistency is reached. This means that the single-particle states of $|\phi\rangle$ do not change anymore during the next iterations. When reaching convergence, the eigenstates and energies of the self consistent mean-field are obtained. The Hartree-Fock optimized single particle basis is widely used in methods, where properties of medium-mass nuclei are computed, like the single-reference IM-SRG [Her+16] or coupled-cluster theory [Hag+14; Hag+16].

The Natural Orbital Basis. Another useful basis for the NCSM are natural orbitals, which are the eigenvectors of a one-body density matrix.

The great advantage of this basis is that the dependency on $\hbar\Omega$ is removed and the N_{\max} convergence behavior is improved. While there are many ways to construct the one-body density matrix Tichai et al. have found that a second-order corrected one-body density matrix can be efficiently derived using Hartree-Fock many-body perturbation theory [Tic+19]. This method is computational much easier to apply compared to the calculation of a fully correlated ground state from the NCSM, where a large model-space is needed. Another advantage is that the occupied and the unoccupied single-particle states contribute to the correlated ground state and the one-body density matrix. Therefore, all single-particle states are optimized during the calculation.

More details on natural orbitals like their construction and a comparison of different NCSM calculations using the HO and Hartree-Fock basis can be found in [Tic+19]. The outstanding properties of the natural orbital basis allow us to use the IM-NCSM more efficiently, which is a reason why we use this basis mostly for our calculations within this work. More about that can be found in the results chapter 8, where we investigate the behavior of the Hartree-Fock and natural orbital basis in comparison to each other.

Note that in other single-particle bases the factorization of the intrinsic and center-of-mass contributions is not correct anymore and only recovered for the exact solution of the NCSM using an infinite value of N_{\max} . Due to this problem we have to choose the strength of the center-of-mass part λ large enough to shift the center-of-mass eigenstates upwards but as small as possible that its action on the intrinsic eigenstates is minimal. Using NCSM calculations it has been found out that the optimal value for λ ranges between 0.2 and 1.0 [Vob20].

3. Normal Ordering and the Wick Theorem

In this chapter, we will discuss normal ordering with respect to different A -body states. Normal ordering with respect to a non-trivial reference state offers the possibility to approximately take operators beyond the two-body rank into account. To perform normal ordering, an A -body reference state is needed. In this work we will present normal ordering with respect to three types of reference states. The physical vacuum $|0\rangle$, a single Slater determinant $|\Phi\rangle$ (single-reference) and a linear combination of Slater determinants $|\Psi\rangle$ (multi-reference). Further, normal ordering with respect to the vacuum is a special case of the single-reference case, which is in turn a special case of the multi-reference case. This work mainly focusses on the multi-reference case and we follow formalism of Kutzelnigg and Mukherjee [KM97].

3.1. Normal Ordering With Respect to the Vacuum

We will start with the following definition [SB09; Wic50]:

Definition 3.1: Normal Ordering with Respect to the Vacuum

A product of fermionic operators is in normal order with respect to the vacuum $|0\rangle$ if all creation operators \hat{a}_p^\dagger are to the left of all annihilation operators \hat{a}_p .

First, we introduce an abbreviation for the creation operator $\hat{a}^p := \hat{a}_p^\dagger$, where the annihilation operator is denoted as \hat{a}_q . Further, let us define a normal-ordering operator $\{\hat{A}_1\hat{A}_2\dots\hat{A}_n\}_{|0\rangle}$, which brings a product of creation and annihilation operators into a normal ordered form with respect to the vacuum with a phase factor due to the permutation of the operators. Now, we show how the normal-ordering operator acts on a product of fermionic operators $\{\hat{A}_1\hat{A}_2\dots\hat{A}_n\}$. Note that the index refers to the reference state. Each of the fermionic operators represents a creation operator \hat{a}^p or an annihilation operator \hat{a}_q

$$\{\hat{A}_1\hat{A}_2\dots\hat{A}_n\}_{|0\rangle} := \text{sgn}(\pi)\hat{A}_{\pi(1)}\hat{A}_{\pi(2)}\dots\hat{A}_{\pi(n)}, \quad (3.15)$$

where $\text{sgn}(\pi)$ denotes the sign of the permutation $\pi \in (1, 2, \dots, n)$, which is needed to bring the operator product into normal order. The normal-ordering operator additionally has

the following properties:

1. Linearity:

$$\begin{aligned} \{\hat{A}_1 \hat{A}_2 \dots \hat{A}_i (\mu \hat{B} + \hat{C}) \hat{A}_{i+1} \dots \hat{A}_n\}_{|0\rangle} &= \mu \{\hat{A}_1 \hat{A}_2 \dots \hat{A}_i \hat{B} \hat{A}_{i+1} \dots \hat{A}_n\}_{|0\rangle} \\ &+ \{\hat{A}_1 \hat{A}_2 \dots \hat{A}_i \hat{C} \hat{A}_{i+1} \dots \hat{A}_n\}_{|0\rangle} \end{aligned}$$

2. Mapping of the identity operator onto itself in the antisymmetric Fock space

3. Antisymmetry under transposition of two different operators:

$$\{\hat{A}_1 \hat{A}_2 \dots \hat{A}_i \hat{A}_j \dots \hat{A}_n\}_{|0\rangle} = -\{\hat{A}_1 \hat{A}_2 \dots \hat{A}_j \hat{A}_i \dots \hat{A}_n\}_{|0\rangle}$$

Another property of operators normal ordered with respect to the vacuum is that their vacuum expectation value vanishes

$$\langle 0 | \{\hat{A}_1 \hat{A}_2 \dots \hat{A}_n\} | 0 \rangle = 0. \quad (3.16)$$

In order to transform a product, which is not in normal order into a normal-ordered product of fermionic operators we can use the following anticommutator relations:

$$\{\hat{a}^p, \hat{a}_q\} = \delta_q^p, \quad \{\hat{a}^p, \hat{a}^q\} = 0, \quad \{\hat{a}_p, \hat{a}_q\} = 0 \quad (3.17)$$

Since this procedure can be very time consuming, we will employ Wick's theorem, which will be presented in the next section.

3.2. Normal Ordering With Respect to a Single-Reference State

In this section we describe how to use the normal-ordering technique with respect to a single Slater determinant in a particle-hole formalism. Let $|\Phi\rangle$ be an A -body single-determinantal reference state

$$|\Phi\rangle = \prod_{i=1}^A \hat{a}^i |0\rangle. \quad (3.18)$$

First of all we want to define the basis and notation of the particle-hole formalism.

Definition 3.2: Basis and Notation of the Particle-Hole Formalism

An orthonormal basis $\{\hat{a}^p |0\rangle : p = 1, 2, \dots\}$ of the one-body Hilbert space is formed by occupied hole states \hat{a}^i and unoccupied particle states \hat{a}^b , which fulfill when acting on the reference state $|\Phi\rangle$

$$\hat{a}^i |\Phi\rangle = 0 \quad \text{with } i = 1, 2, \dots, A \quad (3.19)$$

and

$$\hat{a}_b |\Phi\rangle = 0 \quad \text{with } b > A. \quad (3.20)$$

The indices i, j, k, \dots are hole and b, c, d, \dots are particle indices. Furthermore, \hat{a}^i and \hat{a}_b are quasiparticle annihilators and \hat{a}_i and \hat{a}^b are quasiparticle creators.

Now we can reformulate the definition of normal ordering with respect to a single-reference state $|\Phi\rangle$.

Definition 3.3: Normal Ordering with Respect to a Single-Reference State

A product of operators is in normal order with respect to a single-reference state $|\Phi\rangle$, if all quasiparticle creators are to the left of all quasiparticle annihilators.

Like in the section before we can now introduce a normal-ordering operator $\{\hat{A}_1 \hat{A}_2 \dots \hat{A}_n\}_{|\Phi\rangle}$ with respect to a single-reference state $|\Phi\rangle$, which fulfills the same three properties as in the vacuum case. This is a special case of an empty single-reference state. One important property of operators in single-reference normal order (SR-NO) is that their expectation value with respect to $|\Phi\rangle$ vanishes

$$\langle \Phi | \{\hat{A}_1 \hat{A}_2 \dots \hat{A}_n\}_{|\Phi\rangle} | \Phi \rangle = 0. \quad (3.21)$$

We can now formulate Wick's theorem with respect to a given single-reference state [Wic50].

Theorem 3.1: Wick's Theorem

An arbitrary product of fermion operators is equal to the corresponding normal-ordered product plus all possible contractions.

$$\hat{A}_1 \hat{A}_2 \dots \hat{A}_n = \{\hat{A}_1 \hat{A}_2 \dots \hat{A}_n\}_{|\Phi\rangle} + \sum_{\text{contractions}} \{\hat{A}_1 \hat{A}_2 \dots \hat{A}_n\}_{|\Phi\rangle} \quad (3.22)$$

A contraction between two operators \hat{A}_1 and \hat{A}_2 , which is a complex number can be written as $\overline{\hat{A}_1 \hat{A}_2}$. Now, let us use Wick's theorem to compute the product of two operators \hat{A}_1 and \hat{A}_2

$$\hat{A}_1 \hat{A}_2 = \{\hat{A}_1 \hat{A}_2\}_{|\Phi\rangle} + \overline{\hat{A}_1 \hat{A}_2}, \quad (3.23)$$

where we used the convention $\{\hat{A}_1 \hat{A}_2\}_{|\Phi\rangle}$ for a product in SR-NO. Using Eq. (3.21), we obtain

$$\overline{\hat{A}_1 \hat{A}_2} = \langle \Phi | \hat{A}_1 \hat{A}_2 | \Phi \rangle. \quad (3.24)$$

Now we can define a contraction between a creator and an annihilator as hole contraction

$$\overline{\hat{a}^p \hat{a}_q} = \langle \Phi | \hat{a}^p \hat{a}_q | \Phi \rangle = \gamma_q^p, \quad (3.25)$$

which is the one-particle density matrix element γ_q^p with respect to the reference state. The particle contraction is, therefore, a contraction between an annihilator and a creator

$$\overline{\hat{a}_q \hat{a}^p} = \langle \Phi | \hat{a}_q \hat{a}^p | \Phi \rangle = \bar{\gamma}_q^p, \quad (3.26)$$

corresponding to an one-hole density matrix element $\bar{\gamma}_q^p$. Further, it is worth mentioning that a contraction between either two creators or two annihilators vanishes. For the single-reference case the one-particle and one-hole densities can be written as

$$\gamma_q^p = \delta_q^p n_p, \quad (3.27)$$

$$\bar{\gamma}_q^p = \delta_q^p (1 - n_p) = \delta_q^p \bar{n}_p, \quad (3.28)$$

where the particle occupation number n_p is introduced and defined as

$$n_p := \begin{cases} 1, & \text{if } p \text{ is occupied in } |\Phi\rangle \\ 0, & \text{else.} \end{cases} \quad (3.29)$$

Taking a closer look into non-vanishing contractions, the contributions of a contraction only do not vanish if both indices are hole indices or if both indices are particle indices. Since we only use products of the same number of creation and annihilation operators, which are particle number conserving, we introduce the following short-hand notation for operators

$$\hat{a}_q^p = \hat{a}^p \hat{a}_q, \quad \hat{a}_{qs}^{pr} = \hat{a}^p \hat{a}^r \hat{a}_s \hat{a}_q, \quad \hat{a}_{qsu}^{prt} = \hat{a}^p \hat{a}^r \hat{a}^t \hat{a}_u \hat{a}_s \hat{a}_q. \quad (3.30)$$

Usually, these operators are normal ordered with respect to the vacuum so we transform them into operators in SR-NO using theorem 3.1. We obtain for the one-body operator

$$\hat{a}_q^p = \{\hat{a}_q^p\}_{|\Phi\rangle} + \gamma_q^p. \quad (3.31)$$

Applying Wick's theorem for a two-body operator leads to

$$\begin{aligned} \hat{a}_{qs}^{pr} &= \{\hat{a}_{qs}^{pr}\}_{|\Phi\rangle} + \gamma_q^p \{\hat{a}_s^r\}_{|\Phi\rangle} + \gamma_s^r \{\hat{a}_q^p\}_{|\Phi\rangle} - \gamma_s^p \{\hat{a}_q^r\}_{|\Phi\rangle} \\ &\quad - \gamma_q^r \{\hat{a}_s^p\}_{|\Phi\rangle} + \gamma_q^p \gamma_s^r - \gamma_s^p \gamma_q^r. \end{aligned} \quad (3.32)$$

Finally, we obtain for a three-body operator

$$\begin{aligned} \hat{a}_{qsu}^{prt} &= \{\hat{a}_{qsu}^{prt}\}_{|\Phi\rangle} + \gamma_q^p \{\hat{a}_{su}^{rt}\}_{|\Phi\rangle} - \gamma_q^r \{\hat{a}_{su}^{pt}\}_{|\Phi\rangle} - \gamma_q^t \{\hat{a}_{su}^{pr}\}_{|\Phi\rangle} - \gamma_s^p \{\hat{a}_{qu}^{rt}\}_{|\Phi\rangle} \\ &\quad + \gamma_s^r \{\hat{a}_{qu}^{pt}\}_{|\Phi\rangle} - \gamma_s^t \{\hat{a}_{qu}^{pr}\}_{|\Phi\rangle} - \gamma_u^p \{\hat{a}_{qs}^{rt}\}_{|\Phi\rangle} - \gamma_u^r \{\hat{a}_{qs}^{pt}\}_{|\Phi\rangle} + \gamma_u^t \{\hat{a}_{qs}^{pr}\}_{|\Phi\rangle} \\ &\quad + \gamma_{qs}^{pr} \{\hat{a}_u^t\}_{|\Phi\rangle} + \gamma_{qu}^{pt} \{\hat{a}_s^r\}_{|\Phi\rangle} + \gamma_{su}^{rt} \{\hat{a}_q^p\}_{|\Phi\rangle} - \gamma_{qu}^{pr} \{\hat{a}_s^t\}_{|\Phi\rangle} - \gamma_{us}^{pr} \{\hat{a}_q^t\}_{|\Phi\rangle} \\ &\quad - \gamma_{qs}^{pt} \{\hat{a}_u^r\}_{|\Phi\rangle} - \gamma_{su}^{pt} \{\hat{a}_q^r\}_{|\Phi\rangle} - \gamma_{sq}^{rt} \{\hat{a}_u^p\}_{|\Phi\rangle} - \gamma_{qu}^{rt} \{\hat{a}_s^p\}_{|\Phi\rangle} + \gamma_{qsu}^{prt}, \end{aligned} \quad (3.33)$$

where

$$\gamma_{qs}^{pr} = \gamma_q^p \gamma_s^r - \gamma_s^p \gamma_q^r \quad (3.34)$$

and

$$\gamma_{qsu}^{prt} = \gamma_q^p \gamma_s^r \gamma_u^t + \gamma_s^p \gamma_u^r \gamma_q^t + \gamma_u^p \gamma_q^r \gamma_s^t - \gamma_s^p \gamma_q^r \gamma_u^t - \gamma_u^p \gamma_s^r \gamma_q^t - \gamma_q^p \gamma_u^r \gamma_s^t. \quad (3.35)$$

3.3. Normal Ordering With Respect to a Multi-Reference State

In this section we will introduce the generalized Wick theorem for normal ordering with respect to a multi-reference state. This is necessary because normal ordering with respect to a single-reference state is limited to closed-shell nuclei [KM97]. A multi-reference state is a linear combination of Slater determinants. For this section we say that \mathcal{H}_n is a finite subspace of the A -body Hilbert space \mathcal{H} and $|\Phi_i\rangle$ is a complete orthonormal basis set of \mathcal{H}_n . Further, $|\Psi\rangle \in \mathcal{H}_n$ is a normalized A -body state with complex coefficients c_i and Slater determinants $|\Phi_i\rangle$

$$|\Psi\rangle = \sum_{i=1}^n c_i |\Phi_i\rangle, \quad (3.36)$$

with respect to which we want to perform normal ordering.

Since a particle-hole scheme is not defined for multi-reference states $|\Psi\rangle$, we have to define normal order in terms of a Wick theorem.

Definition 3.4: Normal Ordering with Respect to a Multi-Reference State
<p>A product of operators $\{\hat{A}_1 \hat{A}_2 \dots \hat{A}_n\}$ is normal ordered with respect to $\Psi\rangle$ if the expectation value of this product of operators with respect to $\Psi\rangle$ vanishes.</p> $\langle \Psi \{\hat{A}_1 \hat{A}_2 \dots \hat{A}_n\} \Psi \rangle = 0. \quad (3.37)$ <p>If $\Psi\rangle$ consists of only a single Slater determinant, the definition of normal ordering with respect to $\Psi\rangle$ has to reduce to the definition of normal ordering with respect to a single-reference state.</p>

Now we can introduce a normal-ordering operator $\{\hat{A}_1 \hat{A}_2 \dots \hat{A}_n\}_{|\Psi\rangle}$ with respect to a multi-reference state $|\Psi\rangle$. The difference to the single-reference case is that it does not order the creation operators to the left of all annihilation operators, but linearity, antisymmetry, and mapping of the identity operator $\mathbb{1}$ onto itself are still fulfilled. Like for the single-reference case we can formulate a Wick theorem for a product of normal-ordered operators with respect to a multi-reference state.

Theorem 3.2: Multi-Reference Wick Theorem

A product of n operators $\hat{A}_1, \hat{A}_2, \dots, \hat{A}_n$ can be written as a normal ordered product and all possible normal-ordered contractions with respect to $|\Psi\rangle$

$$\hat{A}_1 \hat{A}_2 \dots \hat{A}_n = \{\hat{A}_1 \hat{A}_2 \dots \hat{A}_n\}_{|\Psi\rangle} + \sum_{\text{contractions}} \{\hat{A}_1 \hat{A}_2 \dots \hat{A}_n\}_{|\Psi\rangle}. \quad (3.38)$$

Concerning contractions, we now do not obtain only single contractions but also contractions between more than two operators, namely the k -body density matrices $\gamma^{[k]}$. Their matrix elements are given by

$$\gamma_{q_1 \dots q_k}^{p_1 \dots p_k} = \langle \Psi | \hat{a}_{q_1 \dots q_k}^{p_1 \dots p_k} | \Psi \rangle. \quad (3.39)$$

For a single contraction we can adopt the definition of a hole contraction

$$\overline{\hat{a}^p \hat{a}_q} = \langle \Psi | \hat{a}^p \hat{a}_q | \Psi \rangle = \gamma_q^p \quad (3.40)$$

and further the definition of a particle contraction

$$\overline{\hat{a}_q \hat{a}^p} = \langle \Psi | \hat{a}_q \hat{a}^p | \Psi \rangle = -\bar{\gamma}_q^p, \quad (3.41)$$

where a contraction is now denoted with an overline for distinction with respect to the single-reference normal ordering.

Furthermore, a multiple contraction is usually a correlation up to the k -body rank, which is denoted as irreducible k -body density matrix $\lambda^{[k]}$, where $2 \leq k \leq A$. They are given as

$$\overline{\hat{a}^p \hat{a}^r \hat{a}_s \hat{a}_q} = \gamma_{qs}^{pr} - \hat{\mathcal{A}}(\gamma_q^p \gamma_s^r) =: \lambda_{qs}^{pr} \quad (3.42)$$

$$\overline{\hat{a}^p \hat{a}^r \hat{a}^t \hat{a}_u \hat{a}_s \hat{a}_q} = \gamma_{qsu}^{prt} - \hat{\mathcal{A}}(\gamma_q^p \gamma_s^r \gamma_u^t + \lambda_{qs}^{pr} \gamma_u^t) =: \lambda_{qsu}^{prt}, \quad (3.43)$$

where $\hat{\mathcal{A}}$ is an index antisymmetrizer, which restores the antisymmetry of an indexed object

$$\hat{\mathcal{A}}(\gamma_q^p \gamma_s^r) = \gamma_q^p \gamma_s^r - \gamma_s^p \gamma_q^r, \quad (3.44)$$

$$\begin{aligned} \hat{\mathcal{A}}(\lambda_{qs}^{pr} \gamma_u^t) &= \lambda_{su}^{rt} \gamma_q^p - \lambda_{qu}^{rt} \gamma_s^p - \lambda_{sq}^{rt} \gamma_u^p - \lambda_{su}^{pt} \gamma_q^r + \lambda_{qu}^{pt} \gamma_s^r - \lambda_{qs}^{pt} \gamma_u^r - \lambda_{us}^{pr} \gamma_q^t \\ &\quad - \lambda_{qu}^{pr} \gamma_s^t + \lambda_{qs}^{pr} \gamma_u^t, \end{aligned} \quad (3.45)$$

$$\hat{\mathcal{A}}(\gamma_q^p \gamma_s^r \gamma_u^t) = \gamma_q^p \gamma_s^r \gamma_u^t + \gamma_u^p \gamma_q^r \gamma_s^t + \gamma_s^p \gamma_u^r \gamma_q^t - \gamma_u^p \gamma_s^r \gamma_q^t - \gamma_s^p \gamma_q^r \gamma_u^t - \gamma_q^p \gamma_u^r \gamma_s^t. \quad (3.46)$$

Now we can use the normal-ordering operator $\{\hat{A}_1 \hat{A}_2 \dots \hat{A}_n\}_{|\Psi\rangle}$ on the one-, two-, three- and n -body operators, which are normal ordered in the vacuum to obtain them in multi-reference normal order (MR-NO). These operators are antisymmetric with respect to an exchange of the upper and lower indices. We can use theorem 3.2 to obtain a n -body operator in vacuum normal order in terms of operators in MR-NO yielding

$$\{\hat{a}_q^p\}_{|0\rangle} = \{\hat{a}_q^p\}_{|\Psi\rangle} + \gamma_q^p \quad (3.47)$$

$$\{\hat{a}_{qs}^{pr}\}_{|0\rangle} = \{\hat{a}_{qs}^{pr}\}_{|\Psi\rangle} + \hat{\mathcal{A}}(\gamma_q^p \{\hat{a}_s^r\}_{|\Psi\rangle}) + \gamma_{qs}^{pr} \quad (3.48)$$

$$\{\hat{a}_{qsu}^{prt}\}_{|0\rangle} = \{\hat{a}_{qsu}^{prt}\}_{|\Psi\rangle} + \hat{\mathcal{A}}(\gamma_q^p \{\hat{a}_{su}^r\}_{|\Psi\rangle}) + \hat{\mathcal{A}}(\gamma_{qs}^{pr} \{\hat{a}_u^t\}_{|\Psi\rangle}) + \gamma_{qsu}^{prt} \quad (3.49)$$

$$\{\hat{a}_{q_1 \dots q_n}^{p_1 \dots p_n}\}_{|0\rangle} = \{\hat{a}_{q_1 \dots q_n}^{p_1 \dots p_n}\}_{|\Psi\rangle} + \sum_{i=1}^{n-1} \hat{\mathcal{A}}(\gamma_{q_1 \dots q_i}^{p_1 \dots p_i} \{\hat{a}_{q_{i+1} \dots q_n}^{p_{i+1} \dots p_n}\}_{|\Psi\rangle}) + \gamma_{q_1 \dots q_n}^{p_1 \dots p_n}. \quad (3.50)$$

Now we can formulate the generalized Wick theorem to compute a product of two reference-state normal-ordered operators in terms of these normal-ordered operators.

Theorem 3.3: Generalized Wick Theorem

A product of two normal-ordered operators can be written as a sum of normal-ordered operators and all possible normal-ordered contractions

$$\{\hat{a}_{q_1 \dots q_n}^{p_1 \dots p_n}\}_{|\Psi\rangle} \{\hat{a}_{s_1 \dots s_m}^{r_1 \dots r_m}\}_{|\Psi\rangle} = \{\hat{a}_{q_1 \dots q_n s_1 \dots s_m}^{p_1 \dots p_n r_1 \dots r_m}\}_{|\Psi\rangle} + \sum_{\text{external contractions}} \{\hat{a}_{q_1 \dots q_n s_1 \dots s_m}^{p_1 \dots p_n r_1 \dots r_m}\}_{|\Psi\rangle} \quad (3.51)$$

It is important to note that each term determined with the generalized Wick Theorem carries a phase factor that can be determined by the number of permutations needed to bring the indices back into the original order.

For an illustration of theorem 3.3 let us compute the product of a normal-ordered two- and one-body operator, which is given by

$$\begin{aligned} \{\hat{a}_{qs}^{pr}\}_{|\Psi\rangle} \{\hat{a}_u^t\}_{|\Psi\rangle} &= + \{\hat{a}_{qsu}^{prt}\}_{|\Psi\rangle} + \bar{\gamma}_q^t \{\hat{a}_{us}^{pr}\}_{|\Psi\rangle} + \bar{\gamma}_s^t \{\hat{a}_{qu}^{pr}\}_{|\Psi\rangle} - \gamma_u^p \{\hat{a}_{qs}^{tr}\}_{|\Psi\rangle} - \gamma_u^r \{\hat{a}_{qs}^{pt}\}_{|\Psi\rangle} \\ &+ (\bar{\gamma}_s^t \gamma_u^r + \lambda_{su}^{rt}) \{\hat{a}_q^p\}_{|\Psi\rangle} - (\bar{\gamma}_s^t \gamma_u^p + \lambda_{su}^{pt}) \{\hat{a}_q^r\}_{|\Psi\rangle} \\ &+ (\bar{\gamma}_q^t \gamma_u^p + \lambda_{qu}^{pt}) \{\hat{a}_s^r\}_{|\Psi\rangle} - (\bar{\gamma}_q^t \gamma_u^r + \lambda_{qu}^{rt}) \{\hat{a}_s^p\}_{|\Psi\rangle} \\ &- \lambda_{sq}^{rt} \{\hat{a}_u^p\}_{|\Psi\rangle} - \lambda_{qs}^{pt} \{\hat{a}_u^r\}_{|\Psi\rangle} - \lambda_{us}^{pr} \{\hat{a}_q^t\}_{|\Psi\rangle} - \lambda_{qu}^{pr} \{\hat{a}_s^t\}_{|\Psi\rangle} \\ &+ \bar{\gamma}_q^t \lambda_{us}^{pr} + \bar{\gamma}_s^t \lambda_{qu}^{pr} - \gamma_u^p \lambda_{sq}^{rt} - \gamma_u^r \lambda_{qs}^{pt} + \lambda_{qsu}^{prt}. \end{aligned} \quad (3.52)$$

In this work we will use the generalized Wick theorem to evaluate commutators of normal-ordered products. This is shown in chapter 6, where we derive a leading-order three-body correction to the multi-reference in-medium similarity renormalization group.

4. The Similarity Renormalization Group

The similarity renormalization group (SRG) transformation [BFP07; BFS10; Rot+14] is a method to transform the initial Hamiltonian. Using the similarity transformed Hamiltonian in subsequent many-body methods like the NCSM, the convergence behavior is improved. Due to the fact that low- and high-energy momenta of NN and 3N potentials are strongly coupled, we want to decouple the high-momentum from low-momentum physics using the free-space SRG approach. Basically, a unitary transformation is applied in such a way that the off-diagonal matrix elements of the Hamiltonian are suppressed. Since we do not want to change the eigenvalues of the operator we can use a unitary transformation to reformulate the many-body problem using a unitary operator $\hat{U}(\alpha)$ depending on the SRG flow parameter α .

The unitary transformation is given by

$$\hat{H}(\alpha) = \hat{U}^\dagger(\alpha)\hat{H}(0)\hat{U}(\alpha), \quad (4.53)$$

where $\hat{H}(\alpha)$ is the SRG-evolved Hamiltonian. The derivative of this Hamiltonian with respect to α is

$$\frac{d\hat{H}(\alpha)}{d\alpha} = \frac{d\hat{U}^\dagger(\alpha)}{d\alpha}\hat{H}(0)\hat{U}(\alpha) + \hat{U}^\dagger(\alpha)\hat{H}(0)\frac{d\hat{U}(\alpha)}{d\alpha}. \quad (4.54)$$

Using the unitarity of the transformation operator $\hat{U}(\alpha)$, i.e., $\hat{U}^\dagger(\alpha)\hat{U}(\alpha) = \mathbb{1}$, we can differentiate this expression with respect to α and obtain

$$\frac{d\hat{U}^\dagger(\alpha)}{d\alpha} = -\hat{U}^\dagger(\alpha)\frac{d\hat{U}(\alpha)}{d\alpha}\hat{U}^\dagger(\alpha). \quad (4.55)$$

Therefore, we can rewrite Eq. (4.54) to obtain

$$\begin{aligned}
\frac{d\hat{H}(\alpha)}{d\alpha} &= -\hat{U}^\dagger(\alpha)\frac{d\hat{U}(\alpha)}{d\alpha}\hat{U}^\dagger(\alpha)\hat{H}(\alpha)\hat{U}(\alpha) + \hat{U}^\dagger(\alpha)\hat{H}(\alpha)\hat{U}(\alpha)\hat{U}^\dagger(\alpha)\frac{d\hat{U}(\alpha)}{d\alpha}. \\
&= -\hat{U}^\dagger(\alpha)\frac{d\hat{U}(\alpha)}{d\alpha}\hat{H}(\alpha) + \hat{H}(\alpha)\hat{U}(\alpha)\frac{d\hat{U}(\alpha)}{d\alpha} \\
&= \left(-\hat{U}^\dagger(\alpha)\frac{d\hat{U}(\alpha)}{d\alpha}\right)\hat{H}(\alpha) - \hat{H}(\alpha)\left(\hat{U}^\dagger(\alpha)\frac{d\hat{U}(\alpha)}{d\alpha}\right) \\
&= \left[-\hat{U}^\dagger(\alpha)\frac{d\hat{U}(\alpha)}{d\alpha}, \hat{H}(\alpha)\right],
\end{aligned} \tag{4.56}$$

where the last term of Eq. (4.56) is the commutator between two operators \hat{A} and \hat{B} , which is defined as $[\hat{A}, \hat{B}] = \hat{A}\hat{B} - \hat{B}\hat{A}$. The generator of the transformation can then be defined as

$$\hat{\eta}(\alpha) = -\hat{U}^\dagger(\alpha)\frac{d\hat{U}(\alpha)}{d\alpha}. \tag{4.57}$$

The operator flow equation is given by

$$\frac{d\hat{H}(\alpha)}{d\alpha} = [\hat{\eta}(\alpha), \hat{H}(\alpha)], \tag{4.58}$$

with the initial condition $\hat{H}(0) = \hat{H}$ needed to compute the SRG-transformed Hamiltonian [Her+16]. The generator of this transformation is anti-Hermitian, meaning $\hat{\eta}^\dagger(\alpha) = -\hat{\eta}(\alpha)$. There are many ways to choose the generator, where the most generic choice is the Wegner generator [Weg94; Weg00], which is typically chosen as the commutator of a Hermitian operator and the SRG-evolved Hamiltonian $\hat{H}(\alpha)$. For the decoupling of low- and high-momentum states we choose the generator of the SRG as follows [BFP07]

$$\hat{\eta}(\alpha) = (2\mu)^2 [\hat{T}_{\text{int}}, \hat{H}(\alpha)] \tag{4.59}$$

with the reduced nucleon mass μ and the intrinsic kinetic energy $\hat{T}_{\text{int}} = \hat{T} - \hat{T}_{\text{cm}}$. This generator choice pre-diagonalizes the Hamiltonian [BFP07]. For this choice of the generator, it should be denoted that the dimension of the flow parameter is fm⁴. The generator is not nucleus or basis dependent making its usage very flexible.

Using the SRG framework and regarding Eq. (4.58) we obtain induced many-body interactions up to an A -particle rank. If the generator is an a -body and the Hamiltonian a b -body operator the evolution of the right-hand side of Eq. (4.58) produces induced interactions up to $a + b - 1$ -particle rank. Since we are not able to compute the unitary transformation in an A -body space we need to truncate these operators, which is usually

done at the three-body level. This truncation violates the unitarity of the transformation. Knowing this, we need to study the impact of those higher-body interactions by exploring the dependence of the Hamiltonian on α .

If we are transforming the Hamiltonian, we also have to transform the operators of other observables, like the radius or electromagnetic E2 operator, consistently.

This can be done similarly to the transformation of the Hamiltonian by performing a unitary transformation $\hat{O}(\alpha) = \hat{U}^\dagger(\alpha)\hat{O}\hat{U}(\alpha)$ of the observable. The unitary transformation can be written as a first-order differential equation

$$\frac{d}{d\alpha}\hat{O}(\alpha) = [\hat{\eta}(\alpha), \hat{O}(\alpha)]. \quad (4.60)$$

When using the in-medium SRG framework, which we will introduce in the next chapter 5, the generator $\hat{\eta}(\alpha)$ depends on the SRG-evolved Hamiltonian. Therefore, we have to evolve the differential equation for observables simultaneously with the equation for the Hamiltonian. More information about the free-space SRG can be found in [Rot+14; BFP07; BFS10; Heb21], where also the consistent evolution of three-body interactions is covered.

5. The In-Medium SRG

In this chapter, we are going to discuss the in-medium SRG (IM-SRG) [Her+16] as a generalization of the SRG, which was discussed in chapter 4. First of all we explain the concept, followed by representation changes of the Hamiltonian between vacuum and reference-state normal order. Afterwards we address the IM-SRG(2) and the so-called Magnus expansion. We are formulating the IM-SRG flow equations in the m -scheme and introduce angular momentum coupling in order to construct the coupled equations for scalar and non-scalar cases. Finally, we introduce the different generators of the IM-SRG. Note that we are following the formalism of [Vob20].

5.1. Motivation and Concept

The concept of the SRG can be used in order to drive the Hamiltonian towards a block-diagonal structure and suppress its off-diagonal part \hat{H}^{od} . We can subdivide the Hamiltonian

$$\hat{H} = \hat{H}^{\text{d}} + \hat{H}^{\text{od}}, \quad (5.61)$$

where the off-diagonal part is chosen in such a way that the structure of the Hamiltonian becomes block-diagonal with respect to a particle-hole many-body basis \mathcal{B} like the Hartree-Fock or natural orbital basis. When we further subdivide the basis into \mathcal{I} and \mathcal{J} , where $\mathcal{B} = \mathcal{I} \cup \mathcal{J}$, the off-diagonal part is chosen such that \mathcal{I} and \mathcal{J} are coupled with each other, which can be written as

$$\hat{H}^{\text{od}} = \sum_{i \in \mathcal{I}} \sum_{j \in \mathcal{J}} \langle i | \hat{H} | j \rangle | i \rangle \langle j | + \text{h.c.} \quad (5.62)$$

The suppression of \hat{H}^{od} leads to a block-diagonal structure of \hat{H} where the span of \mathcal{I} is an invariant subspace of the Hamiltonian, which is shown in Fig. 5.1. The advantage is that we only have to solve the eigenvalue problem in this subspace spanned by \mathcal{I} instead of the model space spanned by \mathcal{B} .

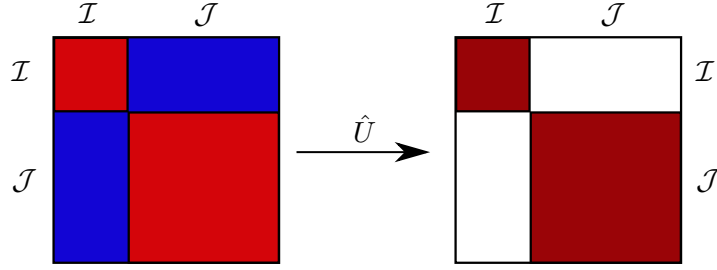


Fig. 5.1.: Schematic representation of the IM-SRG where the left drawing is the initial and the right one the final Hamiltonian. Herein, the initial Hamiltonian couples the matrix elements of \mathcal{I} and \mathcal{J} , which are after the unitary transformation \hat{U} decoupled in such a way that the off-diagonal elements of the Hamiltonian are suppressed.

In order to achieve this behavior, we have to transform the initial Hamiltonian $\hat{H}(s)$ using a continuous unitary transformation similar as in chapter 4

$$\hat{H}(s) = \hat{U}^\dagger(s) \hat{H}(0) \hat{U}(s), \quad (5.63)$$

where the initial Hamiltonian is $\hat{H}(0) = \hat{H}$ and s is a continuous flow parameter. The unitary transformation can be reformulated as a first-order differential equation, also known as flow equation

$$\frac{d}{ds} \hat{H}(s) = [\hat{\eta}(s), \hat{H}(s)], \quad (5.64)$$

where $\hat{\eta}(s)$ is the anti-Hermitian generator of that unitary transformation. For other observables $\hat{O}(s)$, the differential equation can be written in a similar way

$$\frac{d}{ds} \hat{O}(s) = [\hat{\eta}(s), \hat{O}(s)]. \quad (5.65)$$

As mentioned in the last chapter, the observables have to be evolved simultaneously together with the Hamiltonian. There is a method to avoid that, which will be explained later in this work.

Furthermore, the operators are normal ordered, using the Wick theorem introduced in chapter 3, at a certain many-body level k meaning that the corresponding operators can be written as

$$\hat{O}(s) = \sum_{i=1}^k \hat{O}^{[i]}(s), \quad \hat{O}^{[i]}(s) = \frac{1}{(i!)^2} \sum_{\substack{p_1 \dots p_i \\ q_1 \dots q_i}} O_{q_1 \dots q_i}^{p_1 \dots p_i}(s) \{\hat{a}_{q_1 \dots q_i}^{p_1 \dots p_i}\}, \quad (5.66)$$

where $\hat{O}^{[i]}(s)$ is an arbitrary operator at i -body level normal-ordered with respect to a certain reference state. Note that we did not attach a reference state in the notation of $\{\hat{a}_{q_1 \dots q_i}^{p_1 \dots p_i}\}$ due to the fact that the reference state can be arbitrary. As an example we take the flow equation for the Hamiltonian and use (5.66) yielding

$$\frac{d}{ds} \hat{H}^{[x]}(s) = (\Pi)^{[x]} \sum_{i=1}^k \sum_{j=1}^k \left[\hat{\eta}^{[i]}(s), \hat{H}^{[j]}(s) \right], \quad (5.67)$$

where $(\Pi)^{[x]}$ is the projector on the x -body space. With this equation we see that the matrix elements of different particle ranks are non-trivially coupled to each other. When evaluating the right-hand side of that equation we obtain induced many-body interactions up to the A -body particle rank. Furthermore, Eq. (5.67) is a system of first-order differential equations, which can be solved numerically. We can conclude that the IM-SRG is exact except for dropped normal-ordered interactions beyond the k -particle rank [Vob20].

5.2. Normal-Ordered Hamiltonian

5.2.1. Vacuum- and Reference-State Normal Ordering

The Hamiltonian $\hat{H}(s)$, as defined in Eq. (2.2), which is used as starting point in the IM-SRG contains contributions up to the three-body rank

$$\hat{H} = \hat{T}_{\text{int}} + \hat{V}^{[2]} + \hat{V}^{[3]}, \quad (5.68)$$

where $\hat{T}_{\text{int}} = \hat{T} - \hat{T}_{\text{cm}}$ is the intrinsic kinetic energy, $\hat{V}^{[2]}$ is the two-body interaction, and $\hat{V}^{[3]}$ is the three-body interaction. The kinetic energy can be written as

$$\hat{T}_{\text{int}} = \frac{1}{A} \sum_{i < j} \frac{(\hat{\mathbf{p}}_i - \hat{\mathbf{p}}_j)^2}{2m}, \quad (5.69)$$

where $\hat{\mathbf{p}}_i$ is the momentum operator for the i -th particle, A is the nucleon number and

m is the nucleon mass.

All operators in the IM-SRG framework are normal ordered with respect to a certain reference state $|\psi_{\text{ref}}\rangle$. We can start with an operator normal ordered with respect to the vacuum containing operators up to the three-body rank

$$\hat{O}_{|0\rangle} = O_0 + \sum_{pq} O_q^p \{\hat{a}_q^p\}_{|0\rangle} + \frac{1}{4} \sum_{pqrs} O_{qs}^{pr} \{\hat{a}_{qs}^{pr}\}_{|0\rangle} + \frac{1}{36} \sum_{prtqsu} O_{qsu}^{prt} \{\hat{a}_{qsu}^{prt}\}_{|0\rangle}. \quad (5.70)$$

Applying the Wick theorem (chapter 3) to this equation we obtain normal-ordered operators with respect to a reference state $|\psi_{\text{ref}}\rangle$

$$\hat{O}_{|\psi_{\text{ref}}\rangle} = \tilde{O}_0 + \sum_{pq} \tilde{O}_q^p \{\hat{a}_q^p\}_{|\psi_{\text{ref}}\rangle} + \frac{1}{4} \sum_{pqrs} \tilde{O}_{qs}^{pr} \{\hat{a}_{qs}^{pr}\}_{|\psi_{\text{ref}}\rangle} + \frac{1}{36} \sum_{prtqsu} \tilde{O}_{qsu}^{prt} \{\hat{a}_{qsu}^{prt}\}_{|\psi_{\text{ref}}\rangle}. \quad (5.71)$$

From now on we will refer to (5.70) as vacuum representation and to (5.71) as reference-state representation of \hat{O} . Using theorem 3.2 and equations (3.47) to (3.49), the reference-state matrix elements in terms of vacuum matrix elements can be written as

$$\tilde{O}_0 = O_0 + \sum_{pq} O_q^p \gamma_q^p + \frac{1}{4} \sum_{pqrs} O_{qs}^{pr} \gamma_{qs}^{pr} + \frac{1}{36} \sum_{prtqsu} O_{qsu}^{prt} \gamma_{qsu}^{prt}, \quad (5.72)$$

$$\tilde{O}_2^1 = O_2^1 + \sum_{pq} O_{2q}^{1p} \gamma_q^p + \frac{1}{4} \sum_{pqrs} O_{2qs}^{1pr} \gamma_{qs}^{pr}, \quad (5.73)$$

$$\tilde{O}_{34}^{12} = O_{34}^{12} + \sum_{pq} O_{34q}^{12p} \gamma_q^p, \quad (5.74)$$

$$\tilde{O}_{456}^{123} = O_{456}^{123}, \quad (5.75)$$

where the numerical indices are fixed, i.e., these are no summation indices.

The reference-state matrix elements can be transformed into vacuum matrix elements, which are given as

$$O_0 = \tilde{O}_0 - \sum_{pq} \tilde{O}_q^p \gamma_q^p - \frac{1}{4} \sum_{pqrs} \tilde{O}_{qs}^{pr} (\gamma_{qs}^{pr} - 4\gamma_q^p \gamma_s^r) - \frac{1}{36} \sum_{prtqsu} \tilde{O}_{qsu}^{prt} (\gamma_{qsu}^{prt} - 18\gamma_q^p \gamma_s^r \gamma_u^t + 36\gamma_q^p \gamma_s^r \gamma_u^t), \quad (5.76)$$

$$O_2^1 = \tilde{O}_2^1 - \sum_{pq} O_{2q}^{1p} \gamma_q^p - \frac{1}{4} \sum_{pqrs} \tilde{O}_{2qs}^{1pr} (\gamma_{qs}^{pr} - 4\gamma_q^p \gamma_s^r), \quad (5.77)$$

$$O_{34}^{12} = \tilde{O}_{34}^{12} - \sum_{pq} \tilde{O}_{34q}^{12p} \gamma_q^p, \quad (5.78)$$

$$O_{456}^{123} = \tilde{O}_{456}^{123}. \quad (5.79)$$

The derivation of these relations can be found in [Geb17].

These equations are written in the m -scheme, meaning that they depend on angular-momentum projection quantum numbers. We perform normal ordering only with respect to reference states with a total angular momentum of zero leading to scalar density matrices. Performing normal ordering with respect to reference states with a non-vanishing total angular momentum leads to non-scalar density matrices increasing the complexity of the IM-SRG framework tremendously.

5.2.2. Normal-Ordered Two-Body Approximation

The normal-ordered two-body approximation (NO2B) is widely used in the IM-SRG framework due to the fact that the inclusion of operators beyond the two-body level is computationally and conceptually expensive but possible, as will be shown later in this work. The starting point for the NO2B is the three-body operator normal ordered with respect to the vacuum

$$\hat{O}_{|0\rangle} = +\frac{1}{36} \sum_{prtqsu} O_{qsu}^{prt} \{\hat{a}_{qsu}^{prt}\}_{|0\rangle}. \quad (5.80)$$

Transforming this operator into the reference-state representation, we obtain

$$\hat{O}_{|\psi_{\text{ref}}\rangle} = \tilde{O}_0 + \sum_{pq} \tilde{O}_q^p \{\hat{a}_q^p\}_{|\psi_{\text{ref}}\rangle} + \frac{1}{4} \sum_{prqs} \tilde{O}_{qs}^{pr} \{\hat{a}_{qs}^{pr}\}_{|\psi_{\text{ref}}\rangle} + \frac{1}{36} \sum_{prtqsu} \tilde{O}_{qsu}^{prt} \{\hat{a}_{qsu}^{prt}\}_{|\psi_{\text{ref}}\rangle}. \quad (5.81)$$

The tree-body part of (5.81) is omitted in the NO2B approximation leading to

$$\begin{aligned} \hat{O}_{\text{NO2B}} &= \tilde{O}_0 + \sum_{pq} \tilde{O}_q^p \{\hat{a}_q^p\}_{|\psi_{\text{ref}}\rangle} + \frac{1}{4} \sum_{prqs} \tilde{O}_{qs}^{pr} \{\hat{a}_{qs}^{pr}\}_{|\psi_{\text{ref}}\rangle} \\ &= \frac{1}{36} \sum_{prtqsu} O_{qsu}^{prt} \gamma_{qsu}^{prt} + \frac{1}{4} \sum_{prtqsu} O_{qsu}^{prt} \gamma_{qs}^{pr} \{\hat{a}_u^t\}_{|\psi_{\text{ref}}\rangle} + \frac{1}{4} \sum_{prtqsu} O_{qsu}^{prt} \gamma_q^p \{\hat{a}_{su}^{rt}\}_{|\psi_{\text{ref}}\rangle}. \end{aligned} \quad (5.82)$$

Note that other many-body methods like the NCSM use vacuum matrix elements as input where \hat{O}_{NO2B} has the form

$$\hat{O}_{\text{NO2B}} = O_0 + \sum_{pq} O_q^p \{\hat{a}_q^p\}_{|0\rangle} + \frac{1}{4} \sum_{pqrs} O_{qs}^{pr} \{\hat{a}_{qs}^{pr}\}_{|0\rangle} \quad (5.83)$$

and the matrix elements can be obtained using the relations (5.76) to (5.79), where \hat{O}_{NO2B} is a zero- plus one- plus two-body operator taking three-body matrix elements in terms of lower particle ranks into account. It has been shown in [Bin+13; Rot+12a; GCR16] that the neglect of the full three-body matrix elements has an effect of 1 - 2 % on ground-state and excited-state energies.

5.3. The IM-SRG(2)

In the IM-SRG(2) framework, the operators are truncated at the NO2B level, where the Hamiltonian $\hat{H}(s)$ and the generator $\hat{\eta}(s)$ are written as

$$\hat{H}(s) = E(s) + \sum_{pq} f_q^p(s) \{\hat{a}_q^p\} + \frac{1}{4} \sum_{pqrs} \Gamma_{qs}^{pr}(s) \{\hat{a}_{qs}^{pr}\}_{|\psi_{\text{ref}}\rangle}, \quad (5.84)$$

$$\hat{\eta}(s) = \sum_{pq} \eta_q^p(s) \{\hat{a}_q^p\} + \frac{1}{4} \sum_{pqrs} \eta_{qs}^{pr}(s) \{\hat{a}_{qs}^{pr}\}_{|\psi_{\text{ref}}\rangle}, \quad (5.85)$$

where we have used the common variables f for the one-body and Γ for the two-body matrix elements of the Hamiltonian. Let us start with the Hamiltonian as defined in (2.2), where $\hat{V}^{[3]}$ is now approximated using the NO2B approximation, which can be written as

$$\hat{V}_{\text{NO2B}} = V(s) + \sum_{pq} V_q^p(s) \{\hat{a}_q^p\}_{|\psi_{\text{ref}}\rangle} + \frac{1}{4} \sum_{pqrs} V_{qs}^{pr}(s) \{\hat{a}_{qs}^{pr}\}_{|\psi_{\text{ref}}\rangle}. \quad (5.86)$$

Using this approximation, the initial Hamiltonian at a flow parameter $s = 0$ can be written as

$$\hat{H}(0) = \hat{T}_{\text{int}} + \hat{V}^{[2]} + \hat{V}_{\text{NO2B}}. \quad (5.87)$$

Inserting (5.84) and (5.85) into the flow equation for $\hat{H}(s)$, we obtain

$$\frac{d}{ds}\hat{H}(s) = \left[\hat{\eta}(s), \hat{H}(s) \right] \quad (5.88)$$

$$\begin{aligned} &= \left[\hat{\eta}^{[1]}(s), \hat{H}^{[1]}(s) \right] + \left[\hat{\eta}^{[1]}(s), \hat{H}^{[2]}(s) \right] \\ &+ \left[\hat{\eta}^{[2]}(s), \hat{H}^{[1]}(s) \right] + \left[\hat{\eta}^{[2]}(s), \hat{H}^{[2]}(s) \right]. \end{aligned} \quad (5.89)$$

Evaluating the right-hand side of this equation using the generalized Wick theorem, we get a system of coupled first-order differential equations for the matrix elements of the Hamiltonian and the generator, where the evaluation and final expressions are shown in section 5.6.

5.4. The IM-SRG With the Magnus Expansion

Until now the IM-SRG framework was discussed using a coupled set of flow equations for the Hamiltonian and other observables of interest. The disadvantage that comes with this approach is that eventually (5.64) and (5.65) have to be solved simultaneously. The number of coupled ordinary differential equations (ODEs) is doubled and especially for other observables the time scale for the evolution can differ compared to the evolution of the Hamiltonian.

We can overcome these limitations by using the so-called Magnus expansion [Mag54], which was first applied to the IM-SRG framework by Morris et al. [MPB15]. The starting point is the differential equation for the unitary operator itself

$$\frac{d}{ds}\hat{U}(s) = -\hat{\eta}(s)\hat{U}(s). \quad (5.90)$$

For $\hat{U}(s)$ the Magnus expansion states that there exists a parametrization

$$\hat{U}(s) = e^{\hat{\Omega}(s)}, \quad (5.91)$$

where $\hat{\Omega}(s)$ is the so-called anti-Hermitian Magnus operator. The Magnus operator satisfies the differential equation [Bla+09]

$$\frac{d}{ds}\hat{\Omega}(s) = \sum_{k=0}^{\infty} \frac{B_k}{k!} \left[\hat{\Omega}(s), \hat{\eta}(s) \right]_k, \quad (5.92)$$

where B_k refers to the Bernoulli numbers. Here, $\left[\hat{\Omega}(s), \hat{\eta}(s)\right]_k$ is a short-hand notation for nested commutators, which can be written recursively as follows

$$\left[\hat{\Omega}(s), \hat{\eta}(s)\right]_k = \left[\hat{\Omega}(s) \left[\hat{\Omega}(s), \hat{\eta}(s)\right]_{k-1}\right], \quad \left[\hat{\Omega}(s), \hat{\eta}(s)\right]_0 = \hat{\eta}(s). \quad (5.93)$$

In order to construct an arbitrary operator $\hat{O}(s)$ we need the Magnus operator and $\hat{O}(0)$. This can be done using the unitary transformation $\hat{U}(s)$ resulting in the Baker-Campbell-Hausdorff (BCH) series for the transformation of any operator of desire

$$\hat{O}(s) = \hat{U}^\dagger(s) \hat{O}(0) \hat{U}(s) = e^{+\hat{\Omega}(s)} \hat{O}(0) e^{-\hat{\Omega}(s)} = \sum_{k=0}^{\infty} \frac{1}{k!} \left[\hat{\Omega}(s), \hat{O}(0)\right]_k. \quad (5.94)$$

From now on, we refer to this kind of evolution as Magnus evolution. Compared to the direct evolution of the ODE, which is an integration by infinitesimal steps, these transformations are combined in the Magnus operator $\hat{\Omega}(s)$, giving us access to the unitary transformations. Another advantage is that we do not have to solve two ODEs simultaneously. Instead, we need to solve (5.92) one time and use the BCH series to obtain the desired operator like the Hamiltonian, radius or electromagnetic multipole operators. Note that the derivation of (5.92) and more details on the construction of $\hat{\Omega}(s)$ can be found in [Bla+09] and [Vob20].

5.5. Magnus(2)

Following the IM-SRG(2), the Magnus operator $\hat{\Omega}(s)$ is also truncated using the NO2B approximation. The equation for the Magnus operator is

$$\hat{\Omega}(s) = \sum_{pq} \Omega_q^p \{\hat{a}_q^p\} + \frac{1}{4} \sum_{prqs} \Omega_{qs}^{pr} \{\hat{a}_{qs}^{pr}\}. \quad (5.95)$$

Also the equations for $\frac{d}{ds} \hat{\Omega}(s)$ and $\hat{O}(s)$ are truncated at the NO2B level, which we refer to as the Magnus(2) expansion

$$\frac{d}{ds} \hat{\Omega}(s) = \sum_{k=0}^{\infty} \frac{B_k}{k!} \left[\hat{\Omega}(s), \hat{\eta}(s)\right]_k, \quad (5.96)$$

$$\hat{O}(s) = \sum_{k=0}^{\infty} \frac{1}{k!} \left[\hat{\Omega}(s), \hat{O}(0) \right]_k. \quad (5.97)$$

Since the Magnus flow-equation and the BCH series are infinite we also have to truncate them. First of all, we solve the nested commutators iteratively, meaning that we store the result of the k -th order and put it into the commutator of the order $k + 1$, making the calculation numerically very efficient. The k -th term of (5.92) can be written as

$$\frac{B_k}{k!} \left[\hat{\Omega}(s), \hat{\eta}(s) \right]_k = \frac{B_k}{k!} \left[\hat{\Omega}(s) \left[\hat{\Omega}(s), \hat{\eta}(s) \right]_{k-1} \right]. \quad (5.98)$$

The derivative of the Magnus operator is then truncated at a certain order x

$$\hat{\Omega}'_x(s) := \sum_{k=0}^x \frac{B_k}{k!} \left[\hat{\Omega}(s), \hat{\eta}(s) \right]_k, \quad (5.99)$$

where the following criterion has to be fulfilled

$$\frac{\|\hat{\Omega}'_x(s) - \hat{\Omega}'_{x-1}(s)\|}{\|\hat{\Omega}'_x(s)\|} < \epsilon := 1 \times 10^{-2} \quad \text{with } B_x \neq 0 \quad (5.100)$$

in order to obtain convergence at order x , where

$$\|\hat{\Omega}\| = \sqrt{\Omega^2 + \sum_{ij} (\Omega_j^i)^2 + \sum_{ijkl} (\Omega_{kl}^{ij})^2} \quad (5.101)$$

is the so-called two-norm. Equation (5.100) states that if the difference of $\hat{\Omega}'(s)$ in orders x and $x - 1$ is small compared to $\hat{\Omega}'(s)$ at order x , the Magnus series is converged.

It has been shown that the value for ϵ is good for practical applications and that the series converges for values of k between 2 and 4. Furthermore, for large values of k the series can diverge [Vob20]. Therefore, another convergence criterion, which has to be fulfilled is

$$\frac{\left\| \left[\hat{\Omega}(s), \hat{\eta}(s) \right]_k \right\|}{\left\| \left[\hat{\Omega}(s), \hat{\eta}(s) \right]_{k-1} \right\|} < 1 \quad \text{for all } k \text{ with } 1 \leq k \leq x, \quad (5.102)$$

with x being the convergence order according to the first convergence criterion (5.100). If this criterion is not fulfilled, the series is considered as divergent and the current integration step is restarted using a smaller stepsize.

Considering the BCH series, the x -th element can be written as

$$\hat{O}_x(s) = \sum_{k=0}^x \frac{1}{k!} \left[\hat{\Omega}(s), \hat{O}_k(s) \right]. \quad (5.103)$$

The convergence criterion for this series is

$$\delta_{\text{norm}}^{[x]} \equiv \frac{\|\hat{O}_x(s)\|}{\|\sum_{k=0}^x \hat{O}_k(s)\|} < \epsilon \ll 1, \quad (5.104)$$

where $\epsilon = 1 \times 10^{-2}$ has been found to be the optimal threshold. This criterion states that the norm of the desired observable $\hat{O}(s)$ at order x has to be small compared to the norm of the sum of \hat{O} at all previous orders. More on the convergence of the Magnus operator and the BCH series can be found in [Vob20].

5.6. Multi-Reference IM-SRG Commutator Equations

In this section we show the commutator equations of the multi-reference IM-SRG in the m -scheme. Since we are using the Magnus-type flow equation and the BCH series, we will show the equations in terms of (5.94), where $\hat{\Omega}(s)$ is the Magnus operator and $\hat{O}(s)$ is an arbitrary operator, which can also be the generator $\hat{\eta}(s)$.

First, we formulate the m -scheme equations of the IM-SRG in a compact way by using symmetry properties. These can be obtained by application of the generalized Wick theorem and a transformation into spherical natural orbitals. Afterwards, we review the theory of angular momentum coupling and show the coupled commutator equations for scalar and non-scalar operators.

5.6.1. Spherical Natural Orbitals and m -Scheme Equations

A very important aspect of the commutator equations is that they are formulated in the so-called spherical natural orbital basis, which is the eigenbasis of the one-body density matrix $\gamma^{[1]}$. The diagonalization of $\gamma^{[1]}$ gives

$$\gamma_q^p \rightarrow n_p \delta_q^p, \quad (5.105)$$

$$\bar{\gamma}_q^p = \delta_q^p - \gamma_q^p \rightarrow (1 - n_p) \delta_q^p = \bar{n}_p \delta_q^p, \quad (5.106)$$

where n_p are the eigenvalues of $\gamma^{[1]}$, the so-called fractional occupation numbers with a range of $0 \leq n_p \leq 1$ and $\bar{n}_p = 1 - n_p$.

We are formulating the Magnus commutator equations in terms of natural orbitals because the computational effort is reduced due to a collapse of summation indices. Furthermore, we are going to partition the single-particle basis into three different spaces: the core space \mathcal{C} , the active space \mathcal{A} and the virtual space \mathcal{V} . For this partitioning we make use of the value of n_p . Assume a reference state $|\psi_{\text{ref}}\rangle$ given as a superposition of Slater determinants $|\phi_i\rangle$

$$|\psi_{\text{ref}}\rangle = \sum_i c_i |\phi_i\rangle. \quad (5.107)$$

The definition of the three subspaces is shown in the following table:

State Type	Occupation Number	Slater Determinant	Second Quantization
$p \in \mathcal{C}$	$n_p = 1$	$p \in \phi_i\rangle$ for all i	$\hat{a}^p \psi_{\text{ref}}\rangle = 0$
$p \in \mathcal{A}$	$0 < n_p < 1$	$p \in \phi_i\rangle$ for at least one i	
$p \in \mathcal{V}$	$n_p = 0$	$p \notin \phi_i\rangle$ for all i	$\hat{a}_p \psi_{\text{ref}}\rangle = 0$

Thus, a core state \mathcal{C} corresponds to a single-particle state that is occupied in all Slater determinants of the reference state. An active state \mathcal{A} is a single-particle state that is occupied in at least one but not all Slater determinants of the reference state. A virtual state \mathcal{V} is a single-particle state that is unoccupied in all Slater determinants of the reference state.

This partitioning is very useful because for some natural orbital single-particle combinations the occupation numbers and irreducible two-body densities vanish. More information about the classification of the single particle basis can be found in [Geb17].

Now we are ready to evaluate a commutator of the form

$$\hat{O}(s) = \left[\hat{\Omega}(s), \hat{O}(0) \right], \quad (5.108)$$

where each operator is normal ordered with respect to $|\psi_{\text{ref}}\rangle$ and truncated at the NO2B level, which can be written as

$$\hat{O} = O_0 + \sum_{pq} O_q^p \{ \hat{a}_q^p \}_{|\psi_{\text{ref}}\rangle} + \sum_{pqrs} O_{qs}^{pr} \{ \hat{a}_{qs}^{pr} \}_{|\psi_{\text{ref}}\rangle}. \quad (5.109)$$

For evaluating the commutator, let us split it up into the different particle ranks

$$\begin{aligned} \hat{O} &= [\hat{\Omega}, \hat{O}] = [\hat{\Omega}^{[0]} + \hat{\Omega}^{[1]} + \hat{\Omega}^{[2]}, \hat{O}^{[0]} + \hat{O}^{[1]} + \hat{O}^{[2]}] \\ &= [\hat{\Omega}^{[1]}, \hat{O}^{[1]}] + [\hat{\Omega}^{[1]}, \hat{O}^{[2]}] + [\hat{\Omega}^{[2]}, \hat{O}^{[1]}] + [\hat{\Omega}^{[2]}, \hat{O}^{[2]}], \end{aligned} \quad (5.110)$$

where the bracket denotes the particle rank of the operator, i.e., $\hat{O}^{[1]} = O_q^p$. These commutators can be evaluated using the generalized Wick theorem (see chapter 3) leading to terms, which contain one-body, irreducible two-body and three-body densities.

As an example let us evaluate the commutator between $\hat{\Omega}^{[2]}$ and $\hat{O}^{[1]}$ and denote the resulting operator as \hat{O}

$$\hat{O} := \left[\frac{1}{4} \sum_{pqrs} \Omega_{qs}^{pr} \{ \hat{a}_{qs}^{pr} \}, \sum_{tu} O_u^t \{ \hat{a}_u^t \} \right] \quad (5.111)$$

$$= \frac{1}{4} \sum_{prtqsu} \Omega_{qs}^{pr} O_u^t (\{ \hat{a}_{qs}^{pr} \} \{ \hat{a}_u^t \} - \{ \hat{a}_u^t \} \{ \hat{a}_{qs}^{pr} \}). \quad (5.112)$$

Note, that we omit the index $|\psi_{\text{ref}}\rangle$ with respect to which the operators are normal ordered to simplify the readability. For evaluating the commutator of normal-ordered products, we use the generalized Wick theorem where we obtain

$$\begin{aligned} \hat{O} &= \frac{1}{4} \sum_{prtqsu} \Omega_{qs}^{pr} O_u^t ((\bar{\gamma}_q^t + \gamma_q^t) \{ \hat{a}_{us}^{pr} \} + (\bar{\gamma}_s^t + \gamma_s^t) \{ \hat{a}_{qu}^{pr} \} - (\gamma_u^p + \bar{\gamma}_u^p) \{ \hat{a}_{qs}^{tr} \} - (\gamma_u^r + \bar{\gamma}_u^r) \{ \hat{a}_{us}^{pr} \} \\ &\quad + (\bar{\gamma}_s^t \gamma_u^r - \gamma_s^t \bar{\gamma}_u^r) \{ \hat{a}_q^p \} - (\bar{\gamma}_s^t \gamma_u^p - \gamma_s^t \bar{\gamma}_u^p) \{ \hat{a}_q^r \} + (\bar{\gamma}_q^t \gamma_u^p - \gamma_q^t \bar{\gamma}_u^p) \{ \hat{a}_s^r \} - (\bar{\gamma}_q^t \gamma_u^r - \gamma_q^t \bar{\gamma}_u^r) \{ \hat{a}_s^p \} \\ &\quad + (\bar{\gamma}_q^t + \gamma_q^t) \lambda_{us}^{pr} + (\bar{\gamma}_s^t + \gamma_s^t) \lambda_{qu}^{pr} - (\gamma_u^p + \bar{\gamma}_u^p) \lambda_{qs}^{rt} - (\gamma_u^r + \bar{\gamma}_u^r) \lambda_{qs}^{pt}). \end{aligned} \quad (5.113)$$

Now we can employ the relations

$$\gamma_q^p + \bar{\gamma}_q^p = \delta_q^p, \quad \gamma_q^p \bar{\gamma}_s^r - \gamma_s^r \bar{\gamma}_q^p = \gamma_q^p \delta_s^r - \gamma_s^r \delta_q^p \quad (5.114)$$

and obtain

$$\begin{aligned}
\hat{O} = \frac{1}{4} \sum_{prtqsu} \Omega_{qs}^{pr} O_u^t & (\delta_q^t \{\hat{a}_{us}^{pr}\} + \delta_s^t \{\hat{a}_{qu}^{pr}\} - \delta_u^p \{\hat{a}_{qs}^{tr}\} - \delta_u^r \{\hat{a}_{qs}^{pt}\}) \\
& + (\delta_s^t \gamma_u^r - \gamma_s^t \delta_u^r) \{\hat{a}_q^p\} - (\delta_s^t \gamma_u^p - \gamma_s^t \delta_u^p) \{\hat{a}_q^r\} \\
& + (\delta_q^t \gamma_u^p - \gamma_q^t \delta_u^p) \{\hat{a}_s^r\} - (\delta_q^t \gamma_u^r - \gamma_q^t \delta_u^r) \{\hat{a}_s^p\} \\
& + \delta_q^t \lambda_{us}^{pr} + \delta_s^t \lambda_{qu}^{pr} - \delta_u^p \lambda_{qs}^{rt} - \delta_u^r \lambda_{qs}^{pt}. \tag{5.115}
\end{aligned}$$

By evaluating the Kronecker deltas and renaming the summation indices we obtain

$$\hat{O} = \frac{1}{4} \sum_{prtqs} (\Omega_{ts}^{pr} O_q^t + \Omega_{qt}^{pr} O_s^t - \Omega_{qs}^{tr} O_t^p - \Omega_{qs}^{pt} O_t^r) \{\hat{a}_{qs}^{pr}\} \tag{5.116}$$

$$+ \sum_{prtqs} (\Omega_{qt}^{pr} O_s^t - \Omega_{qs}^{pt} O_t^r) \gamma_s^r \{\hat{a}_q^p\} \tag{5.117}$$

$$+ \frac{1}{2} \sum_{prtqs} (\Omega_{ts}^{pr} O_q^t - \Omega_{qs}^{tr} O_t^p) \lambda_{qs}^{pr} \tag{5.118}$$

$$\stackrel{!}{=} O_0 + \sum_{pq} O_q^p \{\hat{a}_q^p\} + \frac{1}{4} \sum_{prqs} O_{qs}^{pr} \{\hat{a}_{qs}^{pr}\}. \tag{5.119}$$

If we compare each particle rank of our result with \hat{O} , we obtain the following expressions for the two-, one- and zero-body part of \hat{O} :

$$\check{O}_{34}^{12} = \sum_t \Omega_{t4}^{12} O_3^t + \Omega_{3t}^{12} O_4^t - \Omega_{34}^{t2} O_t^1 - \Omega_{34}^{1t} O_t^2, \tag{5.120}$$

$$\check{O}_2^1 = \sum_{rts} (\Omega_{2t}^{1r} O_s^t - \Omega_{2s}^{1t} O_t^r) \gamma_s^r, \tag{5.121}$$

$$\check{O}_0 = \frac{1}{2} \sum_{prtqs} (\Omega_{ts}^{pr} O_q^t - \Omega_{qs}^{tr} O_t^p) \lambda_{qs}^{pr}, \tag{5.122}$$

where we used \check{O} to denote the matrix elements on the left-hand side. The final step is the single-particle basis transformation into spherical natural orbitals, where the right-hand side of the one-body part simplifies to

$$\check{O}_2^1 = \sum_{rt} \Omega_{2t}^{1r} O_r^t (n_r - n_t). \tag{5.123}$$

Until now we did not exploit any symmetries of the operators and also did not use the symmetry under Hermitian conjugation. For this we define symmetrizers

$$\hat{\Xi}_{2B} = \frac{1}{8} [(1 - P_{12} - P_{34} + P_{12}P_{34})(1 \pm P_{13}P_{24})], \quad (5.124)$$

$$\hat{\Xi}_{1B} = \frac{1}{2} (1 \pm P_{12}), \quad (5.125)$$

where P_{12} is an index permutation symbol, which interchanges the attached indices. Note that the \pm sign in the last terms indicates the behavior of the matrix element under complex conjugation. Using these symmetrizers we obtain

$$\check{O}_2^1 = \hat{\Xi}_{1B} \sum_{rt} \Omega_{2t}^{1r} O_r^t (n_r - n_t), \quad (5.126)$$

$$\check{O}_{34}^{12} = -4\hat{\Xi}_{2B} \sum_t \Omega_{34}^{t2} O_t^1. \quad (5.127)$$

Repeating this procedure for all remaining terms of (5.110), we obtain

$$\check{O}_{34}^{12} = +\hat{\Xi}_{2B} \sum_p 4\Omega_p^1 O_{34}^{p2} \quad (5.128)$$

$$-\hat{\Xi}_{2B} \sum_p 4O_p^1 \Omega_{34}^{p2} \quad (5.129)$$

$$+\hat{\Xi}_{2B} \sum_{pq} \Omega_{pq}^{12} O_{34}^{pq} (1 - n_p - n_q) \quad (5.130)$$

$$+\hat{\Xi}_{2B} \sum_{pq} 4\Omega_{3q}^{1p} O_{4p}^{2q} (n_p - n_q), \quad (5.131)$$

$$\check{O}_2^1 = +2\hat{\Xi}_{1B} \sum_p \Omega_p^1 O_2^p \quad (5.132)$$

$$+\hat{\Xi}_{1B} \sum_{pq} \left(\Omega_q^p O_{p2}^{q1} \right) (n_p - n_q) \quad (5.133)$$

$$+\hat{\Xi}_{1B} \sum_{pq} \left(O_q^p \Omega_{p2}^{q1} \right) (n_p - n_q) \quad (5.134)$$

$$+\hat{\Xi}_{1B} \sum_{pqr} \Omega_{qr}^{1p} O_{2p}^{qr} (n_p \bar{n}_q \bar{n}_r + \bar{n}_p n_q n_r) \quad (5.135)$$

$$+\hat{\Xi}_{1B} \sum_{rtvs} \frac{1}{2} \Omega_{sv}^{1t} O_{2t}^{rv} \lambda_{rv}^{sw} \quad (5.136)$$

$$+\hat{\Xi}_{1B} \sum_{rtvs} (-2) \Omega_{st}^{1r} O_{2w}^{vt} \lambda_{vr}^{sw} \quad (5.137)$$

$$+ \hat{\Xi}_{1B} \sum_{rtvsw} \Omega_{t2}^{1r} O_{sw}^{tv} \lambda_{vr}^{sw} \quad (5.138)$$

$$- \hat{\Xi}_{1B} \sum_{rtvsw} \Omega_{sw}^{tv} O_{t2}^{1r} \lambda_{vr}^{sw}, \quad (5.139)$$

$$\check{O}_0 = + \sum_{pq} \Omega_q^p O_p^q (n_p - n_q) \quad (5.140)$$

$$+ \frac{1}{4} \sum_{prqs} (\Omega_{qs}^{pr} O_{pr}^{qs} - \Omega_{pr}^{qs} O_{qs}^{pr}) n_p n_r \bar{n}_q \bar{n}_s \quad (5.141)$$

$$+ \frac{1}{4} \sum_{prqs} O_{qs}^{pr} \lambda_{qs}^{pr} + \mathcal{O}(\lambda^{[3]}). \quad (5.142)$$

These equations usually are referred to be the m -scheme equations because they depend on projection quantum numbers. In the zero-body part we also obtain terms involving irreducible three-body densities $\lambda^{[3]}$, which can be neglected due to their small contributions to the ground-state energy, which is a few keV, as shown in [Geb17]. Furthermore, we obtain the single-reference IM-SRG equations by setting all irreducible two-body densities $\lambda^{[2]}$ to zero indicating that the single-reference equations are a subset of the multi-reference equations. More about the derivation of the m -scheme equations and the derivation of the symmetrized equations can be found in [Geb17; Vob20].

5.7. Angular Momentum Theory

At the moment, the m -scheme equations still depend on projection quantum numbers. In order to remove this dependence and reduce the computational effort for solving the flow equations, we need to perform angular momentum coupling. Therefore, we are going to discuss angular momentum theory and the Wigner-Eckart theorem, which is important for the coupling of non-scalar tensor operators. More information beyond our discussions can be found in [KMV88; Suh07].

5.7.1. Angular Momentum Coupling

The quantity \hat{j} is an angular momentum operator if its components \hat{j}_x , \hat{j}_y and \hat{j}_z satisfy the following relations

$$\hat{j}_k^\dagger = j_k \quad \text{and} \quad [\hat{j}_i, \hat{j}_j] = i\hbar \sum_k \epsilon_{ijk} \hat{j}_k, \quad (5.143)$$

where $k = x, y, z$ and ϵ_{ijk} is the antisymmetric three-dimensional Levi-Civita tensor.

The angular momentum operator also fulfills the following eigenvalue relations

$$\hat{\mathbf{j}}^2 |jm\rangle = j(j+1)\hbar^2 |jm\rangle \quad (5.144)$$

$$\hat{j}_z |jm\rangle = m\hbar |jm\rangle, \quad (5.145)$$

where $-j \leq m \leq j$. Furthermore, the angular momentum is related to the rotation group with the components as generators.

With these basic properties we are ready to start with angular momentum coupling. When combining two commuting angular momentum operators $\hat{\mathbf{j}}_1$ and $\hat{\mathbf{j}}_2$ the sum $\hat{\mathbf{j}} = \hat{\mathbf{j}}_1 + \hat{\mathbf{j}}_2$ is again an angular momentum operator, where the angular momenta could be an orbital and spin angular momentum of a particle for example. We call the complete set of states $\{|j_1 m_1 j_2 m_2\rangle\}$ uncoupled basis with respect to the following mutually commuting angular momentum operators $\{\hat{\mathbf{j}}_1^2, \hat{j}_{1z}, \hat{\mathbf{j}}_2^2, \hat{j}_{2z}\}$. The coupled basis is then the complete set of states $\{|(j_1 j_2) JM\rangle\}$ with respect to the operators $\{\hat{\mathbf{j}}_1, \hat{\mathbf{j}}_2, \hat{\mathbf{j}}^2, \hat{j}_z\}$. The transformation between the coupled and uncoupled basis is unitary and can be written as

$$|(j_1 j_2) JM\rangle = \sum_{m_1 m_2} |j_1 m_1 j_2 m_2\rangle \langle j_1 m_1 j_2 m_2 | (j_1 j_2) JM\rangle \quad (5.146)$$

$$= \sum_{m_1 m_2} \begin{pmatrix} j_1 & j_2 & J \\ m_1 & m_2 & M \end{pmatrix} |j_1 m_1 j_2 m_2\rangle, \quad (5.147)$$

where the overlap of the uncoupled and coupled basis states is the so-called Clebsch-Gordan coefficient defining a linear unitary transformation. The coupled angular momenta have to fulfill the triangular condition, which is

$$|j_1 - j_2| \leq J \leq j_1 + j_2. \quad (5.148)$$

Further, the Clebsch-Gordan coefficients fulfill the orthogonality relations

$$\sum_{m_1 m_2} \begin{pmatrix} j_1 & j_2 & J \\ m_1 & m_2 & M \end{pmatrix} \begin{pmatrix} j_1 & j_2 & J' \\ m_1 & m_2 & M' \end{pmatrix} = \delta_{J'}^J \delta_{M'}^M, \quad (5.149)$$

$$\sum_{JM} \begin{pmatrix} j_1 & j_2 & J \\ m_1 & m_2 & M \end{pmatrix} \begin{pmatrix} j_1 & j_2 & J \\ m'_1 & m'_2 & M \end{pmatrix} = \delta_{m'_1}^{m_1} \delta_{m'_2}^{m_2}. \quad (5.150)$$

The inverse coupling relation in order to transform from the coupled to the uncoupled

basis is

$$|j_1 m_1 j_2 m_2\rangle = \sum_{JM} \begin{pmatrix} j_1 & j_2 & J \\ m_1 & m_2 & M \end{pmatrix} |(j_1 j_2) JM\rangle. \quad (5.151)$$

Another useful more symmetric coupling coefficient is the so-called $3j$ symbol, which can be obtained from the Clebsch-Gordan coefficients

$$\begin{pmatrix} j_1 & j_2 & J \\ m_1 & m_2 & M \end{pmatrix} := (-1)^{j_1 - j_2 - M} \hat{J}^{-1} \begin{pmatrix} j_1 & j_2 & J \\ m_1 & m_2 & -M \end{pmatrix}, \quad (5.152)$$

$$\begin{pmatrix} j_1 & j_2 & J \\ m_1 & m_2 & M \end{pmatrix} = (-1)^{j_2 - j_1 - M} \hat{J} \begin{pmatrix} j_1 & j_2 & J \\ m_1 & m_2 & -M \end{pmatrix}, \quad (5.153)$$

where we defined the so-called hat factor as

$$\hat{J} := \sqrt{2J + 1}. \quad (5.154)$$

In comparison to Clebsch-Gordan coefficients, $3j$ symbols exhibit additional symmetry properties like the exchange of two angular momenta producing a phase factor only

$$\begin{pmatrix} j_2 & j_1 & J \\ m_2 & m_1 & M \end{pmatrix} = (-1)^{j_1 + j_2 + J} \begin{pmatrix} j_1 & j_2 & J \\ m_1 & m_2 & M \end{pmatrix} \quad (5.155)$$

and the inversion of projection quantum numbers

$$\begin{pmatrix} j_1 & j_2 & J \\ -m_1 & -m_2 & -M \end{pmatrix} = (-1)^{j_1 + j_2 + J} \begin{pmatrix} j_1 & j_2 & J \\ m_1 & m_2 & M \end{pmatrix}. \quad (5.156)$$

Another useful relation for $3j$ symbols is

$$\begin{pmatrix} j_1 & j_2 & 0 \\ m_1 & m_2 & 0 \end{pmatrix} = (-1)^{j_1 - m_1} \hat{j}_1^{-1} \delta_{j_2}^{j_1} \delta^{m_1, -m_2}. \quad (5.157)$$

When coupling three angular momenta, these angular momenta can be coupled in three different ways depending on the coupling order. The $6j$ symbol arises as a transformation between two basis sets, which can be written in terms of $3j$ symbols

$$\left\{ \begin{matrix} j_1 & j_2 & j_3 \\ J_1 & J_2 & J_3 \end{matrix} \right\} = \sum_{M_1 M_2 M_3 m_1 m_2 m_3} (-1)^{J_1 - M_1 + J_2 - M_2 + J_3 - M_3} \begin{pmatrix} j_1 & j_2 & j_3 \\ m_1 & m_2 & m_3 \end{pmatrix} \begin{pmatrix} j_1 & J_2 & J_3 \\ -m_1 & -M_2 & M_3 \end{pmatrix} \begin{pmatrix} J_1 & j_2 & j_3 \\ M_1 & m_2 & -M_3 \end{pmatrix} \begin{pmatrix} J_1 & J_2 & j_3 \\ -M_1 & M_2 & m_3 \end{pmatrix}. \quad (5.158)$$

The symmetries of the $6j$ symbol are invariance under the exchange of two columns and by the exchange of the upper and lower arguments in two columns.

When coupling four angular momenta the so-called $9j$ symbol arises, which can be written as

$$\left\{ \begin{matrix} j_1 & j_2 & J_{12} \\ j_3 & j_4 & J_{34} \\ J_{13} & J_{24} & J \end{matrix} \right\} = \sum_{m_1 m_2 m_3 m_4 M_{12} M_{34} M_{13} M_{24} M} \begin{pmatrix} j_1 & j_2 & J_{12} \\ m_1 & m_2 & M_{12} \end{pmatrix} \begin{pmatrix} j_3 & j_4 & J_{34} \\ m_3 & m_4 & M_{34} \end{pmatrix} \begin{pmatrix} J_{13} & J_{24} & J \\ M_{13} & M_{24} & M \end{pmatrix} \begin{pmatrix} j_1 & j_3 & J_{13} \\ m_1 & m_3 & M_{13} \end{pmatrix} \begin{pmatrix} j_2 & j_4 & J_{24} \\ m_2 & m_4 & M_{24} \end{pmatrix} \begin{pmatrix} J_{12} & J_{34} & J \\ M_{12} & M_{34} & M \end{pmatrix}. \quad (5.159)$$

The basic symmetries of the $9j$ are the invariance under interchange of its columns and rows. Further, an exchange of two columns or two rows changes the symbol by a phase $(-1)^\Sigma$, where Σ is the sum of all values of J within the $9j$ symbol.

Another useful relation is the so-called Pandya transformation [Suh07], which is defined as

$$\bar{O}_{(34)\bar{J}}^{(12)\bar{J}} = - \sum_J \left\{ \begin{matrix} j_1 & j_2 & \bar{J} \\ j_3 & j_4 & J \end{matrix} \right\} O_{(32)J}^{(14)J}, \quad (5.160)$$

where the inverse relation has exactly the same form and $O_{(32)J}^{(14)J}$ is a short-hand notation for

$$O_{(32)J}^{(14)J} = \langle 14; J | O | 32; J \rangle. \quad (5.161)$$

The Pandya transformation is a cross-coupling between the single-particle states in bra and ket. For non-scalar operators the Pandya transformation is defined as [Vob20]

$$(\bar{O}^L)_{(34)\bar{J}}^{(12)J} = - \sum_{JJ'} \hat{J}\hat{J}'\hat{J} \left\{ \begin{matrix} j_1 & j_2 & \bar{J} \\ j_4 & j_3 & \bar{J}' \\ J & J' & L \end{matrix} \right\} (-1)^{j_2+j_4+\bar{J}+J'} (O^L)_{(32)J}^{(14)J}. \quad (5.162)$$

5.7.2. The Wigner-Eckart Theorem

The Wigner-Eckart Theorem [Eck30; Wig31] simplifies calculations of matrix elements of operators. We start with observables written in terms of spherical tensor operators by exploiting their transformation properties. We are able to define a reduced matrix element, which does not depend on projection quantum numbers anymore and contains all physical information, which is carried by the wave function of the nucleus. Let us define a matrix element $\langle \psi; JM | \hat{T}_{M_L}^L | \psi'; J'M' \rangle$, where $\hat{T}_{M_L}^L$ is a component of a spherical tensor operator \hat{T}^L of rank L , J is the angular momentum and M its projection. With that we can state the Wigner-Eckart Theorem.

Theorem 5.1: Wigner-Eckart Theorem

A matrix element of a spherical tensor operator can be written as a product of a geometric factor containing the projection quantum numbers M, M_L and M' and a matrix element not containing them.

$$\langle \psi; JM | \hat{T}_{M_L}^L | \psi'; J'M' \rangle = (-1)^{J-M} \begin{pmatrix} J & L & J' \\ -M & M_L & M' \end{pmatrix} \langle \psi; J || \hat{T}^L || \psi'; J' \rangle, \quad (5.163)$$

where $\langle \psi; J || \hat{T}^L || \psi'; J' \rangle$ is the so-called reduced matrix element.

The Wigner-Eckart theorem states that it is possible to extract a factor which contains all J quantum numbers but no projection quantum numbers. Another useful relation in connection with the Wigner-Eckart theorem is

$$\langle \psi; J || \hat{T}^L || \psi'; J' \rangle = \sum_{MM'M_L} (-1)^{J-M} \begin{pmatrix} J & L & J' \\ -M & M_L & M' \end{pmatrix} \langle \psi; JM | \hat{T}_{M_L}^L | \psi'; J'M' \rangle. \quad (5.164)$$

We can deduce from the properties of $3j$ symbols that the triangular condition and the projection quantum number conservation have to be fulfilled, which can be written as

$$\langle \psi; JM | \hat{T}_{M_L}^L | \psi'; J'M' \rangle = 0 \quad \text{unless} \quad \begin{cases} |J - L| \leq J' \leq J + L, \text{ and} \\ M_L + M' = M \end{cases}. \quad (5.165)$$

Another important relation is the behavior of the reduced matrix element under complex conjugation

$$\langle \psi; J | \hat{T}^L | \psi'; J' \rangle = (-1)^{J-J'} \langle \psi'; J' | \hat{T}^L | \psi; J \rangle^*. \quad (5.166)$$

The Wigner-Eckart theorem for scalar operators is a special case since L and M_L vanish the equation can be simplified to

$$\langle \psi; JM | \hat{T}_0^0 | \psi'; J' M' \rangle = \hat{J}^{-1} \langle \psi; J | \hat{T}^0 | \psi'; J' \rangle \delta_{J'}^J \delta_{M'}^M. \quad (5.167)$$

From this we can see that the coupled matrix elements of scalar operators are only non-zero if its total angular momentum and their projections have the same value in bra and ket. Furthermore, we can replace the reduced and the coupled matrix elements with each other due to the independence of the matrix element on the specific value of the protection. More on spherical tensor operators can be found in [Vob20].

5.7.3. Vacuum- and Reference-State Normal Ordering for Spherical Equations

Now where we discussed angular momentum coupling and non-scalar operators we can show the equations for vacuum- and reference-state normal ordering for non-scalar spherical equations. When the operator \hat{O}^L is a spherical tensor operator with tensor rank L , equations (5.72) to (5.75) and (5.76) to (5.79) are angular-momentum coupled and written in terms of reduced matrix elements, i.e., they do not depend on the projection quantum numbers anymore. The non-scalar reference-state matrix elements in terms of vacuum matrix elements are

$$\left(\tilde{O}^L \right)_q^p = \left(O^L \right)_q^p + \sum_q \hat{j}_q n_q \left(\bar{O}^L \right)_{(qq)0}^{(pr)L}, \quad (5.168)$$

$$\left(\tilde{O}^L \right)_{(qs)J'}^{(pr)J} = \left(O^L \right)_{(qs)J'}^{(pr)J}. \quad (5.169)$$

The vacuum matrix elements in terms of reference-state matrix elements can be written as

$$\left(O^L \right)_q^p = \left(\tilde{O}^L \right)_q^p - \sum_q \hat{j}_q n_q \left(\bar{\bar{O}}^L \right)_{(qq)0}^{(pr)L} \quad (5.170)$$

$$(O^L)_{(qs)J'}^{(pr)J} = (\tilde{O}^L)_{(qs)J'}^{(pr)J} \quad (5.171)$$

Instructions for the derivation of these equations can be found in [Vob20].

5.8. J -Coupled Scalar Commutator Equations in Natural Orbitals

Since the J -coupled flow equations and their derivation can be found in [Geb17], we will only give an overview about the final equations in natural orbitals. Also, the symmetrizers need to be coupled resulting in the so-called spherical symmetrizers. These can be written as [Vob20]

$$\hat{\Xi}_{1B}^J = \frac{1}{2} (1 \pm (-1)^{j_1 - j_2} P_{12}) \quad (5.172)$$

$$\hat{\Xi}_{2B}^J = \frac{1}{8} \left(1 + (-1)^{j_1 + j_2 + J + 1} P_{12} \right) \left(1 + (-1)^{j_3 + j_4 + J' + 1} P_{34} \right) \left(1 \pm (-1)^{J + J'} P_{13} P_{24} P_{JJ'} \right). \quad (5.173)$$

With these we can summarize the scalar J -coupled commutator equations of the multi-reference IM-SRG(2)

$$\check{O}_{(34)J}^{(12)J} = + \hat{\Xi}_{2B}^J \sum_p 4\Omega_p^1 O_{(34)J}^{(p2)J} \quad (5.174)$$

$$- \hat{\Xi}_{2B}^J \sum_p 4O_p^1 \Omega_{(34)J}^{(p2)J} \quad (5.175)$$

$$+ \hat{\Xi}_{2B}^J \sum_{pq} \Omega_{(pq)J}^{(12)J} O_{(34)J}^{(pq)J} (1 - n_p - n_q) \quad (5.176)$$

$$+ \hat{\Xi}_{2B}^J \sum_{pq} \sum_{J'} 4\hat{J}^2 \left\{ \begin{matrix} J & j_1 & j_2 \\ J' & j_3 & j_4 \end{matrix} \right\} \bar{\Omega}_{(pq)\bar{J}'}^{(13)\bar{J}'} \bar{O}_{(24)\bar{J}'}^{(pq)\bar{J}'} (n_p - n_q), \quad (5.177)$$

$$\check{O}_2^1 = + 2 \hat{\Xi}_{1B}^J \sum_p \Omega_p^1 O_2^p \quad (5.178)$$

$$+ \hat{\Xi}_{1B}^J \hat{J}_1^{-2} \sum_{pq} \sum_J \hat{J}^2 \left(\Omega_q^p O_{(p2)J}^{(q1)J} \right) (n_p - n_q) \quad (5.179)$$

$$+ \hat{\Xi}_{1B}^J \hat{J}_1^{-2} \sum_{pq} \sum_J \hat{J}^2 \left(O_q^p \Omega_{(p2)J}^{(q1)J} \right) (n_p - n_q) \quad (5.180)$$

$$+ \frac{1}{2} \hat{\Xi}_{1B}^J \hat{J}_1^{-2} \sum_{pqr} \sum_J \hat{J}^2 \Omega_{(qr)J}^{(1p)J} O_{(2p)J}^{(qr)J} (n_p \bar{n}_q \bar{n}_r + \bar{n}_p n_q n_r) \quad (5.181)$$

$$+ \hat{\Xi}_{1B}^J \hat{J}_1^{-2} \sum_{rtvsu} \sum_J \frac{1}{2} \hat{J}^2 \Omega_{(su)J}^{(1t)J} O_{(2t)J}^{(rv)J} \lambda_{(rv)J}^{(su)J} \quad (5.182)$$

$$+ \hat{\Xi}_{1B}^J \hat{J}_1^{-2} \sum_{rtvsu} \sum_{\bar{J}} (-2) \bar{\Omega}_{(sr)\bar{J}}^{(1t)\bar{J}} \bar{O}_{(2t)\bar{J}}^{(vu)\bar{J}} \bar{\lambda}_{(vu)\bar{J}}^{(sr)\bar{J}} \quad (5.183)$$

$$+ \hat{\Xi}_{1B}^J \hat{J}_1^{-2} \sum_{rtvsu} \sum_{J_1 J_2} \hat{J}_1^2 \hat{J}_2^2 \delta_{jt}^{jr} \hat{J}_r^{-2} \Omega_{(t2)J_1}^{(1r)J_1} O_{(su)J_2}^{(tv)J_2} \lambda_{(vr)J_2}^{(sw)J_2} \quad (5.184)$$

$$- \hat{\Xi}_{1B}^J \hat{J}_1^{-2} \sum_{rtvsu} \sum_{J_1 J_2} \hat{J}_1^2 \hat{J}_2^2 \delta_{jt}^{jr} \hat{J}_r^{-2} \Omega_{(su)J_2}^{(tv)J_2} O_{(t2)J_1}^{(1r)J_1} \lambda_{(vr)J_2}^{(sw)J_2}, \quad (5.185)$$

$$\check{O}_0 = + \sum_{pq} \Omega_q^p O_p^q (n_p - n_q) \quad (5.186)$$

$$+ \frac{1}{4} \sum_{prqs} \sum_J \hat{J}^2 \left(\Omega_{(qs)J}^{(pr)J} O_{(pr)J}^{(qs)J} - \Omega_{(pr)J}^{(qs)J} O_{(qs)J}^{(pr)J} \right) n_p n_r \bar{n}_q \bar{n}_s \quad (5.187)$$

$$+ \frac{1}{4} \sum_{prqs} \sum_J \hat{J}^2 O_{(qs)J}^{(pr)J} \lambda_{(qs)J}^{(pr)J} + \mathcal{O}(\lambda^{[3]}). \quad (5.188)$$

Note that until now an index p was a m -scheme collective index $|p\rangle = |nljm_jt\rangle$. From now on we will refer to p as a spherical collective single-particle index $|p\rangle = |nljt\rangle$ in a j -coupled basis. More on the implementation of these commutator equations can be found in [Geb17], where they are reformulated in such a way that the matrix elements can be written in matrices. The advantage is that the commutator equations can then be written in terms of matrix products to improve the computational efficiency.

5.9. J -Coupled Non-Scalar Commutator Equations in Natural Orbitals

For non-scalar operators, the J -coupling procedure is more complicated due to the fact that also the tensor rank L is involved resulting in more $6j$ symbols and a more complicated coupling pattern. The derivation of these is based on a diagrammatic approach following [KMV88] and can be found in [Vob20]. We only give an overview of the J -coupled non-scalar commutator equations. The equations are written in terms of reduced matrix elements. These can be written as

$$\left(\check{O}^L \right)_{(34)J'}^{(12)J} = + \hat{\Xi}_{2B}^J \sum_p 4 \left(\Omega^0 \right)_p^1 \left(O^L \right)_{(34)J'}^{(p2)J} \hat{J}_1^{-1} \quad (5.189)$$

$$- \hat{\Xi}_{2B}^J \sum_p 4 \hat{J} (O^L)_p^1 (\Omega^0)_{(34)J'}^{(p2)J} (-1)^{L+J'+j_1+j_2} \left\{ \begin{matrix} j_1 & J & j_2 \\ J' & j_p & L \end{matrix} \right\} \quad (5.190)$$

$$+ \hat{\Xi}_{2B}^J \sum_{pq} \hat{J}^{-1} (\Omega^0)_{(pq)J}^{(12)J} (O^L)_{(34)J'}^{(pq)J} (1 - n_p - n_q) \quad (5.191)$$

$$+ \hat{\Xi}_{2B}^J \sum_{pq} 4 (\bar{\Omega}^0)_{(pq)\bar{J}_1}^{(13)\bar{J}_1} (\bar{O})_{(24)\bar{J}_2}^{(pq)\bar{J}_2} (n_p - n_q), \quad (5.192)$$

$$\left(\check{O}^L \right)_2^1 = + 2 \hat{\Xi}_{1B}^J \sum_p \hat{J}_1^{-1} (\Omega^0)_p^1 (O^L)_2^p \quad (5.193)$$

$$+ \hat{\Xi}_{1B}^J \sum_{pq} (\Omega^0)_q^p (\bar{O}^L)_{(pq)0}^{(12)L} (n_p - n_q) \quad (5.194)$$

$$+ \hat{\Xi}_{1B}^J \sum_{pq} (O^L)_q^p (\bar{\Omega}^0)_{(pq)L}^{(12)L} (n_p - n_q) \quad (5.195)$$

$$+ \hat{\Xi}_{1B}^J \sum_{pqr} \sum_{JJ'} \hat{J}' (\Omega^0)_{(qr)J}^{(1p)J} (O^L)_{(2p)J'}^{(qr)J} (-1)^{j_1+j_p+J'+L} \left\{ \begin{matrix} j_2 & j_1 & L \\ J & J' & j_p \end{matrix} \right\} (n_p \bar{n}_q \bar{n}_r + \bar{n}_p n_q n_r) \quad (5.196)$$

$$+ \frac{\hat{\Xi}_{1B}^J}{2} \sum_{rtvs} \sum_{JJ'} (\Omega^0)_{(sw)J}^{(1t)J} (O^L)_{(2t)J'}^{(rv)J} (\lambda^0)_{(rv)J}^{(sw)J} (-1)^{L+J'+j_1+j_t} \hat{J}^{-1} \hat{J}' \left\{ \begin{matrix} L & J & J' \\ j_t & j_2 & j_1 \end{matrix} \right\} \quad (5.197)$$

$$+ \hat{\Xi}_{1B}^J \sum_{rtvs} \sum_{\bar{J}\bar{J}'} (+2) \hat{J} \hat{J}' (\bar{\Omega}^0)_{(sr)\bar{J}}^{(1t)\bar{J}} (\bar{O}^L)_{(2t)\bar{J}'}^{(vw)\bar{J}} (\bar{\lambda}^0)_{(vw)\bar{J}}^{(sr)\bar{J}} \quad (5.198)$$

$$+ \hat{\Xi}_1^J \sum_{rtvs} (\bar{\Omega}^0)_{(tr)L}^{(12)L} (O^L)_{(sw)J'}^{(tv)J} (\lambda^0)_{(vr)J'}^{(sw)J} \hat{J} \hat{J}' (-1)^{j_t+j_v+L+J'} \left\{ \begin{matrix} L & j_t & j_r \\ j_v & J' & J \end{matrix} \right\} \quad (5.199)$$

$$- \hat{\Xi}_{1B}^J \sum_{rtvs} \sum_J (-1)^{2j_r+j_v+j_t+J} \hat{J}_t^{-1} \hat{J}^2 \delta_{j_t}^{j_r} (\Omega^0)_{(sw)J}^{(tv)J} (\bar{O}^L)_{(tr)0}^{(12)L} (\lambda^0)_{(vr)J}^{(sw)J}, \quad (5.200)$$

$$\check{O}_0 = + \sum_{pq} (\Omega^0)_q^p (O^0)_p^q \delta_0^L (n_p - n_q) \quad (5.201)$$

$$+ \frac{1}{4} \sum_{prqs} \sum_J \left((\Omega^0)_{(qs)J}^{(pr)J} (O^L)_{(pr)J}^{(qs)J} - (\Omega^0)_{(pr)J}^{(qs)J} (O^L)_{(qs)J}^{(pr)J} \right) n_p n_r \bar{n}_q \bar{n}_s \delta_0^L \quad (5.202)$$

$$+ \frac{1}{4} \sum_{pqrs} \sum_J (O^L)_{(qs)J}^{(pr)J} (\lambda^0)_{(qs)J}^{(pr)J} \delta_0^L, \quad (5.203)$$

where (O^L) is a matrix element of a non-scalar tensor operator \hat{O}^L with the tensor rank L and scalar matrix elements are denoted as (O^0) . Due to the fact that the matrix elements of \hat{O}^L are not diagonal in the total angular momentum, the computational cost is increasing significantly. Consequently, only the Magnus evolution is implemented for non-scalar operators since a direct evolution is computationally too demanding.

5.10. Generators of the IM-SRG

The aim of the IM-SRG is to suppress a specific off-diagonal part of the Hamiltonian in such a way that we obtain a decoupling pattern. In this work, the off-diagonal part is defined as the part, which couples a reference state $|\psi_{\text{ref}}\rangle$ to its particle-hole excitations, where the final Hamiltonian of the IM-SRG evolution is given by $\hat{H}(\infty)$. For suppressing the off-diagonal part of the Hamiltonian, there exist different generator types $\hat{\eta}(s)$. There are many ways to come from the initial Hamiltonian $\hat{H}(0)$ to the final Hamiltonian. These paths are called decoupling pattern and depend on the choice of the generator. The generators differ in their decoupling behavior and control the numerical stability and efficiency during the IM-SRG evolution. The generator type and decoupling pattern are independent of each other, making the IM-SRG very flexible in terms of targeting different states and open-shell nuclei.

In this work we will use two different types of generators, namely the White [Whi02] and the imaginary-time [Car+15] generator. Further, we will also give an overview of the Wegner [Weg94] generator, which is the most simple choice for the IM-SRG.

5.10.1. The Wegner Generator

The Wegner generator was first proposed by Wegner [Weg94] and is defined as the commutator of the diagonal part of the Hamiltonian $\hat{H}^{\text{d}}(s)$ and the off-diagonal part of the Hamiltonian $\hat{H}^{\text{od}}(s)$

$$\hat{\eta}(s) = \left[\hat{H}^{\text{d}}(s), \hat{H}^{\text{od}}(s) \right]. \quad (5.204)$$

A fixed point of the flow is reached if $\hat{H}^{\text{od}}(s)$ vanishes. However, the Wegner generator is leading to stiff ODEs due to the fact that we obtain cubic terms in the Hamiltonian [Her+16].

Analyzing the asymptotic behavior of the off-diagonal part of the Hamiltonian, we obtain

$$\langle i | \hat{H}^{\text{od}}(s) | j \rangle \approx \langle i | \hat{H}^{\text{od}}(s_0) | j \rangle e^{-(E_i - E_j)^2 (s - s_0)}, \quad s > s_0, \quad (5.205)$$

where s_0 has to be large enough. From this behavior we can see that the Wegner generator yields real renormalization group transformations, i.e., matrix elements between states with large energy differences decay at smaller flow parameters s compared to states with small energy differences. This shows that the decoupling path can be longer compared to other generators [Her+16].

The off-diagonal part of the Hamiltonian can be written as

$$\hat{H}^{\text{od}}(s) = \sum_{pq} (f^{\text{od}})_q^p \{ \hat{a}_q^p \} + \sum_{prqs} (\Gamma^{\text{od}})_{qs}^{pr} \{ \hat{a}_{qs}^{pr} \}, \quad (5.206)$$

where the off-diagonal matrix elements $(f^{\text{od}})_q^p$ and $(\Gamma^{\text{od}})_{qs}^{pr}$ can be written as

$$(f^{\text{od}})_q^p = \langle \psi_{\text{ref}} | \hat{H} \{ \hat{a}_q^p \} | \psi_{\text{ref}} \rangle + [p \leftrightarrow q], \quad (5.207)$$

$$(\Gamma^{\text{od}})_{qs}^{pr} = \langle \psi_{\text{ref}} | \hat{H} \{ \hat{a}_{qs}^{pr} \} | \psi_{\text{ref}} \rangle + [(pr) \leftrightarrow (qs)], \quad (5.208)$$

where $(f^{\text{od}})_q^p$ decouples one-particle one-hole (1p1h) and $(\Gamma^{\text{od}})_{qs}^{pr}$ decouples two-particle two-hole (2p2h) states from the reference state. Note that $[p \leftrightarrow q]$ indicates that the indices p and q are exchanged and $[(pr) \leftrightarrow (qs)]$ indicates that the indices pr and qs are permuted.

5.10.2. The White- and Imaginary-Time Generators

In this work we are mostly using the White and imaginary-time generators. The White generator was first proposed by White and used in the context of canonical transformation theory in quantum chemistry [Whi02; TBS11]. The imaginary-time generator on the other hand is frequently used in Quantum Monte Carlo methods [Car+15]. Compared to the Wegner generator, these generators show an improved decoupling behavior and result in less stiff ODEs.

We start with the general form of the generator in second quantization

$$\hat{\eta}(s) = \sum_{pq} \eta_q^p \{ \hat{a}_q^p \} + \frac{1}{4} \sum_{prqs} \eta_{qs}^{pr} \{ \hat{a}_{qs}^{pr} \}, \quad (5.209)$$

where its matrix elements in case of the White and imaginary-time generators are given

as

$$\eta_q^p = \mathcal{F}(\Delta_q^p)(f^{\text{od}})_q^p - [p \leftrightarrow q], \quad (5.210)$$

$$\eta_{qs}^{pr} = \mathcal{F}(\Delta_{qs}^{pr})(\Gamma^{\text{od}})_{qs}^{pr} - [(pr) \leftrightarrow (qs)] \quad (5.211)$$

with

$$\mathcal{F}(\Delta) := \begin{cases} \frac{1}{\Delta} & \text{for White} \\ \text{sgn}(\Delta) & \text{for imaginary-time} \end{cases}, \quad (5.212)$$

where Δ_q^p and Δ_{qs}^{pr} are the so-called Epstein-Nesbet energies, which are the difference between the expectation values of the Hamiltonian with respect to the reference state and its excitations

$$\begin{aligned} \Delta_q^p &= \langle \psi_{\text{ref}} | \{ \hat{a}_q^p \}^\dagger \hat{H} \{ \hat{a}_q^p \} | \psi_{\text{ref}} \rangle - \langle \psi_{\text{ref}} | \hat{H} | \psi_{\text{ref}} \rangle \\ &= -\bar{n}_p^2 n_q^2 \Gamma_{pq}^{pq} + \bar{n}_p^2 n_q f_p^p - \bar{n}_p n_q^2 f_q^q + E(\bar{n}_p n_q - 1) + \mathcal{O}(\lambda^{[2]}), \end{aligned} \quad (5.213)$$

$$\begin{aligned} \Delta_{qs}^{pr} &= \langle \psi_{\text{ref}} | \{ \hat{a}_{qs}^{pr} \}^\dagger \hat{H} \{ \hat{a}_{qs}^{pr} \} | \psi_{\text{ref}} \rangle - \langle \psi_{\text{ref}} | \hat{H} | \psi_{\text{ref}} \rangle \\ &= (1 + \hat{\tau}_q^p \hat{\tau}_s^r) \left(\bar{n}_p \bar{n}_r n_q n_s \left(\frac{1}{2} \bar{n}_p \bar{n}_r \Gamma_{pr}^{pr} + \frac{1}{2} n_q n_s \Gamma_{qs}^{qs} - \bar{n}_p n_s \Gamma_{ps}^{ps} - \bar{n}_p n_q \Gamma_{pq}^{pq} \right) \right. \\ &\quad \left. + \bar{n}_p \bar{n}_r n_q n_s (\bar{n}_p f_p^p - n_q f_q^q) + \frac{1}{2} E(\bar{n}_p \bar{n}_r n_q n_s - 1) + \mathcal{O}(\lambda^{[2]}) \right). \end{aligned} \quad (5.214)$$

5.10.3. Decoupling Patterns

Using the Wegner, imaginary-time or White generators, the reference state $|\psi_{\text{ref}}\rangle$ can be decoupled from all 1p1h and 2p2h excitations, i.e., the following set of many-body states

$$\mathcal{E}_{1\text{p}1\text{h}} = \{ \{ \hat{a}_q^p \} |\psi_{\text{ref}}\rangle \}, \quad \mathcal{E}_{2\text{p}2\text{h}} = \{ \{ \hat{a}_{qs}^{pr} \} |\psi_{\text{ref}}\rangle \}. \quad (5.215)$$

The decoupling condition for the 1p1h excitations is

$$\begin{aligned} 0 &\stackrel{\dagger}{=} D_1(1, 2) := \langle \psi_{\text{ref}} | \hat{H} \{ \hat{a}_2^1 \} | \psi_{\text{ref}} \rangle = n_1 \bar{n}_2 f_2^1 + \sum_{pq} f_q^p \lambda_{q2}^{p1} \\ &+ \frac{1}{2} \sum_{prq} \left(\bar{n}_1 \lambda_{2q}^{pr} \Gamma_{1q}^{pr} - n_2 \Gamma_{pr}^{2q} \lambda_{pr}^{1q} \right) + \mathcal{O} \left(\lambda^{[3]} \right). \end{aligned} \quad (5.216)$$

Further, the decoupling condition for 2p2h excitations can be written as

$$\begin{aligned} 0 &\stackrel{\dagger}{=} D_2(1, 2, 3, 4) := \langle \psi_{\text{ref}} | \hat{H} \{ \hat{a}_{34}^{12} \} | \psi_{\text{ref}} \rangle = \bar{n}_1 \bar{n}_2 n_3 n_4 \Gamma_{12}^{34} \\ &+ (1 - P_{34}) n_4 \sum_p f_p^4 \lambda_{p3}^{12} - (1 - P_{12}) \bar{n}_2 \sum_p f_2^p \lambda_{34}^{p1} \\ &+ \frac{1}{2} \bar{n}_1 \bar{n}_2 \sum_{pq} \Gamma_{12}^{pq} \lambda_{34}^{pq} + \frac{1}{2} n_3 n_4 \sum_{pq} \Gamma_{pq}^{34} \lambda_{pq}^{12} \\ &- (1 - P_{12})(1 - P_{34}) n_3 \bar{n}_1 \sum_{pq} \Gamma_{1q}^{p3} \lambda_{q4}^{p2} + \mathcal{O}(\dots), \end{aligned} \quad (5.217)$$

where all higher contributions to the irreducible density matrices beyond the two-body rank and also quadratic terms of the two-body irreducible density matrices are neglected. From the emergence of these terms we can conclude that the reference state is coupled to its excitations in a non-trivial way [Vob20].

This strict decoupling pattern has been relaxed in such a way that the reference state $|\psi_{\text{ref}}\rangle$ does not get decoupled from all excitations. Instead, $|\psi_{\text{ref}}\rangle$ gets decoupled from the basis states lying in the reference model space. Formally, only the particle-hole excitations, where the sum of the single-particle energies e of the annihilated and created particles is not equal, are decoupled.

$$\mathcal{E}'_{1\text{p}1\text{h}} = \{ \{ \hat{a}_q^p \} |\psi_{\text{ref}}\rangle | e(p) \neq e(q) \}, \quad (5.218)$$

$$\mathcal{E}'_{2\text{p}2\text{h}} = \{ \{ \hat{a}_{qs}^{pr} \} |\psi_{\text{ref}}\rangle | e(p_1) + e(p_2) \neq e(q_1) + e(q_2) \}, \quad (5.219)$$

and the new decoupling conditions are now

$$0 = \tilde{D}_1(p_1, p_2) = \begin{cases} D_1(p_1, p_2) & \text{if } e(p_1) \neq e(p_2), \\ 0 & \text{else} \end{cases}, \quad (5.220)$$

$$0 = \tilde{D}_2(p_1, p_2, p_3, p_4) = \begin{cases} D_2(p_1, p_2, p_3, p_4) & \text{if } e(p_1) + e(p_2) \neq e(p_3) + e(p_4), \\ 0 & \text{else} \end{cases}. \quad (5.221)$$

More on these optimizations like the illustration that the slightly relaxed decoupling scheme is sufficient can be found in [Vob20].

Finally, we have different choices for the generators. In this work when not stated otherwise we use the White generator with the modified decoupling scheme since its decoupling is faster compared to the imaginary-time generator [Her+16].

6. Derivation of a Leading-Order Three-Body Correction

In this chapter we are going to derive a so-called leading-order three-body correction (LOTC) to the multi-reference IM-SRG. Until now, the formalism includes interaction contributions up to the two-body rank only, i.e., it uses the NO2B approximation. As was found in [Par+17] and [Vob20], non-scalar observables like $B(E2)$ transition strengths and electric quadrupole moments Q cannot be described accurately using the NO2B approximation only. Two examples are the oxygen and neon isotopic chains, where the $B(E2)$ transition strengths are systematically underestimated compared to experimental results. In [Vob20] it was shown that induced two-body terms of the electric quadrupole operator show a much larger contribution to the transition strength compared to the one-body terms, which partially do not contribute or show approximately half of the contribution. Therefore, the question of induced three-body contributions arises. But since a complete evaluation of the IM-SRG(3) is computationally expensive in terms of CPU time and memory, we have developed a leading-order three-body correction for the BCH series in the observable transformation.

This chapter is split in four sections. In the first section we present the strategy and Ansatz for the LOTC. In the second section we derive the three-body commutator equations for the multi-reference IM-SRG, where we use the generalized Wick theorem for the evaluation of commutators. Afterwards we normal-order all three-body observable terms. In the second section we will focus on the implementation of the LOTC and optimizations using intermediate tensors. The last section will describe a custom program in Python we used for the symbolic derivation of the three-body commutators. We did this programmatically because the derivation by hand is very time consuming and error prone.

6.1. Strategy for the LOTC

Before starting with the evaluation of the induced three-body commutators, we present the strategy and ingredients needed for the LOTC. We use the Magnus formulation of the IM-SRG(2) to construct the Magnus operator $\hat{\Omega}(s)$ and to compute the desired observable $\hat{O}(s)$ using the NO2B approximation. The Magnus operator is then used for

the three-body correction in the evaluation of the BCH series. This ansatz is comfortable because the flow equation does not change and we only need to pick the leading-order part, where three-body terms are induced in the evaluation of the BCH series.

6.2. Three-Body Commutators and the LOTC

6.2.1. Derivation of the Three-Body Commutators

For the derivation of the three-body contributions to the IM-SRG(2) we need the BCH series in the Magnus formalism given by

$$\hat{O}(s) = \sum_{k=0}^{\infty} \frac{1}{k!} \left[\hat{\Omega}(s), \hat{O}(0) \right]_k \quad (6.222)$$

beyond the NO2B approximation by taking induced three-body contributions into account, which has never been done before for the multi-reference IM-SRG.

Each of the operators is normal ordered with respect to a multi-determinantal reference state $|\Psi_{\text{ref}}\rangle$ and $\hat{O}(s)$ is truncated at the NO3B level, which can be written as

$$\hat{\Omega}(s) = \hat{\Omega}^{[1]} + \hat{\Omega}^{[2]} = \sum_{pq} \Omega_q^p \{ \hat{a}_q^p \} + \frac{1}{4} \sum_{pqrs} \Omega_{qs}^{pr} \{ \hat{a}_{qs}^{pr} \} \quad (6.223)$$

$$\begin{aligned} \hat{O}(s) &= \hat{O}^{[0]} + \hat{O}^{[1]} + \hat{O}^{[2]} + \hat{O}^{[3]} \\ &= O_0 + \sum_{pq} O_q^p \{ \hat{a}_q^p \} + \frac{1}{4} \sum_{pqrs} O_{qs}^{pr} \{ \hat{a}_{qs}^{pr} \} + \frac{1}{36} \sum_{prtqsu} O_{qsu}^{prt} \{ \hat{a}_{qsu}^{prt} \}. \end{aligned} \quad (6.224)$$

Note that we truncated $\hat{\Omega}(s)$ at NO2B since we do not solve the IM-SRG(3) flow-equation, i.e., the three-body part of the Magnus operator $\hat{\Omega}^{[3]}$ is not available.

Splitting up the commutator evaluation with respect to the particle ranks, we obtain

$$\begin{aligned} \hat{O}(s) &= \left[\hat{\Omega}(s), \hat{O}(0) \right] = \left[\hat{\Omega}^{[1]} + \hat{\Omega}^{[2]}, \hat{O}^{[0]} + \hat{O}^{[1]} + \hat{O}^{[2]} + \hat{O}^{[3]} \right] \\ &= \left[\hat{\Omega}^{[1]}, \hat{O}^{[1]} \right] + \left[\hat{\Omega}^{[1]}, \hat{O}^{[2]} \right] + \left[\hat{\Omega}^{[2]}, \hat{O}^{[1]} \right] + \left[\hat{\Omega}^{[2]}, \hat{O}^{[2]} \right] \\ &\quad + \left[\hat{\Omega}^{[1]}, \hat{O}^{[3]} \right] + \left[\hat{\Omega}^{[2]}, \hat{O}^{[3]} \right]. \end{aligned} \quad (6.225)$$

We will only evaluate the commutators beyond the two-body rank because the other expressions are part of the IM-SRG(2) formulation already. We will derive the commutators $\left[\hat{\Omega}^{[1]}, \hat{O}^{[2]} \right]$ and $\left[\hat{\Omega}^{[2]}, \hat{O}^{[3]} \right]$ using the generalized Wick theorem.

In addition, we need the three body part of $[\hat{\Omega}^{[2]}, \hat{O}^{[2]}]$, which is given by

$$[\hat{\Omega}^{[2]}, \hat{O}^{[2]}]_{3B} = \frac{1}{8} \sum_{\substack{prt \\ qsu}} \left(\sum_v \Omega_{sv}^{pr} O_{qu}^{tv} + \Omega_{qs}^{pv} O_{uv}^{rt} - \Omega_{qv}^{pr} O_{su}^{tv} - \Omega_{qs}^{rv} O_{uv}^{pt} \right) \{ \hat{a}_{qsu}^{prt} \}, \quad (6.226)$$

where $[\hat{\Omega}^{[2]}, \hat{O}^{[2]}]_{3B}$ denotes the three-body part of the commutator.

As an example, let us evaluate the first term of the commutator $[\hat{\Omega}^{[1]}, \hat{O}^{[3]}]$, which is given by

$$[\hat{\Omega}^{[1]}, \hat{O}^{[3]}]_{3B} = \frac{1}{36} \sum_{\substack{prt \\ qsuw}} \Omega_q^p O_{suw}^{rtv} [\{ \hat{a}_q^p \}, \{ \hat{a}_{suw}^{rtv} \}] \quad (6.227)$$

$$= \frac{1}{36} \sum_{\substack{prt \\ qsuw}} \Omega_q^p O_{suw}^{rtv} (\{ \hat{a}_q^p \} \{ \hat{a}_{suw}^{rtv} \} - \{ \hat{a}_{suw}^{rtv} \} \{ \hat{a}_q^p \}) \quad (6.228)$$

$$= \frac{1}{36} \sum_{\substack{prt \\ qsuw}} \Omega_q^p O_{suw}^{rtv} (-\gamma_s^p \{ \hat{a}_{quw}^{rtv} \} + \gamma_u^p \{ \hat{a}_{qsw}^{rtv} \} - \gamma_w^p \{ \hat{a}_{qsu}^{rtv} \} - \bar{\gamma}_q^r \{ \hat{a}_{suw}^{ptv} \} \\ + \bar{\gamma}_q^t \{ \hat{a}_{suw}^{prv} \} - \bar{\gamma}_q^v \{ \hat{a}_{suw}^{prt} \} - \gamma_q^r \{ \hat{a}_{suw}^{ptv} \} + \gamma_q^t \{ \hat{a}_{suw}^{prv} \} \\ - \gamma_q^v \{ \hat{a}_{suw}^{prt} \} - \bar{\gamma}_s^p \{ \hat{a}_{quw}^{rtv} \} + \bar{\gamma}_u^p \{ \hat{a}_{qsw}^{rtv} \} - \bar{\gamma}_w^p \{ \hat{a}_{qsu}^{rtv} \}). \quad (6.229)$$

Now we can use the relation $\bar{\gamma}_q^p + \gamma_q^p = \delta_q^p$ and obtain

$$[\hat{\Omega}^{[1]}, \hat{O}^{[3]}]_{3B} = \frac{1}{36} \sum_{\substack{prt \\ qsuw}} \Omega_q^p O_{suw}^{rtv} (-\delta_s^p \{ \hat{a}_{quw}^{rtv} \} + \delta_u^p \{ \hat{a}_{qsw}^{rtv} \} - \delta_w^p \{ \hat{a}_{qsu}^{rtv} \} + \delta_q^t \{ \hat{a}_{suw}^{prv} \} \\ - \delta_q^r \{ \hat{a}_{suw}^{ptv} \} - \delta_q^v \{ \hat{a}_{suw}^{prt} \}). \quad (6.230)$$

The next step is to relabel the summation indices of the matrix elements of the tensors in order to obtain a form, which is compliant with (6.224). For the first term for example, we need to relabel p by v and s by w . Doing this for all terms, we arrive at

$$[\hat{\Omega}^{[1]}, \hat{O}^{[3]}]_{3B} = \frac{1}{36} \sum_{\substack{prt \\ qsuw}} (O_w^p \Omega_{qsu}^{rtv} - O_w^r \Omega_{qsu}^{ptv} + O_w^t \Omega_{qsu}^{prv} \\ - O_q^v \Omega_{suw}^{prt} + O_s^v \Omega_{quw}^{prt} - O_u^v \Omega_{qsw}^{prt}) \delta_w^v \{ \hat{a}_{qsu}^{prt} \}. \quad (6.231)$$

Finally, we can evaluate the Kronecker delta to eliminate the summation index w and obtain

$$\begin{aligned} \left[\hat{\Omega}^{[1]}, \hat{O}^{[3]} \right]_{3B} = & \frac{1}{36} \sum_{\substack{prt \\ qsu}} \left(\sum_v + O_v^p \Omega_{qsu}^{rtv} - O_v^r \Omega_{qsu}^{ptv} + O_v^t \Omega_{qsu}^{prv} \right. \\ & \left. - O_q^v \Omega_{suv}^{prt} + O_s^v \Omega_{quv}^{prt} - O_u^v \Omega_{qsv}^{prt} \right) \{ \hat{a}_{qsu}^{prt} \}. \end{aligned} \quad (6.232)$$

For the two-, one- and zero-body-part of $\left[\hat{\Omega}^{[1]}, \hat{O}^{[3]} \right]$ we obtain

$$\begin{aligned} \left[\hat{\Omega}^{[1]}, \hat{O}^{[3]} \right] = & + \frac{1}{36} \sum_{\substack{prt \\ qsu}} \left(\sum_v \Omega_v^p O_{qsu}^{rtv} - \Omega_v^r O_{qsu}^{ptv} + \Omega_v^t O_{qsu}^{prv} - \Omega_q^v O_{suv}^{prt} + \Omega_s^v O_{quv}^{prt} - \Omega_u^v O_{qsv}^{prt} \right) \{ \hat{a}_{qsu}^{prt} \} \\ & + \frac{1}{4} \sum_{\substack{pr \\ qs}} \left(\sum_{tv} \Omega_t^v O_{qsv}^{prt} (n_v - n_t) \right) \{ \hat{a}_{qs}^{pr} \} \\ & + \frac{1}{2} \sum_{\substack{p \\ q}} \left(\sum_{\substack{rtv \\ su}} (\Omega_s^v O_{quv}^{prt} - \Omega_v^r O_{qsu}^{ptv}) \lambda_{su}^{rt} \right) \{ \hat{a}_q^p \} \\ & + \frac{1}{12} \sum_{\substack{prtv \\ qsu}} (\Omega_v^p O_{qsu}^{rtv} - \Omega_q^v O_{suv}^{prt}) \lambda_{qsu}^{prt}. \end{aligned} \quad (6.233)$$

Since the result of $\left[\hat{\Omega}^{[2]}, \hat{O}^{[3]} \right]$ is quite lengthy, we will sort it by many-body ranks like

$$\begin{aligned} \left[\hat{\Omega}^{[2]}, \hat{O}^{[3]} \right] = & + \left[\hat{\Omega}^{[2]}, \hat{O}^{[3]} \right]_{4B} + \left[\hat{\Omega}^{[2]}, \hat{O}^{[3]} \right]_{3B} + \left[\hat{\Omega}^{[2]}, \hat{O}^{[3]} \right]_{2B} \\ & + \left[\hat{\Omega}^{[2]}, \hat{O}^{[3]} \right]_{1B} + \left[\hat{\Omega}^{[2]}, \hat{O}^{[3]} \right]_{0B}. \end{aligned} \quad (6.234)$$

The result for the four-body part is

$$\begin{aligned} \left[\hat{\Omega}^{[2]}, \hat{O}^{[3]} \right]_{4B} = & + \frac{1}{72} \sum_{\substack{prt \\ qsuw}} \left(\sum_x \left(\Omega_{wx}^{rv} O_{qsu}^{ptx} - \Omega_{wx}^{tv} O_{qsu}^{prx} - \Omega_{wx}^{pv} O_{qsu}^{rtx} \right. \right. \\ & \left. \left. + \Omega_{qw}^{vx} O_{sux}^{prt} - \Omega_{sw}^{vx} O_{qux}^{prt} + \Omega_{uw}^{vx} O_{qsx}^{prt} \right) \right) \{ \hat{a}_{qsuw}^{prt} \}. \end{aligned} \quad (6.235)$$

Next, we get to the three-body part, where we obtain

$$\begin{aligned} \left[\hat{\Omega}^{[2]}, \hat{O}^{[3]} \right]_{3B} = & + \frac{1}{72} \sum_{\substack{prt \\ qsu}} \left(\sum_{vx} \left(\Omega_{vx}^{pr} O_{qsu}^{tvx} + \Omega_{vx}^{rt} O_{qsu}^{pvx} + \Omega_{qu}^{vx} O_{svx}^{prt} \right. \right. \\ & - \Omega_{qs}^{vx} O_{uvx}^{prt} - \Omega_{su}^{vx} O_{qvz}^{prt} - \Omega_{vx}^{pt} O_{qsu}^{rvx} \left. \right) (1 - n_v - n_x) \\ & + \frac{1}{36} \left(\Omega_{sx}^{pv} O_{quv}^{rtx} + \Omega_{qv}^{px} O_{sux}^{rtv} + \Omega_{uv}^{px} O_{qsx}^{rtv} + \Omega_{qx}^{rv} O_{suv}^{ptx} \right. \\ & + \Omega_{ux}^{rv} O_{qsv}^{ptx} + \Omega_{sv}^{rx} O_{qux}^{ptv} + \Omega_{sx}^{tv} O_{quv}^{prx} + \Omega_{qu}^{tx} O_{svx}^{prv} \\ & \left. \left. + \Omega_{uv}^{tx} O_{qsx}^{prv} \right) (n_x - n_v) \right) \{ \hat{a}_{qsu}^{prt} \}. \end{aligned} \quad (6.236)$$

For the two-body part, we obtain the following set of equations

$$\begin{aligned} \left[\hat{\Omega}^{[2]}, \hat{O}^{[3]} \right]_{2B} = & + \frac{1}{8} \sum_{\substack{pr \\ qs}} \left(\sum_{tvx} \left(+\Omega_{qt}^{vx} O_{svx}^{prt} + \Omega_{vx}^{rt} O_{qst}^{pvx} - \Omega_{vx}^{pt} O_{qst}^{rvx} - \Omega_{st}^{vx} O_{qvz}^{prt} \right) \right. \\ & \left. (\bar{n}_t n_v n_x + n_t \bar{n}_v \bar{n}_x) \right) \{ \hat{a}_{qs}^{pr} \} \\ & + \sum_{\substack{pr \\ qs}} \left(\sum_{\substack{tvx \\ uw}} \left(\frac{1}{16} \left(\Omega_{qx}^{tv} O_{suw}^{prx} + \Omega_{uw}^{rx} O_{qsx}^{ptv} - \Omega_{sx}^{tv} O_{quw}^{prx} - \Omega_{uw}^{px} O_{qsx}^{rtv} \right) \right. \right. \\ & + \frac{1}{8} \left(\Omega_{qu}^{px} O_{svx}^{rtv} + \Omega_{sw}^{px} O_{qux}^{rtv} - \Omega_{qx}^{pt} O_{suw}^{rvx} - \Omega_{sx}^{pv} O_{quw}^{rtx} \right. \\ & + \Omega_{qw}^{rx} O_{svx}^{ptv} + \Omega_{su}^{rx} O_{qvz}^{ptv} - \Omega_{qx}^{rv} O_{suw}^{ptx} - \Omega_{sx}^{rt} O_{quw}^{pvx} \\ & + \Omega_{qs}^{vx} O_{uvx}^{prt} + \Omega_{uw}^{vx} O_{qsx}^{prt} - \Omega_{wx}^{pr} O_{qsu}^{tvx} - \Omega_{wx}^{tv} O_{qsu}^{prx} \left. \right) \\ & \left. \left. + \frac{1}{4} \left(\Omega_{qw}^{vx} O_{svx}^{prt} + \Omega_{su}^{vx} O_{qvz}^{prt} - \Omega_{wx}^{pv} O_{qsu}^{rtx} - \Omega_{wx}^{rt} O_{qsu}^{pvx} \right) \lambda_{uw}^{tv} \right) \right) \{ \hat{a}_{qs}^{pr} \}. \end{aligned}$$

(6.237)

The one-body part is then given by

$$\begin{aligned}
\left[\hat{\Omega}^{[2]}, \hat{O}^{[3]}\right]_{1B} &= +\frac{1}{4} \sum_{\substack{p \\ q}} \left(\sum_{rtvx} \Omega_{rt}^{vx} O_{qv}^{prt} (\bar{n}_r \bar{n}_t n_v n_x - \bar{n}_v \bar{n}_x n_r n_t) \right) \{ \hat{a}_q^p \} \\
&+ \sum_{\substack{p \\ q}} \left(\sum_{rtvx} \left(\left(\frac{1}{8} (\Omega_{vx}^{rt} O_{qsu}^{pvx} - \Omega_{su}^{vx} O_{qv}^{prt}) + \frac{1}{4} (-\Omega_{vx}^{pt} O_{qsu}^{rvx} - \Omega_{qs}^{vx} O_{uv}^{prt}) \right) \right. \right. \\
&\quad \left. \left. (1 - n_v - n_x) \right. \right. \\
&+ \left. \left. \left(\frac{1}{2} (\Omega_{sx}^{pv} O_{quv}^{rtx} - \Omega_{qv}^{rx} O_{sux}^{ptv}) + \Omega_{sv}^{rx} O_{qux}^{ptv} \right) (n_x - n_v) \right) \lambda_{su}^{rt} \right) \{ \hat{a}_q^p \} \\
&+ \sum_{\substack{p \\ q}} \left(\sum_{rtvx} \left(\frac{1}{12} (\Omega_{qu}^{px} O_{svx}^{rtv} + \Omega_{qx}^{tv} O_{suw}^{prx} - \Omega_{qx}^{pt} O_{suw}^{rvx} - \Omega_{uw}^{px} O_{qsx}^{rtv}) \right. \right. \\
&\quad \left. \left. + \frac{1}{4} (\Omega_{wx}^{pt} O_{qsu}^{rvx} + \Omega_{uw}^{vx} O_{qsx}^{prt} - \Omega_{wx}^{tv} O_{qsu}^{prx} - \Omega_{qu}^{vx} O_{svx}^{prt}) \right) \lambda_{suw}^{rtv} \right) \{ \hat{a}_q^p \}.
\end{aligned} \tag{6.238}$$

Finally, we obtain the equations for the zero-body part, which are given by

$$\begin{aligned}
\left[\hat{\Omega}^{[2]}, \hat{O}^{[3]}\right]_{0B} &= - \sum_{\substack{prt vx \\ qs}} \frac{1}{4} \left((\Omega_{vx}^{pt} O_{qst}^{rvx} + \Omega_{st}^{vx} O_{qv}^{prt}) (\bar{n}_t n_v n_x + n_t \bar{n}_v \bar{n}_x) \right) \lambda_{qs}^{pr} \\
&+ \sum_{\substack{prt vx \\ qs uw}} \left(+\frac{1}{12} \Omega_{qs}^{vx} O_{uw}^{prt} - \frac{1}{24} \Omega_{uw}^{px} O_{qsx}^{rtv} + \frac{1}{8} \Omega_{qx}^{tv} O_{suw}^{prx} \right. \\
&\quad \left. - \frac{1}{6} \Omega_{qu}^{rx} O_{svx}^{ptv} - \frac{1}{4} (\Omega_{wx}^{pv} O_{qsu}^{rtx} + \Omega_{qx}^{pv} O_{suw}^{rtx}) - \frac{1}{3} \Omega_{qu}^{vx} O_{svx}^{prt} \right) \lambda_{qs}^{pr} \lambda_{uw}^{tv} \\
&+ \sum_{\substack{prt vx \\ qs u}} \left(\frac{1}{24} (\Omega_{qu}^{vx} O_{svx}^{prt} - \Omega_{vx}^{pt} O_{qsu}^{rvx}) (1 - n_v - n_x) \right. \\
&\quad \left. + \frac{1}{4} \Omega_{sv}^{rx} O_{qux}^{ptv} (n_x - n_v) \right) \lambda_{qsu}^{prt}.
\end{aligned} \tag{6.239}$$

In the following we will neglect all terms with a irreducible three-body density $\lambda^{[3]}$, as mentioned in section 5.6, and all terms containing a multiplication of two irreducible

two-body densities $\lambda^{[2]}$. We have renamed the indices of O_{qsu}^{prt} to O_{456}^{123} , since these indices are fixed by Eq. (6.224). Now, alphabetic indices are considered as summation indices and numeric indices are fixed and should not be relabelled. The final equations of the commutator evaluation for the three-body part are given by

$$\check{O}_{456}^{123} = + \frac{9}{2} \sum_v (\Omega_{5v}^{12} O_{46}^{3v} + \Omega_{45}^{1v} O_{6v}^{23} - \Omega_{4v}^{12} O_{56}^{3v} - \Omega_{45}^{2v} O_{6v}^{13}) \quad (6.240)$$

$$+ \sum_v \Omega_v^1 O_{456}^{23v} - \Omega_v^2 O_{456}^{13v} + \Omega_v^3 O_{456}^{12v} - \Omega_4^v O_{56v}^{123} + \Omega_5^v O_{46v}^{123} - \Omega_6^v O_{45v}^{123} \quad (6.241)$$

$$+ \frac{1}{2} \sum_{vx} (\Omega_{45}^{vx} O_{6vx}^{123} + \Omega_{56}^{vx} O_{4vx}^{123} + \Omega_{vx}^{13} O_{456}^{2vx} - \Omega_{vx}^{12} O_{456}^{3vx} - \Omega_{vx}^{23} O_{456}^{1vx} - \Omega_{46}^{vx} O_{5vx}^{123}) (1 - n_v - n_x) \quad (6.242)$$

$$+ \sum_{vx} (\Omega_{5x}^{1v} O_{46v}^{23x} + \Omega_{4v}^{1x} O_{56x}^{23v} + \Omega_{6v}^{1x} O_{45x}^{23v} + \Omega_{4x}^{2v} O_{56v}^{13x} + \Omega_{6x}^{2v} O_{45v}^{13x} + \Omega_{5v}^{2x} O_{46v}^{13v} + \Omega_{5x}^{3v} O_{46v}^{12x} + \Omega_{4v}^{3x} O_{56v}^{12v} + \Omega_{6v}^{3x} O_{45v}^{12v}) (n_v - n_x). \quad (6.243)$$

For the two-body part we obtain

$$\check{O}_{34}^{12} = + \sum_{tv} \Omega_t^v O_{34v}^{12t} (n_v - n_t) \quad (6.244)$$

$$+ \frac{1}{2} \sum_{tvx} (\Omega_{3t}^{vx} O_{4vx}^{12t} + \Omega_{vx}^{2t} O_{34t}^{1vx} - \Omega_{vx}^{1t} O_{34t}^{2vx} - \Omega_{4t}^{vx} O_{3vx}^{12t}) (\bar{n}_t n_v n_x + n_t \bar{n}_v \bar{n}_x) \quad (6.245)$$

$$+ \frac{1}{4} \sum_{\substack{tvx \\ uw}} (\Omega_{3x}^{tv} O_{4uw}^{12x} + \Omega_{uw}^{2x} O_{34x}^{1tv} - \Omega_{4x}^{tv} O_{3uw}^{12x} - \Omega_{uw}^{1x} O_{34x}^{2tv}) \lambda_{tv}^{uw} \quad (6.246)$$

$$+ \frac{1}{2} \sum_{\substack{tvx \\ uw}} (\Omega_{3u}^{1x} O_{4wx}^{2tv} + \Omega_{4w}^{1x} O_{3ux}^{2tv} - \Omega_{3x}^{1t} O_{4uw}^{2vx} - \Omega_{4x}^{1v} O_{3uw}^{2tx} + \Omega_{3w}^{2x} O_{4ux}^{1tv} + \Omega_{4u}^{2x} O_{3wx}^{1tv} - \Omega_{3x}^{2v} O_{4uw}^{1tx} - \Omega_{4x}^{2t} O_{3uw}^{1vx}) \lambda_{tv}^{uw} \quad (6.247)$$

$$+ \frac{1}{2} \sum_{\substack{tvx \\ uw}} (\Omega_{34}^{vx} O_{uwx}^{12t} - \Omega_{wx}^{12} O_{34u}^{tvx}) \lambda_{tv}^{uw} \quad (6.248)$$

$$+ \frac{1}{2} \sum_{\substack{tvx \\ uw}} (\Omega_{uw}^{vx} O_{34x}^{12t} - \Omega_{wx}^{tv} O_{34u}^{12x}) \lambda_{tv}^{uw} \quad (6.249)$$

$$+ \sum_{\substack{tvx \\ uw}} (\Omega_{3w}^{vx} O_{4ux}^{12t} + \Omega_{4u}^{vx} O_{3wx}^{12t} - \Omega_{wx}^{1v} O_{34u}^{2tx} - \Omega_{wx}^{2t} O_{34u}^{1vx}) \lambda_{tv}^{uw}. \quad (6.250)$$

The one-body part is given by

$$\check{O}_2^1 = + \frac{1}{4} \sum_{\substack{rtv \\ su}} (\Omega_s^v O_{2uv}^{1rt} + \Omega_v^t O_{2su}^{1rv} - \Omega_v^r O_{2su}^{1tv} - \Omega_u^v O_{2sv}^{1rt}) \lambda_{rt}^{su} \quad (6.251)$$

$$+ \frac{1}{4} \sum_{rtvx} \Omega_{rt}^{vx} O_{2vx}^{1rt} (\bar{n}_r \bar{n}_t n_v n_x - \bar{n}_v \bar{n}_x n_r n_t) \quad (6.252)$$

$$+ \frac{1}{8} \sum_{\substack{rtvx \\ su}} (\Omega_{vx}^{rt} O_{2su}^{1vx} - \Omega_{su}^{vx} O_{2vx}^{1rt}) (1 - n_v - n_x) \lambda_{rt}^{su} \quad (6.253)$$

$$- \frac{1}{4} \sum_{\substack{rtvx \\ su}} (\Omega_{vx}^{1t} O_{2su}^{rvx} + \Omega_{2s}^{vx} O_{uvx}^{1rt}) (1 - n_v - n_x) \lambda_{rt}^{su} \quad (6.254)$$

$$+ \frac{1}{2} \sum_{\substack{rtvx \\ su}} (\Omega_{sx}^{1v} O_{2uv}^{rtx} - \Omega_{2v}^{rx} O_{sux}^{1tv}) (n_x - n_v) \lambda_{rt}^{su} \quad (6.255)$$

$$+ \sum_{\substack{rtvx \\ su}} \Omega_{sv}^{rx} O_{2ux}^{1tv} (n_x - n_v) \lambda_{rt}^{su}. \quad (6.256)$$

Finally, we obtain for the zero-body part

$$\check{O}_0 = - \sum_{\substack{prtvx \\ qs}} \frac{1}{4} ((\Omega_{vx}^{pt} O_{qst}^{rvx} + \Omega_{st}^{vx} O_{qvx}^{prt}) (\bar{n}_t n_v n_x + n_t \bar{n}_v \bar{n}_x)) \lambda_{pr}^{qs}. \quad (6.257)$$

Note that we omitted the four-body part because we only want to consider three-body terms as a maximal particle rank. In order to obtain a clearer form of the commutator results, we can use one- and two-body symmetrizers. The one-body symmetrizer exploits the Hermitian symmetry and the two-body symmetrizer uses the antisymmetry for an exchange between two particles additionally.

As an example, let us take the second two-body term (6.245) and express it in terms of the two-body symmetrizer, which is given by

$$\hat{\Xi}_{2B} = \frac{1}{8} (1 - P_{12} - P_{34} + P_{12}P_{34}) (1 \pm P_{13}P_{24}). \quad (6.258)$$

The strategy is to pick one summand of

$$\check{O}_{34,II}^{12} = \frac{1}{2} \sum_{tvx} (\Omega_{3t}^{vx} O_{4vx}^{12t} + \Omega_{vx}^{2t} O_{34t}^{1vx} - \Omega_{vx}^{1t} O_{34t}^{2vx} - \Omega_{4t}^{vx} O_{3vx}^{12t}) (\bar{n}_t n_v n_x + n_t \bar{n}_v \bar{n}_x), \quad (6.259)$$

where $\check{O}_{34,II}^{12}$ stands for the second term of the two-body equations. We let $\hat{\Xi}_{2B}$ act on the first summand of Eq. (6.245) and obtain

$$\begin{aligned}\hat{\Xi}_{2B}^I \check{O}_{34,II}^{12} &= \frac{1}{8} (1 - P_{12} - P_{34} + P_{12}P_{34}) (1 \pm P_{13}P_{34}) \sum_{tvx} \Omega_{3t}^{vx} O_{4vx}^{12t} (\bar{n}_t n_v n_x + n_t \bar{n}_v \bar{n}_x) \\ &= \frac{1}{4} \sum_{tvx} (\Omega_{3t}^{vx} O_{4vx}^{12t} - \Omega_{4t}^{vx} O_{3vx}^{12t} - \Omega_{vx}^{1t} O_{34t}^{2vx} + \Omega_{vx}^{2t} O_{34t}^{1vx}) (\bar{n}_t n_v n_x + n_t \bar{n}_v \bar{n}_x),\end{aligned}\tag{6.260}$$

where ${}^I\check{O}_{34,II}^{12}$ denotes the first summand of the second two-body term. We recognize that the application of $\hat{\Xi}_{2B}$ fully reproduces (6.245). The last step is the comparison of the obtained prefactor, which is $\frac{1}{4}$ with the prefactor of the second term, which is $\frac{1}{2}$. Doing this, we obtain

$$\check{O}_{34,II}^{12} = 2 \hat{\Xi}_{2B} \sum_{tvx} \Omega_{3t}^{vx} O_{4vx}^{12t} (\bar{n}_t n_v n_x + n_t \bar{n}_v \bar{n}_x).\tag{6.261}$$

Following this procedure for every term, the symmetrized results for the two-body terms are

$$\check{O}_{34}^{12} = + \hat{\Xi}_{2B} \sum_{tv} \Omega_t^v O_{34v}^{12t} (n_t - n_v)\tag{6.262}$$

$$+ \hat{\Xi}_{2B} 2 \sum_{tvx} \Omega_{3t}^{vx} O_{4vx}^{12t} (\bar{n}_t n_v n_x + n_t \bar{n}_v \bar{n}_x)\tag{6.263}$$

$$+ \hat{\Xi}_{2B} \sum_{tvxuw} \Omega_{3x}^{tv} O_{4uw}^{12x} \lambda_{tv}^{uw}\tag{6.264}$$

$$+ \hat{\Xi}_{2B} 4 \sum_{tvxuw} \Omega_{3u}^{1x} O_{4wx}^{2tv} \lambda_{tv}^{uw}\tag{6.265}$$

$$+ \hat{\Xi}_{2B} \sum_{tvxuw} \Omega_{34}^{vx} O_{uw}^{12t} \lambda_{tv}^{uw}\tag{6.266}$$

$$+ \hat{\Xi}_{2B} \sum_{tvxuw} \Omega_{uw}^{vx} O_{34x}^{12t} \lambda_{tv}^{uw}\tag{6.267}$$

$$+ \hat{\Xi}_{2B} 4 \sum_{tvxuw} \Omega_{3w}^{vx} O_{4ux}^{12t} \lambda_{tv}^{uw}.\tag{6.268}$$

Regarding the one-body terms and using the one-body symmetrizer

$$\hat{\Xi}_{1B} = \frac{1}{2} (1 \pm P_{12}),\tag{6.269}$$

we obtain

$$\check{O}_2^1 = + \hat{\Xi}_{1B} \frac{1}{2} \sum_{rtvsu} (\Omega_v^t O_{2su}^{1rv} - \Omega_v^r O_{2su}^{1tv}) \lambda_{rt}^{su} \quad (6.270)$$

$$+ \hat{\Xi}_{1B} \frac{1}{4} \sum_{rtvx} \Omega_{rt}^{vx} O_{2vx}^{1rt} (\bar{n}_r \bar{n}_t n_v n_x - n_r n_t \bar{n}_v \bar{n}_x) \quad (6.271)$$

$$+ \hat{\Xi}_{1B} \frac{1}{4} \sum_{rtvxsu} \Omega_{vx}^{rt} O_{2su}^{1vx} (1 - n_v - n_x) \lambda_{rt}^{su} \quad (6.272)$$

$$+ \hat{\Xi}_{1B} \frac{1}{2} \sum_{rtvxsu} \Omega_{vx}^{1r} O_{2su}^{tvx} (1 - n_v - n_x) \lambda_{rt}^{su} \quad (6.273)$$

$$+ \hat{\Xi}_{1B} \sum_{rtvxsu} \Omega_{sx}^{1v} O_{2uv}^{rtx} (n_x - n_v) \lambda_{rt}^{su} \quad (6.274)$$

$$+ \hat{\Xi}_{1B} \sum_{rtvxsu} \Omega_{sv}^{rx} O_{2ux}^{1tv} (n_x - n_v) \lambda_{rt}^{su}. \quad (6.275)$$

For the zero-body term there is no symmetrizer available, therefore it belongs unchanged

$$\check{O}_0 = -\frac{1}{4} \sum_{prtvsqs} (\Omega_{vx}^{pt} O_{qst}^{rvx} + \Omega_{st}^{vx} O_{qvx}^{prt}) (\bar{n}_t n_v n_x + n_t \bar{n}_v \bar{n}_x) \lambda_{pr}^{qs}. \quad (6.276)$$

6.2.2. LOTC Approximation

The LOTC approximation can be described as follows: We compute a three-body correction to the desired observable \hat{O} , where we express every three-body operator $\hat{O}^{[3]}$ in terms of two-body operators. Therefore, we pick the first term of \check{O}_{456}^{123} (see Eq. (6.240)) and replace every three-body operator by this term, i.e., we normal order the three-body terms on the fly. Furthermore, when regarding the BCH series (6.222), the leading-order part can be written as

$$\hat{O}(s)_{LO} = \frac{1}{2} \left[\hat{\Omega}(s), \left[\hat{\Omega}(s), \hat{O}(0) \right] \right]. \quad (6.277)$$

Since we only want to compute a correction for the zero-, one- and two-body part of the IM-SRG(2), we can write Eq. (6.277) in terms of induced many-body parts

$$\begin{aligned} \hat{O}_{\text{LOTC}} = & + \frac{1}{2} \left[\hat{\Omega}^{[1]}, \left[\hat{\Omega}^{[2]}, \hat{O}^{[2]} \right]_{3B} \right]_{1B} + \frac{1}{2} \left[\hat{\Omega}^{[1]}, \left[\hat{\Omega}^{[2]}, \hat{O}^{[2]} \right]_{3B} \right]_{2B} + \frac{1}{2} \left[\hat{\Omega}^{[2]}, \left[\hat{\Omega}^{[2]}, \hat{O}^{[2]} \right]_{3B} \right]_{0B} \\ & + \frac{1}{2} \left[\hat{\Omega}^{[2]}, \left[\hat{\Omega}^{[2]}, \hat{O}^{[2]} \right]_{3B} \right]_{1B} + \frac{1}{2} \left[\hat{\Omega}^{[2]}, \left[\hat{\Omega}^{[2]}, \hat{O}^{[2]} \right]_{3B} \right]_{2B}. \end{aligned} \quad (6.278)$$

Let us take the first two-body term (6.262)

$$\check{O}_{34,I}^{12} = +\hat{\Xi}_{2B} \sum_{tv} \Omega_t^v O_{34v}^{12t} (n_t - n_v) \quad (6.279)$$

and replace the three-body tensor O_{34v}^{12t} by (6.240). We obtain

$$\check{O}_{34,I}^{12} = +\frac{9}{2} \hat{\Xi}_{2B} \sum_{tvx} \Omega_t^v (\Omega_{4x}^{12} O_{3v}^{tx} + \Omega_{34}^{1x} O_{vx}^{2t} - \Omega_{3x}^{12} O_{4v}^{tx} - \Omega_{34}^{2x} O_{vx}^{1t}) (n_t - n_v). \quad (6.280)$$

Note that the replacement of O_{34v}^{12t} results in an additional summation index x entering the equation. We can split up \hat{O}_{LOTC} by many-body parts

$$\hat{O}_{\text{LOTC}} = \hat{O}_{\text{LOTC}}^{[2]} + \hat{O}_{\text{LOTC}}^{[1]} + \hat{O}_{\text{LOTC}}^{[0]} \quad (6.281)$$

and obtain

$$\check{O}_{34,\text{LOTC}}^{12} = +\frac{9}{2} \hat{\Xi}_{2B} \sum_{tvx} \Omega_t^v (\Omega_{4x}^{12} O_{3v}^{tx} + \Omega_{34}^{1x} O_{vx}^{2t} - \Omega_{3x}^{12} O_{4v}^{tx} - \Omega_{34}^{2x} O_{vx}^{1t}) (n_t - n_v) \quad (6.282)$$

$$+ 9 \hat{\Xi}_{2B} \sum_{tvxz} \Omega_{3t}^{vx} (\Omega_{vz}^{12} O_{4x}^{tz} + \Omega_{4v}^{1z} O_{xz}^{2t} - \Omega_{4z}^{12} O_{vx}^{tz} - \Omega_{4v}^{2z} O_{xz}^{1t}) (\bar{n}_t n_v n_x + n_t \bar{n}_v \bar{n}_x) \quad (6.283)$$

$$+ \frac{9}{2} \hat{\Xi}_{2B} \sum_{tvxzuw} \Omega_{3x}^{tv} (\Omega_{uz}^{12} O_{4w}^{xz} + \Omega_{4u}^{1z} O_{wz}^{2x} - \Omega_{4z}^{12} O_{uw}^{xz} - \Omega_{4u}^{2z} O_{wz}^{1x}) \lambda_{tv}^{uw} \quad (6.284)$$

$$+ 18 \hat{\Xi}_{2B} \sum_{tvxzuw} \Omega_{3u}^{1x} (\Omega_{wz}^{2t} O_{4x}^{vz} + \Omega_{4w}^{2z} O_{xz}^{tv} - \Omega_{4z}^{2t} O_{wx}^{vz} - \Omega_{4w}^{tz} O_{xz}^{2v}) \lambda_{tv}^{uw} \quad (6.285)$$

$$+ \frac{9}{2} \hat{\Xi}_{2B} \sum_{tvxzuw} \Omega_{34}^{vx} (\Omega_{wz}^{12} O_{ux}^{tz} + \Omega_{uw}^{1z} O_{xz}^{2t} - \Omega_{uz}^{12} O_{wx}^{tz} - \Omega_{uw}^{2z} O_{xz}^{1t}) \lambda_{tv}^{uw} \quad (6.286)$$

$$+ \frac{9}{2} \hat{\Xi}_{2B} \sum_{tvxzuw} \Omega_{uw}^{vx} (\Omega_{4z}^{12} O_{3x}^{tz} + \Omega_{34}^{1z} O_{xz}^{2t} - \Omega_{3z}^{12} O_{4x}^{tz} - \Omega_{34}^{2z} O_{xz}^{1t}) \lambda_{tv}^{uw} \quad (6.287)$$

$$+ 18 \hat{\Xi}_{2B} \sum_{tvxzuw} \Omega_{3w}^{vx} (\Omega_{uz}^{12} O_{4x}^{tz} + \Omega_{4u}^{1z} O_{xz}^{2t} - \Omega_{4z}^{12} O_{ux}^{tz} - \Omega_{4u}^{2z} O_{xz}^{1t}) \lambda_{tv}^{uw}, \quad (6.288)$$

$$\check{O}_{2,\text{LOTC}}^1 = +\frac{9}{4} \hat{\Xi}_{1B} \sum_{rtvxsu} \Omega_v^t (\Omega_{sx}^{1r} O_{2u}^{vx} + \Omega_{2s}^{1x} O_{ux}^{rv} - \Omega_{2x}^{1r} O_{su}^{vx} - \Omega_{2s}^{rx} O_{ux}^{1v}) \lambda_{rt}^{su} \quad (6.289)$$

$$- \frac{9}{4} \hat{\Xi}_{1B} \sum_{rtvxsu} \Omega_v^r (\Omega_{sx}^{1t} O_{2u}^{vx} + \Omega_{2s}^{1x} O_{ux}^{tv} - \Omega_{2x}^{1t} O_{su}^{vx} - \Omega_{2s}^{tx} O_{ux}^{1v}) \lambda_{rt}^{su} \quad (6.290)$$

$$\begin{aligned}
& + \frac{9}{8} \hat{\Xi}_{1B} \sum_{rtvzx} \Omega_{vt}^{vx} (\Omega_{vz}^{1r} O_{2x}^{tz} + \Omega_{2v}^{1z} O_{xz}^{rt} - \Omega_{2z}^{1r} O_{vx}^{tz} - \Omega_{2v}^{rz} O_{xz}^{1t}) \\
& (\bar{n}_r \bar{n}_t n_v n_x - n_r n_t \bar{n}_v \bar{n}_x) \tag{6.291}
\end{aligned}$$

$$\begin{aligned}
& + \frac{9}{8} \hat{\Xi}_{1B} \sum_{rtvzxsu} \Omega_{vx}^{rt} (\Omega_{sz}^{1v} O_{2u}^{xz} + \Omega_{2s}^{1z} O_{uz}^{vx} - \Omega_{2z}^{1v} O_{su}^{xz} - \Omega_{2s}^{vz} O_{uz}^{1x}) \\
& (1 - n_v - n_x) \lambda_{rt}^{su} \tag{6.292}
\end{aligned}$$

$$\begin{aligned}
& + \frac{9}{4} \hat{\Xi}_{1B} \sum_{rtvzxsu} \Omega_{vx}^{1r} (\Omega_{sz}^{tv} O_{2u}^{xz} + \Omega_{2s}^{tz} O_{uz}^{vx} - \Omega_{2z}^{tv} O_{su}^{xz} - \Omega_{2s}^{vz} O_{uz}^{tx}) \\
& (1 - n_v - n_x) \lambda_{rt}^{su} \tag{6.293}
\end{aligned}$$

$$\begin{aligned}
& + \frac{9}{2} \hat{\Xi}_{1B} \sum_{rtvzxsu} \Omega_{sx}^{1v} (\Omega_{uz}^{rt} O_{2v}^{xz} + \Omega_{2u}^{rz} O_{vz}^{tx} - \Omega_{2z}^{rt} O_{uv}^{xz} - \Omega_{2u}^{tz} O_{vz}^{rx}) (n_x - n_v) \lambda_{rt}^{su} \\
& \tag{6.294}
\end{aligned}$$

$$\begin{aligned}
& + \frac{9}{2} \hat{\Xi}_{1B} \sum_{rtvzxsu} \Omega_{sv}^{rx} (\Omega_{uz}^{1t} O_{2x}^{vz} + \Omega_{2u}^{1z} O_{xz}^{tv} - \Omega_{2z}^{1t} O_{ux}^{vz} - \Omega_{2u}^{tz} O_{xz}^{1v}) (n_x - n_v) \lambda_{rt}^{su}, \\
& \tag{6.295}
\end{aligned}$$

$$\begin{aligned}
\check{O}_{0, \text{LOTC}} = & - \frac{9}{8} \sum_{prt vxzqs} [\Omega_{vx}^{pt} (\Omega_{sz}^{rv} O_{qt}^{xz} + \Omega_{qs}^{rz} O_{tz}^{vx} - \Omega_{qz}^{rv} O_{st}^{xz} - \Omega_{qs}^{vz} O_{tz}^{rx}) \\
& + \Omega_{st}^{vx} (\Omega_{vz}^{pr} O_{qx}^{tz} + \Omega_{qv}^{pz} O_{xz}^{rt} - \Omega_{qz}^{pr} O_{vx}^{tz} - \Omega_{qv}^{rz} O_{xz}^{pt})] (\bar{n}_t n_v n_x + n_t \bar{n}_v \bar{n}_x) \lambda_{pr}^{qs}. \tag{6.296}
\end{aligned}$$

These are the equations used in the LOTC approximation. In this approximation we left out that the commutators $[\hat{\Omega}^{[1]} [\hat{\Omega}^{[2]}, \hat{O}^{[2]}]]$ and $[\hat{\Omega}^{[2]} [\hat{\Omega}^{[2]}, \hat{O}^{[2]}]]$ also produce induced three-body terms. These are not included because we compute a correction to the NO2B approximation, which includes operators up to the two-body rank only. Furthermore, the BCH series also includes the commutator $[\hat{\Omega}^{[2]}, \hat{O}^{[2]}]_{3B}$, which is also neglected in the LOTC approximation. Another point is that we compute the LOTC equations in the m -scheme due to that fact that the angular momentum coupling of these equations result in complicated expressions including $9j$ and $12j$ symbols. These are more error prone to implement compared to the m -scheme equations.

6.3. Implementation of the Two-Body Equations

Since we will compute the LOTC in the m -scheme, we are forced to define the two-body equations of the LOTC in terms of intermediate tensors in order to save computing time. This is necessary because in the implementation we use nested for-loops to loop over all external indices $1, 2, 3, \dots$ and summation indices p, q, r, \dots , which is very time consuming

and not feasible for every two-body term. Note that the first two-body term is the only term we can compute without using intermediate tensors. The intermediate tensors are constructed using tensor contraction as it has been done in [Sig+15].

For the sake of completeness, let us consider the first two-body term of the LOTC given by

$$\check{O}_{34,\text{LOTC},I}^{12} = +\frac{9}{2} \hat{\Xi}_{2\text{B}} \sum_{tvx} \Omega_t^v (\Omega_{4x}^{12} O_{3v}^{tx} + \Omega_{34}^{1x} O_{vx}^{2t} - \Omega_{3x}^{12} O_{4v}^{tx} - \Omega_{34}^{2x} O_{vx}^{1t}) (n_t - n_v). \quad (6.297)$$

Regarding the first summand of $\check{O}_{34,\text{LOTC},I}^{12}$, we see that Ω_t^v and O_{3v}^{tx} have two common upper and lower indices v and t indicating that these tensors can be used for the definition of an intermediate one-body tensor χ_q^p with arbitrary indices p and q , which can be written as

$$\chi_q^p := - \sum_{tv} \Omega_t^v O_{vq}^{tp} (n_t - n_v). \quad (6.298)$$

For the other three summands of the first two-body term we observe that the other intermediate tensors are the same and we can write the two-body part as

$$\check{O}_{34,\text{LOTC},I}^{12} = +\frac{9}{2} \hat{\Xi}_{2\text{B}} \sum_x (\chi_3^x \Omega_{4x}^{12} + \chi_x^2 \Omega_{34}^{1x} - \chi_4^x \Omega_{3x}^{12} - \chi_x^1 \Omega_{34}^{2x}). \quad (6.299)$$

Regarding computing time, the first two-body term of the LOTC needs seven nested for-loops for the implementation resulting in a polynomial scaling of $\mathcal{O}(N^7)$. For the implementation of (6.299), only five nested for-loops are necessary leading to a scaling of $\mathcal{O}(N^5)$.

The second two-body term can also be expressed in terms of intermediate tensors where we need two intermediates for each term due to the multiplicative nature of the occupation numbers. We start with the second two-body term, given by

$$\begin{aligned} \check{O}_{34,\text{LOTC},II}^{12} = +9 \hat{\Xi}_{2\text{B}} \sum_{tvxz} \Omega_{3t}^{vx} (\Omega_{vz}^{12} O_{4x}^{tz} + \Omega_{4v}^{1z} O_{xz}^{2t} - \Omega_{4z}^{12} O_{vx}^{tz} - \Omega_{4v}^{2z} O_{xz}^{1t}) \\ (\bar{n}_t n_v n_x + n_t \bar{n}_v \bar{n}_x). \end{aligned} \quad (6.300)$$

Performing the tensor contractions for the first summand of the second two-body term,

the result is

$$\begin{aligned}
{}^I\check{O}_{34,\text{LOTC},II}^{12} &= +9 \hat{\Xi}_{2\text{B}} \sum_{tvxz} - (\Omega_{3t}^{vx} O_{4x}^{zt} \bar{n}_t n_x \Omega_{vz}^{12} n_v + \Omega_{3t}^{vx} O_{4x}^{zt} n_t \bar{n}_x \Omega_{vz}^{12} \bar{n}_v) \\
&= +9 \hat{\Xi}_{2\text{B}} \sum_{vz} (\Omega_{vz}^{12} \chi_{34}^{vz} n_v + \Omega_{vz}^{12} \bar{\chi}_{34}^{vz} \bar{n}_v). \tag{6.301}
\end{aligned}$$

For the other terms we obtain

$$\begin{aligned}
\check{O}_{34,\text{LOTC},II}^{12} &= +9 \hat{\Xi}_{2\text{B}} \sum_{vz} (\Omega_{vz}^{12} \chi_{34}^{vz} + \Omega_{4v}^{1z} \chi_{3z}^{v2} - \Omega_{4z}^{12} \chi_3^z - \Omega_{4v}^{2z} \chi_{3z}^{v1}) n_v \\
&\quad + (\Omega_{vz}^{12} \bar{\chi}_{34}^{vz} + \Omega_{4v}^{1z} \bar{\chi}_{3z}^{v2} - \Omega_{4z}^{12} \bar{\chi}_3^z - \Omega_{4v}^{2z} \bar{\chi}_{3z}^{v1}) \bar{n}_v \tag{6.302}
\end{aligned}$$

with

$$\begin{aligned}
\chi_{qs}^{pr} &:= - \sum_{tx} \Omega_{qt}^{px} O_{sx}^{rt} \bar{n}_t n_x & \bar{\chi}_{qs}^{pr} &:= - \sum_{tx} \Omega_{qt}^{px} O_{sx}^{rt} n_t \bar{n}_x \\
\chi_q^p &:= - \sum_{tvx} \Omega_{qt}^{vx} O_{vx}^{pt} \bar{n}_t n_x & \bar{\chi}_q^p &:= - \sum_{tvx} \Omega_{qt}^{vx} O_{vx}^{pt} n_t \bar{n}_x,
\end{aligned}$$

where the computing time is again reduced from $\mathcal{O}(N^8)$ to $\mathcal{O}(N^6)$ by eliminating the summation indices t and x .

The third two-body term (6.284) consists of four tensors due to the irreducible two-body density. Therefore, we can perform the tensor contraction using $\Omega^{[2]}$, $\lambda^{[2]}$ and $O^{[2]}$ to obtain a two-body intermediate. The third two-body term is now given as

$$\check{O}_{34,\text{LOTC},III}^{12} = +\frac{9}{2} \hat{\Xi}_{2\text{B}} \sum_{zu} (\Omega_{uz}^{12} \chi_{34}^{zu} + \Omega_{4u}^{1z} \chi_{3z}^{u2} - \Omega_{4z}^{12} \chi_3^z - \Omega_{4u}^{2z} \chi_{3z}^{u1}), \tag{6.303}$$

with

$$\begin{aligned}
\chi_{qs}^{pr} &:= - \sum_{tvxw} \Omega_{qx}^{tv} O_{sw}^{px} \lambda_{tv}^{rw} \\
\chi_q^p &:= - \sum_{tvxuw} \Omega_{qx}^{tv} O_{uw}^{px} \lambda_{tv}^{uw}
\end{aligned}$$

reducing the computation time by four orders of magnitude from $\mathcal{O}(N^{10})$ to $\mathcal{O}(N^6)$.
Now, let us consider the fourth two-body term (6.285), where we obtain

$$\check{O}_{34,\text{LOTC},IV}^{12} = + 18 \hat{\Xi}_{2\text{B}} \sum_{xu} \Omega_{3u}^{1x} (\chi_{4x}^{2u} + \Phi_{4x}^{2u} - \Psi_{4x}^{2u} - \Theta_{4x}^{2u}) \quad (6.304)$$

with

$$\begin{aligned} \chi_{qs}^{pr} &:= + \sum_{tvzw} \Omega_{zw}^{pt} O_{qs}^{zv} \lambda_{tv}^{rw} \\ \Phi_{qs}^{pr} &:= + \sum_{tvzw} \Omega_{qw}^{pz} O_{sz}^{tv} \lambda_{tv}^{rw} \\ \Psi_{qs}^{pr} &:= + \sum_{tvzw} \Omega_{zq}^{tp} O_{sw}^{zv} \lambda_{tv}^{rw} \\ \Theta_{qs}^{pr} &:= + \sum_{tvzw} \Omega_{qw}^{tz} O_{sz}^{pv} \lambda_{tv}^{rw}, \end{aligned}$$

where the computing time is reduced from $\mathcal{O}(N^{10})$ to $\mathcal{O}(N^6)$. Having a closer look at the fifth two-body term (6.286), we can also reduce its computing time by four orders of magnitudes, which gives

$$\check{O}_{34,\text{LOTC},V}^{12} = + \frac{9}{2} \hat{\Xi}_{2\text{B}} \sum_{vx} \Omega_{34}^{vx} (\chi_{xv}^{12} + \Phi_{xv}^{12} - \Psi_{xv}^{12} - \Theta_{xv}^{21}) \quad (6.305)$$

with

$$\begin{aligned} \chi_{qs}^{pr} &:= - \sum_{tzuw} \Omega_{zw}^{pr} O_{uq}^{zt} \lambda_{st}^{uw} \\ \Phi_{qs}^{pr} &:= - \sum_{tzuw} \Omega_{uw}^{pz} O_{qz}^{rt} \lambda_{st}^{uw} \\ \Psi_{qs}^{pr} &:= - \sum_{tzuw} \Omega_{uz}^{pr} O_{sw}^{tz} \lambda_{ts}^{uw} \\ \Theta_{qs}^{rp} &:= - \sum_{tzuw} \Omega_{uw}^{rz} O_{qz}^{pt} \lambda_{st}^{uw}, \end{aligned}$$

reducing the computing time from $\mathcal{O}(N^{10})$ to $\mathcal{O}(N^6)$.

The sixth two-body term (6.287) can be expressed by the definition of a one-body intermediate resulting in

$$\check{O}_{34,\text{LOTC},VI}^{12} = +\frac{9}{2} \hat{\Xi}_{2\text{B}} \sum_z (\Omega_{4z}^{12} \chi_3^z + \Omega_{34}^{1z} \chi_z^2 - \Omega_{3z}^{12} \chi_4^z - \Omega_{34}^{2z} \chi_z^1) \quad (6.306)$$

with

$$\chi_q^p := \sum_{tvxuw} \Omega_{uv}^{vx} O_{qx}^{pt} \lambda_{vt}^{uw}.$$

The last two-body term (6.288) can be written as

$$\check{O}_{34,\text{LOTC},VII}^{12} = +18 \hat{\Xi}_{2\text{B}} \sum_{zu} (\Omega_{uz}^{12} \chi_{34}^{zu} + \Omega_{4u}^{1z} \chi_{3z}^{2u} - \Omega_{4z}^{12} \chi_z^3 - \Omega_{4u}^{2z} \chi_{3z}^{1u}) \quad (6.307)$$

with

$$\begin{aligned} \chi_{qs}^{pr} &:= \sum_{tvxw} \Omega_{qw}^{vx} O_{sx}^{pt} \lambda_{vt}^{rw} \\ \chi_q^p &:= \sum_{tvxwu} \Omega_{pw}^{vx} O_{ux}^{qt} \lambda_{vt}^{uw}. \end{aligned}$$

Finally, let us summarize all the equations

$$\begin{aligned} \check{O}_{34,\text{LOTC}}^{12} &= +\frac{9}{2} \hat{\Xi}_{2\text{B}} \sum_x (\chi_3^x \Omega_{4x}^{12} + \chi_x^2 \Omega_{34}^{1x} - \chi_4^x \Omega_{3x}^{12} - \chi_x^1 \Omega_{34}^{2x}) \\ &\quad + 9 \hat{\Xi}_{2\text{B}} \sum_{vz} ((\Omega_{vz}^{12} \chi_{34}^{vz} + \Omega_{4v}^{1z} \chi_{3z}^{v2} - \Omega_{4z}^{12} \chi_3^z - \Omega_{4v}^{2z} \chi_{3z}^{v1}) n_v \\ &\quad + (\Omega_{vz}^{12} \bar{\chi}_{34}^{vz} + \Omega_{4v}^{1z} \bar{\chi}_{3z}^{v2} - \Omega_{4z}^{12} \bar{\chi}_3^z - \Omega_{4v}^{2z} \bar{\chi}_{3z}^{v1}) \bar{n}_v) \\ &\quad + \frac{9}{2} \hat{\Xi}_{2\text{B}} \sum_{zu} (\Omega_{uz}^{12} \chi_{34}^{zu} + \Omega_{4u}^{1z} \chi_{3z}^{2u} - \Omega_{4z}^{12} \chi_z^3 - \Omega_{4u}^{2z} \chi_{3z}^{1u}) \\ &\quad + 18 \hat{\Xi}_{2\text{B}} \sum_{xu} \Omega_{3u}^{1x} (\chi_{4x}^{2u} + \Phi_{4x}^{2u} - \Psi_{4x}^{2u} - \Theta_{4x}^{2u}) \\ &\quad + \frac{9}{2} \hat{\Xi}_{2\text{B}} \sum_{vx} \Omega_{34}^{vx} (\chi_{xv}^{12} + \Phi_{xv}^{12} - \Psi_{xv}^{12} - \Theta_{xv}^{21}) \\ &\quad + \frac{9}{2} \hat{\Xi}_{2\text{B}} \sum_z (\Omega_{4z}^{12} \chi_3^z + \Omega_{34}^{1z} \chi_z^2 - \Omega_{3z}^{12} \chi_4^z - \Omega_{34}^{2z} \chi_z^1) \\ &\quad + 18 \hat{\Xi}_{2\text{B}} \sum_{zu} (\Omega_{uz}^{12} \chi_{34}^{zu} + \Omega_{4u}^{1z} \chi_{3z}^{2u} - \Omega_{4z}^{12} \chi_z^3 - \Omega_{4u}^{2z} \chi_{3z}^{1u}). \end{aligned} \quad (6.308)$$

6.4. Programmatical Derivation of Commutators for the IM-SRG Framework

The programmatical derivation of the IM-SRG commutator equations is done with a custom program in Python using the SymPy library [Meu+17]. In this section we will describe the function of the program. It basically consists of three steps:

1. Evaluation of products between two normal-ordered operators by computing all possible one- and two-body contractions according to the generalized Wick theorem.
2. Evaluation of the desired commutator.
3. Relabeling of summation indices to simplify the output and combining equal terms.

As an example, let us define the following operators with its prefactors

$$\hat{\Omega}^{[1]} := \sum_{pq} \Omega_q^p \{\hat{a}_q^p\}, \quad (6.309)$$

$$\hat{O}^{[3]} := \frac{1}{36} \sum_{rtvsuw} O_{suw}^{rtv} \{\hat{a}_{suw}^{rtv}\}. \quad (6.310)$$

These operators are needed by the program to compute a commutator, for example let us consider the following commutator

$$\hat{O} = [\hat{\Omega}^{[1]}, \hat{O}^{[3]}] = \sum_{prtvsuw} \frac{1}{36} \Omega_q^p O_{suw}^{rtv} [\{\hat{a}_q^p\}, \{\hat{a}_{suw}^{rtv}\}]. \quad (6.311)$$

The program is written in an object oriented style. An object 'General_Wick_Theorem' is defined, where the bra and ket indices of two operators as well as the one- and two-body densities are initialized. A 'General_Wick_Theorem' object is just a set of indices, which the code operates on. For example, let us define lists of upper and lower indices for the two tensors Ω_q^p and O_{suw}^{rtv}

$$u_1 = [0], \quad (6.312)$$

$$l_1 = [0], \quad (6.313)$$

$$u_2 = [0, 1, 2], \quad (6.314)$$

$$l_2 = [0, 1, 2]. \quad (6.315)$$

Furthermore, the indices p, q, r, \dots have to be defined as dummy symbols in separate lists like

$$us_1 = [p], \quad (6.316)$$

$$ls_1 = [q], \quad (6.317)$$

$$us_2 = [r, t, v], \quad (6.318)$$

$$ls_2 = [s, u, w], \quad (6.319)$$

in order to map the indices with the numbers, i.e., $u_1 \hat{=} us_1$.

In the first step, all possible one- and two-body contractions according to the generalized Wick theorem (see theorem 3.3) are computed by executing a method, which computes all contractions, i.e. a product of normal-ordered operators is computed. From this we obtain the one-particle density matrix elements $\gamma^{[1]}$, the one-hole density matrix elements $\bar{\gamma}^{[1]}$ and the irreducible two-body densities $\lambda^{[2]}$. First, all possible single contractions are determined using the methods 'get_all_gammas' and 'get_all_gammabars', where all $\gamma^{[1]}$ and $\bar{\gamma}^{[1]}$ are added to a set. Afterwards, the method 'get_all_lambda2s' is executed to obtain all irreducible two-body densities. For example, we obtain two sets

$$\gamma^{[1]} := \{-\gamma_s^p \hat{a}_{quw}^{rtv}\}, \quad (6.320)$$

$$\bar{\gamma}^{[1]} := \{-\bar{\gamma}_q^r \hat{a}_{suw}^{ptv}\}, \quad (6.321)$$

where for each set a dictionary is constructed containing the phase, the $\gamma^{[1]}$, the $\bar{\gamma}^{[1]}$, the irreducible two-body densities $\lambda^{[2]}$ and the remaining indices u_1, u_2, l_1 , and l_2 . For the first set $\gamma^{[1]}$, the dictionary looks like

$$\{\text{phase} : -1, \gamma^{[1]} : \{(0, 0)\}, \bar{\gamma}^{[1]} : \{\}, \lambda^{[2]} : \{\}, u_1 : [], u_2 : [0, 1, 2], l_1 : [0], l_2 : [1, 2]\}. \quad (6.322)$$

For each possible single and double contraction, a new dictionary is created and a list with the results is expanded. This process is done recursively, meaning that if each single- and double-contraction is determined, the next set of contractions is computed using the results list again. Note that the sets are hashed to avoid duplicates. During the computation of contractions, the lists of upper and lower indices are modified in such a way that the index used for the one- and two-body contractions are deleted. Regarding (6.322), there is no possibility to compute another $\gamma^{[1]}$ but a $\bar{\gamma}^{[1]}$ or $\lambda^{[2]}$ can be computed. As an example we will compute a $\bar{\gamma}^{[1]}$ and obtain for the dictionary

$$\{\text{phase} : +1, \gamma^{[1]} : \{(0, 0)\}, \bar{\gamma}^{[1]} : \{(0, 0)\}, \lambda^{[2]} : \{\}, u_1 : [], u_2 : [1, 2], l_1 : [], l_2 : [1, 2]\}, \quad (6.323)$$

which is equivalent to $\gamma_s^p \bar{\gamma}_q^r \hat{a}_{uw}^{tv}$. This procedure continues until u_1 , u_2 , l_1 and l_2 are empty or until only indices of one operator are left. For the considered commutator we obtain four-, three-, two-, one- and zero-body terms. Note that for the given dictionary no more contraction is possible because only contractions between two normal-ordered operators are determined. Note that the program is also able to compute terms including irreducible three-body densities $\lambda^{[3]}$ and it can be simply expanded to compute normal-ordered products of two three-body operators.

The next step is the evaluation of normal-ordered products between two operators using the method 'eval_product', where the contractions are put together and converted into antisymmetric tensor objects. In the end, we obtain a list of all terms created by the evaluation of a normal-ordered product like $\{\hat{a}_q^p\}\{\hat{a}_{suw}^{rtv}\}$ sorted by the many-body rank. Note that the evaluation of the normal ordered product also has to be done for $\{\hat{a}_{suw}^{rtv}\}\{\hat{a}_q^p\}$.

The last step is the commutator evaluation using the function 'get_commutator', which needs the results of the generalized Wick theorem, antisymmetric tensors and the summation indices as input. The commutator is then evaluated according to $[\{\hat{a}_q^p\}, \{\hat{a}_{suw}^{rtv}\}]$. The relabeling is finally done as shown in the derivation of three-body commutators (see section 6.2). For this process, the substitution function of SymPy was rewritten in order to restrict the exchange of indices. In this function an upper index is only allowed to be exchanged by an upper index and vice versa. The result is a simplified equation for the desired commutator.

7. The In-Medium No-Core Shell Model

In chapter 5, we saw that the multi-reference IM-SRG decouples a multi-determinantal reference state $|\psi_{\text{ref}}\rangle$ from its particle-hole excitations by suppressing the off-diagonal elements of the Hamiltonian. This is done by solving the Magnus type flow-equations and BCH series numerically. The IM-SRG evolved Hamiltonian can then be used in a subsequent NCSM calculation, where the convergence with respect to N_{max} is massively improved. Since the multi-reference version of the IM-SRG framework is used, the reference state is calculated using the NCSM. Therefore, the in-medium no-core shell model (IM-NCSM) [Geb+17] is a combination of the multi-reference IM-SRG and the NCSM. The IM-NCSM overcomes the limits of both methods. The disadvantage of the IM-SRG in its basic formulation is that the calculation of only ground-state observables is possible. The NCSM instead is limited by the growing model-space size with increasing number of nucleons. Since the IM-SRG can be seen as a pre-diagonalization of the Hamilton matrix, the post-diagonalization with the NCSM is computationally less demanding. This makes the method suitable for the computation of observables for medium-mass nuclei ranging from the p- to the upper sd-shell.

In this chapter, we describe the different steps of an IM-NCSM calculation followed by the so-called particle-attached particle-removed framework for the calculation of odd nuclei. Afterwards, we discuss the radius operator and electromagnetic observables. Finally, we describe the Hamiltonians we use for the IM-NCSM framework followed by a discussion of the uncertainty estimation.

7.1. The IM-NCSM Scheme

The whole IM-NCSM scheme consists of four steps.

Natural Orbital Basis. The first step of the IM-NCSM is a transformation of the single-particle basis. A first approximation for the ground state is a single Slater determinant, which is computed with an initial Hartree-Fock calculation. This is the starting point for the one-body density matrix $\gamma^{[1]}$ from many-body perturbation theory. The natural orbitals are then the eigenstates of $\gamma^{[1]}$.

Reference State and NO2B Transformation. The next step is a NCSM calculation using a small model space, typically $N_{\max}^{\text{ref}} = 0$ or 2 , for constructing the reference state $|\psi_{\text{ref}}\rangle$. The one- and two-body density matrices, $\gamma^{[1]}$ and $\gamma^{[2]}$ are then computed using the reference state $|\psi_{\text{ref}}\rangle$. Afterwards, the three-body forces are approximated using the multi-reference NO2B approximation. Especially for heavier nuclei in the *sd*-shell like ^{30}Ne we are not able to compute a reference state using $N_{\max}^{\text{ref}} = 2$ since the model space is too large. But we can avoid this problem using the IT-NCSM for the reference state construction.

In-Medium SRG Calculation. Afterwards, the reference state $|\psi_{\text{ref}}\rangle$ and the density matrices $\gamma^{[1]}$ and $\gamma^{[2]}$ are used for the multi-reference IM-SRG calculation, where the density matrices are essential for describing the desired open-shell nucleus. The aim of the IM-SRG is to decouple the reference state from its excitations. We are using the Magnus formalism, where we first solve the ODE for the Magnus operator $\hat{\Omega}(s)$ and then transform the observable $\hat{O}(s)$ using the BCH series.

NCSM Post-Diagonalization. The last step is the calculation of observables using the IM-SRG transformed Hamiltonian $\hat{H}(s)$ and the transformed operators $\hat{O}(s)$ as input for the NCSM calculation. The post-diagonalization is performed at $N_{\max} \geq N_{\max}^{\text{ref}}$ giving converged results for the ground state and low-lying excited states, which have a similar structure compared to the reference state.

7.2. Particle Attachment and Removal

The particle-attached particle-removed scheme [Vob20] is a method for computing properties of odd nuclei. The eigenstates of nuclei with odd mass numbers, like ^{13}C , have a half-integer total angular momentum. This is no problem when using the *m*-scheme version of the multi-reference IM-SRG. But since for large model-space sizes this is very costly, we have to use the *j*-coupled formalism of the multi-reference IM-SRG. In this version, odd-mass nuclei are not applicable due to the fact that their density matrices are not scalar anymore. This results in non-conserved spherical tensor ranks, which is both analytically and computationally demanding.

In the particle-attached particle-removed approach, we define the odd-*A* target nucleus and an even-*A* parent nucleus in the vicinity of the target nucleus. The construction of the reference state and the IM-SRG evolution are carried out for the even parent nucleus and the post-diagonalization for the odd target nucleus.

The advantage of this method is that not only the eigenstate of the parent nucleus is

decoupled from its excitations but also the eigenstates of the target nucleus get decoupled, since they are similar to the reference state of the parent nucleus. This results in an accelerated N_{\max} convergence.

If the number of protons or number of neutrons of the target nucleus is larger than the numbers of the parent nucleus we define a particle attachment and in the opposite case we have a particle removal scheme.

Special attention is needed for operators with an explicit dependence on the particle number, like the intrinsic kinetic energy operator

$$\hat{T}_{\text{int}} = \frac{1}{A_{\text{target}}} \sum_{i < j} \frac{(\hat{\mathbf{p}}_i - \hat{\mathbf{p}}_j)^2}{2m}. \quad (7.324)$$

Note that the kinetic energy operator is the only part of the Hamiltonian that includes information about the odd-mass target nucleus.

7.3. Observables in the IM-NCSM

The IM-NCSM enables the computation of a lot of observables known in the world of nuclear structure physics like mean-square radii \hat{r}_{ms} or electric quadrupole operators \hat{M}_M^L . In this section, we discuss the formulation of the scalar radius operators and non-scalar electromagnetic operators.

7.3.1. Radius Operator

The translationally invariant mean-square radius operator can be defined as

$$\hat{r}_{\text{ms}} = \frac{1}{A} \sum_{i=1}^A \left(\hat{\mathbf{r}}_i - \hat{\mathbf{R}} \right)^2, \quad (7.325)$$

where $\hat{\mathbf{r}}_i$ is the coordinate operator of the i -th particle and $\hat{\mathbf{R}}$ is the center-of-mass coordinate operator, which can be written as

$$\hat{\mathbf{R}} = \frac{1}{A} \sum_{i=1}^A \hat{\mathbf{r}}_i. \quad (7.326)$$

After some simplification steps and using the two-body relative coordinate operator $\hat{\mathbf{r}}_{ij} = \hat{\mathbf{r}}_i - \hat{\mathbf{r}}_j$ we obtain

$$\hat{r}_{\text{ms}} = \frac{1}{A^2} \sum_{i < j}^A \hat{r}_{ij}^2. \quad (7.327)$$

We can rewrite \hat{r}_{ms} into second quantization giving

$$\hat{r}_{\text{ms}} = \frac{1}{4A^2} \sum_{prqs} \langle pr | \hat{r}_{12}^2 | qs \rangle \hat{a}_{qs}^{pr}. \quad (7.328)$$

Now, we define the point-proton and point-neutron mean-square radii, which can be written as

$$\hat{r}_{\text{pms}} = \frac{1}{Z} \sum_{i=1}^A \left(\hat{r}_i - \hat{\mathbf{R}} \right)^2 \hat{\Pi}_i^{\text{p}}, \quad (7.329)$$

where $\hat{\Pi}_i^{\text{p}}$ is the proton projector. For the point-neutron mean-square radius we only need to use $\hat{\Pi}_i^{\text{n}}$, the neutron projector

$$\hat{r}_{\text{nms}} = \frac{1}{N} \sum_{i=1}^A \left(\hat{r}_i - \hat{\mathbf{R}} \right)^2 \hat{\Pi}_i^{\text{n}}. \quad (7.330)$$

If we now express \hat{r}_{pms} and \hat{r}_{nms} in terms of \hat{r}_{ij} we obtain

$$\hat{r}_{\text{pms}} = \frac{1}{ZA} \sum_{i < j}^A \hat{r}_{ij}^2 \left(2\hat{\Pi}_i^{\text{p}}\hat{\Pi}_j^{\text{p}} + \hat{\Pi}_i^{\text{p}}\hat{\Pi}_j^{\text{n}} + \hat{\Pi}_i^{\text{n}}\hat{\Pi}_j^{\text{p}} \right) - \hat{r}_{\text{ms}}, \quad (7.331)$$

$$\hat{r}_{\text{nms}} = \frac{1}{NA} \sum_{i < j}^A \hat{r}_{ij}^2 \left(2\hat{\Pi}_i^{\text{n}}\hat{\Pi}_j^{\text{n}} + \hat{\Pi}_i^{\text{n}}\hat{\Pi}_j^{\text{p}} + \hat{\Pi}_i^{\text{p}}\hat{\Pi}_j^{\text{n}} \right) - \hat{r}_{\text{ms}}. \quad (7.332)$$

All these radius operators are related through

$$\hat{r}_{\text{nms}} = \frac{A}{N} \hat{r}_{\text{ms}} - \frac{Z}{N} \hat{r}_{\text{pms}}. \quad (7.333)$$

Using these operators and the eigenstates of the Hamiltonian we can define the corresponding root-mean-square radii

$$R_{\text{rms}} = \sqrt{\langle \psi_i | \hat{r}_{\text{ms}} | \psi_i \rangle}, \quad (7.334)$$

$$R_{\text{prms}} = \sqrt{\langle \psi_i | \hat{r}_{\text{pms}} | \psi_i \rangle}, \quad (7.335)$$

$$R_{\text{nrms}} = \sqrt{\langle \psi_i | \hat{r}_{\text{nms}} | \psi_i \rangle}, \quad (7.336)$$

where $|\psi_i\rangle$ is the eigenstate of the Hamiltonian. Finally, the charge radius, which is experimentally measured, can be computed from the point-proton rms radius using [FMS97]

$$R_{\text{ch}}^2 = R_{\text{prms}}^2 + \left(r_{\text{p}}^2 + \frac{3}{4m_{\text{p}}^2} \right) + \frac{N}{Z} r_{\text{n}}^2, \quad (7.337)$$

where $r_{\text{p}}^2 = 0.770 \text{ fm}^2$ and $r_{\text{n}}^2 = -0.1161 \text{ fm}^2$ are the charge radii of the proton and neutron [Ber+12].

7.3.2. Electromagnetic Observables

In this section we introduce electromagnetic multipole operators leading to electromagnetic multipole moments and transition strengths. These observables are well suited for testing the underlying nuclear models due to their sensitivity to changes in the wavefunction [Suh07].

Electromagnetic transitions are described as an interaction of the nucleus with an external electromagnetic field consisting of an electric field \mathbf{E} and a magnetic field \mathbf{B} , where the interaction between the nucleus and the field is expressed by the four-vector potential (ϕ, \mathbf{A}) . Here, ϕ is the scalar potential, which couples to the nuclear charge density ρ , and \mathbf{A} is the vector potential coupling to the nuclear current density \mathbf{j} . The field is quantized in terms of photons and interacts weakly, i.e., it can be described perturbatively, where the external field is expanded in terms of multipoles. The transition probabilities can be described by the golden rule of time-dependent perturbation theory

$$T_{fi}^{(\sigma\lambda\mu)} = \frac{2}{\epsilon_0 \hbar} \frac{\lambda + 1}{\lambda [(2\lambda + 1)!!]^2} \left(\frac{E_\gamma}{\hbar c} \right)^{2\lambda+1} |\langle \psi_f; J_f M_f | \hat{M}_{\sigma\lambda\mu} | \psi_i; J_i M_i \rangle|^2, \quad (7.338)$$

where E_γ is the transition energy and $\hat{M}_{\sigma\lambda\mu}$ is the operator of the multipole radiation field $\sigma\lambda\mu$. Here, σ is the type of transition, which is E for electric and M for magnetic and $\lambda\mu$ are the multipole components of the field. Due to the fact that magnetic substates cannot be experimentally observed separately, we need to average over initial substates M_i and sum over all final substates M_f and all projections μ to obtain the transition

probability

$$T_{fi}^{(\sigma\lambda)} = \frac{1}{2J_i + 1} \sum_{M_i M_f \mu} T_{fi}^{(\sigma\lambda\mu)} \quad (7.339)$$

$$= \frac{2}{\epsilon_0 \hbar} \frac{\lambda + 1}{\lambda [(2\lambda + 1)!!]^2} \left(\frac{E_\gamma}{\hbar c} \right)^{2\lambda+1} B(\sigma\lambda; \psi_i \rightarrow \psi_f). \quad (7.340)$$

Here, $B(\sigma\lambda; \psi_i \rightarrow \psi_f)$ is the reduced transition probability, which can be written as

$$B(\sigma\lambda; \psi_i \rightarrow \psi_f) = \frac{1}{2J_i + 1} |\langle \psi_f; J_f | \hat{M}_{\sigma\lambda} | \psi_i; J_i \rangle|^2. \quad (7.341)$$

Note that the reduced matrix element emerges by averaging (7.338) over the initial substates and a summation over all final substates and values of μ . The components of the electric and magnetic multipole operators can be written as

$$\hat{M}_{\lambda\mu}^{\text{el}} = \sum_{i=1}^A \hat{e}_i \hat{r}_i^\lambda Y_{\lambda\mu}(\hat{\Omega}_i), \quad (7.342)$$

$$\hat{M}_{\lambda\mu}^{\text{mag}} = \frac{\mu_N}{\hbar c} \sum_{i=1}^A \left[\frac{2}{\lambda + 1} g_l^{(i)} \hat{\mathbf{l}}_i + g_s^{(i)} \hat{\mathbf{s}}_i \right] \cdot \nabla_i \left[\hat{r}_i^\lambda Y_{\lambda\mu}(\hat{\Omega}_i) \right], \quad (7.343)$$

where \hat{e}_i is the electric charge, $\hat{\mathbf{l}}_i$ and $\hat{\mathbf{s}}_i$ are the orbital and spin angular momenta of the nucleon i . $g_l^{(i)}$ and $g_s^{(i)}$ are the gyromagnetic factors for the orbital and spin, where $g_l^{(i)} = 1$ for protons and 0 for neutrons. The spin gyromagnetic factor $g_s^{(i)}$ is 5.586 for the proton and -3.826 for the neutron. Further, m_p is the proton mass and μ_N is the nuclear magneton with a value of 0.10515 c e fm [Suh07].

In general, electromagnetic transitions can be classified regarding their multipole order and the structure of electric and magnetic multipole operators. Regarding parity, we obtain the following selection rule

$$\pi_i \pi_f = \begin{cases} (-1)^\lambda & \text{for } E\lambda \\ (-1)^{\lambda+1} & \text{for } M\lambda \end{cases}, \quad (7.344)$$

where π_i and π_f are the parities for the initial and final state, respectively. Furthermore, the transition probability is lower with increasing multipolarity. Another important selection rule is the angular momentum rule, where for a transition between two states with angular momentum J_i and J_f the triangular condition $J_f - \lambda \leq J_i \leq J_f + \lambda$ has to

be fulfilled.

Other important observables are the electric and the magnetic multipole moments with the general form

$$M(\sigma\lambda) = \langle \psi; JM_J | \hat{M}_{\sigma\lambda 0} | \psi; JM_J \rangle \quad (7.345)$$

$$= \begin{pmatrix} J & \lambda & J \\ -J & 0 & J \end{pmatrix} \langle \psi; J | \hat{M}_{\sigma\lambda 0} | \psi; J \rangle. \quad (7.346)$$

Finally, we can define the electric quadrupole moment Q and the magnetic dipole moment μ by insertion of the $3j$ symbol as

$$eQ = \sqrt{\frac{16\pi}{5}} M(E2) = \sqrt{\frac{16\pi}{5}} \sqrt{\frac{J(2J-1)}{(J+1)(2J+1)(2J+3)}} \langle \psi; J | \hat{M}_{e2}^2 | \psi; J \rangle \quad (7.347)$$

$$\frac{\mu}{c} = \sqrt{\frac{4\pi}{3}} M(M1) = \sqrt{\frac{4\pi}{3}} \sqrt{\frac{J}{(J+1)(2J+1)}} \langle \psi; J | \hat{M}_{\text{mag}1} | \psi; J \rangle, \quad (7.348)$$

where the conditions for non-vanishing E2 and M1 moments are $J \geq 1$ and $J \geq \frac{1}{2}$. More about electromagnetic multipole operators can be found in [Suh07].

7.4. Hamiltonians and Uncertainty Estimation

7.4.1. Hamiltonians and Truncations

In this work we are using interactions from chiral effective field theory, more precisely the NN interaction by Entem, Machleidt and Nosyk (EMN) [EMN17] with a cutoff of $\Lambda_{\text{NN}} = 500$ MeV and a non-local 3N interaction by Hütther et al. [Hüt+20] with the same cutoff. The chiral truncation ranges from LO up to N³LO. These interactions use 3N low-energy constants that are optimized in many-body calculations, i.e. the one-pion two-nucleon-contact constant c_{D} is fitted using the ¹⁶O ground-state energy and the triton ground-state energy is used to fix the three-nucleon-contact parameter c_{E} . We use the different chiral truncation orders for the uncertainty estimation, which will be addressed in the next section. Further, we use the free-space SRG transformation at the three-body level to soften the interactions with a flow parameter of $\alpha = 0.04$ fm⁴ [JNF09; Rot+11; Heb12; Rot+14; BFP07].

7.4.2. Uncertainty Estimation

In this section we address two kinds of uncertainties. One arising from the many-body calculation and the other from the interaction itself.

Many-Body Uncertainties. In the IM-NCSM, multiple sources of uncertainties can arise like the uncertainty in the IM-SRG evolution, the N_{\max} truncation and the uncertainty in the variation of the reference-state truncation N_{\max}^{ref} . The error of the IM-SRG truncation is determined depending on the flow parameter s . We evaluate the Magnus flow equation up to a desired flow parameter s and solve the BCH series for two flow parameters s and $\frac{s}{2}$. The uncertainty is then computed using $\delta O(s) = O(s) - O(s/2)$. Since we are interested in converged results with respect to N_{\max} and N_{\max}^{ref} , the many-body uncertainties can be computed as the difference of the observable between the two largest values of N_{\max} , which gives the N_{\max} error $\delta O_{N_{\max}}$. The second many-body error we compute is the absolute difference between the two neighbouring values of N_{\max}^{ref} , where the N_{\max} truncation parameter has to be the same within the difference resulting in $\delta O_{N_{\max}^{\text{ref}}}$. For the final many-body uncertainty we choose the maximum of these errors.

Interaction Uncertainties. For the interaction uncertainties we use an error estimation based on Bayesian statistics, which was proposed by the BUQEYE collaboration, the so-called pointwise model [Mel+19]. This model is designed to address errors introduced by the truncation of chiral effective field theory (χ -EFT), where the interaction parts occur in terms of a power counting scheme. We define an observable y_n , which is calculated with an EFT of order Q^n and its corrections Δy_n , where n is the order in the EFT. Furthermore, we define a set of observables \vec{y}_n and coefficients \vec{c}_n as

$$\vec{y}_n := \{y_0, y_1, \dots, y_n\} \quad (7.349)$$

$$\vec{c}_n := \{c_0, c_1, \dots, c_n\}. \quad (7.350)$$

The chiral expansion is assumed to be valid, not only for the interaction, but also for the observable y_n

$$y_n = y_0 + \Delta y_1 + \dots + \Delta y_n. \quad (7.351)$$

The expansion can be suppressed in a dimensionless expansion parameter Q according to the EFT power counting, where the correction of the n -th order Δy_n is absorbed into Q^n , which can be written as

$$y_n = y_{\text{ref}} \sum_{k=0}^n c_k Q^k, \quad (7.352)$$

where y_{ref} is a scaling parameter and c_k are dimensionless coefficients, which are natural or of order 1. Using the results of lower chiral orders, we can compute the expansion coefficients c_k . The truncation error δy_n , which consists of all omitted terms can be written as

$$\delta y_n = y_{\text{ref}} \sum_{k=n+1}^{\infty} c_k Q^k. \quad (7.353)$$

All coefficients c_k with $k > n$ are unknown and need to be predicted for computing the truncation error and it is assumed that the properties of the unknown coefficients are the same as for the known ones. The k -th coefficient is computed using

$$c_k = \frac{y_0}{y_{\text{ref}}} + \sum_{n=1}^k \frac{y_n - y_{n-1}}{y_{\text{ref}} \cdot Q^n}, \quad (7.354)$$

indicating that each unknown coefficient c_k is computed using the coefficients of the lower orders. Afterwards we determine the hyperparameters ν and τ

$$\nu = \nu_0 + n_c \quad (7.355)$$

$$\nu \tau^2 = \nu_0 \tau_0^2 + \vec{c}_n^2, \quad (7.356)$$

where n_c is the number of coefficients in \vec{c}_n and $\nu_0 = \tau_0 = 1$.

Finally, a Student-t distribution $T_{k,\nu}$ is used to estimate the uncertainty of an observable y_k given as

$$T_{k,\nu}(c_k | \vec{c}_n) = \frac{1}{\sqrt{\pi \nu \tau^2}} \frac{\Gamma(\frac{\nu+1}{2})}{\Gamma(\frac{\nu}{2})} \left(1 + \frac{c_k^2}{\nu \tau^2}\right)^{-\frac{\nu+1}{2}} = T_{k,\nu}(0, \tau^2). \quad (7.357)$$

Using $y = y_n + \delta y_n$ the Student-t distribution can be written as

$$T_{k,\nu} \left(y_n, y_{\text{ref}}^2 \frac{Q^{2(n+1)}}{1-Q^2} \tau^2 \right) = \frac{1}{\sqrt{\pi \nu y_{\text{ref}}^2 \frac{Q^{2(n+1)}}{1-Q^2} \tau^2}} \frac{\Gamma\left(\frac{\nu+1}{2}\right)}{\Gamma\left(\frac{\nu}{2}\right)} \left(1 + \frac{y_n^2}{\nu y_{\text{ref}}^2 \frac{Q^{2(n+1)}}{1-Q^2} \tau^2} \right)^{-\frac{\nu+1}{2}}. \quad (7.358)$$

We obtain the uncertainty by integrating over this Student-t distribution until we reach a certain degree of belief. The degree of belief we used for the integration is 68%. Furthermore, it is assumed that the expansion parameter Q is known, which can also be computed using a Bayesian process [Hüt21]. In this work we use $Q \approx \frac{1}{3}$. Note that the coefficient c_1 in the chiral expansion is zero. We consider this by treating the leading order as Q^1 , i.e. we are starting the chiral expansion at $n = 1$. For more about the pointwise model like the derivation see [Mel+19].

8. Results

In this chapter we present results from the IM-NCSM for the oxygen, carbon, and neon isotopic chains. For these isotopic chains we explore ground-state energies, spectra, and charge radii as well as electromagnetic moments and transition strengths. Furthermore, we investigated the convergence behavior of different observables regarding the IM-SRG evolution itself and also the convergence with respect to N_{\max} and the chiral order of the underlying interaction.

The single-particle basis includes 13 major shells, i.e., $e_{\max} = 12$, and the initial three-body matrix elements are truncated with $E_{3\max} = 14$. Note that the error due to the truncation of e_{\max} and $E_{3\max}$ for these values is below 1% and, therefore, negligible [Rot+12b; Bin+13; Her+13b; Her+13a]. The harmonic oscillator frequency is $\hbar\Omega = 20$ MeV [Rot+12a; Bin+13; Her+13b; Her+13a]. If not stated otherwise we use the White generator for the multi-reference IM-SRG decoupling.

Oxygen isotopes are well-known as benchmark for many-body theories and Hamiltonians, since their proton subshell is closed and ^{16}O is a doubly magic nucleus. Its experimental ground-state energy can be well reproduced by different many-body methods like coupled-cluster theory [Hag+14; Jan+14; Eks+15; Hag+16], IM-SRG [Her+13b; Her+13a; Heb+15; Lap+16; Geb+17; Str+17; Miy+20], self-consistent Green's function theory [CBN15; Som+20], no-core shell model approaches like the (IT)-NCSM [Rot09], and perturbation theory approaches [Tic+18a; Tic+18b]. The semi-magic character of oxygen isotopes ensures that deformation effects can be neglected [Som+20]. Also, ^{22}O and ^{24}O are very interesting due to the fact that they have a closed neutron subshell and proton major shell [Thi+00; Oza+00; Hof+09; Kan+09], where ^{24}O is the heaviest bound nucleus in the oxygen chain.

The carbon isotopic chain is another interesting case for theoretical calculations [Jan+14; Eks+15; Par+17; Tra+18; Tic+18a] and experimental nuclear structure physics, especially for lifetime measurements resulting in $B(E2)$ transition strengths [Wie+08; Ong+08; Pet+11; Pet+12; McC+12; Vos+12]. Also, for IM-NCSM calculations, the neutron-rich carbon isotopes are interesting, since these are difficult to converge using (IT)-NCSM calculations [FRN13].

The last isotopic chain we will discuss in this chapter is the neon chain. Neon isotopes are very interesting for nuclear structure theory because they are completely open-shell

nuclei and the neutron-rich isotopes reach the so-called island of inversion [Nov+20]. The island of inversion is an area in the nuclear chart, where shell closures predicted by the shell-model are obsolete and new shell closures occur. A prominent example are neutron-rich neon, sodium, and magnesium isotopes, where the magic number $N = 20$ disappears [PR87; WBB90; CNP14]. This can lead to stronger correlations between valence nucleons, which can result in particle-hole excitations to higher-lying single-particle states leading to a decrease of energy for deformed configurations [Wim+10]. The disappearance of the $N = 20$ neutron magic number for neon, sodium and magnesium isotopes has been explored in experimental [Iwa+01; Yor+07; Doo+13; Doo+16] and theoretical [Cau+98; Uts+99; YV04; Tsu+17] studies. But not only the isotopes in the island-of-inversion are interesting, $^{20-22}\text{Ne}$ for example also have been studied due to their intrinsically deformed ground states [Mar+11; Zho+16; Mar+18]. In [Fro+22a] it has been shown that in ^{20}Ne configuration mixing occurs ranging from a $\alpha+^{12}\text{C}+\alpha$ to a quasi- $^{16}\text{C}+\alpha$ structure. The neon isotopic chain has been intensely studied using different ab-initio methods [Sig+15; Str+16; Jan+16; Her16; Str+19; AGZ20; Nov+20; Miy+20; Fro+22a]. In this work we compare results of the projected generator coordinate method (PGCM) with IM-NCSM results for $^{18-30}\text{Ne}$.

8.1. Analysis of ^{12}C

In this section we focus on the analysis of ^{12}C , which was published in [DA1+20]. In this work we collaborated with d'Alessio et al., who measured the $B(E2, 2_1^+ \rightarrow 0_1^+)$ transition strength of ^{12}C at the S-DALINAC in an (e, e') scattering experiment. The previous measured $B(E2)$ transition strength was $7.94(40) \text{ e}^2\text{fm}^4$ [Pri+16] and the updated value is $7.62(19) \text{ e}^2\text{fm}^4$, where the uncertainty is reduced to 2.5% [DA1+20]. The motivation was to obtain an improved value of the experimental $B(E2)$ transition strength as benchmark for nuclear structure calculations, which is then compared with IM-NCSM calculations. Furthermore, a correlation between the $B(E2)$ transition strength and quadrupole moment Q was observed in [CR16]. In order to obtain an electric quadrupole moment from the experimental data using this correlation, the $B(E2)$ transition strength needs to be known as precisely as possible. We start with the IM-SRG flow of the ground-state energy and the first two excited states of ^{12}C . Afterwards we consider spectra, $B(E2)$ transition strengths, and electric quadrupole moments of ^{12}C as function of N_{max} and the chiral interaction order ranging from NLO to N³LO. Moreover, we investigate the correlation of the transition strength and the electric quadrupole moment.

In Fig. 8.1 the ground-state energy of ^{12}C is plotted against the flow parameter s in a logarithmic scale for different generators and bases. We use different labels for the generators and bases: 'White' and 'ImaginaryTime' are the generators using the

decoupling pattern presented in Eq. (5.215); 'WhiteNmax0' and 'ImaginaryTimeNmax0' indicate the generators using the optimized decoupling patterns shown in Eq. (5.218) and (5.219). Furthermore, HF indicates the use of the Hartree-Fock basis and NAT the use of the natural orbital basis. In the upper and middle panels of Fig. 8.1, the results using the HF basis are presented and in the lower panels, the results using the NAT basis are presented. The results using the White generators are shown in the left-hand panels and the results of the imaginary-time generator are shown in the right-hand panels. The symbols represent different values of N_{\max} ranging from $N_{\max} = 0$ to $N_{\max} = 8$ with $N_{\max}^{\text{ref}} = 0$. Note that in this section we used interactions from [Hüt+20].

The original White generator first shows a plateau but falls for large flow parameters s due to induced many-body interactions. Therefore, it was necessary in the past to investigate a flow parameter in a region, where a stable plateau is formed in the plot. The optimized White and imaginary-time generators for the HF basis show a plateau also for large values of s . In comparison with the NAT basis we also obtain a plateau for large flow parameters.

Figure 8.2 shows the first two excited states of ^{12}C as function of the flow parameter following the same terminology as in Fig. 8.1. For the first two excited states, we can see that a plateau is reached for the NAT basis, which is also obtained when using the HF basis (see middle panels). When using the unoptimized generators (see upper panels), the flow does not stabilize for large flow parameters for both generators. The most stable result for large flow parameters is obtained using the optimized White generator and the HF basis. In general, the flows are more stable using the White generator for the first two excited states compared to the imaginary-time generator.

Figure 8.3 depicts the excitation spectrum (upper panel), the $B(E2, 2_1^+ \rightarrow 0_1^+)$ transition strength (middle panel), and electric quadrupole moment $Q(2_1^+)$ (lower panel) as function of N_{\max} for different values of N_{\max}^{ref} . In the left-hand panels, the results for $N_{\max}^{\text{ref}} = 0$ are shown. The two following columns show the results for $N_{\max}^{\text{ref}} = 2$ and 4 and in the right-hand panel, the experimental results are shown. The flow parameter s is fixed at 48 integration steps, which is $s \approx 80$. Note that due to the fact that the flow parameter changes during the integration of the ODEs in dependency of the convergence in the Magnus flow evolution, the flow parameter can also be slightly larger or smaller after 48 integration steps. The error bars indicate many-body uncertainties from the variation of the reference space and shaded bands are the dependency of the IM-SRG evolution in s as shown in section 7.4.2. The dependency of our results on the flow parameter is small. Therefore, we do not discuss it anymore.

We see that the energies of the excited states, the $B(E2)$ transition strengths and the quadrupole moments are converged with respect to N_{\max} . For all values of N_{\max}^{ref} , the excitation energies agree well with the experimental values. This is also the case for the

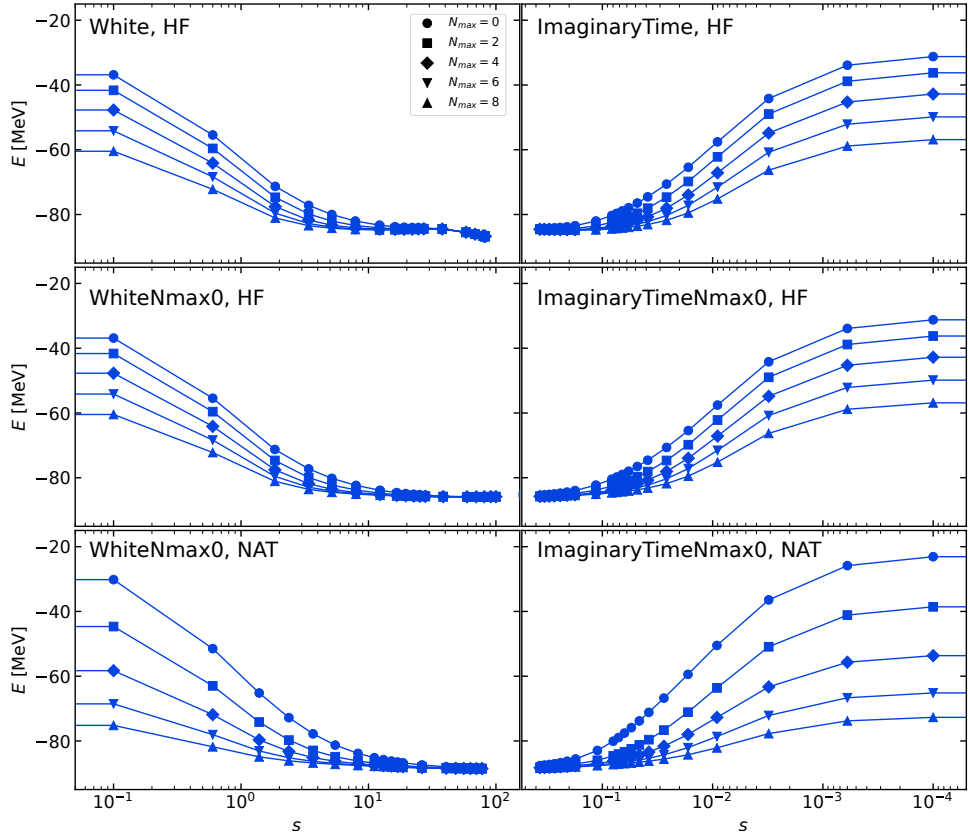


Fig. 8.1.: Ground-state energy of ^{12}C as function of the flow parameter s for the unoptimized and optimized White and imaginary-time generators for $N_{\text{max}}^{\text{ref}} = 0$ and values of N_{max} ranging from 0 to 8. All calculations were performed with the chiral two- plus three-body interaction at N^3LO with a cutoff of $\Lambda = 500$ MeV/c.

$B(E2)$ transition strength and the quadrupole moment, which is in perfect agreement with the experimental value. The dependency on $N_{\text{max}}^{\text{ref}}$ for the excited-state energies and quadrupole moments is quite small. For the $B(E2)$ transition strengths, the many-body uncertainty for $N_{\text{max}}^{\text{ref}} = 2$ is larger compared to the spectra and quadrupole moments. This indirectly probes the effect of neglected normal-ordered three-body matrix elements in the IM-SRG [DAI+20]. The effect of normal-ordered three-body terms on $B(E2)$ transition strengths will be discussed later in this work.

Now we expand the discussion to the robustness of our results with respect to the order and the cutoff Λ of the chiral interaction. In Fig. 8.4, the ground-state energy (top row), low-lying excited states (second row), $B(E2)$ transition strengths (third row) and electric quadrupole moments (bottom row) of ^{12}C are shown as function of the chiral interaction order. The cutoff used for these calculations is $\Lambda = 450$ MeV/c. The arrangement of the $N_{\text{max}}^{\text{ref}}$ variation is the same as in Fig. 8.3. The error bars are interaction uncertainties from a pointwise Bayesian model as presented in section 7.4.2 and the shaded bands

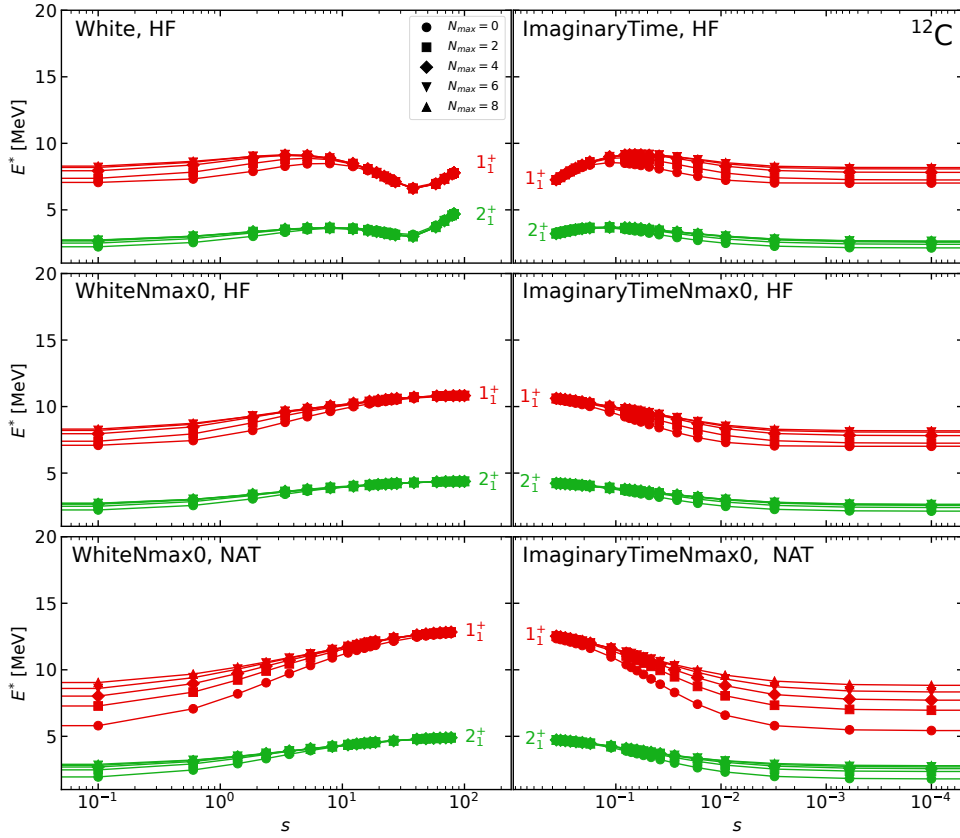


Fig. 8.2.: First two excited states of ^{12}C as function of the flow parameter s for the unoptimized and optimized White and imaginary-time generators for $N_{\text{max}}^{\text{ref}} = 0$ and values of N_{max} ranging from 0 to 8. All calculations were performed with the chiral two- plus three-body interaction at N^3LO with a cutoff of $\Lambda = 500$ MeV/c.

depict combined many-body and interaction uncertainties.

For the ground-state energy, the results for $N_{\text{max}}^{\text{ref}} = 2$ and 4 are in good agreement with the experimental result for N^2LO and N^3LO , which is not the case for the ground-state energy at $N_{\text{max}}^{\text{ref}} = 0$. This indicates that the reference-space at $N_{\text{max}}^{\text{ref}} = 0$ is not large enough to describe the ground-state energy properly. Furthermore, the many-body uncertainties of the ground-state energies for $N_{\text{max}}^{\text{ref}} = 2$ and 4 are quite large due to the result at $N_{\text{max}}^{\text{ref}} = 0$. For the spectra, the results are in good agreement with experimental for all values of $N_{\text{max}}^{\text{ref}}$. Coming to the electromagnetic observables, the $B(E2)$ transition strength and the quadrupole moment are also in good agreement with the experimental values. Note that the experimental uncertainty for the electric quadrupole moment $Q(2_1^+)$ is 50% [Ver+83], which needs to be examined.

The results for $\Lambda = 500$ MeV/c are shown in Fig. 8.5 with the same arrangement as in Fig. 8.4. We find that all states at N^3LO agree with experimental results for the ground-state energy and in the spectrum. The only state, which is underestimated at

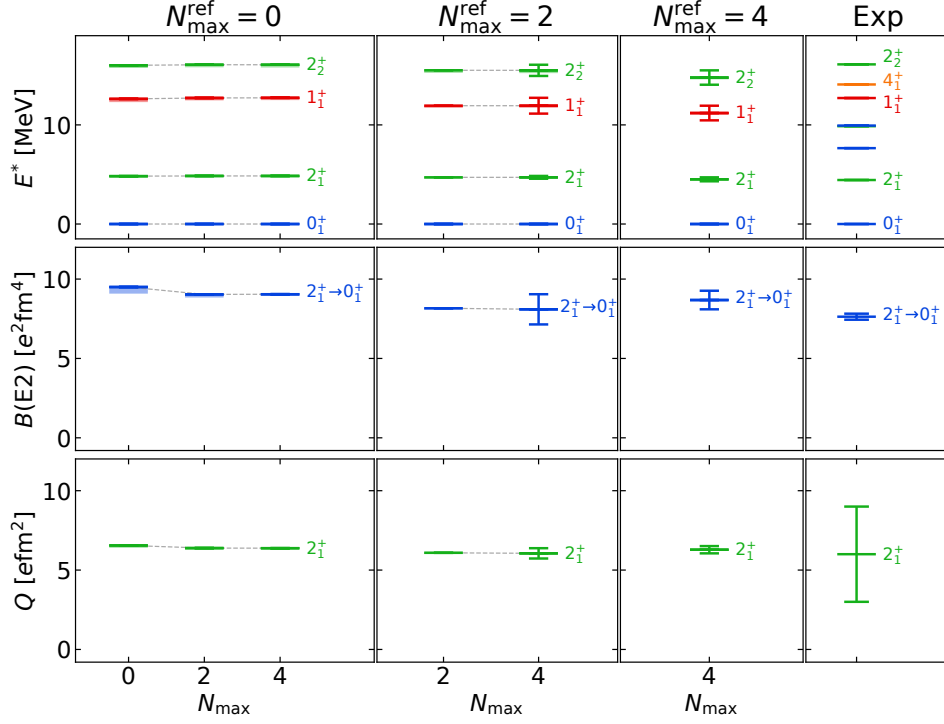


Fig. 8.3.: Excitation spectrum, $B(E2)$ transition strength and electric quadrupole moment for ^{12}C obtained from the IM-NCSM for different reference-space truncations $N_{\text{max}}^{\text{ref}}$ as function of N_{max} . All calculations were performed with the chiral two- plus three-body interaction at N^3LO with a cutoff of $\Lambda = 500$ MeV/c. The error bars indicate many-body uncertainties. Experimental results are taken from [KPS17; DA1+20; Ver+83].

N^2LO is the 1_1^+ state. This could be due to a more complicated structure of the state itself. For the $B(E2)$ transition strength and the quadrupole moment, the agreement with the experiment is also good, particularly for $N_{\text{max}}^{\text{ref}} = 2$ and 4 at N^2LO and N^3LO . Now we move on to the calculations for $\Lambda = 550$ MeV/c, which are shown in Fig. 8.6. The panels are the same as in the figure showing the results for $\Lambda = 500$ MeV/c. For all observables at $N_{\text{max}}^{\text{ref}} = 2$, the many-body uncertainties at N^3LO are large due to the fact that the results are not fully converged at $N_{\text{max}}^{\text{ref}} = 0$. But when moving to $N_{\text{max}}^{\text{ref}} = 4$, we see that the results are converged with respect to $N_{\text{max}}^{\text{ref}}$. Furthermore, we obtain an anomaly regarding the results at N^2LO for $\Lambda = 550$ MeV/c. All in all, it is remarkable that most of the results are in agreement with experimental values for all cutoffs.

As a final result for ^{12}C , we consider the correlation behavior between $B(E2, 2_1^+ \rightarrow 0_1^+)$ and $Q(2_1^+)$ in a correlation plot shown in Fig. 8.7. In this plot, the results for the $B(E2)$ transition strength are shown as function of the quadrupole moment Q for ^{12}C obtained at N^2LO (open symbols) and N^3LO (closed symbols) for cutoffs of 450, 500, and 550 MeV/c. The calculations have been performed using $N_{\text{max}} = N_{\text{max}}^{\text{ref}} = 4$ and

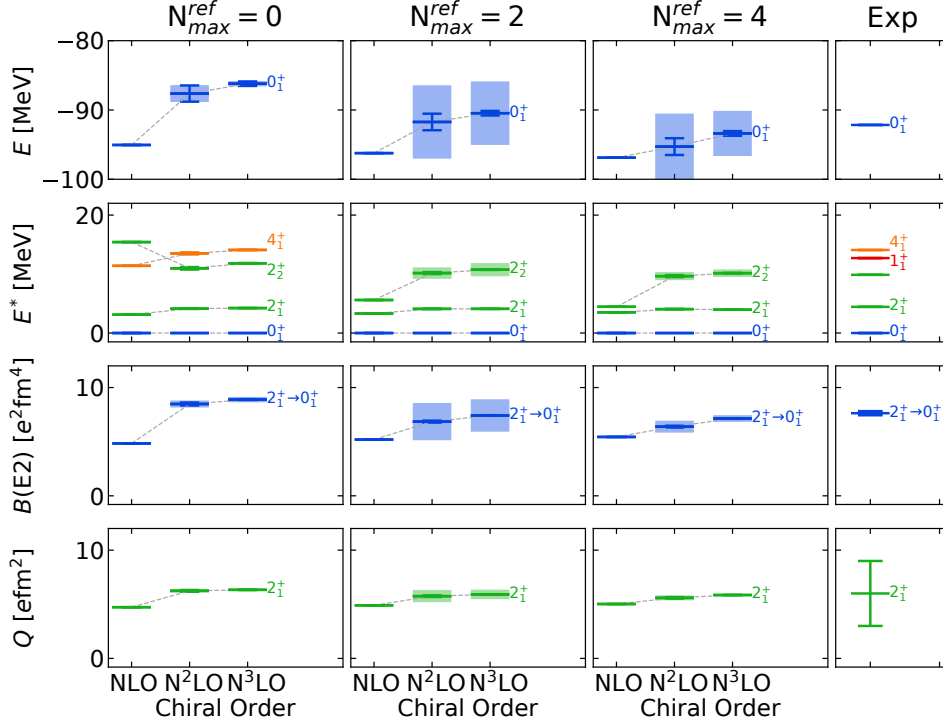


Fig. 8.4.: Ground-state energy, excitation spectrum, $B(E2)$ transition strength and electric quadrupole moment for ^{12}C obtained from the IM-NCSM for different reference-space truncations N_{\max}^{ref} as function of the chiral interaction order. All calculations were performed with the chiral two- plus three-body interaction with a cutoff of $\Lambda = 450$ MeV/c. The error bars indicate interaction uncertainties and the error bands combined many-body and interaction uncertainties. Experimental results are taken from [Wan+17; KPS17; DA1+20; Ver+83].

the error bars indicate combined many-body and interaction uncertainties. The lines show a prediction of a simple rigid rotor (dashed) and a fitted (solid) rotor model. The horizontal and vertical red shaded bands indicate the experimental $B(E2)$ and the $Q(2_1^+)$ value derived from the intersection with the model correlation. The red area indicates the experimental limits from value of the quadrupole moment obtained in this work and the experimental result of the $B(E2)$ transition strength obtained in [DA1+20]. The grey area indicates the experimental limits from the experimental quadrupole moment measured in [Ver+83] and the $B(E2)$ transition strength from [Pri+16]. For all six interactions, the results fall on a line, which was already observed in [CR16] for first-generation chiral interactions. We fitted the data using the simple rotational model by Bohr and Mottelson [BM98], where the observables in the laboratory frame are connected with the intrinsic quadrupole moment Q_0 resulting in

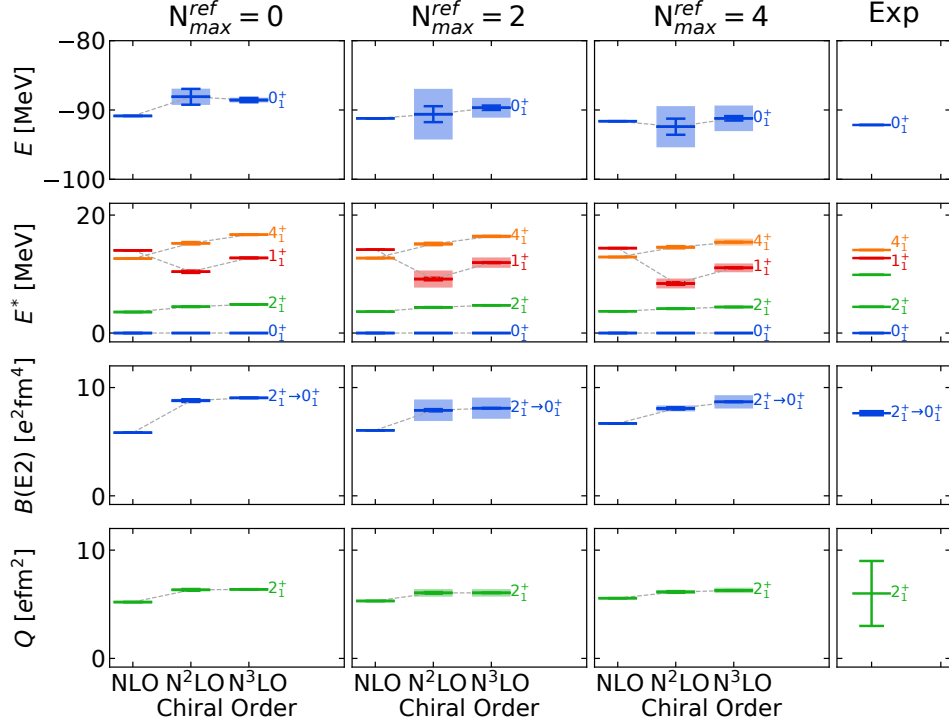


Fig. 8.5.: Ground-state energy, excitation spectrum, $B(E2)$ transition strength and electric quadrupole moment for ^{12}C obtained from the IM-NCSM for different reference-space truncations $N_{\text{max}}^{\text{ref}}$ as function of the chiral interaction order. All calculations were performed with the chiral two- plus three-body interaction with a cutoff of $\Lambda = 500$ MeV/c. The error bars indicate interaction uncertainties and the error bands combined many-body and interaction uncertainties. Experimental results are taken from [Wan+17; KPS17; DA1+20; Ver+83].

$$Q(J) = \frac{3K^2 - J(J+1)}{(J+1)(2J+3)} Q_{0,s} \quad (8.359)$$

$$B(E2, J_i \rightarrow J_f) = \frac{5}{16\pi} Q_{0,t}^2 \begin{pmatrix} J_i & 2 & J_f \\ K & 0 & K \end{pmatrix}. \quad (8.360)$$

Here, J is the angular momentum and K the projection of J on the symmetry axis of the deformed nucleus. The indices of the intrinsic quadrupole moment indicate s for the static quadrupole moment $Q(J)$ and t for the intrinsic quadrupole moment of the $B(E2)$ transition strength. Both formulas can be combined to obtain a ratio of the intrinsic quadrupole moments $Q_{0,t}/Q_{0,s}$ relating $B(E2, J_i \rightarrow J_f)$ and $Q(J)$

$$B(E2, J_i \rightarrow J_f) = \frac{5}{16\pi} \frac{((J+1)(2J+3))^2}{(3K^2 - J(J+1))^2} \begin{pmatrix} J_i & 2 & J_f \\ K & 0 & K \end{pmatrix} \left(\frac{Q_{0,t}}{Q_{0,s}} \right) Q(J)^2. \quad (8.361)$$

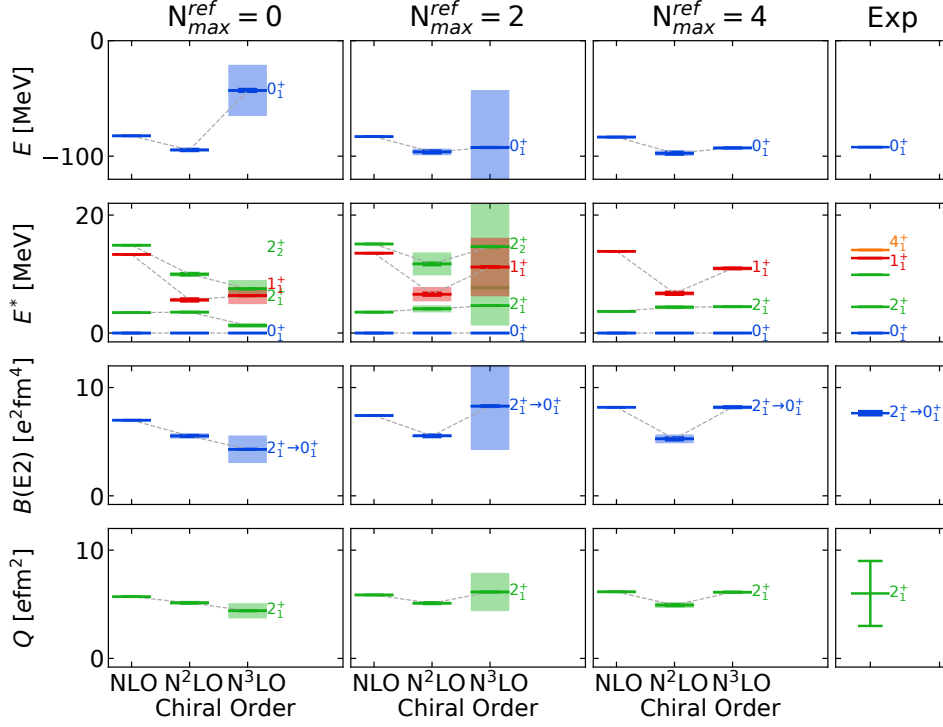


Fig. 8.6.: Ground-state energy, excitation spectrum, $B(E2)$ transition strength and electric quadrupole moment for ^{12}C obtained from the IM-NCSM for different reference-space truncations N_{\max}^{ref} as function of the chiral interaction order. All calculations were performed with the chiral two- plus three-body interaction with a cutoff of $\Lambda = 550$ MeV/c. The error bars indicate interaction uncertainties and the error bands combined many-body and interaction uncertainties. Experimental results are taken from [Wan+17; KPS17; DA1+20; Ver+83].

In this formula, the E2 matrix elements are assumed to be expressed in terms of one single parameter Q_0 .

First of all, we observe that the results for N²LO show a larger cutoff dependence compared to the N³LO results, which also cross the experimental $B(E2)$ value. The green dashed line shows a correlation predicted by a rigid rotor, where $Q_{0,t}/Q_{0,s} = 1$. The black line shows the fit with the Bohr-Mottelson model, where the ratio of the intrinsic quadrupole moments is used as fit parameter. We obtained a ratio of $Q_{0,t}/Q_{0,s} = 0.967$. In [CR16], almost the same ratio of these quadrupole moments, $Q_{0,t}/Q_{0,s} = 0.964$, was found based on a set of interactions, which is completely different compared to the ones we used. This correlation can be combined with the experimental value for the $B(E2)$ transition strength $B(E2, 2_1^+ \rightarrow 0_1^+) = 7.63(19) \text{ e}^2\text{fm}^4$ [DA1+20]. We obtain a quadrupole moment of $Q(2_1^+) = 5.97(30) \text{ efm}^2$. The uncertainties include the average many-body and interaction uncertainties of the N³LO calculations for the quadrupole moment and the experimental uncertainties of the transition strength propagated via

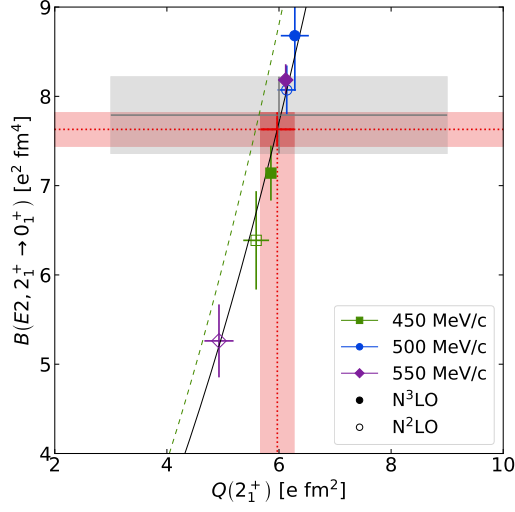


Fig. 8.7.: Correlation of the $B(E2, 2_1^+ \rightarrow 0_1^+)$ transition strength and the electric quadrupole moment $Q(2_1^+)$ for ^{12}C obtained with N^2LO and N^3LO interactions for three different cutoffs. All IM-NCSM calculations are performed using $N_{\text{max}} = N_{\text{max}}^{\text{ref}} = 4$. The error bars indicate combined many-body and interaction uncertainties. The lines show the prediction of a simple rigid rotor (dashed) and a fitted (solid) rotor model (see text). The horizontal and vertical red shaded bands indicate the experimental $B(E2)$ value and the $Q(2_1^+)$ value derived from the intersection with the model correlation. The grey and red areas indicate the experimental limits from literature values [Ver+83; Pri+16] and from [DA1+20].

the correlation. This value is compatible within uncertainties of the $Q(2_1^+)$ results of the IM-NCSM with N^3LO interactions for all cutoffs.

8.2. Ground-State Energies and Charge Radii

In this section we will discuss ground-state energies and charge radii of the oxygen isotopic chain $^{14-26}\text{O}$, the carbon chain $^{10-20}\text{C}$ and the neon chain $^{18-36}\text{Ne}$. We begin with the discussion of ground-state energies of oxygen isotopes followed by the carbon, and neon isotopic chains. Afterwards, we discuss the charge radii of all these isotopes following the same order.

8.2.1. Ground-State Energies

Ground-State Energies of Even and Odd Oxygen Isotopes. The ground-state energies of even oxygen isotopes as function of the chiral interaction order ranging from LO to N^3LO are shown in Fig. 8.8. Each panel shows the results for one isotope. The red bars are the results for $N_{\text{max}}^{\text{ref}} = 0$ and the blue bars depict the results for $N_{\text{max}}^{\text{ref}} = 2$. All ground-state energies are computed using $N_{\text{max}} = 4$. A blue solid line indicates the experimental value for the ground-state energy. Furthermore, the error bars are interaction uncertainties and error bands show combined interaction and many-body uncertainties.

We see that the experimental ground-state energy is well reproduced for all even oxygen isotopes at N^3LO and N^2LO . Furthermore, the interaction uncertainties become smaller with higher interaction order, which is a common trend [Hüt+20]. The interaction uncertainties for ground-state energies at NLO are very large and also LO and NLO do not perform well due to the lack of three-body interactions, which is also the case for other observables. Therefore, we will mainly discuss the results at N^2LO and N^3LO . Compared to the results of [Hag+16; Geb+17; Tic+18a; Tic+18b; Som+20], who used other interactions, all computed ground-state energies for the oxygen isotopes are in good agreement with these calculations. Furthermore, in previous works, where shell-model interactions from the IM-SRG were obtained, slight overbinding [Bog+14; Str+17] was seen, especially for the neutron-rich oxygen isotopes. It is remarkable that the results agree not only for N^3LO but also for N^2LO . We can also reproduce the neutron drip line at ^{24}O . All in all, the results at N^3LO are converged with respect to N_{max} . For ^{26}O , we also obtain converged results, which was not the case in previous calculations [Her+13a] but this is a first description of ^{26}O without taking any continuum effects into account. The ground-state energies of selected odd isotopes of oxygen $^{15-21}\text{O}$ are shown in Fig. 8.9. The plot is arranged the same way as 8.8. The downward triangles indicate calculations using the particle-removal scheme, as explained in section 7.2. Note that we did not compute results using particle attachment, since the particle-removal scheme is more robust in terms of the N_{max} convergence behavior [Vob20]. Also, the ground-state energies for odd oxygen isotopes agree well with the experimental values at N^3LO and

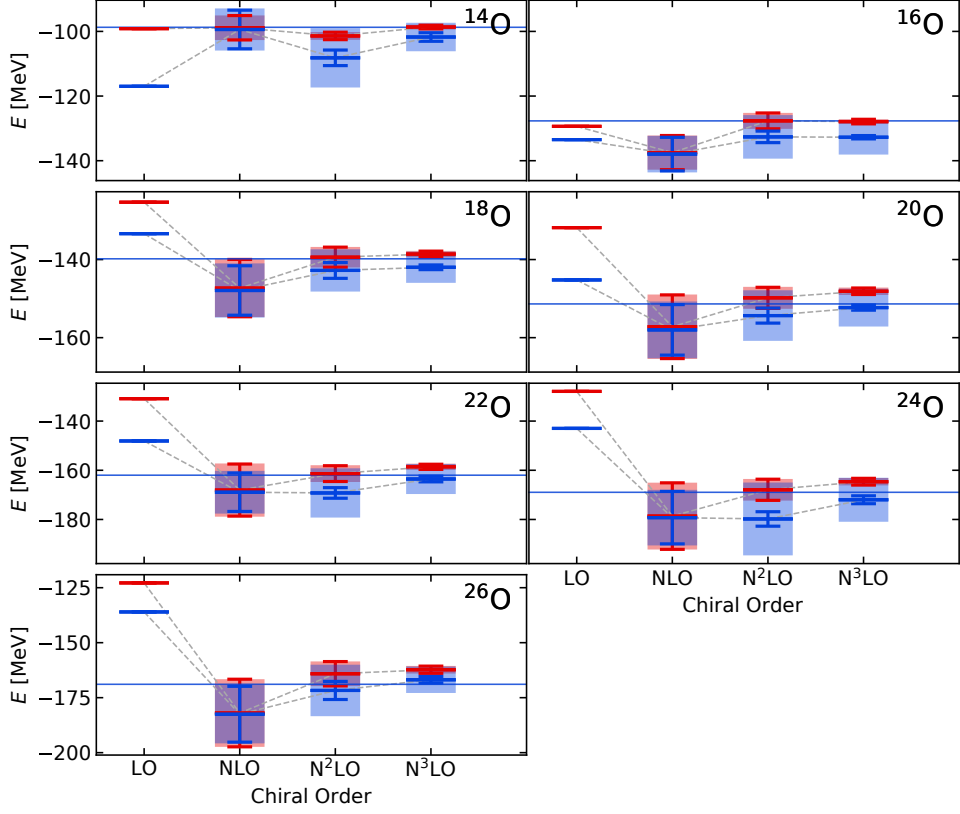


Fig. 8.8.: Ground-state energies for even oxygen isotopes ranging from ^{14}O to ^{26}O as function of the chiral interaction order. Error bars indicate interaction uncertainties and bands are combined many-body and interaction uncertainties. Red symbols are results for $N_{\max}^{\text{ref}} = 0$ and blue symbols are the results for $N_{\max}^{\text{ref}} = 2$. All ground-state energies are computed using $N_{\max} = 4$. Experimental ground-state energies are taken from [Wan+17].

N^2LO for $N_{\max}^{\text{ref}} = 2$. At $N_{\max}^{\text{ref}} = 0$, the binding energies of all odd oxygen isotopes are slightly overestimated, which indicates that $N_{\max}^{\text{ref}} = 2$ is a better choice for the reference space. Furthermore, the ground-state energies are converged with respect to N_{\max} and N_{\max}^{ref} .

Ground-State Energies of Even Carbon Isotopes. The ground-state energies of even carbon isotopes $^{10-20}\text{C}$ are shown in dependence of the chiral order in Fig. 8.10. The plot is built the same way as in Fig. 8.8. For all carbon isotopes, the agreement between our results and the experimental values is excellent at N^2LO and N^3LO . For the ground-state energies of ^{16}C at $N_{\max}^{\text{ref}} = 0$ and ^{20}C at both values of N_{\max}^{ref} , we obtained a large interaction error for the NLO results, which is due to the large underbinding of the ground-state energies at leading-order.

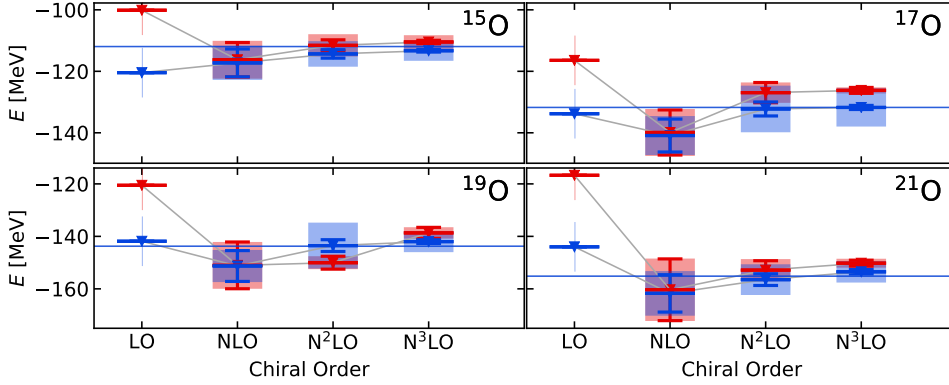


Fig. 8.9.: Ground-state energies for odd oxygen isotopes ranging from ^{15}O to ^{21}O as function of the chiral interaction order. Error bars indicate interaction uncertainties and bands are combined many-body and interaction uncertainties. Red symbols are results for $N_{\max}^{\text{ref}} = 0$ and blue symbols are the results for $N_{\max}^{\text{ref}} = 2$. All ground-state energies are computed using $N_{\max} = 4$. Experimental ground-state energies are taken from [Wan+17].

Ground-State Energies for Even and Odd Neon Isotopes. Now we proceed to the discussion of the neon isotopic chain. The ground-state energies of even neon isotopes $^{18-36}\text{Ne}$ are shown as function of the chiral interaction order in Fig. 8.11 following the same terminology as in Fig. 8.10. Note that for ^{34}Ne and ^{36}Ne , the ground-state energies are only shown at $N_{\max}^{\text{ref}} = 0$ due to the fact that the number of basis states for $N_{\max}^{\text{ref}} = 2$ is very large. Furthermore, we used the importance truncation for the computation of the reference state for $N_{\max}^{\text{ref}} = 2$ and in the NCSM post-diagonalization for $^{20-36}\text{Ne}$ at $N_{\max} = 4$. For all even neon isotopes, our results are converged with respect to N_{\max}^{ref} and N_{\max} . The many-body uncertainties are smaller than the interaction errors. Furthermore, the agreement between theoretical and experimental ground-state energies for all even neon isotopes at N^3LO and N^2LO is excellent and for ^{36}Ne we are able to predict a ground-state energy. Compared to other studies like [Jan+16], who computed ground-state energies of neon isotopes using a coupled-cluster effective interaction, our results agree with their calculations with $< 1\%$ deviation for $^{18-28}\text{Ne}$. We are able to obtain good results for the neutron-rich neon isotopes around the island-of-inversion, which were often underbound [Jan+16; Nov+20; Miy+20].

The ground-state energies of $^{19-25}\text{Ne}$ are shown as function of the chiral interaction order in Fig. 8.12. The plot is organized the same way as in Fig. 8.9. Also for the odd isotopes our results agree well with experiment. Furthermore, the results at N^2LO and N^3LO are converged with respect to the chiral interaction order.

Another study of the neon isotopic chain was performed by the group of Thomas Duguet at CEA Saclay, who developed the PGCM-PT method, a combination of the projected generator coordinate method (PGCM) with perturbation theory [Fro+22b; Fro+22a;

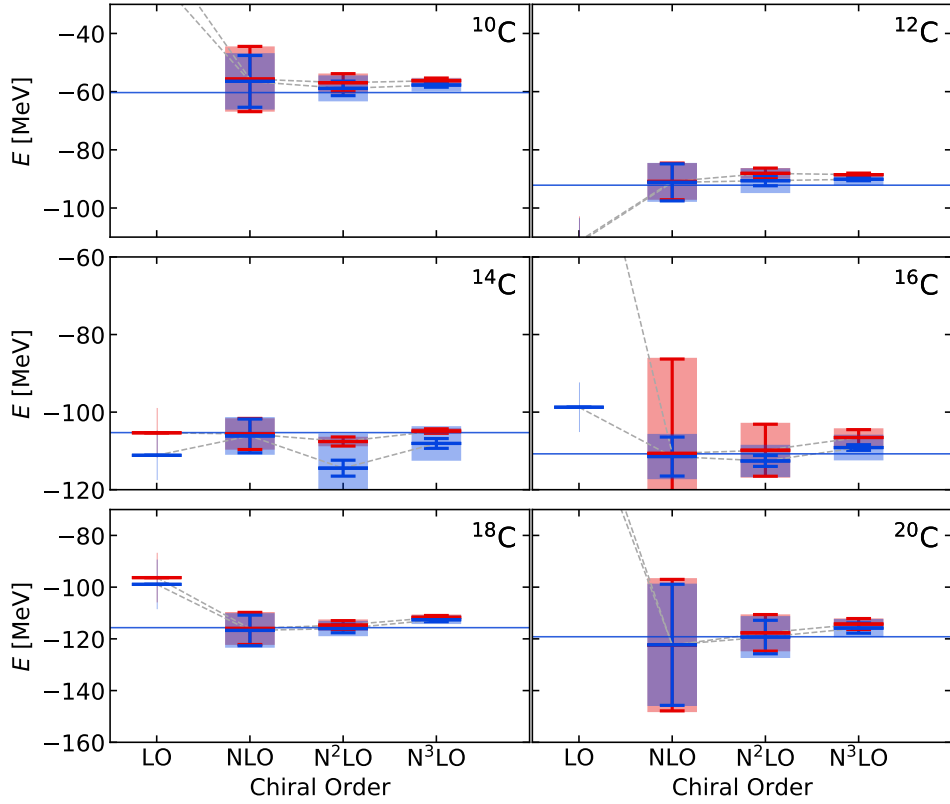


Fig. 8.10.: Ground-state energies for even carbon isotopes ranging from ^{10}C to ^{20}C as function of the chiral interaction order. Error bars indicate interaction uncertainties and bands are combined many-body and interaction uncertainties. Red symbols are results for $N_{\text{max}}^{\text{ref}} = 0$ and blue symbols are the results for $N_{\text{max}}^{\text{ref}} = 2$. All ground-state energies are computed using $N_{\text{max}} = 4$. Experimental ground-state energies are taken from [Wan+17].

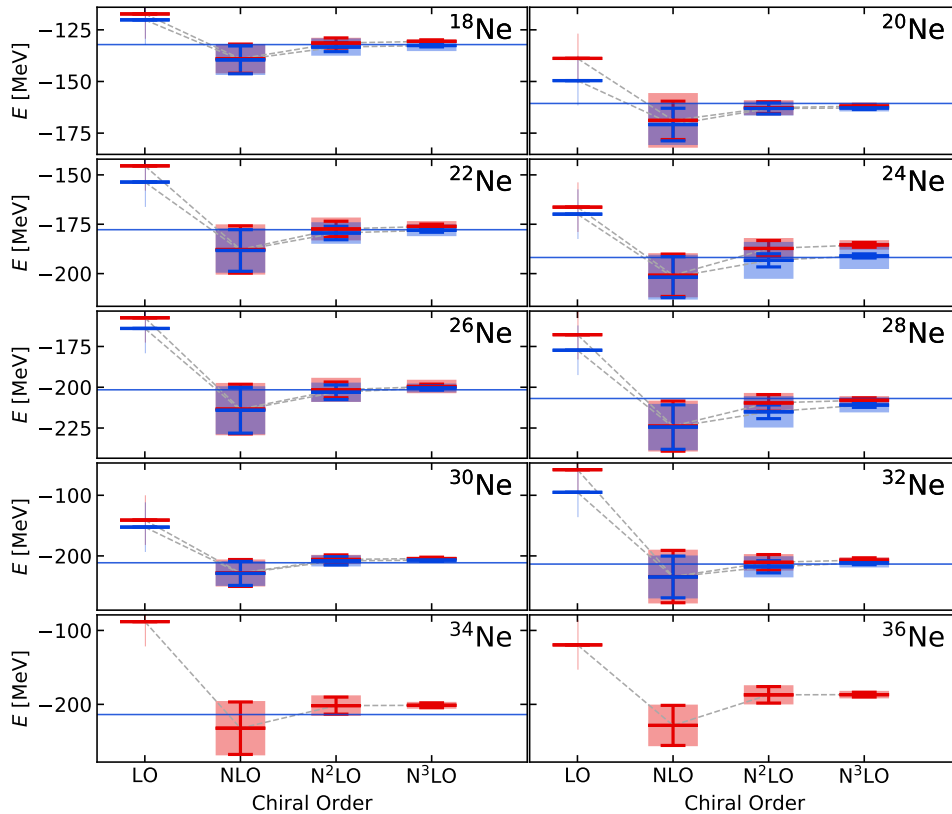


Fig. 8.11.: Ground-state energies for even neon isotopes ranging from ^{18}Ne to ^{36}Ne as function of the chiral interaction order. Error bars indicate interaction uncertainties and bands are combined many-body and interaction uncertainties. Red symbols are results for $N_{\max}^{\text{ref}} = 0$ and blue symbols are the results for $N_{\max}^{\text{ref}} = 2$. All ground-state energies are computed using $N_{\max} = 4$. Experimental ground-state energies are taken from [Wan+17].

Fro+22c]. In [Fro+22a], our IM-NCSM results are used as benchmark for the PGCM framework, which is based on the solution of constrained Hartree-Fock-Bogoliubov equations using the same family of chiral interactions. The PGCM-PT is suited to capture strong static correlation effects arising from the deformation of nuclei. In this work, results from the PGCM are compared to IM-NCSM calculations for ground-state energies, charge radii, low-lying excited states, and electromagnetic observables for even neon isotopes ranging from ^{18}Ne to ^{30}Ne . The PGCM underbinds the ground-state energy for all isotopes due to missing dynamical correlations. This behavior is improved using corrections from perturbation theory in [Fro+22c]. Since our results agree with experimental, the IM-NCSM can be used as a standard tool for benchmarking many-body methods.

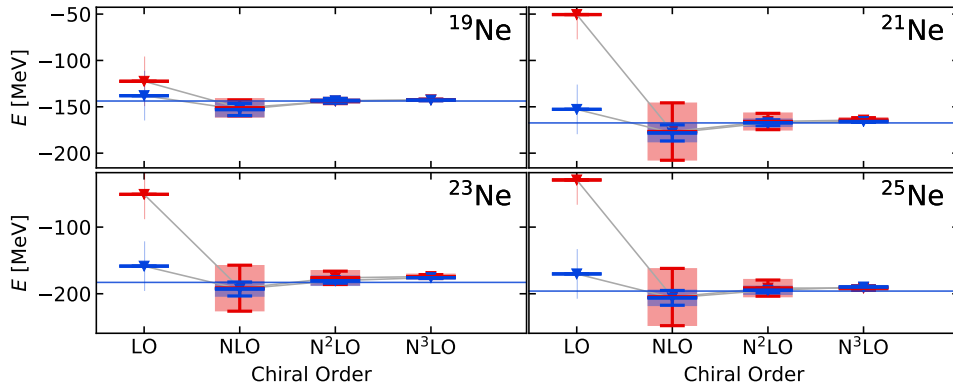


Fig. 8.12.: Ground-state energies for odd neon isotopes ranging from ^{19}Ne to ^{25}Ne as function of the chiral interaction order. Error bars indicate interaction uncertainties and bands are combined many-body and interaction uncertainties. Red symbols are results for $N_{\text{max}}^{\text{ref}} = 0$ and blue symbols are the results for $N_{\text{max}}^{\text{ref}} = 2$. All ground-state energies are computed using $N_{\text{max}} = 4$. Experimental ground-state energies are taken from [Wan+17].

8.2.2. Charge Radii

Charge Radii of Even and Odd Oxygen isotopes. Now we present charge radii for even oxygen isotopes shown in Fig. 8.13. The charge radii are shown as function of the chiral interaction and the plot is arranged as in Fig. 8.11, where the shaded grey bands around the experimental charge radii depict the experimental uncertainties.

For ^{16}O and ^{18}O , the experimental charge radii are well reproduced at N^2LO within the uncertainties. At N^3LO the charge radii are underestimated by 2-3%. In case of the other isotopes, there is no experimental charge radius available but we are able to give a theoretical prediction. Furthermore, all results are well converged regarding the reference space and we notice an enhancement of the charge radius for all oxygen isotopes when comparing the results at NLO to the results at N^2LO . This could be due to missing inclusion of 3N forces in the NLO results.

For even oxygen isotopes, the new family of chiral interactions performs well, especially in comparison to former NN interactions at N^3LO by Entem and Machleidt [EM03] supplemented with 3N interactions at N^2LO using a local regulator scheme [Nav07; GQN09; GQN19]. With these interactions, ground-state energies are in good agreement with experimental data, but the charge radii of the oxygen isotopes were underestimated [Bin+14; Lap+16; Vob20]. Another interaction used to compute radii is the so-called NNLO_{sat} [Eks+15], which includes fitted low-energy constants with respect to experimental energies and charge radii of carbon and oxygen isotopes [Lap+16]. This interaction is also able to reproduce experimental radii and ground-state energies of some oxygen and carbon isotopes [Som+20]. Since the NNLO_{sat} interaction is determined for one chiral order only, it cannot be used to compute interaction uncertainties.

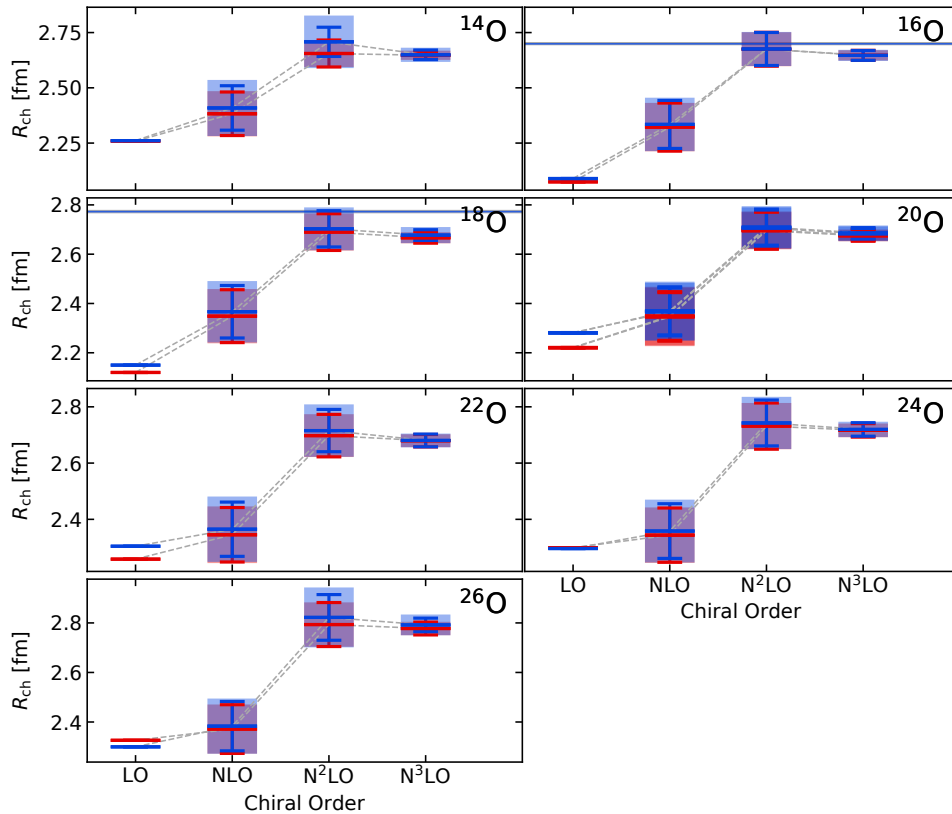


Fig. 8.13.: Charge radii for even oxygen isotopes ranging from ^{14}O to ^{26}O as function of the chiral interaction order. Error bars indicate interaction uncertainties and bands are combined many-body and interaction uncertainties. Experimental values are taken from [AM13].

Now, with the new family of interactions with optimized low-energy constants c_D , which are fitted to the ground-state energy of ^{16}O and fixed values of c_E , which are fitted to the triton ground-state energy [Hüt+20; Hüt21], we are able to reproduce experimental ground-state energies and charge radii.

The charge radii for odd oxygen isotopes ranging from ^{15}O to ^{21}O are shown in dependence of the chiral interaction order in Fig. 8.14. The panels of the plot are built up like in 8.12. For ^{17}O , we are able to reproduce the experimental charge radius and for ^{15}O , ^{19}O and ^{21}O , we obtained a prediction due to missing experimental values. Furthermore, we obtained converged results with respect to N_{\max}^{ref} and N_{\max} for all odd oxygen isotopes at N^2LO and N^3LO .

Charge Radii of Even Carbon Isotopes. The charge radii for even carbon isotopes $^{10-20}\text{C}$ are shown in Fig. 8.15. The charge radii are again shown as function of the chiral interaction order. Experimental results are available for ^{12}C and ^{14}C . The experimental charge radius of ^{12}C is overestimated by 4% and the experimental charge radius of ^{14}C is

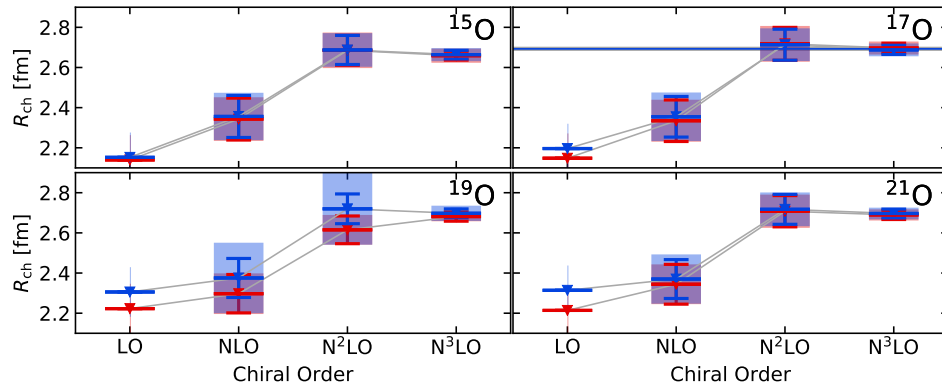


Fig. 8.14.: Charge radii for odd oxygen isotopes ranging from ^{15}O to ^{21}O as function of the chiral interaction order. Error bars indicate interaction uncertainties and bands are combined many-body and interaction uncertainties. Experimental values are taken from [AM13].

underestimated by 1% when taking combined many-body and interaction uncertainties into account. For the other carbon isotopes ^{10}C and $^{16-20}\text{C}$ we can predict a value for the charge radius.

Charge Radii of Even and Odd Neon Isotopes The charge radii in dependence of the chiral interaction order for even neon isotopes are shown in Fig. 8.16. Compared to the experiment, we obtained good results for $^{24-28}\text{Ne}$. For the lighter isotopes $^{18-22}\text{Ne}$, the charge radii are underestimated by 2% for ^{18}Ne and ^{20}Ne and $<1\%$ for ^{22}Ne . For $^{30-36}\text{Ne}$ we predict charge radii, where the value of the charge radius grows with the number of neutrons. In conclusion, we are able to compute open-shell nuclei, which show a deformation and clustering behavior.

The $\Delta\text{NNLO}_{\text{GO}}$ interaction [Jia+20], which includes Δ degrees of freedom is another interaction providing good results compared to the experiment. Our results are in good agreement with [Jia+20] when considering the uncertainties. This interaction also yield accurate ground-state energies and radii for medium-mass nuclei. When comparing our results for the neon isotopic chain to PGCM calculations [Fro+22a], it was found that charge radii obtained by the PGCM are overestimated by about 0.1 fm due to missing dynamical correlations as it was the case for ground-state energies.

Figure 8.17 depicts the charge radii as function of the chiral interaction order for $^{19-25}\text{Ne}$ following the style of Fig. 8.14. For these isotopes, we are able to reproduce all experimental results for N^2LO and N^3LO , where the convergence behavior with respect to N_{max} and $N_{\text{max}}^{\text{ref}}$ is very good.

All in all, we conclude that we are able overcome the problems of underestimated experimental charge radii with the new family of chiral interactions [Hüt+20].

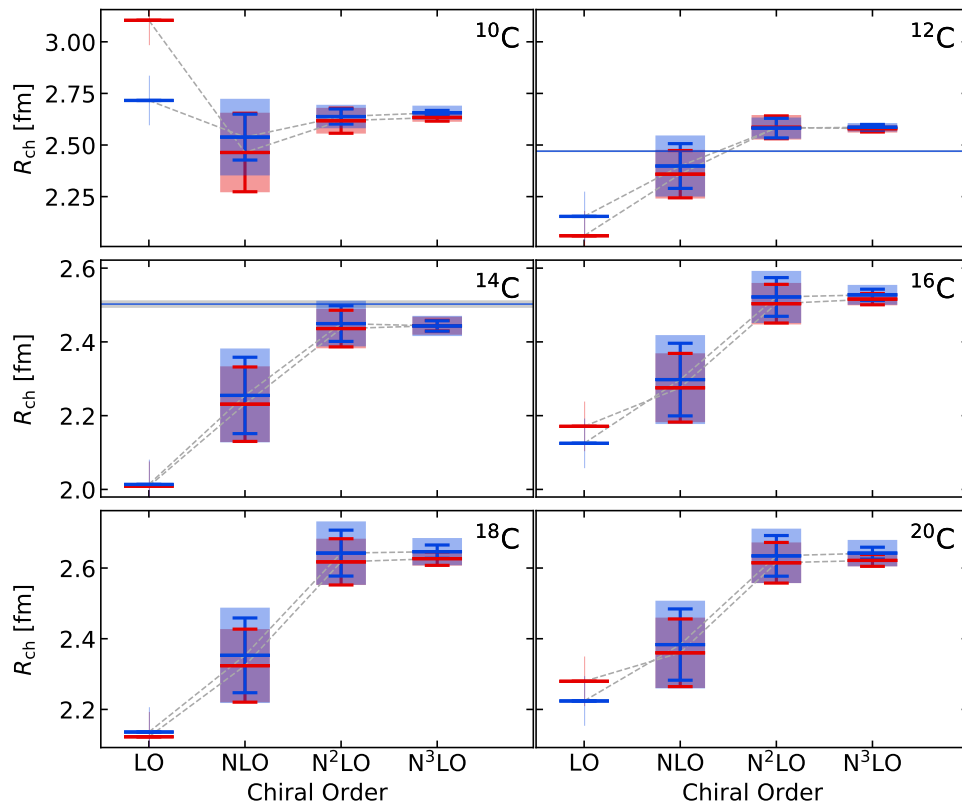


Fig. 8.15.: Charge radii for even carbon isotopes ranging from ^{10}C to ^{20}C as function of the chiral interaction order. Error bars indicate interaction uncertainties and bands are combined many-body and interaction uncertainties. Experimental values are taken from [AM13].

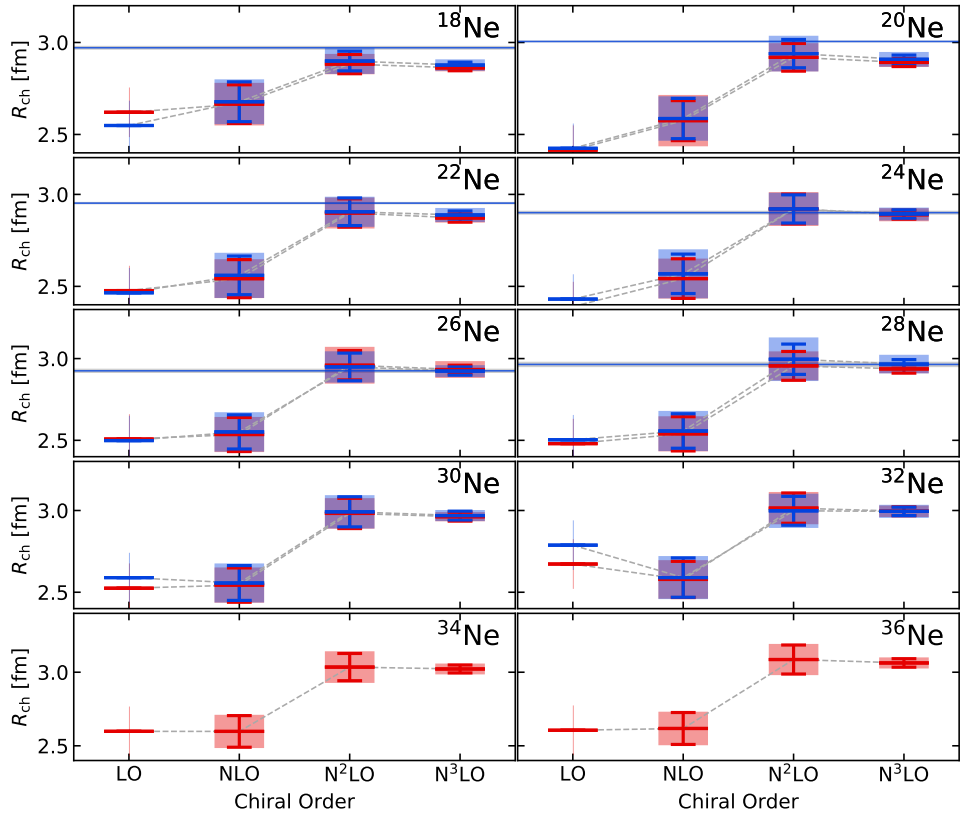


Fig. 8.16.: Charge radii for even neon isotopes ranging from ^{18}Ne to ^{36}Ne as function of the chiral interaction order. Error bars indicate interaction uncertainties and bands are combined many-body and interaction uncertainties. Experimental values are taken from [AM13].

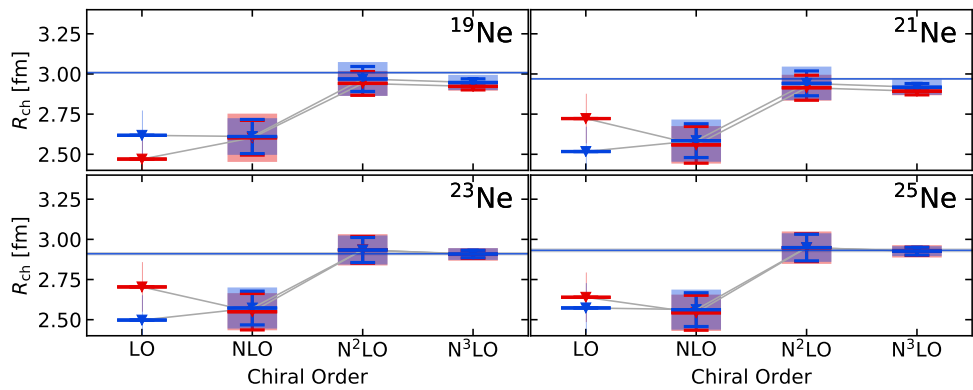


Fig. 8.17.: Charge radii for odd neon isotopes ranging from ^{19}Ne to ^{25}Ne as function of the chiral interaction order. Error bars indicate interaction uncertainties and bands are combined many-body and interaction uncertainties. Experimental values are taken from [AM13].

8.3. Excitation Spectra

In this section we discuss spectra for the oxygen, carbon, and neon isotopic chains. We begin with the spectra of even and odd oxygen isotopes, followed by spectra of even carbon isotopes. Finally, we show the spectra for even and odd neon isotopes.

Spectra of Even and Odd Oxygen Isotopes. In Fig. 8.18, the spectra for even oxygen isotopes $^{14-26}\text{O}$ as function of the chiral interaction order ranging from NLO to N³LO are shown. Note that the estimation of the interaction uncertainties has been computed including LO results. The interaction uncertainties for NLO are not shown for sake of clarity. We only show the results for $N_{\text{max}}^{\text{ref}} = 2$. The bars on the right side of each panel depict the experimental spectra. Each color encodes a value for J to differentiate between the states. Similar to the last section, error bars represent interaction uncertainties and shaded error bands are combined many-body and interaction uncertainties.

For all even oxygen isotopes, the states are in correct order compared to the experiment besides the 0_2^+ states. Furthermore, the most low-lying excited states in the spectra are converged with respect to N_{max} . We observe that the 0_2^+ states of all oxygen isotopes have large many-body uncertainties indicating a poor convergence behavior. Therefore, we cannot compare them to experimental values. We will come back to this point later in this section. We also see that the many-body and the interaction uncertainties of the 1_1^+ states are quite large, especially for results at N²LO. We can conclude that these states are sensitive to the chiral interaction order. For ^{14}O and ^{22}O , the 2_1^+ state agrees well with experiment. Also, the 3_1^+ state of ^{22}O shows a good agreement within uncertainties. Regarding ^{18}O and ^{20}O , the first two excited states underestimate the measured excitation energy, while the 2_2^+ state is again in a good agreement. For the doubly magic ^{24}O the 2_1^+ state is too low compared to experimental results and the spectrum is too dense. For the unbound ^{26}O nucleus however, we obtain an excellent agreement for the first excited state. For ^{16}O we have found that the energy of the 2_1^+ state is much too large compared to experimental results. This seems to be a common behavior for well bound doubly-magic nuclei, which was also obtained in [Miy+20], [HJP16] and [Sim+17]. Especially in [HJP16], it was demonstrated that adding triples to coupled cluster calculations lowers the energy of the first excited state. This indicates that a highly correlated reference state is needed to describe the 2_1^+ state of ^{16}O , which cannot be accessed using the IM-NCSM.

Coming to the odd oxygen isotopes $^{15-21}\text{O}$, their spectra are shown in Fig. 8.19 as function of the chiral interaction order. Overall, many states for $^{17-21}\text{O}$ are in agreement with experimental excited-state energies within uncertainties. For ^{21}O , the $3/2_1^+$ state was experimental unknown, which has been examined in [Hei+20], who studied the

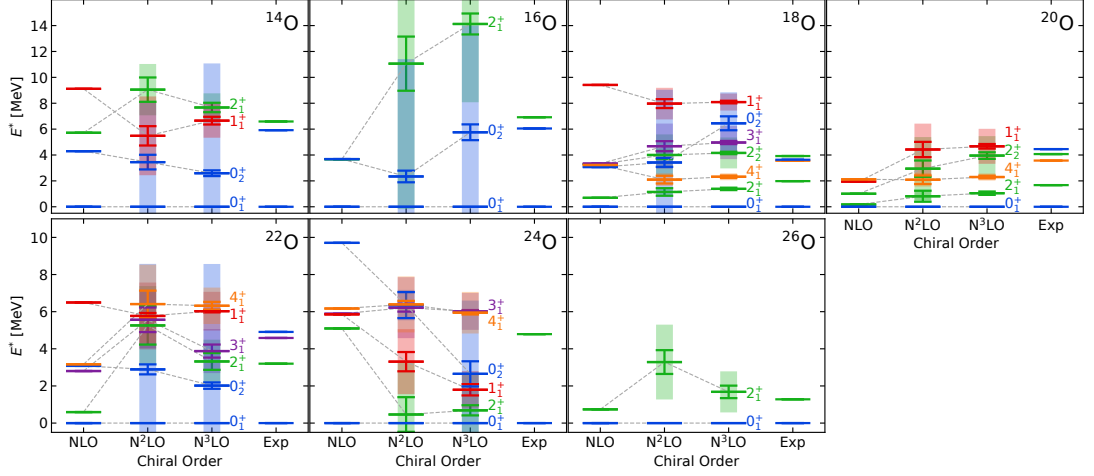


Fig. 8.18.: Spectra for even oxygen isotopes ranging from ^{14}O to ^{26}O as function of the chiral interaction order. Error bars indicate interaction uncertainties and bands are combined many-body and interaction uncertainties. Experimental results are taken from [Ajz91; TWC93; Til+95; Til+98; Bas15; Tsh+12; Kon+16]

low-lying structure of ^{21}O using lifetime measurements. Compared to the results of [Bog+14], we now obtained the right order of the first two excited states in ^{21}O , but the order of the third and fourth excited states is still reversed. For ^{19}O , we also obtained that the order of the third and fourth excited states is changed as it was observed with NCSM-PT calculations in [Tic+18a]. But since the many-body uncertainty of the $1/2_1^+$ state is large, it could lower in energy with increasing N_{max} . In the spectrum of ^{15}O , the experimental energy of the $3/2_1^-$ state is overestimated by about 0.7% within uncertainties.

Spectra of Even Carbon Isotopes Figure 8.20 shows spectra of even carbon isotopes $^{10-20}\text{C}$ as function of the chiral interaction order. The overall agreement between our results and experiment is good for ^{10}C , ^{12}C , ^{14}C and ^{20}C , where most states lay within the error bars. Again, the 0_2^+ states show a poor convergence behavior with respect to N_{max} . For the 1_1^+ and the 4_1^+ state of ^{12}C , we obtained larger error bars, which is also the case for the 2_1^+ state of ^{14}C and the 3_1^+ state of ^{16}C . The convergence behavior for these states is slower. This could indicate that these states lay in the part of the model space, which is not decoupled completely during the IM-SRG evolution. For $^{12-16}\text{C}$, the interaction uncertainties of the 1_1^+ state are quite large. Furthermore, we obtained that the many-body uncertainties of the 2^+ excited states of ^{18}C are large, which is due to a slower convergence with respect to N_{max} . In ^{10}C , the experimental state with unknown parity and J could be a 1_1^+ but we need more information from the experimental side for confirmation.

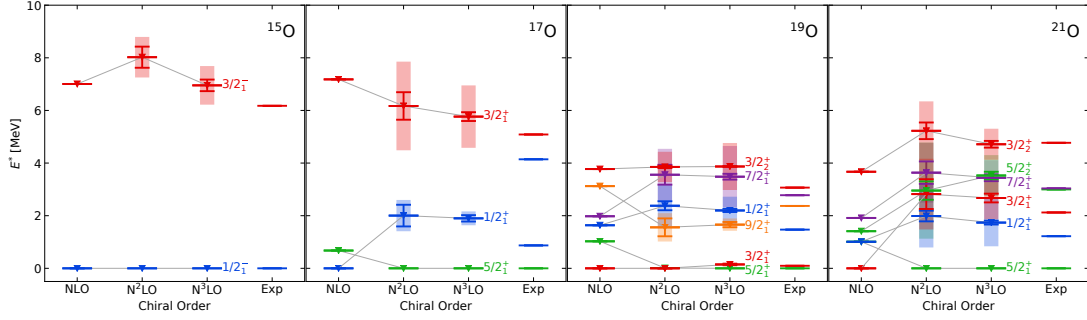


Fig. 8.19.: Spectra for odd oxygen isotopes ranging from ^{15}O to ^{21}O as function of the chiral interaction order. Error bars indicate interaction uncertainties and bands are combined many-body and interaction uncertainties. Experimental results are taken from [Ajz91; TWC93; Til+95; Fir15].

Spectra of Even and Odd Neon Isotopes The spectra of even neon isotopes $^{18-36}\text{Ne}$ are plotted in Fig. 8.21 as function of the chiral interaction order. Overall, the results are in good agreement with experiment but not for all states. As presented in [Str+16], we also find that the unidentified excited state in ^{26}Ne is a 4^+ state. Also, the ordering of the states is in agreement with experimental results. In comparison to studies by Miyagi et al. [Miy+20], who overestimate the energies of the 2_1^+ states in all neon isotopes using the IM-SRG framework with valence-space Hamiltonians, we can say that the NO2B approximation is able to reproduce these energies when using the IM-NCSM. This is due to inclusion of static correlations in the reference states and therefore due to the lack of correlations in the IM-SRG framework. Furthermore, our results are in agreement with coupled cluster studies by Jansen et al. [Jan+16]. In comparison to PGCM studies [Fro+22a], the trend of the 2_1^+ and 4_1^+ energies is reproduced by the PGCM for $^{18-24}\text{Ne}$ but the decrease in energy beyond ^{26}Ne cannot be captured. This situation is improved when adding triaxial configurations to the PGCM.

The spectra of odd neon isotopes $^{19-25}\text{Ne}$ are shown in Fig. 8.22 as function of the chiral interaction order. The overall agreement between experiment and theory is good for the most low-lying excited states when taking the uncertainties into account. In ^{19}Ne , for example, the $3/2_1^+$ excitation energy is underestimated and the spectrum of ^{25}Ne is too compressed. Furthermore, the order of the states is exchanged. But since their error bars are overlapping, the order could change again by using a larger model space. Also, in ^{21}Ne the $5/2_1^+$ state is too low at N^3LO compared to experiment.

Many-Body Convergence Behavior of Selected Oxygen, Carbon and Neon Isotopes.

Now we deal with the convergence behavior of spectra from selected oxygen, carbon and neon isotopes in order to explain large many-body uncertainties. The spectra for $^{14-18}\text{O}$ and $^{22-26}\text{O}$ are shown as function of N_{max} in Fig. 8.23. The left-hand panels show the

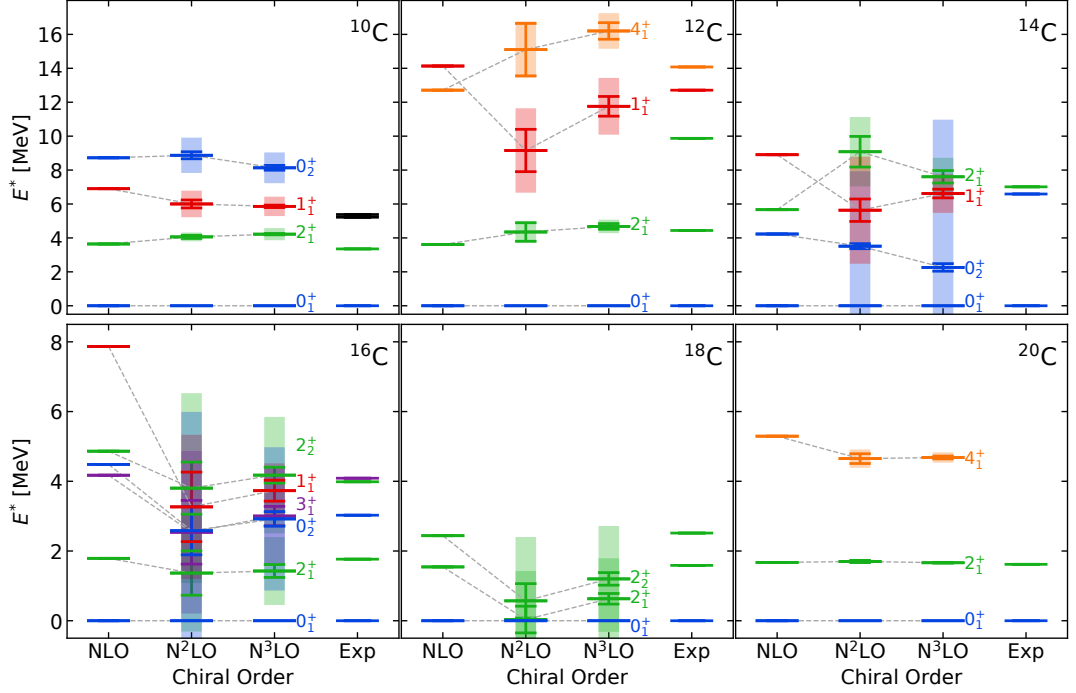


Fig. 8.20.: Spectra for even carbon isotopes ranging from ^{10}C to ^{20}C as function of the chiral interaction order. Error bars indicate interaction uncertainties and bands are combined many-body and interaction uncertainties. Experimental results are taken from [Til+04; KPS17; Ajz91; TWC93; Pet+11]

spectra for $N_{\text{max}}^{\text{ref}} = 0$ and the spectra with $N_{\text{max}}^{\text{ref}} = 2$ are shown on the right-hand side. In each row, one isotope is shown. The experimental excitation energies are shown in the right panels. For the oxygen isotopes, especially the 0_2^+ and 1_1^+ states are hard to converge. This could be due to the fact that these states are not completely decoupled during the IM-SRG evolution. Especially in the spectra of $^{14-18}\text{O}$, the 0_2^+ state is not converged for $N_{\text{max}}^{\text{ref}} = 2$. For ^{14}O and ^{18}O the 2_1^+ states are converged with respect to N_{max} , which is also the case for the 4_1^+ state of ^{18}O . Furthermore, the 2_1^+ state of ^{16}O is not converged and far above the experimental value, which is due to the doubly magic character of ^{16}O . The semi-magic character of ^{22}O and magic character of ^{24}O could contribute to a slower convergence behavior of some excited states in their spectra. Especially the 0_2^+ states are problematic to converge. For $N_{\text{max}}^{\text{ref}} = 0$, all excited states of ^{22}O and ^{24}O show a slow convergence behavior.

We proceed to the spectra of $^{14-18}\text{C}$, which are shown in Fig. 8.24. The structure of the plot is the same as before. It is noticeable that the 0_2^+ states in the spectra of ^{14}C and ^{16}C are not converged with respect to $N_{\text{max}}^{\text{ref}}$. Furthermore, the many-body uncertainties of the excitation energies in ^{16}C are larger compared to the ones in ^{14}C . This could be due to a more complicated structure of the states in ^{16}C in general. The first two excited

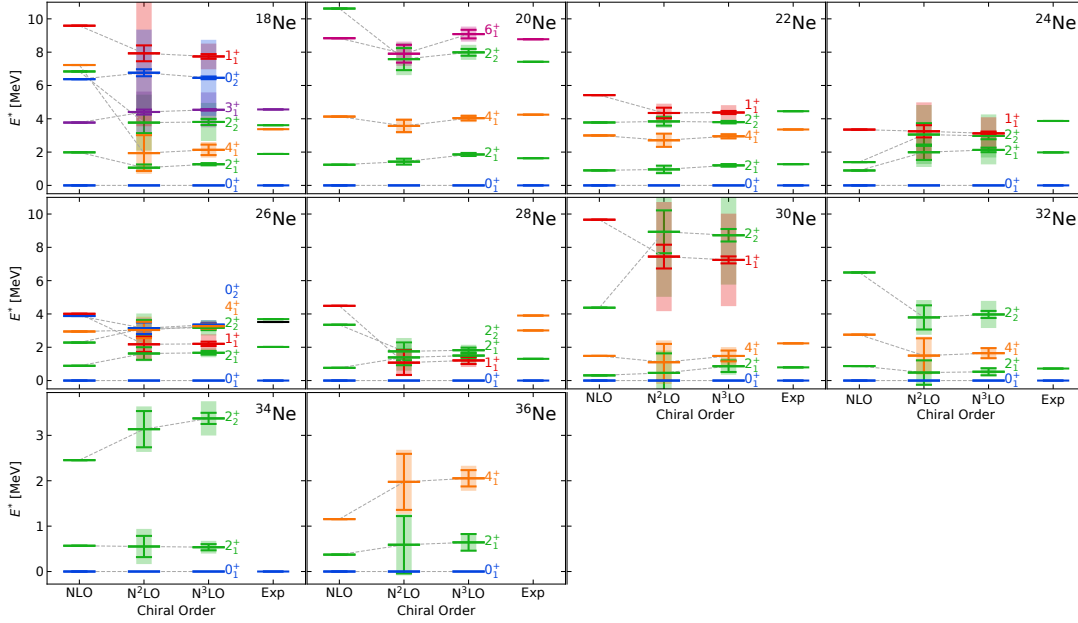


Fig. 8.21.: Spectra for even neon isotopes ranging from ^{18}Ne to ^{36}Ne as function of the chiral interaction order. Error bars indicate interaction uncertainties and bands are combined many-body and interaction uncertainties. Experimental values are taken from [Til+95; Til+98; Bas15; Fir07; BH16; Sha13; Sha10; OS11]

states of ^{18}C are also not converged properly and the agreement with the experiment gets worse when moving from $N_{\text{max}}^{\text{ref}} = 0$ to $N_{\text{max}}^{\text{ref}} = 2$. This indicates that a larger reference space is necessary to describe the spectrum for ^{18}C properly in comparison to experimental results.

A selection of odd isotopes as function of N_{max} is shown in Fig. 8.24 . We see that the $1/2_1^+$ state of ^{19}O is not converged. It could, as mentioned before, move below the $9/2_1^+$ state when using larger values of N_{max} . The $9/2_1^+$ state could then move further towards the experimental value. For ^{21}Ne and ^{25}Ne , we see that most states are converged but the $1/2_1^+$ state of ^{21}Ne moves away from the experiment, which is also the case for the $5/2_1^+$ state of ^{25}Ne .

We conclude that not all states in the spectra of isotopes from the oxygen, carbon and neon isotopic chains are converged with respect to N_{max} . Therefore, especially for the description of the excitation energy of the 1_1^+ states and higher-lying states, a larger reference space is needed.

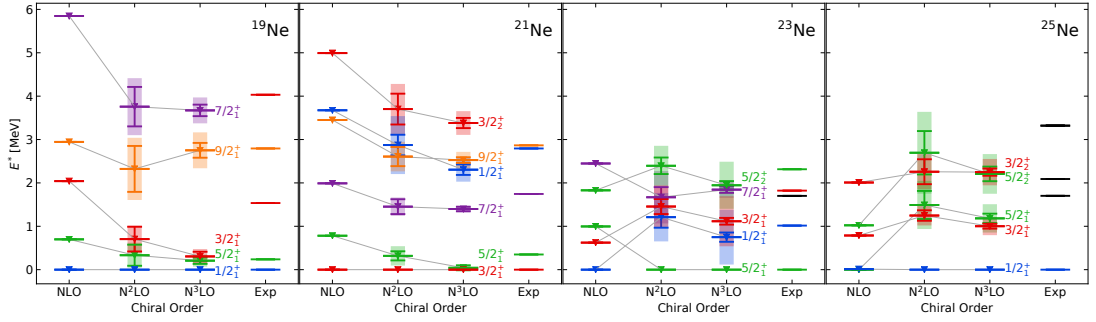
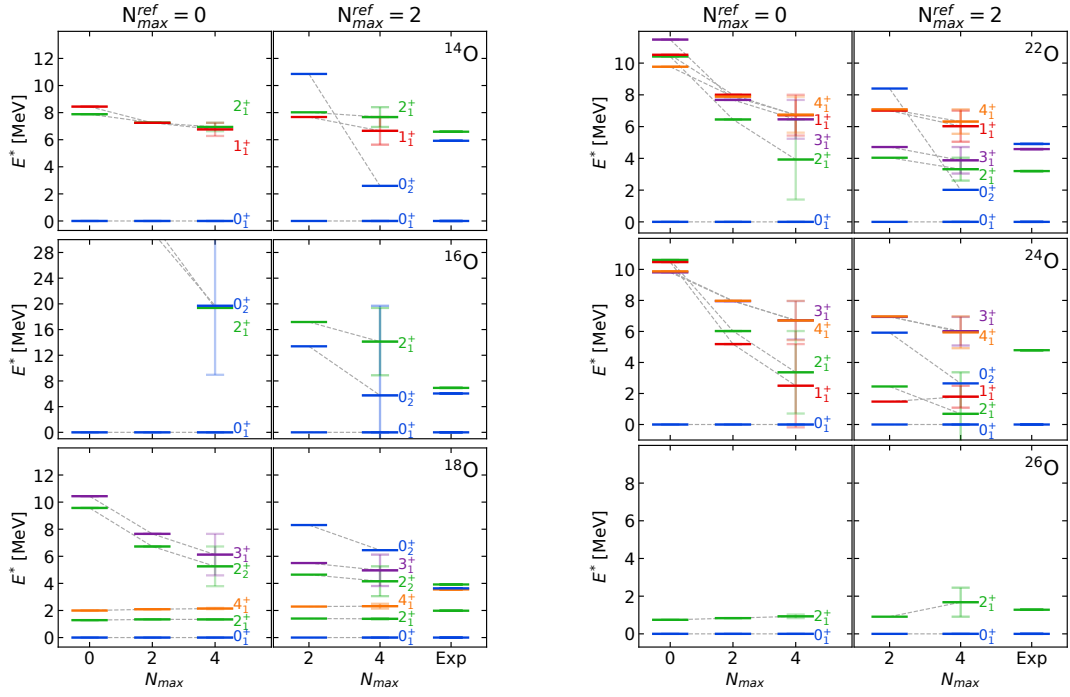


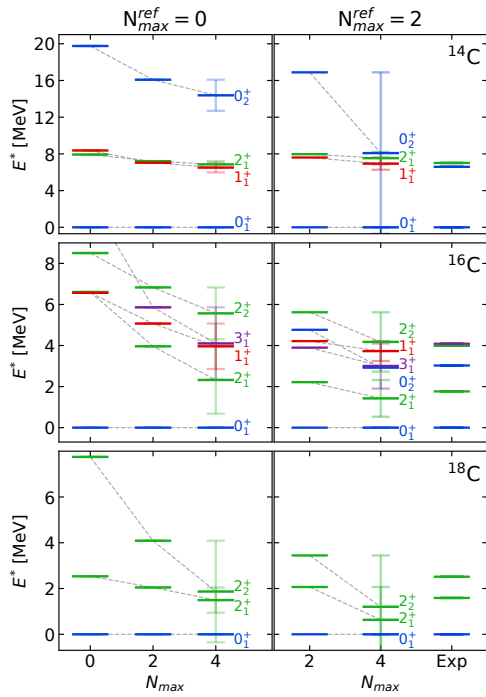
Fig. 8.22.: Spectra for odd neon isotopes ranging from ^{19}Ne to ^{25}Ne as function of the chiral interaction order. Error bars indicate interaction uncertainties and bands are combined many-body and interaction uncertainties. Experimental values are taken from [Til+95; Fir15; SC21; Fir09]



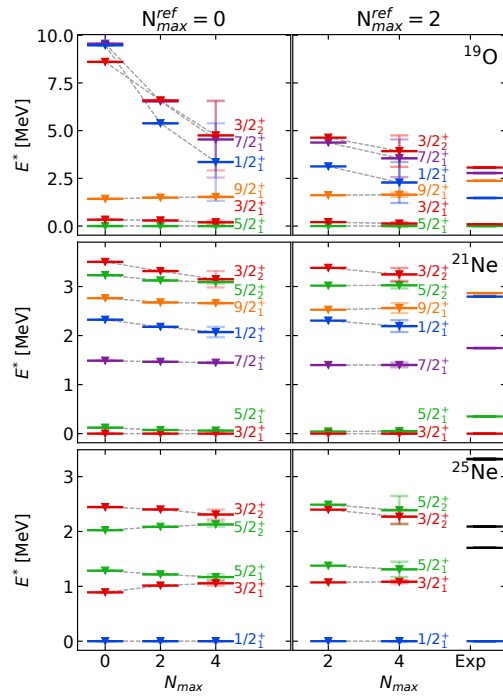
(a) Excited states of $^{14-18}\text{O}$ as function of N_{max} for different values of $N_{\text{max}}^{\text{ref}}$.

(b) Excited states of $^{22-26}\text{O}$ as function of N_{max} for different values of $N_{\text{max}}^{\text{ref}}$.

Fig. 8.23.: N_{max} convergence of selected even isotopes from the oxygen isotopic chain. Error bars are either the absolute difference of the largest values of N_{max} or $N_{\text{max}}^{\text{ref}}$.



(a) Excited states of $^{14-18}\text{C}$ as function of N_{max} for different values of $N_{\text{max}}^{\text{ref}}$.



(b) Excited states of ^{19}O , ^{21}Ne and ^{25}Ne as function of N_{max} for different values of $N_{\text{max}}^{\text{ref}}$.

Fig. 8.24.: N_{max} convergence of selected even and odd isotopes from the oxygen, carbon, and neon isotopic chain. Error bars are either the absolute difference of the largest values of N_{max} or $N_{\text{max}}^{\text{ref}}$.

8.4. Electromagnetic Observables

In this section we will discuss electromagnetic observables from the IM-NCSM. We will start with electric $B(E2)$ transition strengths and quadrupole moments Q for oxygen, carbon, and neon isotopes, followed by magnetic $B(M1)$ transition strengths and dipole moments μ of oxygen and neon isotopes.

8.4.1. Electric Quadrupole Observables

Oxygen Isotopes. The $B(E2, 2_1^+ \rightarrow 0_1^+)$ transition strengths of even oxygen isotopes are shown in Fig. 8.25 as function of the chiral interaction order ranging from LO to N³LO. Each panel contains the results for one isotope. Red bars indicate the results for $N_{\max}^{\text{ref}} = 0$ and blue bars show the results for $N_{\max}^{\text{ref}} = 2$. The solid line represents the experimental value of the $B(E2)$ transition strength with grey shaded uncertainties. Error bars indicate interaction uncertainties and combined interaction and many-body uncertainties are shown as shaded bands.

For all even oxygen isotopes, the many-body and interaction uncertainties are small indicating good convergence. It is noticeable that for ^{16–22}O, all $B(E2)$ transition strengths are systematically underestimated compared to the experiment, which matches the findings in [Vob20]. We will discuss this behavior later in this work. It is also noticeable that all the transition strengths are close to zero.

The electric quadrupole moments of the first excited states $Q(2_1^+)$ of even oxygen isotopes are shown in Fig. 8.26 as function of the chiral interaction order. The only experimental value, which is available is the electric quadrupole moment of ¹⁸O, which is overestimated in our calculations by a factor of 10. We further notice that with increasing N_{\max}^{ref} , the results at N²LO and N³LO come closer to the experimental value, which could be an indicator that using a reference state within a larger reference space might bring the electric quadrupole moment closer to the experiment. For the other even oxygen isotopes we can predict values for the electric quadrupole moment. Furthermore, the many-body uncertainties for the quadrupole moments of ²⁶O are quite large at $N_{\max}^{\text{ref}} = 2$, which could be harder to converge due to its unbound character.

The $B(E2)$ transition strengths of the odd oxygen isotopes are depicted in Fig. 8.27. Again we obtain converged results for all odd oxygen isotopes. For ¹⁹O and ²¹O, our results are close to the experimental $B(E2)$ value within combined uncertainties. For ¹⁷O, the discrepancy is larger. We predict a value for the $B(E2)$ transition strength for ¹⁵O, since no experimental results are available.

Figure 8.28 shows the electric quadrupole moments of odd oxygen isotopes obtained by the particle-removal scheme. For ¹⁷O and ¹⁹O, our results differ by about 50% from the experimental value. For ¹⁵O and ²¹O, we predict a value for the electric quadrupole

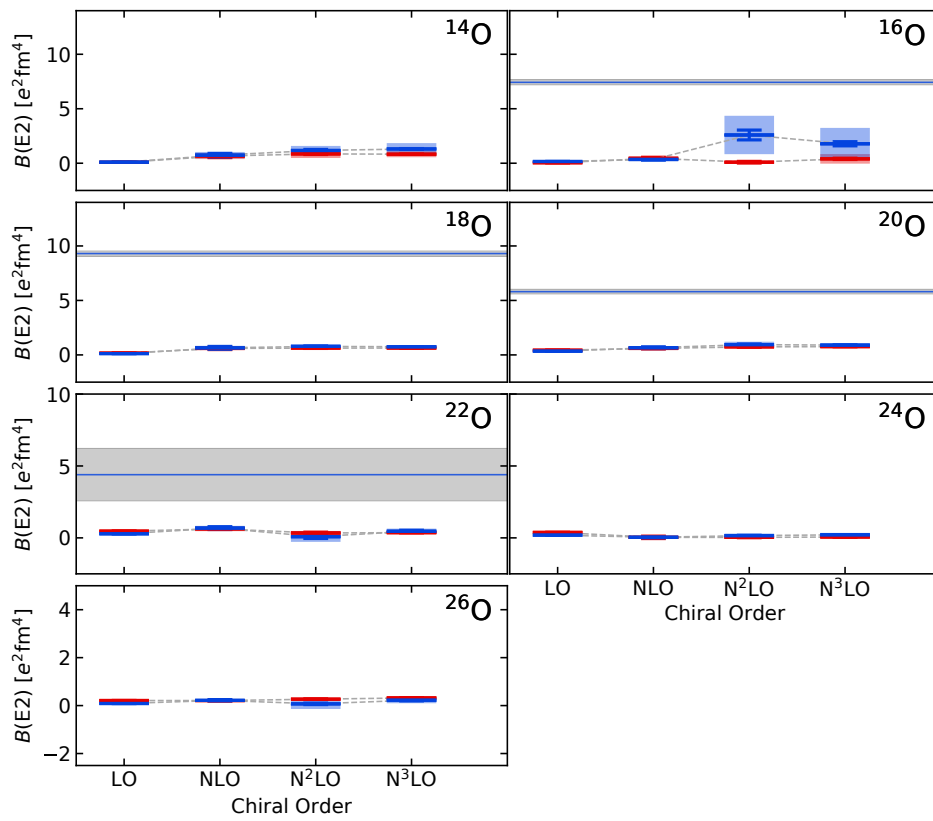


Fig. 8.25.: $B(E2)$ transition strengths for even oxygen isotopes ranging from ^{14}O to ^{26}O as function of the chiral interaction order. Error bars indicate interaction uncertainties and bands are combined many-body and interaction uncertainties. Experimental values are taken from [TWC93; Til+95; Ram+87; Thi+00].

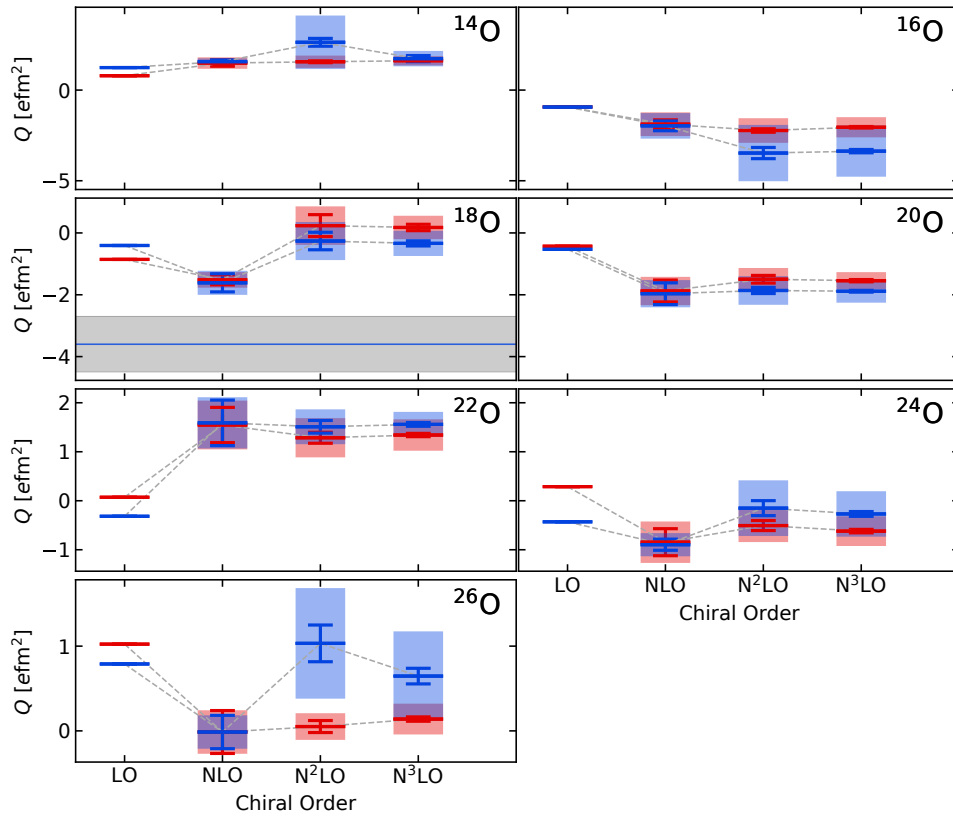


Fig. 8.26.: Electric quadrupole moments for even oxygen isotopes ranging from ^{14}O to ^{26}O as function of the chiral interaction order. Error bars indicate interaction uncertainties and bands are combined many-body and interaction uncertainties. The experimental quadrupole moment of ^{18}O is taken from [Sto05].

moment. Furthermore, the interaction and many-body uncertainties for all odd isotopes are small.

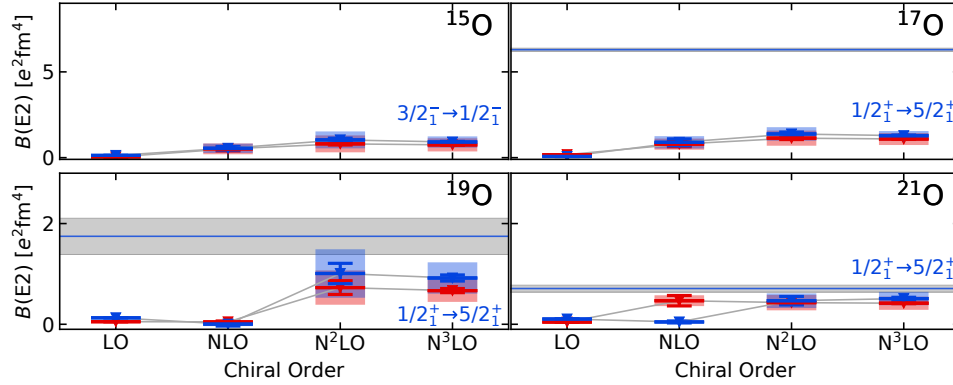


Fig. 8.27.: $B(E2)$ transition strengths for odd oxygen isotopes ranging from ^{15}O to ^{21}O as function of the chiral interaction order. Error bars indicate interaction uncertainties and bands are combined many-body and interaction uncertainties. Experimental results are taken from [TWC93; Til+95; Fir15].

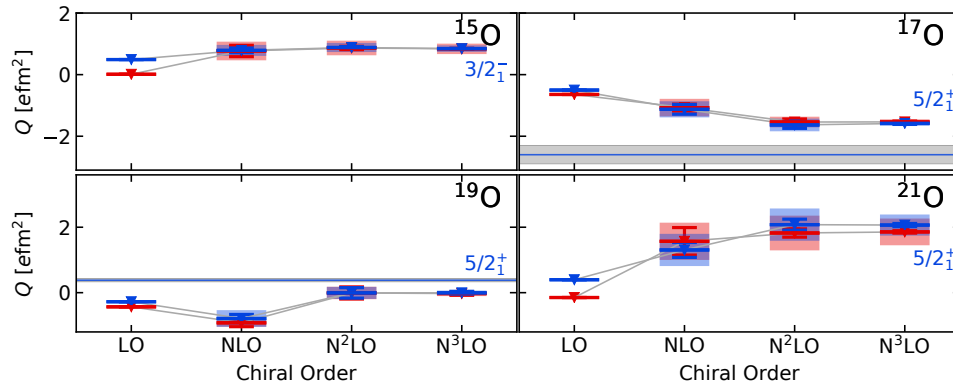


Fig. 8.28.: Electric quadrupole moments for odd oxygen isotopes ranging from ^{15}O to ^{21}O as function of the chiral interaction order. Error bars indicate interaction uncertainties and bands are combined many-body and interaction uncertainties. Experimental results are taken from [Sto05].

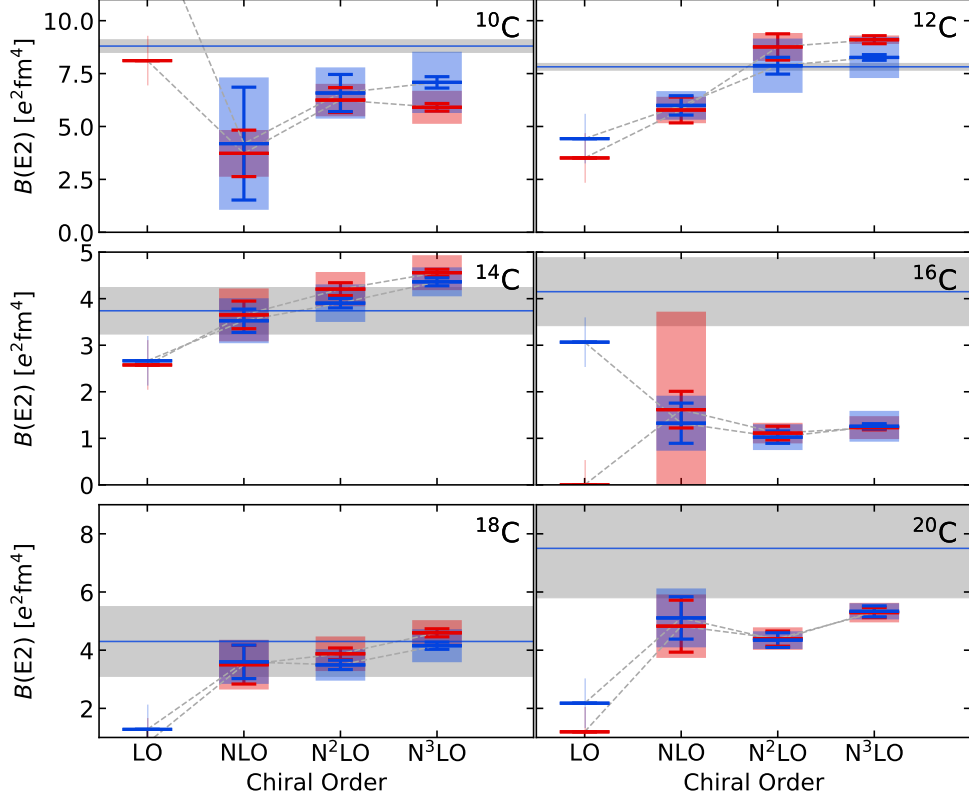


Fig. 8.29.: $B(E2)$ transition strengths for even carbon isotopes ranging from ^{10}C to ^{20}C as function of the chiral interaction order. Error bars indicate interaction uncertainties and bands are combined many-body and interaction uncertainties. Experimental results are taken from [Ajz91; Wie+08; Pet+11; McC+12; Vos+12; DA1+20].

Even Carbon Isotopes. Now we discuss the $B(E2, 2_1^+ \rightarrow 0_1^+)$ transition strengths and electric quadrupole moments $Q(2_1^+)$ for the carbon isotopic chain. In Fig. 8.29, the $B(E2)$ transitions strengths for even carbon isotopes are shown as function of the chiral order. The plot is built similar to Fig 8.25. Here, the picture of underestimated $B(E2)$ transition strengths turns into another story. All our results match with the experimental values at $N^3\text{LO}$ and $N^2\text{LO}$, which is remarkable. The only exception is the $B(E2)$ transition strength of ^{16}C , which is underestimated by about 50% within uncertainties. We already saw the same behavior for the isotopes in the oxygen isotopic chain. Furthermore, all carbon isotopes are converged with respect to N_{max} and $N_{\text{max}}^{\text{ref}}$. For ^{10}C , we obtain a large interaction uncertainty at NLO due to the large $B(E2)$ value at LO. The many-body uncertainty of the $B(E2)$ transition strength in ^{16}C at NLO is very large for $N_{\text{max}}^{\text{ref}} = 0$ indicating a slow N_{max} convergence. But compared to the oxygen isotopes, the new family of interactions performs much better for the $B(E2)$ transition strengths of the carbon isotopic chain.

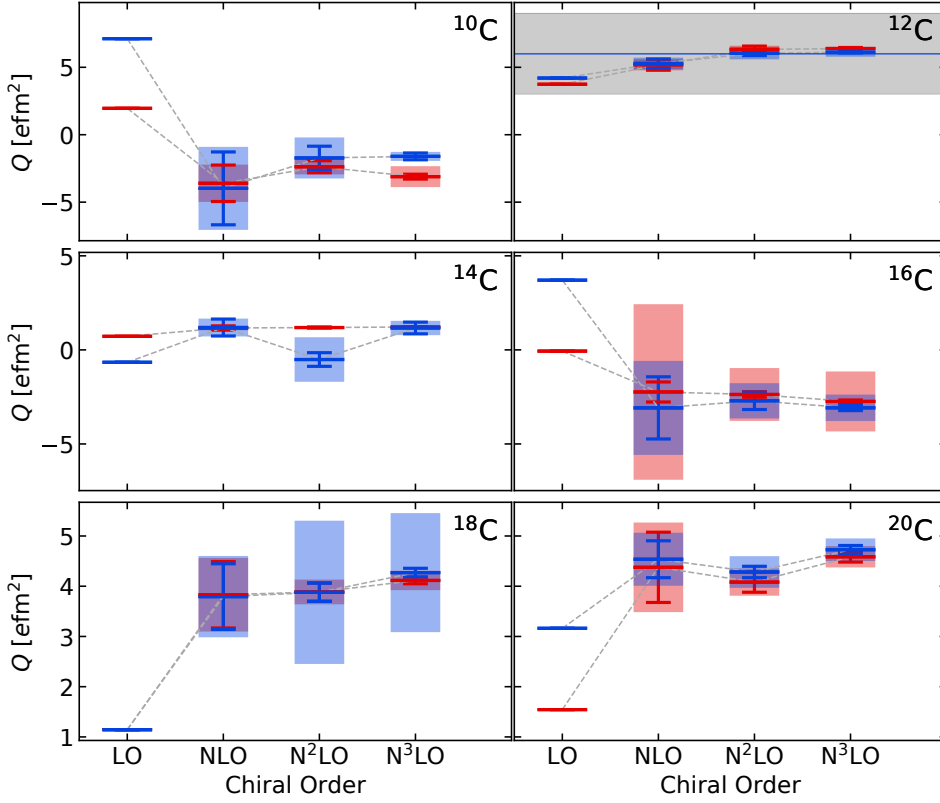


Fig. 8.30.: Electric quadrupole moments for even carbon isotopes ranging from ^{10}C to ^{20}C as function of the chiral interaction order. Error bars indicate interaction uncertainties and bands are combined many-body and interaction uncertainties. For ^{12}C the experimental quadrupole moment is taken from [Ver+83].

We can now discuss the electric quadrupole moments of isotopes for the carbon isotopes shown in Fig. 8.30. The only experimental quadrupole moment available is for ^{12}C , which is perfectly reproduced by our IM-NCSM results as discussed in section 8.1. For the quadrupole moments of the other even carbon isotopes, we obtain predictions for their values. As for the $B(E2)$ transition strength, the many-body uncertainty at $N_{\text{max}}^{\text{ref}} = 0$ for ^{16}C is quite large. Furthermore, the many-body uncertainties for the electric quadrupole moment of ^{18}C at $N_{\text{max}}^{\text{ref}} = 2$ are large for the two highest interaction orders. This indicates a slow convergence with respect to N_{max} , which is not observed for $N_{\text{max}}^{\text{ref}} = 0$. But all in all, we see that the results for the two reference spaces do not differ a lot.

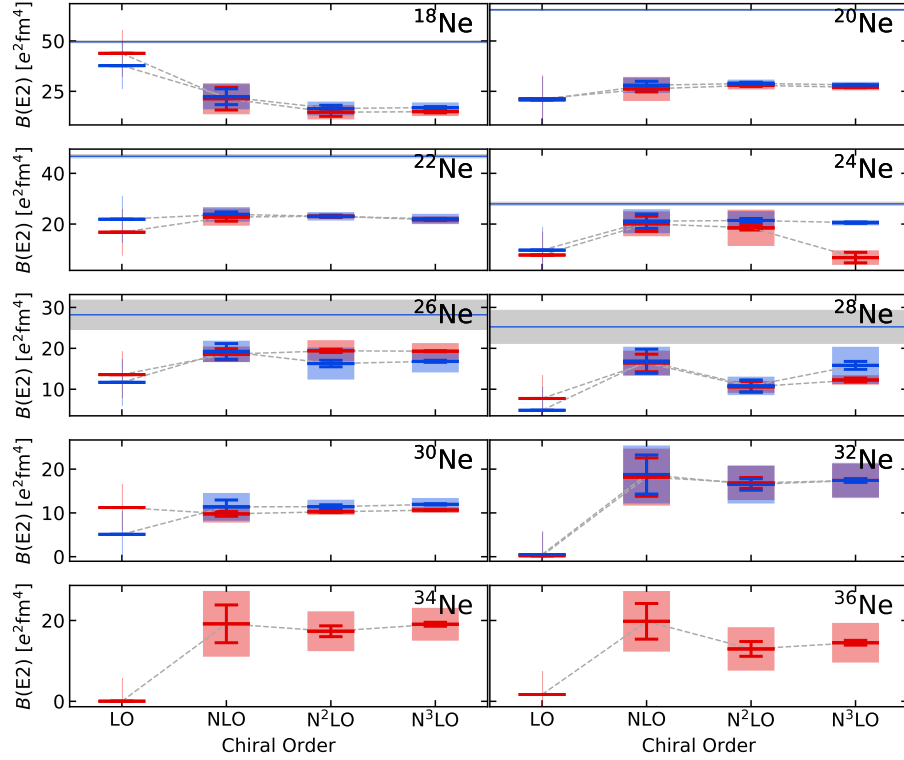


Fig. 8.31.: $B(E2)$ transition strengths for even neon isotopes ranging from ^{18}Ne to ^{36}Ne as function of the chiral interaction order. Error bars indicate interaction uncertainties and bands are combined many-body and interaction uncertainties. Experimental values are taken from [Til+95; Til+98; Bas15; Fir07; BH16; Sha13].

Neon Isotopes. Coming to the $B(E2)$ transition strengths of the neon isotopic chain, we observe a similar behavior as for the oxygen isotopic chain. The $B(E2)$ transition strengths are depicted as function of the chiral interaction order in Fig. 8.31. Experimental results are available for $^{18-28}\text{Ne}$. For $^{30-32}\text{Ne}$ we give a prediction of the value. The largest deviations with a factor of two to three are obtained for $^{18-22}\text{Ne}$. Surprisingly, the $B(E2)$ transition strengths for the more neutron-rich isotopes ^{24}Ne and ^{26}Ne are with about 20% deviation from the experiment closer to the experimental results compared to the lighter neon isotopes. The results for ^{28}Ne underestimate the experiment by about 4%, i.e., they are very close to experimental values taking combined many-body and interaction uncertainties at N³LO into account. Overall, the $B(E2)$ transition strengths in the even neon isotopes are with an underestimation of about 20-65% closer to the experiments compared to the results for oxygen isotopes, where the deviation ranges between 75% and 90%. Furthermore, the results are converged with respect to N_{max} throughout the complete neon isotopic chain.

The $B(E2)$ transition strengths of odd neon isotopes $^{19-25}\text{Ne}$ are shown as function of the

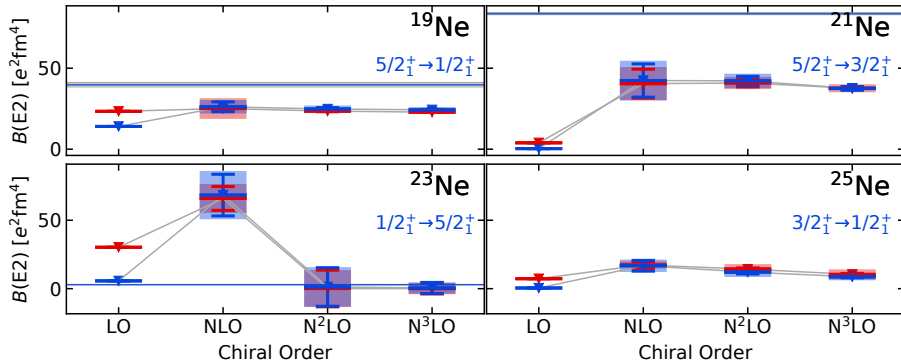


Fig. 8.32.: $B(E2)$ transition strengths for odd neon isotopes ranging from ^{19}Ne to ^{25}Ne as function of the chiral interaction order. Error bars indicate interaction uncertainties and bands are combined many-body and interaction uncertainties. Experimental results are taken from [Til+95; Fir15; SC21; Fir09].

chiral order in Fig. 8.32. We predict a $B(E2)$ transition strength for ^{25}Ne , which is close to zero. For ^{23}Ne , the experimental value for the transition strength is reproduced within uncertainties. The results are again underestimated for ^{19}Ne and ^{21}Ne compared to the experiment. Note that the $B(E2)$ transition strength of ^{19}Ne is with a deviation of 17% closer to the experiment as for ^{21}Ne , which deviates by 53% from the experiment. The $B(E2)$ transition strength for ^{23}Ne at NLO is far away from the experiment compared to the results at other interaction orders, which could be due to missing three-body forces at NLO.

We proceed to the electric quadrupole moments in the neon isotopic chain, the results for even neon isotopes are shown as function of the chiral order in Fig. 8.33. For ^{20}Ne and ^{22}Ne experimental results are available, which are overestimated by about 50%. For the other isotopes ^{18}Ne and $^{24-36}\text{Ne}$ we are able to give predictions for the electric quadrupole moment, since no experiments are available. The many-body and interaction uncertainties are small for all even neon isotopes besides for ^{28}Ne , where the many-body uncertainties are larger.

The quadrupole moments of odd neon isotopes $^{19-25}\text{Ne}$ are depicted in Fig. 8.34. Experimental results are only available for ^{21}Ne , which are nearly reproduced by our calculations. For the other isotopes we give predictions for the electric quadrupole moments. All odd neon isotopes are converged with respect to N_{max} and $N_{\text{max}}^{\text{ref}}$.

Coming back to the comparison with the PGCM, we obtained the opposite behavior, i.e., the experimental $B(E2)$ transition strengths of $^{24-28}\text{Ne}$ are overestimated and the transitions below ^{24}Ne are well reproduced in the PGCM due to the collective character of the corresponding theory. The PGCM method is able to reproduce the experimental values of the quadrupole moment for ^{20}Ne and ^{22}Ne [Fro+22a].

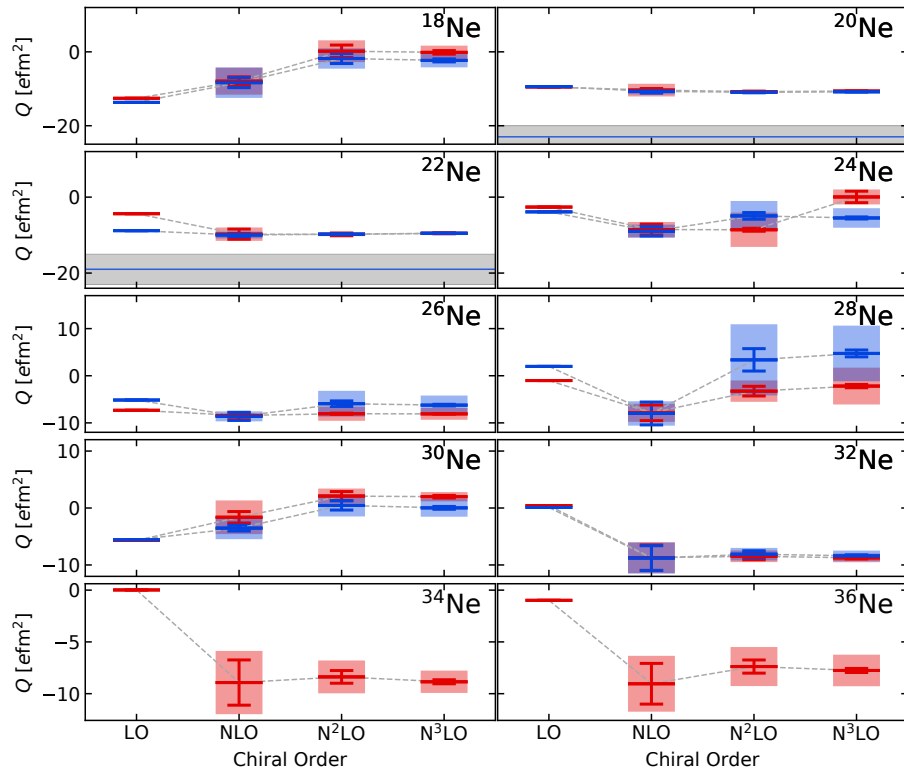


Fig. 8.33.: Electric quadrupole moments for even neon isotopes ranging from ^{18}Ne to ^{36}Ne as function of the chiral interaction order. Error bars indicate interaction uncertainties and bands are combined many-body and interaction uncertainties. Experimental values are taken from [Sto05].

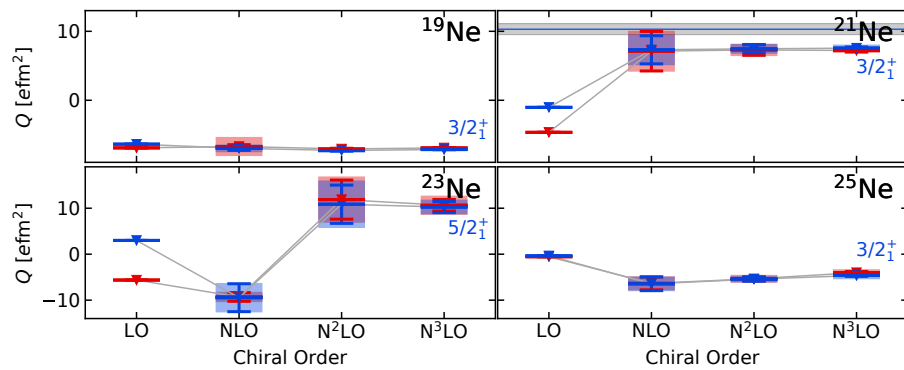


Fig. 8.34.: Electric quadrupole moments for odd neon isotopes ranging from ^{19}Ne to ^{25}Ne as function of the chiral interaction order. Error bars indicate interaction uncertainties and bands are combined many-body and interaction uncertainties. Experimental values are taken from [Sto05].

Discussion of the Electric Quadrupole Observables. Now we try to find reasons why the electric quadrupole transitions and moments do not agree with the experimental values for the most oxygen and neon isotopes and why the agreement in the carbon isotopic chain is better. In [Vob20], the main reason for this behavior was rooted in deficiencies of the interaction and limitations of the model space of the IM-NCSM. Comparing our results with the new family of interactions to the results with previous interactions, we see that the $B(E2)$ transition strengths and the electric quadrupole moments only barely depend on the interactions. Therefore, we can conclude that the deviations are of another nature, with a possible candidate being the truncations in the IM-NCSM. In the evolution of the IM-SRG we use the NO2B approximation and we may need to take induced normal-ordered terms up to three- or even higher-body level into account. Also, Parzuchowski et al., who computed electromagnetic observables using the IM-SRG in a valence-space version and an equation of motion approach found that at the IM-SRG(2) level it is not possible to reproduce experimental $B(E2)$ transition strengths for many nuclei [Par+17]. Another explanation they provided is that their interaction underpredicts the nuclear radii as the reason for the diminished electric quadrupole observables due to their radial dependence, which is similar to point-nucleon radius operator. But since the radii using the new family of interactions are in agreement with experimental results, this explanation is ruled out. Another reason could be that the generators and decoupling patterns are not able to include the needed correlations, which is also a goal for further improvements of the IM-NCSM.

The idea about missing induced three-body contributions in the IM-NCSM is due to a phenomenon called hierarchy inversion, which was described in [Vob20]. It means that the induced two-body terms in non-scalar observables, like the $B(E2)$ transition strength, dominate over the corresponding one-body contributions. To show this we first perform a full IM-NCSM calculation with the full operator up to the two-body level and, for comparison, with only the one-body terms.

The results for ^{16}C are shown for the energy of the first excited state, the $B(E2, 2_1^+ \rightarrow 0_1^+)$ transition strength and the electric quadrupole moment $Q(2_1^+)$ in Fig. 8.35 in dependence of the flow parameter s . The squares are results for $N_{\text{max}} = 2$ and calculations using $N_{\text{max}} = 4$ are depicted by diamond symbols. In the left-hand panels the observables are shown for the imaginary-time generator and for the results in the right-hand panel the White generator has been used. The calculations including only the one-body part are shown as open symbols and the full calculations are depicted by closed symbols. For the energy of the excited 2_1^+ state, the results for the full calculations and for the one-body part only are the same. In case of the $B(E2)$ transition strength, the results with the one-body part become approximately half of the result obtained from the full calculation. This indicates that the contribution to the $B(E2)$ transition strength is largely shifted

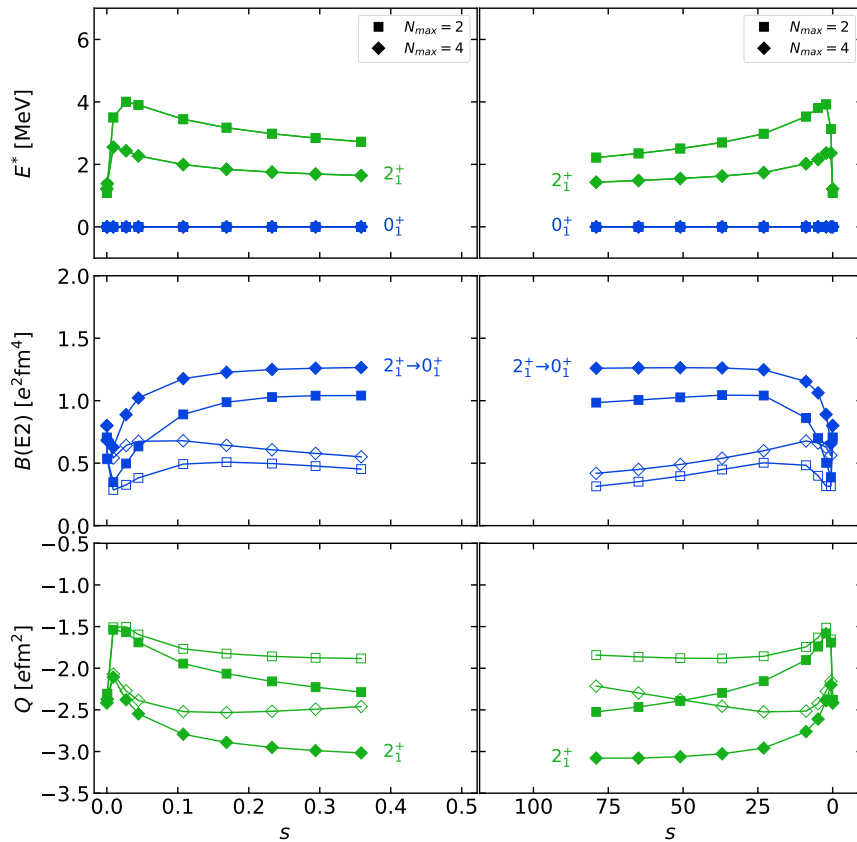


Fig. 8.35.: First excited state, $B(E2)$ transition strength and electric quadrupole moment for ^{16}C as function of the flow parameter s with a reference space $N_{\text{max}}^{\text{ref}} = 2$. On the left side results for the imaginary-time and on the right results for the White generator are shown. Closed symbols denote full calculations with the induced zero-, one- and two-body part and open symbols are results where only the zero- and one-body parts are used.

into the induced two-body terms. For the quadrupole moment the behavior is similar, i.e., the induced two-body contributions dominate over the one-body terms. Since the two-body part dominates over the one-body part for the $B(E2)$ transition strength and the electric quadrupole moment, one might ask how important induced many-body terms beyond the NO2B approximation are. This is the point where the LOTC becomes interesting, which will be discussed in section 8.6.

Now we discuss the behavior of the electric quadrupole observables with respect to the considered isotopic chains. The isotopes in the oxygen isotopic chain have a magic proton shell closure. Therefore, it might be that the IM-NCSM framework with the NO2B approximation is not able to describe the induced neutron contributions properly. In case of the carbon isotopes, only the $1p_{3/2}$ subshell is closed indicating that protons could contribute to the electric quadrupole observables, which could be a reason for the good agreement with experiment for the most carbon isotopes. We further saw that

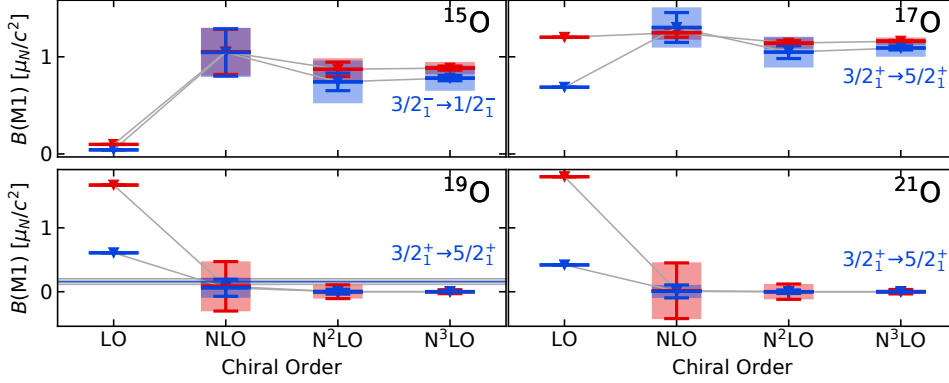


Fig. 8.36.: $B(M1)$ transition strengths for odd oxygen isotopes ranging from ^{15}O to ^{21}O as function of the chiral interaction order. Error bars indicate interaction uncertainties and bands are combined many-body and interaction uncertainties. The experimental $B(M1)$ transition strength of ^{19}O is taken from [Til+95].

the IM-NCSM is able to describe correlation effects for deformed neon isotopes. But since the $B(E2)$ transition strengths are underestimated, it could be that not enough deformation effects are captured.

8.4.2. Magnetic Dipole Observables

In this section we consider magnetic dipole transition strengths and moments for oxygen and neon isotopes. We start with the $B(M1)$ transition strengths and magnetic dipole moments μ of odd oxygen isotopes. Afterwards we will discuss these observables for isotopes from the neon isotopic chain.

Odd Oxygen Isotopes. The $B(M1, 3/2_1^- \rightarrow 1/2_1^-)$ and $B(M1, 5/2_1^+ \rightarrow 3/2_1^+)$ transition strengths for odd oxygen isotopes $^{15-21}\text{O}$ are shown in Fig. 8.36 in dependence of the chiral interaction order. Like in the section before, results at $N_{\max}^{\text{ref}} = 0$ are shown as red symbols and blue symbols denote results for $N_{\max}^{\text{ref}} = 2$. All results are shown for $N_{\max} = 4$ and obtained using the particle-removed scheme. Interaction uncertainties are represented by error bars and combined many-body and interaction uncertainties are shown as shaded bands. For all isotopes they are well converged with respect to N_{\max} and N_{\max}^{ref} . We are able to reproduce the $B(M1)$ transition strength of ^{19}O and give predictions for $^{15-17}\text{O}$ and ^{21}O .

The magnetic dipole moments μ of $^{15-21}\text{O}$ are shown in Fig. 8.37. Experimental results are available for ^{17}O and ^{19}O , which are slightly overestimated by our calculations. For ^{15}O and ^{21}O we are able to predict a value for the magnetic dipole moment. As for the computed $B(M1)$ transition strengths, our results for the dipole moments are converged.

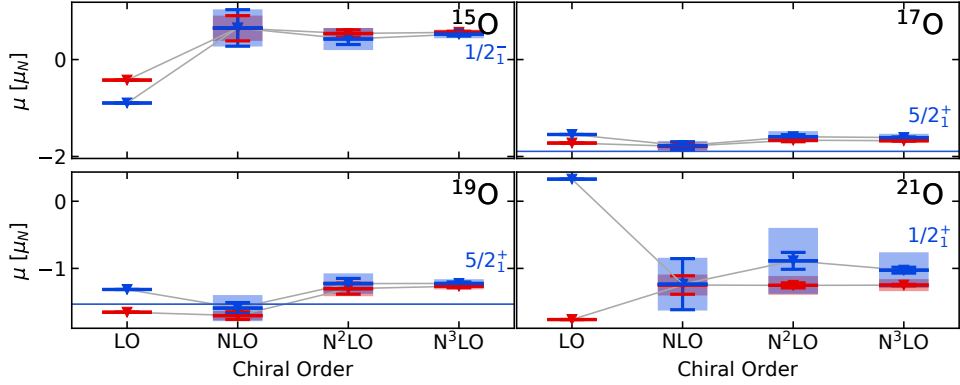


Fig. 8.37.: Magnetic dipole moments for odd oxygen isotopes ranging from ^{15}O to ^{21}O as function of the chiral interaction order. Error bars indicate interaction uncertainties and bands are combined many-body and interaction uncertainties.

Neon Isotopes. The $B(M1)$ transition strengths of $^{18-21}\text{Ne}$ and $^{23,25}\text{Ne}$ are shown in Fig. 8.38 as function of the chiral interaction order. The symbols have the same meaning as in Fig. 8.36. Experimental results are available for ^{18}Ne , ^{20}Ne and ^{21}Ne . For ^{18}Ne and ^{21}Ne , the experimental $B(M1)$ transition strength is slightly underestimated. For ^{20}Ne we are able to reproduce the experimental value. For ^{19}Ne and $^{23,25}\text{Ne}$ we are able to predict a $B(M1)$ transition strength. Furthermore, we obtained large interaction uncertainties for the $B(M1)$ strength at NLO for ^{18}Ne and ^{20}Ne at $N_{\text{max}}^{\text{ref}} = 0$, which can also be seen for ^{23}Ne at N^2LO and N^3LO . This indicates that $N_{\text{max}}^{\text{ref}} = 0$ is not sufficient enough to obtain converged results for the $B(M1)$ transition strengths of these isotopes. For the neon isotopic chain ranging from ^{18}Ne to ^{25}Ne , magnetic dipole moments are shown in Fig. 8.39. Experimental results are available for $^{19-23}\text{Ne}$ and we reproduce most of these. Only for ^{22}Ne we underestimate the experimental result and for ^{23}Ne we see a slight overestimation. All magnetic dipole moments, except the dipole moment of ^{24}Ne at $N_{\text{max}}^{\text{ref}} = 0$ are converged with respect to $N_{\text{max}}^{\text{ref}}$ and the chiral interaction order. Compared to the PGCM results in [Fro+22a], our results for $^{18-24}\text{Ne}$ do not differ a lot. In comparison to experimental results, the $B(M1)$ transition strengths and magnetic dipole moments μ from the IM-NCSM of all isotopes are in a much better agreement compared to the electric quadrupole observables.

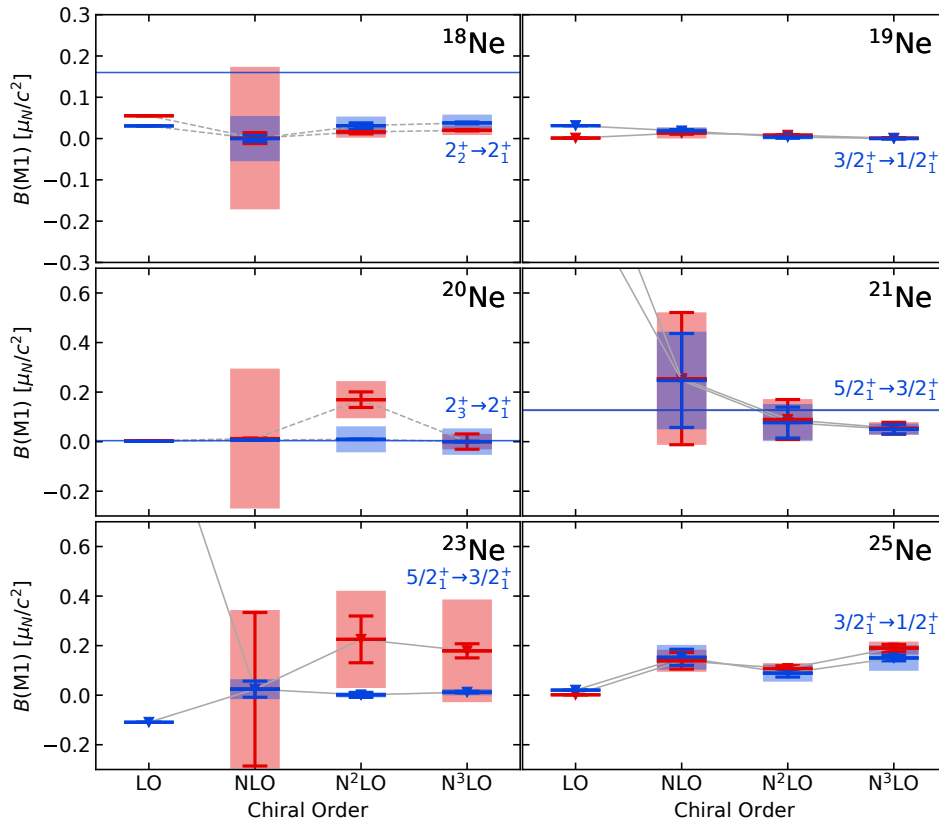


Fig. 8.38.: $B(M1)$ transition strengths for even and odd neon isotopes ranging from ^{18}Ne to ^{25}Ne as function of the chiral interaction order. Error bars indicate interaction uncertainties and bands are combined many-body and interaction uncertainties. Experimental values are taken from [Til+95; Til+98; Fir15].

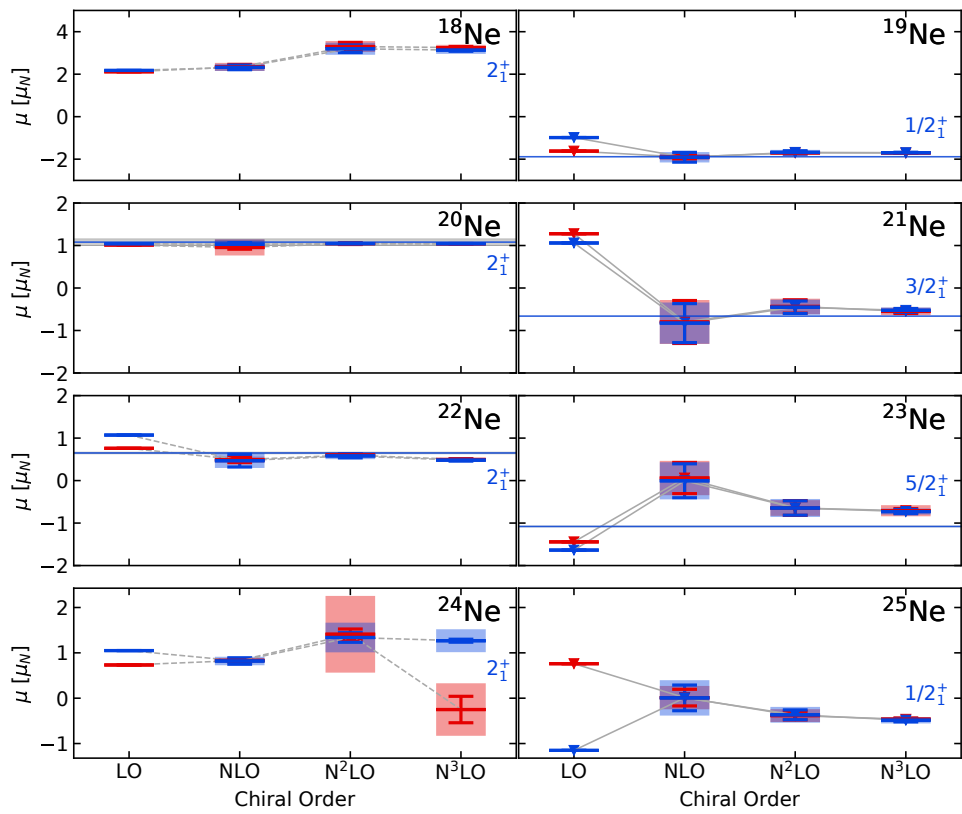


Fig. 8.39.: Magnetic dipole moments for even and odd neon isotopes ranging from ^{18}Ne to ^{25}Ne as function of the chiral interaction order. Error bars indicate interaction uncertainties and bands are combined many-body and interaction uncertainties.

8.5. Isotopic Chains

In this section we summarize the results for the oxygen, carbon, and neon isotopic chains. Figure 8.40 shows ground-state energies (first panel), 2_1^+ excited state energies (second panel), $B(E2, 2_1^+ \rightarrow 0_1^+)$ transition strengths (third panel), electric quadrupole moments $Q(2_1^+)$ (fourth panel) and charge radii (bottom panel) for even oxygen isotopes as function of the isotope. The error bands are combined many-body and interaction uncertainties. The blue closed symbols are results at N³LO, the red closed symbols are results at N²LO and the results at NLO are depicted by open grey symbols. For all oxygen isotopes we obtain a good agreement with experiment for ground-state energies, first excited states and charge radii at N²LO and N³LO. The experimental $B(E2)$ transition strengths are systematically underestimated, i.e., we are not even able to reproduce the experimental trend. Also, the electric quadrupole moment Q cannot be reproduced.

The same summary is shown for the carbon isotopic chain in Fig. 8.41. For the carbon isotopic chain, the family of chiral interactions performs well for all observables compared to experimental results. The only observable we are not able to reproduce is the $B(E2)$ transition strength of ¹⁶C. Furthermore, we obtain the same trend for the electric quadrupole observables shown in [FRN13] including a negative electric quadrupole moment Q for the first excited state of ¹⁶C and a small value of Q for ¹⁰C.

The ground-state energies, first excited state energies, $B(E2)$ transition strengths, electric quadrupole moments and charge radii for the neon isotopes are summarized in Fig. 8.42 as function of the isotope. The figure is constructed in the same way as Fig. 8.41. Also for the neon isotopic chain, the experimental ground-state energies, first excited states and charge radii are well reproduced compared to experimental. The $B(E2)$ transition strengths are underestimated, especially for the lighter isotopes ^{18–22}Ne. But for ^{18–24}Ne we do reproduce the experimental trend.

In summary we can state that the new family of chiral interactions performs very well for ground-state energies, spectra, and charge radii. The systematic underestimation of $B(E2)$ transition strengths in the oxygen and neon isotopic chain seems to be an issue of the NO2B approximation. Therefore, it could be very important to include induced three-body terms in the IM-SRG framework.

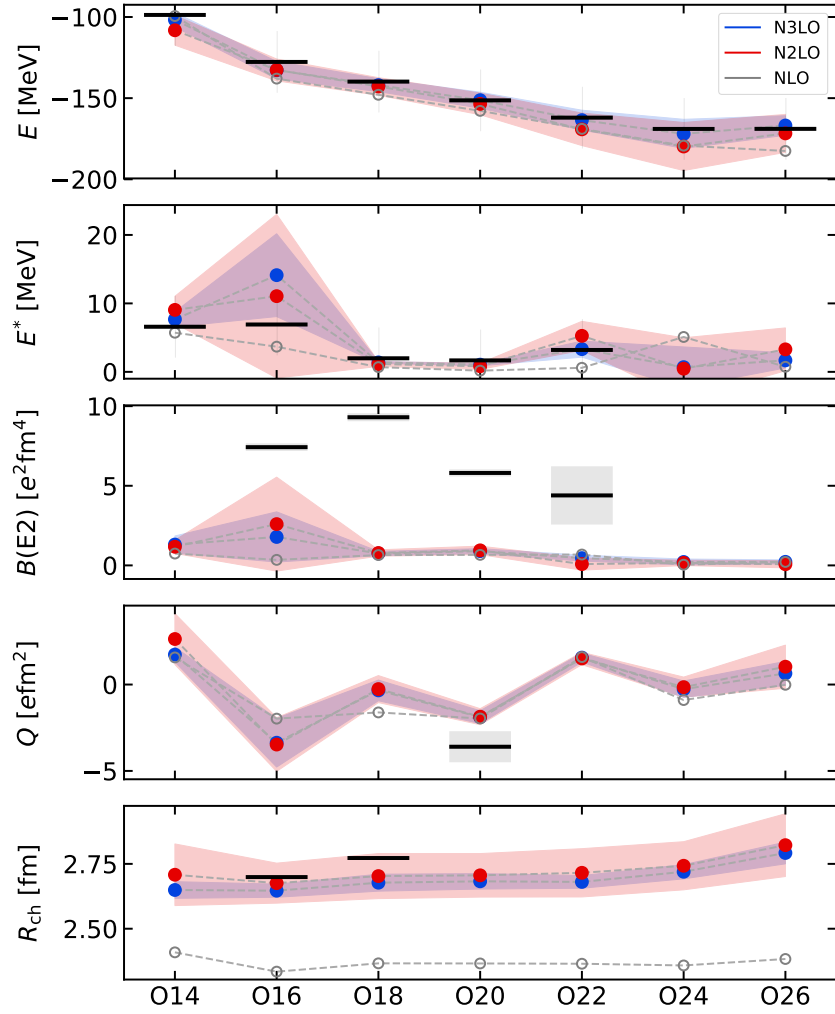


Fig. 8.40.: Ground-state energies, first excited state, $B(E2)$ transition strengths, electric quadrupole moments and charge radii for even oxygen isotopes. Error bands indicate combined interaction and many-body uncertainties.

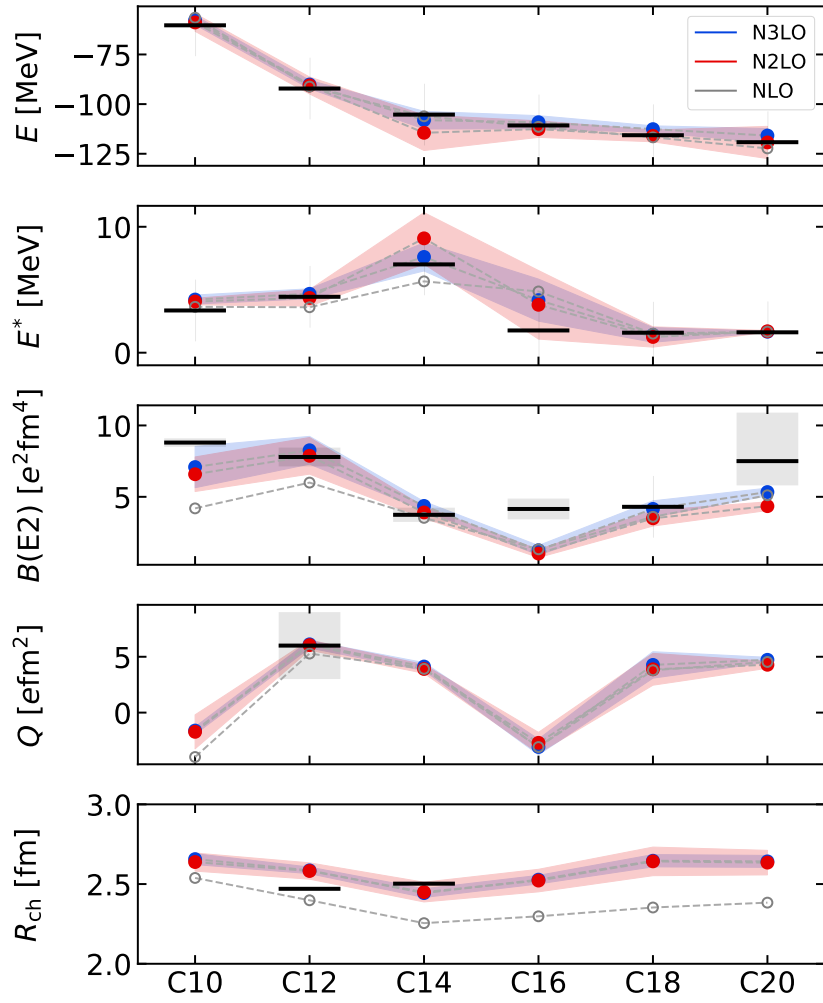


Fig. 8.41.: Same as Fig. (8.40) for even carbon isotopes.

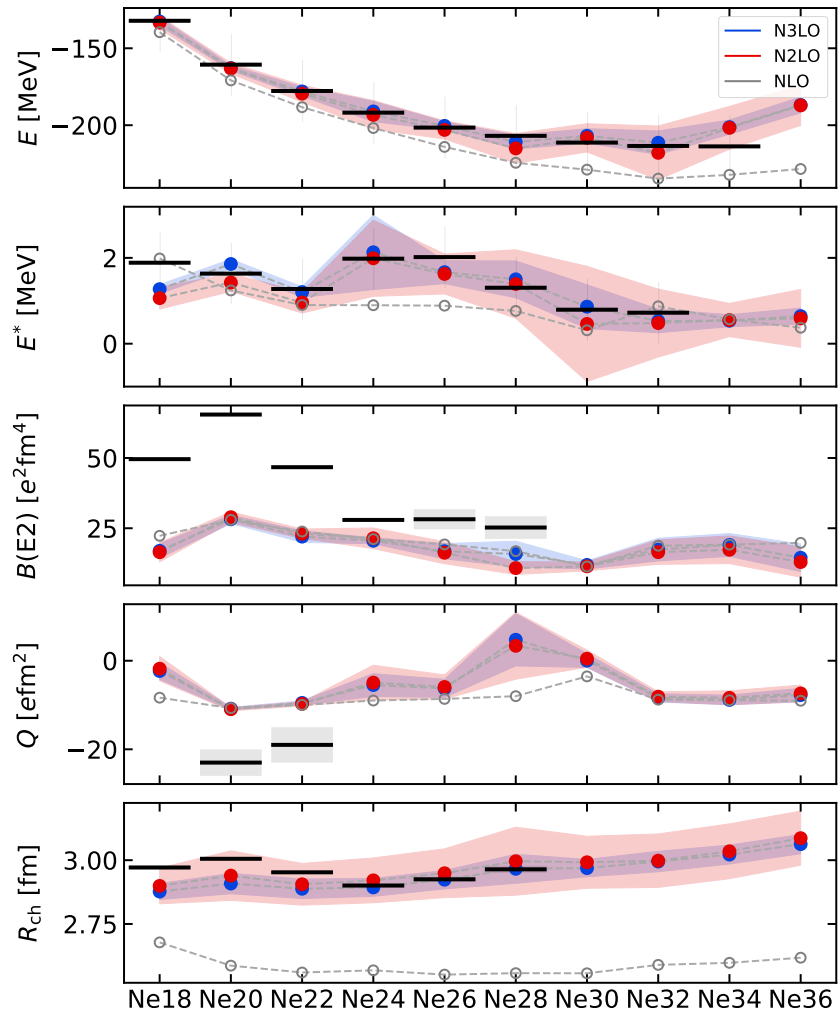


Fig. 8.42.: Same as Fig. (8.40) for even neon isotopes.

8.6. Leading-Order Three-Body Correction

The LOTC approximation, as derived in chapter 6, is an approximation for the evaluation of induced three-body terms in the observable transformation step of the multi-reference IM-SRG. Since we compute the contributions from the LOTC in the m -scheme, we can only perform the calculation for small model spaces like $e_{\max} = 2$ or $e_{\max} = 4$.

The steps for the IM-NCSM including the LOTC approximation are:

1. Solve the ODE in order to obtain the Magnus operator $\hat{\Omega}(s)$ using an $e_{\max} = 12$ truncation.
2. Calculation of observables using the same model-space truncation.
3. Conversion of the matrix elements into a smaller model-space like $e_{\max} = 4$ or 2 .
4. Using the LOTC in the m -scheme to obtain three-body corrections and add them to the output of step 2.

Lastly, the usual post-diagonalization step is performed for both matrix elements with and without LOTC. With the LOTC we correct the matrix elements of the Hamiltonian $\hat{H}(s)$ and the electric quadrupole operator $\hat{M}_{\text{el}2}^2(s)$.

The results for the application of the LOTC approximation (open symbols) for ^{12}C and ^{16}C are shown in Fig. 8.43 in comparison to results using the NO2B approximation (closed symbols). The ground-state energies, lowest excited states and $B(E2)$ transition strengths are shown as function of the flow parameter s . Results for $N_{\max} = 0$ are represented as circles and squares show the results for $N_{\max} = 2$. The LOTC calculations are truncated using $e_{\max} = 4$ for ^{12}C and for ^{16}C an $e_{\max} = 2$ truncation has been used. Furthermore, for the multi-reference IM-SRG evolution we used the White generator. The influence of the LOTC on the ground-state energy for ^{12}C and ^{16}C is very small. For the lowest excited states of ^{16}C , the influence of the LOTC is also very small. In case of ^{12}C the energies of all excited states are shifted into a larger energy regime. For the $B(E2)$ transition strength, there is quasi no influence for ^{16}C and for ^{12}C we see a slight correction of the $B(E2)$ transition strengths towards larger values.

The same observables are shown for ^{16}O , ^{18}O and ^{20}Ne as function of the flow parameter in Fig. 8.44. For ^{18}O and ^{20}Ne , we computed the LOTC using $N_{\max}^{\text{ref}} = 0$ and $e_{\max} = 2$. For ^{16}O we used $e_{\max} = N_{\max}^{\text{ref}} = 2$.

As we can see, the influence of the induced three-body correction on the ground-state energy of ^{20}Ne is very small. For the oxygen isotopes instead, the LOTC correction leads to a stronger overbinding compared to the NO2B approximation. In comparison to [Hei+21], who performed full single-reference IM-SRG(3) calculations for ^{16}O , our results show the opposite behavior, i.e., when using the single-reference IM-SRG(3),

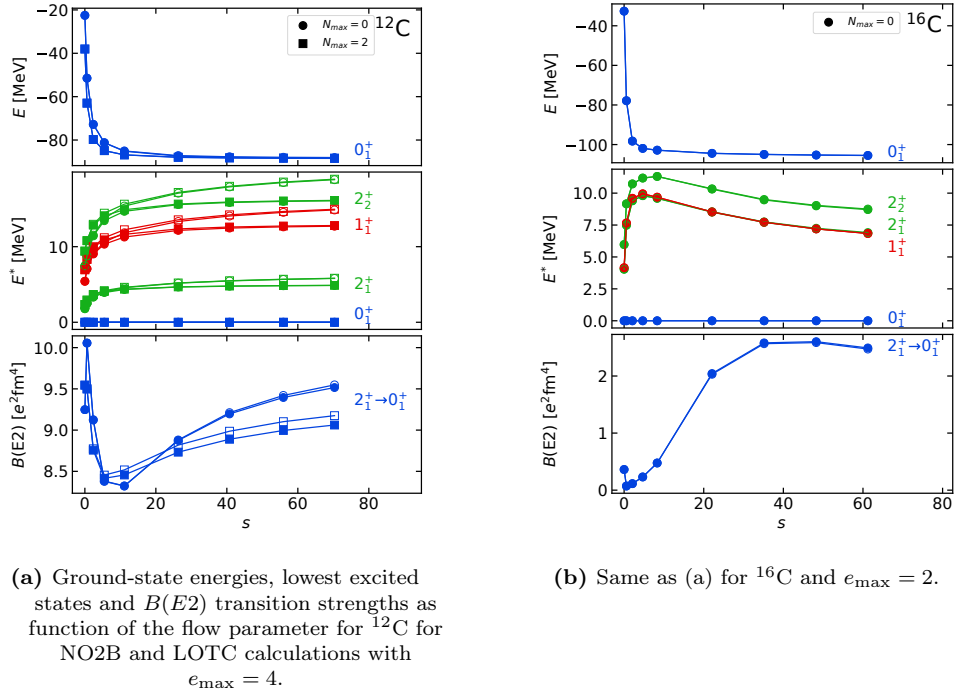
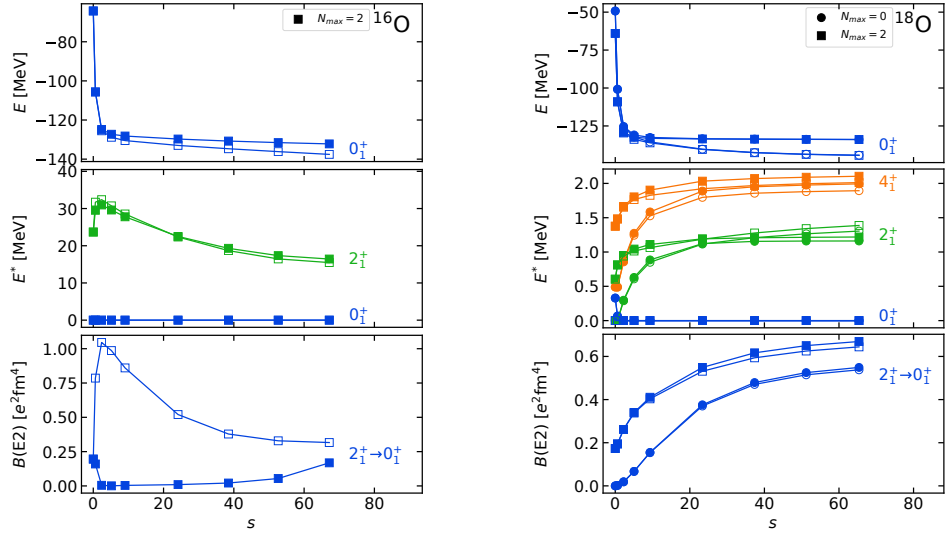


Fig. 8.43.: Ground-state energies, lowest excited states and $B(E2)$ transition strengths for ^{12}C and ^{16}C as function of the flow parameter s . Closed symbols are results with the NO2B approximation and open symbols are the results with the LOTC approximation on top.

the ground-state energy is corrected towards higher energies. For ^{16}O , the 2_1^+ state is slightly corrected towards lower energies by the LOTC approximation. In case of ^{18}O the opposite behavior occurs, but the 4_1^+ state is corrected towards lower energies. Considering the $B(E2)$ transition strengths of the oxygen isotopes, the LOTC corrects the $B(E2)$ transition strength towards larger values for ^{16}O and towards smaller values for ^{18}O . The effect of the LOTC approximation for ^{20}Ne is the same as in ^{16}C for all observables, the effect is extremely small. We also see that the flow stabilizes slower when using the LOTC approximation, especially for the observables of ^{12}C and $^{16,18}\text{O}$. This is expected due to the fact that we do not decouple three-body matrix elements explicitly. But for the $B(E2)$ transition strength of ^{16}O and ^{18}O we obtain a more stable flow for large flow parameters compared to the NO2B approximation. This indicates that induced three-body contributions play an important role for $B(E2)$ transition strengths. Due to the fact that the influence of the LOTC approximation, especially on the $B(E2)$ transition strengths is extremely small when using model space sizes up to $e_{\max} = 4$, we can conclude that the LOTC approximation can only be used as an uncertainty estimation for neglecting three-body forces in the IM-NCSM.

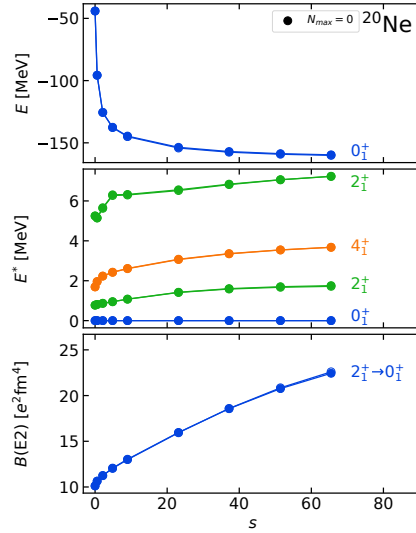
There could be a number of reasons for the small influence of LOTC. First of all, we only compute a correction to the BCH series. As a consequence, induced three-body terms in

the reference state are not explicitly decoupled from higher lying ph-excitations. Another point is that the commutator $[\hat{\Omega}^{[3]}, \hat{O}^{[3]}]$ is not included in the observable transformation, which is also the case for the three-body part of $[\hat{\Omega}^{[2]}, \hat{O}^{[2]}]$. These expressions could have a large impact on the results. Furthermore, we only perform a leading-order correction to the BCH series, including the first nested commutator ($k = 2$), which may be extended to $k = 3$ or $k = 4$. Another influence could be the small model-space dimension, which can be increased by performing j -coupling or using a massively parallelized code. But the j -coupled equations in the LOTC approximation include $9j$ and $12j$ symbols, which are expensive to compute and making the implementation error prone. All in all, a lot of effort is needed to find a solution for the systematic underestimation of $B(E2)$ transition strengths in the oxygen and neon isotopic chain. Especially for the multi-reference IM-SRG, the effort is much larger compared to the single-reference version, since irreducible two-body densities are an additional part of the equations. Therefore, it might be easier to develop alternative decoupling patterns or optimize the existing ones instead of pushing the multi-reference IM-SRG(3) forward.



(a) Ground-state energies, lowest excited states and $B(E2)$ transition strengths as function of the flow parameter for ^{16}O for NO2B and LOTC calculations using $N_{\max}^{\text{ref}} = 2$ and $\epsilon_{\max} = 2$.

(b) Same as (a) for ^{18}O and $N_{\max}^{\text{ref}} = 0$.



(c) Same as (b) for ^{20}Ne .

Fig. 8.44.: Same as Fig. (8.43) for ^{16}O , ^{18}O and ^{20}Ne .

9. Conclusion and Outlook

In this thesis we have used and extended the IM-NCSM to describe the properties of medium-mass nuclei with fully quantified many-body and interaction uncertainties. The IM-NCSM is a combination of the best features of the IM-SRG and the NCSM.

The NCSM is an exact method to solve the stationary many-body Schrödinger equation in form of a matrix eigenvalue problem, giving direct access to ground- and excited-state properties of light nuclei. Due to the fast-growing model-space size, the application of the NCSM is limited to nuclei in the p -shell. The IM-SRG is a method designed for medium-mass nuclei, which aims for a pre-diagonalization of the Hamiltonian, i.e., the decoupling of a reference state from all particle-hole excitations. In the single-reference IM-SRG a single Slater determinant is used as reference state, which is restricted to the description of closed-shell nuclei. The multi-reference IM-SRG instead uses a multi-determinantal reference state giving access to properties of open-shell nuclei. Since we are not able to take A -body interactions into account, the IM-SRG is truncated using the NO2B approximation.

The IM-NCSM consists of four stages. First, a single-particle basis transformation into the natural orbitals is applied. Afterwards, the reference state is computed in a small model space using the NCSM. The third step is the decoupling within the IM-SRG framework and the last step is the post-diagonalization in the NCSM. For the decoupling we have used the Magnus formulation of the IM-SRG, which allows us to evaluate non-scalar electromagnetic multipole operators as well. The advantage of the IM-NCSM compared to the NCSM is that the calculated observables converge much faster. Using particle-attachment and particle-removal schemes, it is also possible to access nuclei with an odd nucleon number.

In this work, we have used a new family of chiral interactions consisting of an NN interactions by Entem, Machleidt and Nosyk supplemented with a non-local 3N interaction, which is optimized with respect to the ground-state energy of oxygen and the triton binding energy. This family of interactions contains contributions from LO to N^3 LO for different cutoffs, which enables us to compute interaction uncertainties using models based on Bayesian statistics. Furthermore, we have quantified many-body uncertainties to investigate the convergence behavior of different observables for a range of medium-mass nuclei.

We have applied the IM-NCSM to three isotopic chains, i.e., to oxygen, carbon, and neon isotopes. We computed ground-state energies, low-lying excited states, charge radii and electromagnetic transitions and moments. With the new family of chiral interactions we are able to reproduce experimental results throughout all considered isotopic chains for ground-state energies, spectra and charge radii. Especially for the neon isotopic chain, this is a great success, since neon isotopes often show clustering and deformation, which is not explicitly covered in the IM-NCSM.

Furthermore, we are able to describe electric $B(E2)$ transition strengths and quadrupole moments for the carbon chain in agreement with the experiment, except for ^{16}C . For the oxygen and neon isotopes, the IM-NCSM typically underestimates the $B(E2)$ transition strengths and overestimates experimental quadrupole moments. Therefore, we have extended the IM-NCSM with a leading-order three-body approximation, which corrects the observable transformation of the IM-SRG in the leading order of the BCH series by taking induced three-body terms into account. We applied this approximation to selected nuclei in the oxygen, carbon, and neon isotopic chain for ground-state energies, spectra and $B(E2)$ transition strengths. We found that the correction in the energy and $B(E2)$ transition strength is small. Therefore, the LOTC does not improve the systematic underestimation of the $B(E2)$ transition strength. This could be due to the fact that the BCH series is only corrected by a leading-order contribution.

So it could be necessary to correct not only the BCH series, but also the flow evolution in the Magnus framework. Another interesting point is that induced three-body operators are not explicitly included in this correction, i.e., the LOTC only corrects operators up to the two-body level by normal ordering three-body contributions on the fly. The inclusion of three-body operators needs a derivation and implementation of a full IM-SRG(3) framework, which is computationally very expensive. Another solution could be to improve the existing generators of the IM-SRG. One way to achieve that is to develop alternative decoupling patterns by decoupling the reference state in a particle-hole scheme instead of the N_{max} scheme we usually use in the IM-NCSM.

Another restriction of the IM-NCSM still results from the reference state, where the dimension of the model space grows significantly with increasing number of nucleons. This problem can be solved by using the IM-NCSM as a multi-reference active-space method using for example ^{16}O as core to reduce the model-space size of the reference-state for sd -shell nuclei. For this, the reference-state has to be computed using a T_{max} truncation, which restricts the number of particle-hole excitations. Afterwards, the target nucleus is decoupled in the multi-reference IM-SRG framework and finally the post-diagonalization in the NCSM will be performed using the T_{max} truncation for the target nucleus. With this method, we will be able to access properties of heavier nuclei like for example magnesium or even isotopes in the calcium and nickel region.

From a practical view also other isotopic chains, like fluorine isotopes are interesting due to the so-called oxygen anomaly, which is a shift of the neutron dripline from $N = 16$ to $N = 22$ when going from oxygen to fluorine, in order to investigate the performance of the new family of chiral interactions.

A. Working Equations of the LOTC

This chapter gives an overview about the equations used in the code for the computation of the LOTC approximation for the IM-NCSM. We have mostly used intermediate tensors for the two-body part due to computational efficiency. The intermediate tensors are defined in chapter 6.

$$\begin{aligned}
O_{34,\text{LOTC}}^{12} = & + \frac{9}{2} \hat{\Xi}_{2\text{B}} \sum_{tvx} \Omega_t^v (\Omega_{4x}^{12} O_{3v}^{tx} + \Omega_{34}^{1x} O_{vx}^{2t} - \Omega_{3x}^{12} O_{4v}^{tx} - \Omega_{34}^{2x} O_{vx}^{1t}) (n_t - n_v) \\
& + 9 \hat{\Xi}_{2\text{B}} \sum_{vz} ((\Omega_{vz}^{12} \chi_{34}^{vz} + \Omega_{4v}^{1z} \chi_{3z}^{v2} - \Omega_{4z}^{12} \chi_3^z - \Omega_{4v}^{2z} \chi_{3z}^{v1}) n_v \\
& + (\Omega_{vz}^{12} \bar{\chi}_{34}^{vz} + \Omega_{4v}^{1z} \bar{\chi}_{3z}^{v2} - \Omega_{4z}^{12} \bar{\chi}_3^z - \Omega_{4v}^{2z} \bar{\chi}_{3z}^{v1}) \bar{n}_v) \\
& + \frac{9}{2} \hat{\Xi}_{2\text{B}} \sum_{zu} (\Omega_{uz}^{12} \chi_{34}^{zu} + \Omega_{4u}^{1z} \chi_{3z}^{u2} - \Omega_{4z}^{12} \chi_3^z - \Omega_{4u}^{2z} \chi_{3z}^{u1}) \\
& + 18 \hat{\Xi}_{2\text{B}} \sum_{xu} \Omega_{3u}^{1x} (\chi_{4x}^{2u} + \Phi_{4x}^{2u} - \Psi_{4x}^{2u} - \Theta_{4x}^{2u}) \\
& + \frac{9}{2} \hat{\Xi}_{2\text{B}} \sum_{vx} \Omega_{34}^{vx} (\chi_{xv}^{12} + \Phi_{xv}^{12} - \Psi_{xv}^{12} - \Theta_{xv}^{21}) \\
& + \frac{9}{2} \hat{\Xi}_{2\text{B}} \sum_z (\Omega_{4z}^{12} \chi_3^z + \Omega_{34}^{1z} \chi_z^2 - \Omega_{3z}^{12} \chi_4^z - \Omega_{34}^{2z} \chi_z^1) \\
& + 18 \hat{\Xi}_{2\text{B}} \sum_{zu} (\Omega_{uz}^{12} \chi_{34}^{zu} + \Omega_{4u}^{1z} \chi_{3z}^{2u} - \Omega_{4z}^{12} \chi_z^3 - \Omega_{4u}^{2z} \chi_{3z}^{1u})
\end{aligned} \tag{A.362}$$

$$\begin{aligned}
O_{2,\text{LOTC}}^1 = & + \frac{9}{4} \hat{\Xi}_{1\text{B}} \sum_{rtvx\text{su}} \Omega_v^t (\Omega_{sx}^{1r} O_{2u}^{vx} + \Omega_{2s}^{1x} O_{ux}^{rv} - \Omega_{2x}^{1r} O_{su}^{vx} - \Omega_{2s}^{rx} O_{ux}^{1v}) \lambda_{rt}^{su} \\
& - \frac{9}{4} \hat{\Xi}_{1\text{B}} \sum_{rtvx\text{su}} \Omega_v^r (\Omega_{sx}^{1t} O_{2u}^{vx} + \Omega_{2s}^{1x} O_{ux}^{tv} - \Omega_{2x}^{1t} O_{su}^{vx} - \Omega_{2s}^{tx} O_{ux}^{1v}) \lambda_{rt}^{su} \\
& + \frac{9}{8} \hat{\Xi}_{1\text{B}} \sum_{rtvxz} \Omega_{rt}^{vx} (\Omega_{vz}^{1r} O_{2x}^{tz} + \Omega_{2v}^{1z} O_{xz}^{rt} - \Omega_{2z}^{1r} O_{vx}^{tz} - \Omega_{2v}^{rz} O_{xz}^{1t}) \\
& (\bar{n}_r \bar{n}_t n_v n_x - n_r n_t \bar{n}_v \bar{n}_x) \\
& + \frac{9}{8} \hat{\Xi}_{1\text{B}} \sum_{rtvxz\text{su}} \Omega_{vx}^{rt} (\Omega_{sz}^{1v} O_{2u}^{xz} + \Omega_{2s}^{1z} O_{uz}^{vx} - \Omega_{2z}^{1v} O_{su}^{xz} - \Omega_{2s}^{vz} O_{uz}^{1x}) \\
& (1 - n_v - n_x) \lambda_{rt}^{su} \\
& + \frac{9}{4} \hat{\Xi}_{1\text{B}} \sum_{rtvxz\text{su}} \Omega_{vx}^{1r} (\Omega_{sz}^{tv} O_{2u}^{xz} + \Omega_{2s}^{tz} O_{uz}^{vx} - \Omega_{2z}^{tv} O_{su}^{xz} - \Omega_{2s}^{vz} O_{uz}^{tx}) \\
& (1 - n_v - n_x) \lambda_{rt}^{su} \\
& + \frac{9}{2} \hat{\Xi}_{1\text{B}} \sum_{rtvxz\text{su}} \Omega_{sx}^{1v} (\Omega_{uz}^{rt} O_{2v}^{xz} + \Omega_{2u}^{rz} O_{vz}^{tx} - \Omega_{2z}^{rt} O_{uv}^{xz} - \Omega_{2u}^{tz} O_{vz}^{rx}) (n_x - n_v) \lambda_{rt}^{su} \\
& + \frac{9}{2} \hat{\Xi}_{1\text{B}} \sum_{rtvxz\text{su}} \Omega_{sv}^{rx} (\Omega_{uz}^{1t} O_{2x}^{vz} + \Omega_{2u}^{1z} O_{xz}^{tv} - \Omega_{2z}^{1t} O_{ux}^{vz} - \Omega_{2u}^{tz} O_{xz}^{1v}) (n_x - n_v) \lambda_{rt}^{su}
\end{aligned} \tag{A.363}$$

$$\begin{aligned}
E_{0,\text{LOTC}} = & - \frac{9}{8} \sum_{prt vxzqs} [\Omega_{vx}^{pt} (\Omega_{sz}^{rv} O_{qt}^{xz} + \Omega_{qs}^{rz} O_{tz}^{vx} - \Omega_{qz}^{rv} O_{st}^{xz} - \Omega_{qs}^{vz} O_{tz}^{rx}) \\
& + \Omega_{st}^{vx} (\Omega_{vz}^{pr} O_{qx}^{tz} + \Omega_{qv}^{pz} O_{xz}^{rt} - \Omega_{qz}^{pr} O_{vx}^{tz} - \Omega_{qv}^{rz} O_{xz}^{pt})] (\bar{n}_t n_v n_x + n_t \bar{n}_v \bar{n}_x) \lambda_{pr}^{qs}
\end{aligned} \tag{A.364}$$

The calculations of the LOTC are carried out after the solution of the BCH series in the IM-SRG using NO2B truncated operators. We still use the BCH series with $\hat{O}(0)$ and $\hat{\Omega}(s)$ and add the results on top of $\hat{O}(s)$.

Bibliography

- [PS95] M. E. Peskin and D. V. Schroeder, *An introduction to quantum field theory* - (Avalon Publishing, New York, 1995).
- [Bea+06] S. R. Beane, P. F. Bedaque, K. Orginos, and M. J. Savage, Phys. Rev. Lett. **97**, 012001 (2006), [10.1103/PhysRevLett.97.012001](https://doi.org/10.1103/PhysRevLett.97.012001).
- [IAH07] N. Ishii, S. Aoki, and T. Hatsuda, Phys. Rev. Lett. **99**, 022001 (2007), [10.1103/PhysRevLett.99.022001](https://doi.org/10.1103/PhysRevLett.99.022001).
- [Ino+10] T. Inoue, N. Ishii, S. Aoki, et al., Prog. Theor. Phys. **124**, 591–603 (2010), [10.1143/PTP.124.591](https://doi.org/10.1143/PTP.124.591).
- [Pan87] G. Pantis, Nucl. Phys. A **469**, 627–636 (1987), [https://doi.org/10.1016/0375-9474\(87\)90017-0](https://doi.org/10.1016/0375-9474(87)90017-0).
- [Har81a] M. Harvey, Nucl. Phys. A **352**, 301–325 (1981), [https://doi.org/10.1016/0375-9474\(81\)90412-7](https://doi.org/10.1016/0375-9474(81)90412-7).
- [Har81b] M. Harvey, Nucl. Phys. A **352**, 326–342 (1981), [https://doi.org/10.1016/0375-9474\(81\)90413-9](https://doi.org/10.1016/0375-9474(81)90413-9).
- [EFV00] D. R. Entem, F. Fernández, and A. Valcarce, Phys. Rev. C **62**, 034002 (2000), [10.1103/PhysRevC.62.034002](https://doi.org/10.1103/PhysRevC.62.034002).
- [Wei79] S. Weinberg, Physica A: Statistical Mechanics and its Applications **96**, 327–340 (1979), [https://doi.org/10.1016/0378-4371\(79\)90223-1](https://doi.org/10.1016/0378-4371(79)90223-1).
- [ME11] R. Machleidt and D. Entem, Phys. Rep. **503**, 1–75 (2011), <https://doi.org/10.1016/j.physrep.2011.02.001>.
- [Wei90] S. Weinberg, Phys. Lett. B **251**, 288–292 (1990), [https://doi.org/10.1016/0370-2693\(90\)90938-3](https://doi.org/10.1016/0370-2693(90)90938-3).
- [Kol94] U. van Kolck, Phys. Rev. C **49**, 2932–2941 (1994), [10.1103/PhysRevC.49.2932](https://doi.org/10.1103/PhysRevC.49.2932).
- [Epe+02] E. Epelbaum, A. Nogga, W. Glöckle, et al., Phys. Rev. C **66**, 064001 (2002), [10.1103/PhysRevC.66.064001](https://doi.org/10.1103/PhysRevC.66.064001).
- [KE07] N. Kalantar-Nayestanaki and E. Epelbaum, Nucl. Phys. News **17**, 22–30 (2007), [10.1080/10506890701404222](https://doi.org/10.1080/10506890701404222).

- [Hüt+20] T. Hüther, K. Vobig, K. Hebeler, et al., *Phys. Lett. B* **808**, 135651 (2020), <https://doi.org/10.1016/j.physletb.2020.135651>.
- [EM02] D. R. Entem and R. Machleidt, *Phys. Rev. C* **66**, 014002 (2002), [10.1103/PhysRevC.66.014002](https://doi.org/10.1103/PhysRevC.66.014002).
- [Nav07] P. Navrátil, *Few-Body Syst.* **41**, 117–140 (2007), [10.1007/s00601-007-0193-3](https://doi.org/10.1007/s00601-007-0193-3).
- [Som+14] V. Somà, A. Cipollone, C. Barbieri, et al., *Phys. Rev. C* **89**, 061301 (2014), [10.1103/PhysRevC.89.061301](https://doi.org/10.1103/PhysRevC.89.061301).
- [Bin+14] S. Binder, J. Langhammer, A. Calci, and R. Roth, *Phys. Lett. B* **736**, 119–123 (2014), <https://doi.org/10.1016/j.physletb.2014.07.010>.
- [CBN15] A. Cipollone, C. Barbieri, and P. Navrátil, *Phys. Rev. C* **92**, 014306 (2015), [10.1103/PhysRevC.92.014306](https://doi.org/10.1103/PhysRevC.92.014306).
- [Lap+16] V. Lapoux, V. Somà, C. Barbieri, et al., *Phys. Rev. Lett.* **117**, 052501 (2016), [10.1103/PhysRevLett.117.052501](https://doi.org/10.1103/PhysRevLett.117.052501).
- [Eks+15] A. Ekström, G. R. Jansen, K. A. Wendt, et al., *Phys. Rev. C* **91**, 051301 (2015), [10.1103/PhysRevC.91.051301](https://doi.org/10.1103/PhysRevC.91.051301).
- [EKM15a] E. Epelbaum, H. Krebs, and U. G. Meißner, *Eur. Phys. J. A* **51** (2015) [10.1140/epja/i2015-15053-8](https://doi.org/10.1140/epja/i2015-15053-8).
- [EKM15b] E. Epelbaum, H. Krebs, and U.-G. Meißner, *Phys. Rev. Lett.* **115**, 122301 (2015), [10.1103/PhysRevLett.115.122301](https://doi.org/10.1103/PhysRevLett.115.122301).
- [EMN17] D. R. Entem, R. Machleidt, and Y. Nosyk, *Phys. Rev. C* **96**, 024004 (2017), [10.1103/PhysRevC.96.024004](https://doi.org/10.1103/PhysRevC.96.024004).
- [Bin+16] S. Binder, A. Calci, E. Epelbaum, et al., *Phys. Rev. C* **93**, 044002 (2016), [10.1103/PhysRevC.93.044002](https://doi.org/10.1103/PhysRevC.93.044002).
- [Bin+18] S. Binder, A. Calci, E. Epelbaum, et al., *Phys. Rev. C* **98**, 014002 (2018), [10.1103/PhysRevC.98.014002](https://doi.org/10.1103/PhysRevC.98.014002).
- [Fur+15] R. J. Furnstahl, N. Klco, D. R. Phillips, and S. Wesolowski, *Phys. Rev. C* **92**, 024005 (2015), [10.1103/PhysRevC.92.024005](https://doi.org/10.1103/PhysRevC.92.024005).
- [MWF17] J. A. Melendez, S. Wesolowski, and R. J. Furnstahl, *Phys. Rev. C* **96**, 024003 (2017), [10.1103/PhysRevC.96.024003](https://doi.org/10.1103/PhysRevC.96.024003).
- [Mel+19] J. Melendez, R. J. Furnstahl, D. R. Phillips, et al., *Phys. Rev. C* **100**, 044001 (2019), [10.1103/PhysRevC.100.044001](https://doi.org/10.1103/PhysRevC.100.044001).
- [Heb+15] K. Hebeler, J. Holt, J. Menéndez, and A. Schwenk, *Annu. Rev. Nucl. Part. Sci.* **65**, 457–484 (2015), [10.1146/annurev-nucl-102313-025446](https://doi.org/10.1146/annurev-nucl-102313-025446).

- [Epe+19] E. Epelbaum, J. Golak, K. Hebeler, et al., *Phys. Rev. C* **99**, 024313 (2019), [10.1103/PhysRevC.99.024313](https://doi.org/10.1103/PhysRevC.99.024313).
- [Mar+21] P. Maris, E. Epelbaum, R. J. Furnstahl, et al., *Phys. Rev. C* **103**, 054001 (2021), [10.1103/PhysRevC.103.054001](https://doi.org/10.1103/PhysRevC.103.054001).
- [BFP07] S. K. Bogner, R. J. Furnstahl, and R. J. Perry, *Phys. Rev. C* **75**, 061001 (2007), [10.1103/PhysRevC.75.061001](https://doi.org/10.1103/PhysRevC.75.061001).
- [BFS10] S. Bogner, R. Furnstahl, and A. Schwenk, *Progr. Part. Nucl. Phys.* **65**, 94–147 (2010), <https://doi.org/10.1016/j.ppnp.2010.03.001>.
- [RNF10] R. Roth, T. L. Neff, and H. T. Feldmeier, *Progr. Part. Nucl. Phys.* **65**, 50–93 (2010).
- [Rot+14] R. Roth, A. Calci, J. Langhammer, and S. Binder, *Phys. Rev. C* **90**, 024325 (2014), [10.1103/PhysRevC.90.024325](https://doi.org/10.1103/PhysRevC.90.024325).
- [Nav+07] P. Navrátil, V. G. Gueorguiev, J. P. Vary, et al., *Phys. Rev. Lett.* **99**, 042501 (2007), [10.1103/PhysRevLett.99.042501](https://doi.org/10.1103/PhysRevLett.99.042501).
- [Nav+09] P. Navrátil, S. Quaglioni, I. Stetcu, and B. R. Barrett, *J. Phys. G: Nucl. Part. Phys.* **36**, 083101 (2009), [10.1088/0954-3899/36/8/083101](https://doi.org/10.1088/0954-3899/36/8/083101).
- [BNV13] B. R. Barrett, P. Navratil, and J. P. Vary, *Progr. Part. Nucl. Phys.* **69**, 131–181 (2013), <https://doi.org/10.1016/j.ppnp.2012.10.003>.
- [Kuo66] T. Kuo, *Nucl. Phys.* **85**, 40–86 (1966), [10.1016/0029-5582\(66\)90131-3](https://doi.org/10.1016/0029-5582(66)90131-3).
- [Cau+05] E. Caurier, G. Martínez-Pinedo, F. Nowacki, et al., *Rev. Mod. Phys.* **77**, 427–488 (2005), [10.1103/RevModPhys.77.427](https://doi.org/10.1103/RevModPhys.77.427).
- [Cor+14] L. Coraggio, A. Covello, A. Gargano, and N. Itaco, *Nucl. Phys.* **928**, 43–50 (2014).
- [RN07] R. Roth and P. Navrátil, *Phys. Rev. Lett.* **99**, 092501 (2007), [10.1103/PhysRevLett.99.092501](https://doi.org/10.1103/PhysRevLett.99.092501).
- [Rot09] R. Roth, *Phys. Rev. C* **79**, 064324 (2009), [10.1103/PhysRevC.79.064324](https://doi.org/10.1103/PhysRevC.79.064324).
- [DB04] W. Dickhoff and C. Barbieri, *Progr. Part. Nucl. Phys.* **52**, 377–496 (2004), <https://doi.org/10.1016/j.ppnp.2004.02.038>.
- [CBN13] A. Cipollone, C. Barbieri, and P. Navrátil, *Phys. Rev. Lett.* **111**, 062501 (2013), [10.1103/PhysRevLett.111.062501](https://doi.org/10.1103/PhysRevLett.111.062501).
- [Hag+07] G. Hagen, T. Papenbrock, D. J. Dean, et al., *Phys. Rev. C* **76**, 034302 (2007), [10.1103/PhysRevC.76.034302](https://doi.org/10.1103/PhysRevC.76.034302).
- [Hag+08] G. Hagen, T. Papenbrock, D. J. Dean, and M. Hjorth-Jensen, *Phys. Rev. Lett.* **101**, 092502 (2008), [10.1103/PhysRevLett.101.092502](https://doi.org/10.1103/PhysRevLett.101.092502).

- [Hag+14] G. Hagen, T. Papenbrock, M. Hjorth-Jensen, and D. J. Dean, *Rep. Prog. Phys.* **77**, 096302 (2014), [10.1088/0034-4885/77/9/096302](https://doi.org/10.1088/0034-4885/77/9/096302).
- [Sig+15] A. Signoracci, T. Duguet, G. Hagen, and G. R. Jansen, *Phys. Rev. C* **91**, 064320 (2015), [10.1103/PhysRevC.91.064320](https://doi.org/10.1103/PhysRevC.91.064320).
- [Hag+16] G. Hagen, M. Hjorth-Jensen, G. R. Jansen, and T. Papenbrock, *Phys. Scr.* **91**, 063006 (2016), [10.1088/0031-8949/91/6/063006](https://doi.org/10.1088/0031-8949/91/6/063006).
- [TBS11] K. Tsukiyama, S. K. Bogner, and A. Schwenk, *Phys. Rev. Lett.* **106**, 222502 (2011), [10.1103/PhysRevLett.106.222502](https://doi.org/10.1103/PhysRevLett.106.222502).
- [TBS12] K. Tsukiyama, S. K. Bogner, and A. Schwenk, *Phys. Rev. C* **85**, 061304 (2012), [10.1103/PhysRevC.85.061304](https://doi.org/10.1103/PhysRevC.85.061304).
- [Her+16] H. Hergert, S. K. Bogner, T. D. Morris, et al., *Phys. Rept.* **621**, 165–222 (2016), [10.1016/j.physrep.2015.12.007](https://doi.org/10.1016/j.physrep.2015.12.007).
- [Her16] H. Hergert, *Phys. Scr.* **92**, 023002 (2016), [10.1088/1402-4896/92/2/023002](https://doi.org/10.1088/1402-4896/92/2/023002).
- [Her+13a] H. Hergert, S. Binder, A. Calci, et al., *Phys. Rev. Lett.* **110**, 242501 (2013), [10.1103/PhysRevLett.110.242501](https://doi.org/10.1103/PhysRevLett.110.242501).
- [Her+14] H. Hergert, S. K. Bogner, T. D. Morris, et al., *Phys. Rev. C* **90**, 041302 (2014), [10.1103/PhysRevC.90.041302](https://doi.org/10.1103/PhysRevC.90.041302).
- [PMB17] N. M. Parzuchowski, T. D. Morris, and S. K. Bogner, *Phys. Rev. C* **95**, 044304 (2017), [10.1103/PhysRevC.95.044304](https://doi.org/10.1103/PhysRevC.95.044304).
- [Str+16] S. R. Stroberg, H. Hergert, J. D. Holt, et al., *Phys. Rev. C* **93**, 051301 (2016), [10.1103/PhysRevC.93.051301](https://doi.org/10.1103/PhysRevC.93.051301).
- [Miy+20] T. Miyagi, S. R. Stroberg, J. D. Holt, and N. Shimizu, *Phys. Rev. C* **102**, 034320 (2020), [10.1103/PhysRevC.102.034320](https://doi.org/10.1103/PhysRevC.102.034320).
- [Geb+17] E. Gebrerufael, K. Vobig, H. Hergert, and R. Roth, *Phys. Rev. Lett.* **118**, 152503 (2017), [10.1103/PhysRevLett.118.152503](https://doi.org/10.1103/PhysRevLett.118.152503).
- [Geb17] E. Gebrerufael, “In-medium no-core shell model for ab initio nuclear structure calculations”, PhD thesis (TU Darmstadt, 2017).
- [Vob20] K. Vobig, “Electromagnetic observables and open-shell nuclei from the in-medium no-core shell model”, PhD thesis (TU Darmstadt, 2020).
- [DAI+20] A. D’Alessio, T. Mongelli, M. Arnold, et al., *Phys. Rev. C* **102**, 011302(R) (2020), [10.1103/PhysRevC.102.011302](https://doi.org/10.1103/PhysRevC.102.011302).
- [Fro+22a] M. Frosini, T. Duguet, J.-P. Ebran, et al., *Eur. Phys. J. A* **58**, 63 (2022), [10.1140/epja/s10050-022-00693-y](https://doi.org/10.1140/epja/s10050-022-00693-y).

- [Mag54] W. Magnus, *Commun. Pure Appl. Math.* **7**, 649–673 (1954), <https://doi.org/10.1002/cpa.3160070404>.
- [Tic+19] A. Tichai, J. Müller, K. Vobig, and R. Roth, *Phys. Rev. C* **99**, 034321 (2019), [10.1103/PhysRevC.99.034321](https://doi.org/10.1103/PhysRevC.99.034321).
- [Hop+21] J. Hoppe, A. Tichai, M. Heinz, et al., *Phys. Rev. C* **103**, 014321 (2021), [10.1103/PhysRevC.103.014321](https://doi.org/10.1103/PhysRevC.103.014321).
- [RGP09] R. Roth, J. R. Gour, and P. Piecuch, *Phys. Lett. B* **679**, 334–339 (2009), <https://doi.org/10.1016/j.physletb.2009.07.071>.
- [Lan50] C. Lanczos, *J. Res. Natl. Bur. Stand.* **45**, 255–282 (1950).
- [MVS09] P. Maris, J. P. Vary, and A. M. Shirokov, *Phys. Rev. C* **79**, 014308 (2009), [10.1103/PhysRevC.79.014308](https://doi.org/10.1103/PhysRevC.79.014308).
- [RSS03] Z. Rolik, Á. Szabados, and P. R. Surján, *J. Chem. Phys.* **119**, 1922–1928 (2003), [10.1063/1.1584424](https://doi.org/10.1063/1.1584424).
- [Sur+04] P. Surján, Z. Rolik, Á. Szabados, and D. Köhalmi, *Ann. Phys.* **13**, 223–231 (2004), <https://doi.org/10.1002/andp.200310074>.
- [RS80] P. Ring and P. Schuck, *The nuclear many-body problem* - (Springer, Berlin, Heidelberg, 1980).
- [Suh07] J. Suhonen, *From nucleons to nucleus - concepts of microscopic nuclear theory* (Springer Science & Business Media, Berlin Heidelberg, 2007).
- [KM97] W. Kutzelnigg and D. Mukherjee, *J. Chem. Phys.* **107**, 432–449 (1997), [10.1063/1.474405](https://doi.org/10.1063/1.474405).
- [SB09] I. Shavitt and R. J. Bartlett, *Many-body methods in chemistry and physics: mbpt and coupled-cluster theory*, Cambridge Molecular Science (Cambridge University Press, 2009), [10.1017/CB09780511596834](https://doi.org/10.1017/CB09780511596834).
- [Wic50] G. C. Wick, *Phys. Rev.* **80**, 268–272 (1950), [10.1103/PhysRev.80.268](https://doi.org/10.1103/PhysRev.80.268).
- [Weg94] F. Wegner, *Ann. Phys.* **506**, 77–91 (1994), [10.1002/andp.19945060203](https://doi.org/10.1002/andp.19945060203).
- [Weg00] F. J. Wegner, *Nucl. Phys. B - Proc. Suppl.* **90**, 141–146 (2000), [https://doi.org/10.1016/S0920-5632\(00\)00911-7](https://doi.org/10.1016/S0920-5632(00)00911-7).
- [Heb21] K. Hebeler, *Phys. Rep.* **890**, 1–116 (2021), <https://doi.org/10.1016/j.physrep.2020.08.009>.
- [Bin+13] S. Binder, J. Langhammer, A. Calci, et al., *Phys. Rev. C* **87**, 021303 (2013), [10.1103/PhysRevC.87.021303](https://doi.org/10.1103/PhysRevC.87.021303).
- [Rot+12a] R. Roth, S. Binder, K. Vobig, et al., *Phys. Rev. Lett.* **109**, 052501 (2012), [10.1103/PhysRevLett.109.052501](https://doi.org/10.1103/PhysRevLett.109.052501).

- [GCR16] E. Gebrerufael, A. Calci, and R. Roth, Phys. Rev. C **93**, 031301 (2016), 10.1103/PhysRevC.93.031301.
- [MPB15] T. D. Morris, N. M. Parzuchowski, and S. K. Bogner, Phys. Rev. C **92**, 034331 (2015), 10.1103/PhysRevC.92.034331.
- [Bla+09] S. Blanes, F. Casas, J. Oteo, and J. Ros, Phys. Rep. **470**, 151–238 (2009), <https://doi.org/10.1016/j.physrep.2008.11.001>.
- [KMV88] V. K. Khersonskii, A. N. Moskalev, and D. A. Varshalovich, *Quantum theory of angular momentum* - (World Scientific, Singapur, 1988).
- [Eck30] C. Eckart, Rev. Mod. Phys. **2**, 305–380 (1930), 10.1103/RevModPhys.2.305.
- [Wig31] E. P. Wigner, *Gruppentheorie und ihre anwendung auf die quantenmechanik der atomspektren, etc* - (Freuburg i.B., 1931).
- [Whi02] S. R. White, J. Chem. Phys. **117**, 7472–7482 (2002), 10.1063/1.1508370.
- [Car+15] J. Carlson, S. Gandolfi, F. Pederiva, et al., Rev. Mod. Phys. **87**, 1067–1118 (2015), 10.1103/RevModPhys.87.1067.
- [Par+17] N. M. Parzuchowski, S. R. Stroberg, P. Navrátil, et al., Phys. Rev. C **96**, 034324 (2017), 10.1103/PhysRevC.96.034324.
- [Meu+17] A. Meurer, C. P. Smith, M. Paprocki, et al., PeerJ Comput. Sci. **3**, e103 (2017), 10.7717/peerj-cs.103.
- [FMS97] J. L. Friar, J. Martorell, and D. W. L. Sprung, Phys. Rev. A **56**, 4579–4586 (1997), 10.1103/PhysRevA.56.4579.
- [Ber+12] J. Beringer, J.-F. Arguin, R. M. Barnett, et al., Phys. Rev. D **86**, 010001 (2012), 10.1103/PhysRevD.86.010001.
- [JNF09] E. D. Jurgenson, P. Navrátil, and R. J. Furnstahl, Phys. Rev. Lett. **103**, 082501 (2009), 10.1103/PhysRevLett.103.082501.
- [Rot+11] R. Roth, J. Langhammer, A. Calci, et al., Phys. Rev. Lett. **107**, 072501 (2011), 10.1103/PhysRevLett.107.072501.
- [Heb12] K. Hebeler, Phys. Rev. C **85**, 021002 (2012), 10.1103/PhysRevC.85.021002.
- [Hüt21] T. Hütter, “Families of chiral two- plus three-nucleon interactions for accurate nuclear structure studies”, PhD thesis (TU Darmstadt, 2021).
- [Rot+12b] R. Roth, S. Binder, K. Vobig, et al., Phys. Rev. Lett. **109**, 052501 (2012), 10.1103/PhysRevLett.109.052501.

- [Her+13b] H. Hergert, S. K. Bogner, S. Binder, et al., *Phys. Rev. C* **87**, 034307 (2013), [10.1103/PhysRevC.87.034307](https://doi.org/10.1103/PhysRevC.87.034307).
- [Jan+14] G. R. Jansen, J. Engel, G. Hagen, et al., *Phys. Rev. Lett.* **113**, 142502 (2014), [10.1103/PhysRevLett.113.142502](https://doi.org/10.1103/PhysRevLett.113.142502).
- [Str+17] S. R. Stroberg, A. Calci, H. Hergert, et al., *Phys. Rev. Lett.* **118**, 032502 (2017), [10.1103/PhysRevLett.118.032502](https://doi.org/10.1103/PhysRevLett.118.032502).
- [Som+20] V. Somà, P. Navrátil, F. Raimondi, et al., *Phys. Rev. C* **101**, 014318 (2020), [10.1103/PhysRevC.101.014318](https://doi.org/10.1103/PhysRevC.101.014318).
- [Tic+18a] A. Tichai, P. Arthuis, T. Duguet, et al., *Phys. Lett. B* **786**, 195–200 (2018), <https://doi.org/10.1016/j.physletb.2018.09.044>.
- [Tic+18b] A. Tichai, E. Gebrerufael, K. Vobig, and R. Roth, *Phys. Lett. B* **786**, 448–452 (2018), <https://doi.org/10.1016/j.physletb.2018.10.029>.
- [Thi+00] P. Thirolf, B. Pritychenko, B. Brown, et al., *Phys. Lett. B* **485**, 16–22 (2000), [https://doi.org/10.1016/S0370-2693\(00\)00720-6](https://doi.org/10.1016/S0370-2693(00)00720-6).
- [Oza+00] A. Ozawa, T. Kobayashi, T. Suzuki, et al., *Phys. Rev. Lett.* **84**, 5493–5495 (2000), [10.1103/PhysRevLett.84.5493](https://doi.org/10.1103/PhysRevLett.84.5493).
- [Hof+09] C. Hoffman, T. Baumann, D. Bazin, et al., *Phys. Lett. B* **672**, 17–21 (2009), <https://doi.org/10.1016/j.physletb.2008.12.066>.
- [Kan+09] R. Kanungo, C. Nociforo, A. Prochazka, et al., *Phys. Rev. Lett.* **102**, 152501 (2009), [10.1103/PhysRevLett.102.152501](https://doi.org/10.1103/PhysRevLett.102.152501).
- [Tra+18] D. T. Tran, H. J. Ong, G. Hagen, et al., *Nat. Commun.* **23** (2018) [10.1038/s41467-018-04024-y](https://doi.org/10.1038/s41467-018-04024-y).
- [Wie+08] M. Wiedeking, P. Fallon, A. O. Macchiavelli, et al., *Phys. Rev. Lett.* **100**, 152501 (2008), [10.1103/PhysRevLett.100.152501](https://doi.org/10.1103/PhysRevLett.100.152501).
- [Ong+08] H. J. Ong, N. Imai, D. Suzuki, et al., *Phys. Rev. C* **78**, 014308 (2008), [10.1103/PhysRevC.78.014308](https://doi.org/10.1103/PhysRevC.78.014308).
- [Pet+11] M. Petri, P. Fallon, A. O. Macchiavelli, et al., *AIP Conf. Proc.* **1377**, 96–103 (2011), [10.1063/1.3628363](https://doi.org/10.1063/1.3628363).
- [Pet+12] M. Petri, S. Paschalis, R. M. Clark, et al., *Phys. Rev. C* **86**, 044329 (2012), [10.1103/PhysRevC.86.044329](https://doi.org/10.1103/PhysRevC.86.044329).
- [McC+12] E. A. McCutchan, C. J. Lister, S. C. Pieper, et al., *Phys. Rev. C* **86**, 014312 (2012), [10.1103/PhysRevC.86.014312](https://doi.org/10.1103/PhysRevC.86.014312).
- [Vos+12] P. Voss, T. Baugher, D. Bazin, et al., *Phys. Rev. C* **86**, 011303 (2012), [10.1103/PhysRevC.86.011303](https://doi.org/10.1103/PhysRevC.86.011303).

- [FRN13] C. Forssén, R. Roth, and P. Navrátil, *J. Phys. G: Nucl. Part. Phys.* **40**, 055105 (2013), [10.1088/0954-3899/40/5/055105](https://doi.org/10.1088/0954-3899/40/5/055105).
- [Nov+20] S. J. Novario, G. Hagen, G. R. Jansen, and T. Papenbrock, *Phys. Rev. C* **102**, 051303 (2020), [10.1103/PhysRevC.102.051303](https://doi.org/10.1103/PhysRevC.102.051303).
- [PR87] A. Poves and J. Retamosa, *Phys. Lett. B* **184**, 311–315 (1987), [https://doi.org/10.1016/0370-2693\(87\)90171-7](https://doi.org/10.1016/0370-2693(87)90171-7).
- [WBB90] E. K. Warburton, J. A. Becker, and B. A. Brown, *Phys. Rev. C* **41**, 1147–1166 (1990), [10.1103/PhysRevC.41.1147](https://doi.org/10.1103/PhysRevC.41.1147).
- [CNP14] E. Caurier, F. Nowacki, and A. Poves, *Phys. Rev. C* **90**, 014302 (2014), [10.1103/PhysRevC.90.014302](https://doi.org/10.1103/PhysRevC.90.014302).
- [Wim+10] K. Wimmer, T. Kröll, R. Krücken, et al., *Phys. Rev. Lett.* **105**, 252501 (2010), [10.1103/PhysRevLett.105.252501](https://doi.org/10.1103/PhysRevLett.105.252501).
- [Iwa+01] H. Iwasaki, T. Motobayashi, H. Sakurai, et al., *Phys. Lett. B* **522**, 227–232 (2001), [https://doi.org/10.1016/S0370-2693\(01\)01244-8](https://doi.org/10.1016/S0370-2693(01)01244-8).
- [Yor+07] D. T. Yordanov, M. Kowalska, K. Blaum, et al., *Phys. Rev. Lett.* **99**, 212501 (2007), [10.1103/PhysRevLett.99.212501](https://doi.org/10.1103/PhysRevLett.99.212501).
- [Doo+13] P. Doornenbal, H. Scheit, S. Takeuchi, et al., *Phys. Rev. Lett.* **111**, 212502 (2013), [10.1103/PhysRevLett.111.212502](https://doi.org/10.1103/PhysRevLett.111.212502).
- [Doo+16] P. Doornenbal, H. Scheit, S. Takeuchi, et al., *Phys. Rev. C* **93**, 044306 (2016), [10.1103/PhysRevC.93.044306](https://doi.org/10.1103/PhysRevC.93.044306).
- [Cau+98] E. Caurier, F. Nowacki, A. Poves, and J. Retamosa, *Phys. Rev. C* **58**, 2033–2040 (1998), [10.1103/PhysRevC.58.2033](https://doi.org/10.1103/PhysRevC.58.2033).
- [Uts+99] Y. Utsuno, T. Otsuka, T. Mizusaki, and M. Honma, *Phys. Rev. C* **60**, 054315 (1999), [10.1103/PhysRevC.60.054315](https://doi.org/10.1103/PhysRevC.60.054315).
- [YV04] M. Yamagami and N. Van Giai, *Phys. Rev. C* **69**, 034301 (2004), [10.1103/PhysRevC.69.034301](https://doi.org/10.1103/PhysRevC.69.034301).
- [Tsu+17] N. Tsunoda, T. Otsuka, N. Shimizu, et al., *Phys. Rev. C* **95**, 021304 (2017), [10.1103/PhysRevC.95.021304](https://doi.org/10.1103/PhysRevC.95.021304).
- [Mar+11] K. Marinova, W. Geithner, M. Kowalska, et al., *Phys. Rev. C* **84**, 034313 (2011), [10.1103/PhysRevC.84.034313](https://doi.org/10.1103/PhysRevC.84.034313).
- [Zho+16] E. Zhou, J. Yao, Z. Li, et al., *Phys. Lett. B* **753**, 227–231 (2016), <https://doi.org/10.1016/j.physletb.2015.12.028>.
- [Mar+18] P. Marević, J.-P. Ebran, E. Khan, et al., *Phys. Rev. C* **97**, 024334 (2018), [10.1103/PhysRevC.97.024334](https://doi.org/10.1103/PhysRevC.97.024334).

- [Jan+16] G. R. Jansen, M. D. Schuster, A. Signoracci, et al., *Phys. Rev. C* **94**, 011301 (2016), [10.1103/PhysRevC.94.011301](https://doi.org/10.1103/PhysRevC.94.011301).
- [Str+19] S. R. Stroberg, H. Hergert, S. K. Bogner, and J. D. Holt, *Annu. Rev. Nucl. Part. Sci.* **69**, 307–362 (2019), [10.1146/annurev-nucl-101917-021120](https://doi.org/10.1146/annurev-nucl-101917-021120).
- [AGZ20] R. An, L.-S. Geng, and S.-S. Zhang, *Phys. Rev. C* **102**, 024307 (2020), [10.1103/PhysRevC.102.024307](https://doi.org/10.1103/PhysRevC.102.024307).
- [Pri+16] B. Pritychenko, M. Birch, B. Singh, and M. Horoi, *At. Data Nucl. Data Tables* **107**, 1–139 (2016), [10.1016/j.adt.2015.10.001](https://doi.org/10.1016/j.adt.2015.10.001).
- [CR16] A. Calci and R. Roth, *Phys. Rev. C* **94**, 014322 (2016), [10.1103/PhysRevC.94.014322](https://doi.org/10.1103/PhysRevC.94.014322).
- [KPS17] J. Kelley, J. Purcell, and C. Sheu, *Nucl. Phys. A* **968**, 71–253 (2017), <https://doi.org/10.1016/j.nuclphysa.2017.07.015>.
- [Ver+83] W. Vermeer, M. Esat, J. Kuehner, et al., *Phys. Lett. B* **122**, 23–26 (1983), [https://doi.org/10.1016/0370-2693\(83\)91160-7](https://doi.org/10.1016/0370-2693(83)91160-7).
- [Wan+17] M. Wang, G. Audi, F. G. Kondev, et al., *Chinese Phys. C* **41**, 030003 (2017), [10.1088/1674-1137/41/3/030003](https://doi.org/10.1088/1674-1137/41/3/030003).
- [BM98] A. Bohr and B. R. Mottelson, *Nuclear structure* (World Scientific, London, 1998).
- [Bog+14] S. K. Bogner, H. Hergert, J. D. Holt, et al., *Phys. Rev. Lett.* **113**, 142501 (2014), [10.1103/PhysRevLett.113.142501](https://doi.org/10.1103/PhysRevLett.113.142501).
- [Fro+22b] M. Frosini, T. Duguet, J.-P. Ebran, and V. Soma, *Eur. Phys. J. A* **58**, 62 (2022), [10.1140/epja/s10050-022-00692-z](https://doi.org/10.1140/epja/s10050-022-00692-z).
- [Fro+22c] M. Frosini, T. Duguet, J.-P. Ebran, et al., *Eur. Phys. J. A* **58**, 64 (2022), [10.1140/epja/s10050-022-00694-x](https://doi.org/10.1140/epja/s10050-022-00694-x).
- [EM03] D. R. Entem and R. Machleidt, *Phys. Rev. C* **68**, 041001 (2003), [10.1103/PhysRevC.68.041001](https://doi.org/10.1103/PhysRevC.68.041001).
- [GQN09] D. Gazit, S. Quaglioni, and P. Navrátil, *Phys. Rev. Lett.* **103**, 102502 (2009), [10.1103/PhysRevLett.103.102502](https://doi.org/10.1103/PhysRevLett.103.102502).
- [GQN19] D. Gazit, S. Quaglioni, and P. Navrátil, *Phys. Rev. Lett.* **122**, 029901 (2019), [10.1103/PhysRevLett.122.029901](https://doi.org/10.1103/PhysRevLett.122.029901).
- [AM13] I. Angeli and K. Marinova, *At. Data Nucl. Data Tables* **99**, 69–95 (2013), <https://doi.org/10.1016/j.adt.2011.12.006>.
- [Jia+20] W. G. Jiang, A. Ekström, C. Forssén, et al., *Phys. Rev. C* **102**, 054301 (2020), [10.1103/PhysRevC.102.054301](https://doi.org/10.1103/PhysRevC.102.054301).

- [HJP16] G. Hagen, G. R. Jansen, and T. Papenbrock, *Phys. Rev. Lett.* **117**, 172501 (2016), [10.1103/PhysRevLett.117.172501](https://doi.org/10.1103/PhysRevLett.117.172501).
- [Sim+17] J. Simonis, S. R. Stroberg, K. Hebeler, et al., *Phys. Rev. C* **96**, 014303 (2017), [10.1103/PhysRevC.96.014303](https://doi.org/10.1103/PhysRevC.96.014303).
- [Ajz91] F. Ajzenberg-Selove, *Nucl. Phys. A* **523**, 1–196 (1991), [https://doi.org/10.1016/0375-9474\(91\)90446-D](https://doi.org/10.1016/0375-9474(91)90446-D).
- [TWC93] D. Tilley, H. Weller, and C. Cheves, *Nucl. Phys. A* **564**, 1–183 (1993), [https://doi.org/10.1016/0375-9474\(93\)90073-7](https://doi.org/10.1016/0375-9474(93)90073-7).
- [Til+95] D. Tilley, H. Weller, C. Cheves, and R. Chasteler, *Nucl. Phys. A* **595**, 1–170 (1995), [https://doi.org/10.1016/0375-9474\(95\)00338-1](https://doi.org/10.1016/0375-9474(95)00338-1).
- [Til+98] D. Tilley, C. Cheves, J. Kelley, et al., *Nucl. Phys. A* **636**, 249–364 (1998), [https://doi.org/10.1016/S0375-9474\(98\)00129-8](https://doi.org/10.1016/S0375-9474(98)00129-8).
- [Bas15] M. S. Basunia, *Nucl. Data Sheets* **127**, 69–190 (2015), <https://doi.org/10.1016/j.nds.2015.07.002>.
- [Tsh+12] K. Tshoo, Y. Satou, H. Bhang, et al., *Phys. Rev. Lett.* **109**, 022501 (2012), [10.1103/PhysRevLett.109.022501](https://doi.org/10.1103/PhysRevLett.109.022501).
- [Kon+16] Y. Kondo, T. Nakamura, R. Tanaka, et al., *Phys. Rev. Lett.* **116**, 102503 (2016), [10.1103/PhysRevLett.116.102503](https://doi.org/10.1103/PhysRevLett.116.102503).
- [Hei+20] S. Heil, M. Petri, K. Vobig, et al., *Phys. Lett. B* **809**, 135678 (2020), <https://doi.org/10.1016/j.physletb.2020.135678>.
- [Fir15] R. Firestone, *Nuclear Data Sheets* **127**, 1–68 (2015), <https://doi.org/10.1016/j.nds.2015.07.001>.
- [Til+04] D. Tilley, J. Kelley, J. Godwin, et al., *Nucl. Phys. A* **745**, 155–362 (2004), <https://doi.org/10.1016/j.nuclphysa.2004.09.059>.
- [Fir07] R. Firestone, *Nucl. Data Sheets* **108**, 2319–2392 (2007), <https://doi.org/10.1016/j.nds.2007.10.001>.
- [BH16] M. Basunia and A. Hurst, *Nucl. Data Sheets* **134**, 1–148 (2016), <https://doi.org/10.1016/j.nds.2016.04.001>.
- [Sha13] M. Shamsuzzoha Basunia, *Nucl. Data Sheets* **114**, 1189–1291 (2013), <https://doi.org/10.1016/j.nds.2013.10.001>.
- [Sha10] M. Shamsuzzoha Basunia, *Nucl. Data Sheets* **111**, 2331–2424 (2010), <https://doi.org/10.1016/j.nds.2010.09.001>.
- [OS11] C. Ouellet and B. Singh, *Nucl. Data Sheets* **112**, 2199–2355 (2011), <https://doi.org/10.1016/j.nds.2011.08.004>.

- [SC21] M. Shamsuzzoha Basunia and A. Chakraborty, Nucl. Data Sheets **171**, 1–252 (2021), <https://doi.org/10.1016/j.nds.2020.12.001>.
- [Fir09] R. Firestone, Nucl. Data Sheets **110**, 1691–1744 (2009), <https://doi.org/10.1016/j.nds.2009.06.001>.
- [Ram+87] S. Raman, C. Malarkey, W. Milner, et al., At. Data Nucl. Data Tables **36**, 1–96 (1987), [https://doi.org/10.1016/0092-640X\(87\)90016-7](https://doi.org/10.1016/0092-640X(87)90016-7).
- [Sto05] N. Stone, At. Data Nucl. Data Tables **90**, 75–176 (2005), <https://doi.org/10.1016/j.adt.2005.04.001>.
- [Hei+21] M. Heinz, A. Tichai, J. Hoppe, et al., Phys. Rev. C **103**, 044318 (2021), [10.1103/PhysRevC.103.044318](https://doi.org/10.1103/PhysRevC.103.044318).

Danksagung

Auf dem Weg zum Zustandekommen dieser Arbeit gibt es einige Menschen, denen ich gerne danken möchte.

Zuerst möchte ich meinem Doktorvater Robert Roth ganz herzlich dafür danken, dass er mich in seine Arbeitsgruppe aufgenommen, meine Promotion betreut und die Arbeit an diesem spannenden Thema erst ermöglicht hat. Außerdem danke ich ihm dafür, dass er eine sehr gute Arbeitsatmosphäre schafft und ich immer mit ihm reden konnte. Weiterhin auch vielen Dank für die hilfreichen Korrekturen, Ratschläge und Diskussionen.

Ich möchte auch Kai Hebler dafür danken, die Rolle des Korreferenten zu übernehmen.

Danke an alle aktiven und ehemaligen Mitglieder der TNP++ Gruppe. Danke an Marco und Julius für das Korrekturlesen meiner Arbeit und vielen Dank an Roland, Tobi und nochmal Julius für alle Tipps theorie- und programmiertechnischer Art. Danke an Klaus für die Einführung in die Thematik und die Geduld und Beantwortung der vielen Fragen, gerade in der Anfangszeit und danke an Laura, Carl, Cedric und Patrick. Danke an Stefan und Thomas für einen schönen Urlaub nach der Konferenz in Vancouver und die gute Arbeitsatmosphäre im Büro.

Danke auch an meine Freunde Kai, Ben und Joshi für Abende zum Abschalten, wenn es mal stressig wurde. Danke an Sonja für Ratschläge und viele Gespräche über Gott und die Welt.

Danke an meine Eltern Michi und Ingo für eure Unterstützung auf meinem Lebensweg.

Schließlich danke ich Pauline für die schönsten Zeiten, dafür, dass du mich immer unterstützt, egal zu welcher Tages- und Nachtzeit.

Akademischer Werdegang

Persönliche Daten

Name	Tobias Mongelli
Geburtsdatum	02.02.1993
Geburtsort	Frankfurt am Main
Nationalität	Deutsch

Akademische Ausbildung

2018-2022	Promotion Physik, TU Darmstadt
2016-2018	Masterstudium Chemie, TU Darmstadt, Abschluss: M.Sc.
2013-2016	Bachelorstudium Chemie, TU Darmstadt, Abschluss: B.Sc.
2004-2013	Carl-Schurz-Schule Frankfurt am Main, Abschluss: Abitur

Publikationen

2020	A. D'Alessio, T. Mongelli, M. Arnold, et al., Precision measurement of the E2 transition strength to the 2_1^+ state of ^{12}C , Phys. Rev. C 102 , 011302(R) (2020)
2022	M. Frosini, T. Duguet, J.-P. Ebran, et al., Multi-reference many-body perturbation theory for nuclei II - Ab initio study of neon isotopes via PGCM and IM-NCSM calculations, Eur. Phys. J. A 58 , 63 (2022)
2022	T. Mongelli, T. Hüther, K. Vobig, et al., Carbon Isotopes from the In-Medium NCSM, in preparation (2022)

Erklärung gemäß §9 Promotionsordnung

Hiermit versichere ich, dass ich die vorliegende Dissertation selbstständig angefertigt und keine anderen als die angegebenen Quellen und Hilfsmittel verwendet habe. Alle wörtlichen und paraphrasierten Zitate wurden angemessen kenntlich gemacht. Die Arbeit hat bisher noch nicht zu Prüfungszwecken gedient.

Datum, Ort

Unterschrift